
UNIVERSITY OF BIRMINGHAM

# Protective Layer Coatings for Solid Oxide Fuel Cell Interconnects by Inkjet Printing

**by**

**SATHISH PANDIYAN**

**(Student ID: 1473487)**

*A Thesis submitted to the University of Birmingham for the*

**Degree of Doctor of Philosophy**

**Supervisor:**
**Prof. Robert Steinberger-Wilckens**

**Co-supervisor:**
**Dr Ahmad El-Kharouf**

**This work was performed at:**
**Centre for Fuel Cell and Hydrogen Research**
**School of Chemical Engineering**
**College of Engineering and Physical Sciences**
**University of Birmingham**
**October 2019**

*“Life is and will ever remain an equation incapable of solution, but it contains certain known factors.”*

*- Nikola Tesla.*

# ABSTRACT

Interconnects form an integral part of the solid oxide fuel cell (SOFC); they provide structural support and electrical connection between individual fuel cell units in a stack. Currently, ferritic based stainless steels (FSSs) are considered as the standard interconnect materials. FSSs forms a protective chromia layer in SOFC cathode conditions at high-temperature operation. The thermally grown oxide layer slows down the oxidation and offers resistance against high-temperature corrosion. However, the thermally grown oxide layer (chromia) formed during the operation of SOFC stacks leads to a continuous degradation in key properties of the FSS interconnect material. Consequently, leading to volatilisation of chromium from the oxide scale with subsequent chromium poisoning of the cathode, and increased electrical contact resistance. To overcome these degradation mechanisms, mitigation methods such as the development of conductive and protective coatings, surface treatment/ modifications, and alloy development are being continuously studied. In this study, inkjet printing technology, a novel, very flexible, and low-cost approach to the coating was employed for the application of protective layer coatings on SOFC metallic interconnects.

The work presented focusses on the formulation of aqueous-based spinel particulate inks for the inkjet printing process using an electro-magnetic inkjet printer. An ink formulation route based on a two-stage ball milling technique was developed to produce a printable ink composition with Manganese Cobalt Oxide ($MnCo_2O_4$, MCO), Manganese Cobalt Ferrite ($MnCo_{1.8}Fe_{0.2}O_4$, MCF) and copper doped MCF ($MnCo_{1.6}Fe_{0.2}Cu_{0.2}$, MCFC) spinels as the coating materials. The printability of the formulated inks was demonstrated by printing them on stainless-steel substrates (K41 and Crofer 22H) and their performance as a protective layer was evaluated based on high-temperature oxidation and area-specific resistance (ASR) measurements  The high-temperature tests were performed at 700 °C in the air with 3%

humidity for 1000 hours, simulating SOFC operating conditions at the cathode side. The performance of the printed layers was assessed based on ASR values and chromium retention. The effect of surface plasma nitriding on K41 stainless steel substrates was studied under similar test conditions. With ASR reduced to a level ~ 0.05Ω $cm^2$ and chromium concentration in the getter (cathode) material below 1 atomic%, close to the detection threshold, the protective layers produced would qualify for SOFC applications.

# Acknowledgements

First and foremost, I would like to express my heartfelt gratefulness to Prof. Robert Steinberger-Wilckens for giving me this opportunity and for being a great mentor. I want to thank him from the bottom of my heart for his trust and faith in me in this PhD journey. The positivity that he feeds in after every discussion has been a great source of motivation and helped me to get through any circumstances with ease all these years.

I want to express my sincere gratitude to Dr. Ahmad El-Kharouf, my co-supervisor. I always looked up to him, always seeking for answers and suggestions whenever I was in transfix with my work. I am thankful for all his time and critical suggestions for my research work.

I would like to appreciate John Hooper, our project manager, such a friendly person who has always been there to help me out. Thank you, John, for everything! I like to extend my thanks to Lynn Draper and everyone in the Chem Engg PG administration office. I want to thank our research technician, Chynthol Kanhimbe, and Dr Mark Taylor from Sci-City lab for their time and help in lab related issues. I like to thank our post-docs Artur, Jong- Eun Hong, Lina and Anissa for their help. I would like to thank Dr Rumen Tomov and Prof R. Vasant kumar for letting me acess the inkjet printing facility for the research work.

To Melissa Oum, my SCORED project partner! For being a wonderful friend one who can always count on. To Kun Zhang, who has been my go-to person all these years. He has been a fantastic friend throughout. To Oujen, the guy who ligthens up smile always. To, Pete, Alan, Liam, Chris, Abby, Bhargav, Naseer, Ahmed each and everyone from my group. Thank you!

To, Tshaiya Devi, who has been an amazing person in this journey, her support, motivation, and time means a lot! To, my friend Shiva and his family (and their little baby girl, Shanaya), for their great support. To, my lovely housemates all these years (Natasha, Fatma, Bhargav, Shreya, Alper, Hassan and Joel) and my landlady, Sarah. Thank you!

With immense pleasure, I want to acknowledge my cricket team in Birmingham, BPCC and my fellow players in the team. I want to thank my friends, Nishanth, Sharvan, Vishal, Tejas, Sudhir, Keerthana, Prasanna, Rajiv, Joel, for all the good time spent through these years. To, all my friends back home: Arthi, Chidam, Anand, Thamari, Mani, Gokul, Ram, Aravinth, Suman, Jayant, Sangeetha, for their constant support. To, Shambavi, for all the well wishes, positive vibes and friendship. Thank you, everyone!

Finally, I would like to thank my family, Appa, Amma and Anna, for their love and support. I am grateful for all the trust and faith they have in me. I am fortunate to enjoy such freedom and pursue my aspirations with their full support and blessings. Special thanks to my brother for being a great support in everything I do.

# Table of Contents

# List of Figures

## Chapter 1



## Chapter 2

## Chapter 3

## Chapter 4

## Chapter 5

## Chapter 6

# List of Tables

## Chapter 2



## Chapter 3



## Chapter 4

## Chapter 5

# List of Abbrevations

| | |
|---|---|
| SOFC | Solid Oxide Fuel Cell |
| FSS | Ferritic Stainless Steel |
| ASR | Area Specific Resistance |
| SRU | Single Repeating Unit |
| DOD | Drop On Demand |
| TPB | Triple Phase Boundary |
| PNNL | Pacific Northwest National Laboratory |
| CTE | Coefficient of Thermal Expansion |
| SS | Stainless Steel |
| BCC | Body Centered Cubic |
| FCC | Face Centered Cubic |
| APU | Axillary Power Unit |
| REO | Reactive Element Oxide |
| PVD | Physical Vapour Deposition |
| ALD | Atomic Layer Deposition |
| PVA | Poly Vinyl Alcohol |
| PEG | Poly Ethylene Glycol |
| IEP | Iso Electric Point |
| EDL | Electrochemical Double Layer |
| PSD | Particle Size Distribution |
| PAV | Piezo Axial Vibrator |
| FVM | Focus-Variation Microscope |
| TGA | Thermo-Grvametric Analysis |
| XRD | X-ray Diffraction |
| SEM | Scanning Electron Microscopy |

| | |
|---|---|
| BSE | Back Scattered Electrons |
| EDS | Energy Dispersive Spectrum |
| MCO | $MnCo_2O_4$ |
| MCF | $MnCo_{1.8}FeO_4$ |
| MCFC | $MnCo_{1.6}Fe_{0.2}Cu_{0.2}$ |
| CMF | $Cu_{1.3}Mn_{1.6}Fe_{0.1}O_4$ |

# *Chapter 1: Introduction and Research objective*

This chapter introduces solid oxide fuel cells (SOFCs), the role of the interconnect component in the operation of an SOFC and highlights the context of this work in the development of SOFC technology. Here, the scope and objectives of the research are put forward with an outline of the thesis.

# 1.1. Introduction

Access to sustainable energy is a prime factor for economic development, human welfare, and a sustainably habitable planet. Energy consumption driven by fossil fuels (coal, oil, gas) supported rapid industrialisation and technological progress over the last two centuries. The excessive consumption of fossil fuels with release of carbon-di-oxide ($CO_2$) and greenhouse gases caused a severe impact on the global climate. The effect is enhanced by the tremendous increase in energy demand throughout the globe due to population growth; expected to reach 9 billion by 2050 [1]. The split of carbon emissions from various sectors such as power generation, transport, manufacturing and other industries is shown in Fig. 1.1. The major global challenge is to set a transition from fossil fuels to renewable energy resources, to achieve a low carbon economy, and to meet the increasing energy demand. The fluctuations of renewable energy sources, though, necessitate considerable capacity of energy storage.

The utilisation of hydrogen as an energy carrier is considered to be a promising solution to the storage needs of renewable energy sources, as the excess energy harvested from renewable energy sources can be utilised to produce hydrogen via electrolysis. The obtained hydrogen can be used as a fuel for fuel cells to produce electrical energy and heat. Fuel cells are energy conversion devices which yield electrical energy and heat by the electrochemical reaction of fuel (hydrogen) with an oxidant (air) [2]. A typical fuel cell consists of an anode, electrolyte, and cathode layers. When a gaseous fuel and an oxidant are fed externally through anode and cathode, respectively, an electrochemical reaction happens at the electrodes to produce electrons which flows via an external circuit. The operation of a fuel cell eliminates the combustion of fuel facilitates higher energy conversion efficiency and lower emission of greenhouse gases and other harmful gases (nitrous oxide, sulphur oxide and $CO_2$), in comparison to other conventional technologies.

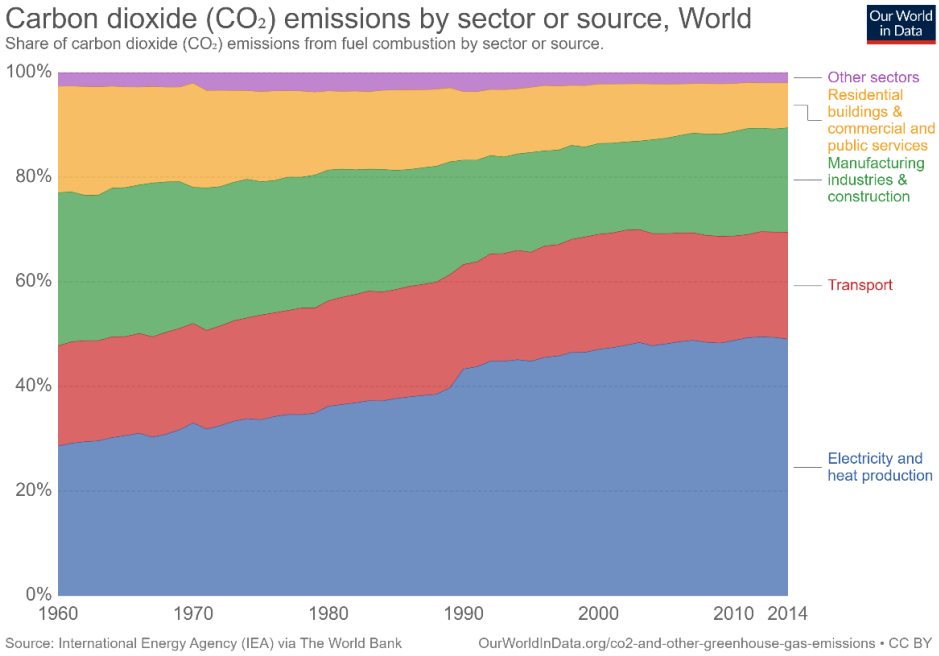


**Figure 1.1:** Representation of $CO_2$ emissions by various sectors from 1960 to 2014. The major contributors were electricity and heat production, transport and manufacturing industries, taken from [3].

Fuel cells can be employed in different applications such as automobile, power generators; large- and small-scale power plants, and portable applications. Fuel cells are classified into different types based on the temperature of operation and the nature of the electrolyte used, as shown in Fig. 1.2 (a). The present work focuses on the Solid Oxide Fuel Cell (SOFC) that operates in the temperature range 600-900 °C. SOFCs have the advantages of flexibility to different fuels (natural gas, biofuels) along with hydrogen offering high efficiency of potentially up to 70% with fuel regeneration [4]. Also, SOFC systems can operate as combined heat and power (CHP) systems, and in the reverse mode; as an electrolyser to produce hydrogen. Despite the advantages, the commercialisation (industrial and domestic) of SOFCs is being challenged due to factors such as complex stack fabrication, expensive functional materials, high operating temperature, and degradation of the cell components during long-time operation.

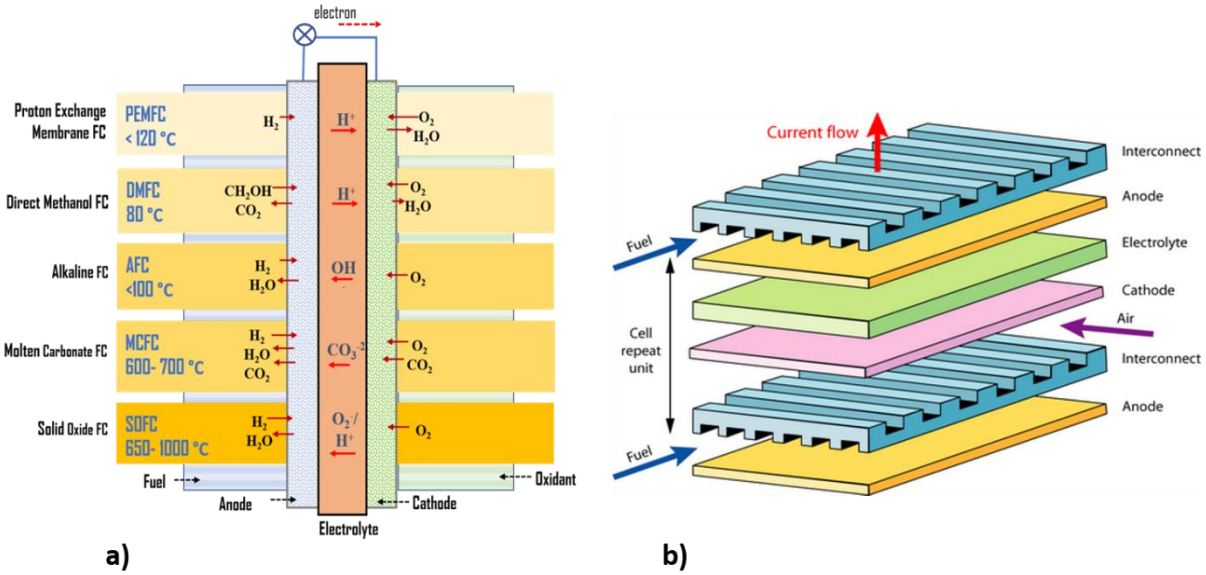


**Figure 1.2:** a) Representation of a typical fuel cell and its types based on the temperature of operation and the nature of the electrolyte, adapted from [5].b) Schematic of a planar SOFC stack [6].

A single SOFC is made of porous electrodes and a dense solid electrolyte, which conducts either oxide ions ($O^{2-}$) or protons ($H^{+}$) as shown in Fig. 1.2 (a). The dense electrolyte, permeable only to ions, prevents the direct interaction between the oxidant and the fuel gases. At high temperature, electrons are generated as a result of the electrochemical reduction and oxidation of oxidant and fuel at the anode and the cathode respectively. Thus, the generated electrons flow towards the cathode from the anode via an electrical circuit to complete the reactions and produce electricity. The electrochemical reactions in an SOFC fed with hydrogen fuel and oxygen at the anode and cathode respectively are shown in Equation 1.1- 1.3.

Reduction of oxygen at the cathode, $\frac{1}{2}O_2 + 2e^- \rightarrow O^{2-}$ (1.1)

Oxidation of hydrogen at the anode, $H_2 + O^{2-} \rightarrow H_2O + 2e^-$ (1.2)

Overall reaction: $\frac{1}{2}O_2 + H_2 \rightarrow H_2O$ (steam) (1.3)

In order to achieve higher power output, multiple cells are stacked in series to form an SOFC stack. In a stack, fuel cells or single repeating units (SRUs) are electrically connected by interconnects. Interconnects form an integral part of a solid oxide fuel cell (SOFC) stack, providing structural support and electrical connection between the individual SRUs, shown in Fig. 1.2 (b). Therefore, the interconnect material must have the following characteristics: (i) good electrical conductivity to transport electrons between the SRUs and the external circuit, i.e., electrical resistivityof less than 0.1 $\Omega$ $cm^2$, (ii) good thermal conductivity to provide even heat distribution across the fuel cell stack, (iii) compatible thermal coefficient of expansion with the other fuel cell materials (12-13×$10^{-6}$/K) to minimise thermal stresses during thermal cycling. (iv) good mechanical stability (high creep resistance to prevent failure during thermal cycling of the stack). (v) impermeability to the fuel and oxidant, (vi) resistance to oxidation, carburisation and sulfurisation and (vii) a stable microstructure at high temperature.

The potential materials that balance the mentioned criteria for SOFC interconnects are ceramic-based (Lanthanum chromate) and metallic based materials (chromium-based alloys and ferritic stainless steels). Ceramic based materials were utilised in high-temperature SOFC operation (900 to 1000 °C). Currently, SOFC units are widely studied and operated in between 700 and 850 °C where metallic based materials are employed as interconnect.

The long term operation of SOFC poses severe material challenges surrounding mechanical failure of functional layers and sealants, thermal gradients in the stack and degradation mechanisms initiated from interconnects [7]. The two significant factors for degradation associated with the metallic interconnects are high-temperature corrosion and mechanical deformation. The present study focuses on the degradation of metallic interconnects concerning their corrosion behaviour.

## 1.2. Background

Ferritic stainless steels are currently considered as the standard interconnects material [8,9]. Fe-based alloys are protected against corrosion by adding 17 to 24% chromium content, which helps to form a protective oxide layer (chromia) over the alloy surface. The protective layer acts as a passivation layer and prevents the base metal from further corrosion at the cathode side of the fuel cell. However, during long-time operation, the thermally growing oxide layer increases the electrical resistance of the fuel cell stack due to their lower electrical conductivity. Also, when in contact with the cathode under SOFC operating conditions, these stainless steels act as a rich source of chromium which migrates towards the interconnect surface and subsequently to the SOFC cathode, resulting in an overall stack degradation due to the following issues:

(i) the volatilisation of chromium that is removed from the grown oxide scale surface, thereby weakening the corrosion resistance of the stainless steel,

(ii) solid state diffusion of chromium species into the cathode material where points of direct contact exist, with subsequent,

(iii) chromium poisoning of the cathode by deposition of the volatilised Cr species within the cathode material (as $Cr_2O_3$, blocking porosity) or

(iv) chemical reaction with the cathode material (depending on the cathode composition), e.g. forming chromium-manganese spinels, thus changing the cathode catalytic performance and electrical and microstructural properties [10–12].

## 1.3. Research motivation

To overcome the mentioned degradation mechanisms, mitigation methods such as the development of conductive and protective coatings, surface treatment/ modification, and alloy development are continuously being studied [13,14]. Alloy modification for improved corrosion resistance, reduced chromium evaporation, and decreased contact resistance is one approach but has not achieved enough suppression of chromium evaporation to avoid chromium poisoning. Hence, the application of protective coatings and surface modification have been suggested as a lower-cost approach to utilise commercially available stainless steels in SOFC applications [15]. Spinel coatings have received significant attention, and different spinel compositions are being analysed to find optimal protective-conductive layers for SOFC interconnects with low oxidation rate, low contact resistance, low electrical resistance, high adhesion, and, above all, low release rates of chromium. Manganese cobalt oxide (MCO) spinel, for instance, deposited on Crofer 22H stainless steel exhibited area specific resistance value of 0.01 Ω $cm^2$ and formed an effective barrier for Cr diffusion at 800 °C after 1000 hours [13,14,16].

The inkjet printing process (IJP) has been widely used in the deposition of functional coatings and patterns in various applications. The deposition process with IJP is automated, precise, and controlled for liquid droplet volume, which ensures consistent deposition over the substrates. The Drop-on-Demand (DOD) mode of inkjet printing ejects ink droplets at pre-determined positions and eliminates the need for masking over 3D structures. Intensive studies have been carried out on inkjet deposition of functional materials in applications for ceramics, electronics, diodes, thin-film transistors, conductive structures, sensors and biological membranes [17]. Few studies have been reported on the use of inkjet printing for the application of SOFC functional layers [18–21]. The electromagnetic print head used in the present study offers

greater flexibility in the ink formulation and is capable of jetting both suspension and solution based inks with variable rheology. Therefore, this study combines developments in spinel inkjet inks and the use of inkjet printing technology for interconnect coatings to be able to apply the ink on ferritic based stainless steel substrates.

## 1.4. Research objective

The present study evaluates the inkjet deposition technique for protective layer coatings in SOFC interconnect applications at 700 °C. Aqueous based spinel inks were formulated and deposited over virgin and surface nitrided interconnect stainless steel substrates to study the effect on corrosion properties of stainless steel samples under SOFC cathode operating conditions. A DOD mode electro-magnetic printer modified from a Domino Macro Jet print head was used for the deposition process. The inkjet deposited coatings were assessed for SOFC protective layer application using ASR measurements and high-temperature exposure corrosion tests. The following aspects were studied:

- Formulation of the aqueous-based inkjet inks using spinel powders (coating materials) for an electromagnetic printer and validate their printability.

- Inkjet printing of the formulated spinel inks on ferritic based stainless steel substrates (virgin and surface modified – nitrided), confirming a suitable coating application.

- Evaluation of the inkjet-printed spinel coatings by high-temperature oxidation test and area-specific resistance measurements developed for SOFC interconnect conditions at 700 °C.

## 1.5. Thesis outline

Chapter 2: This chapter briefly discusses the oxidation mechanisms in a metal/alloy at high-temperature environment and lists out the materials used for SOFC interconnect applications. The cause of degradation in ferritic stainless steel and their mitigation process are discussed. The various coating materials and deposition techniques for protective layer application are briefly reviewed. The basics of inkjet printing and requirements for the deposition of colloidal suspensions are discussed. Inkjet printing used for the deposition of functional materials and types of inkjet printers in SOFC research are reviewed.

Chapter 3: This chapter lists out the stainless steel substrates, coating materials, and the ink components used in the study. The development route for the formulation of spinel inkjet inks based on two-stage ball milling process and the characterisation techniques used were discussed. The experimental set-up of the high-temperature oxidation, area-specific measurements and post-test characterisation techniques are explained.

Chapter 4: In this chapter, the formulation and optimisation of the aqueous-based spinel inkjet inks are discussed. The optimisation steps adapted for each ink component with respect to the inkjet printer requirements is reported. Finally, the printability and the deposition of the formulated inks are assessed and demonstrated.

Chapter 5: This chapter evaluates the performance of the inkjet-printed protective layers over the stainless steel substrates in SOFC cathode environment based on the high-temperature tests. The effect of the nitriding process on K41 substrates and the effect of Fe and Cu doping in Mn-Co spinel are analysed.

Chapter 6: In this chapter, the key conclusions from work are drawn together, and future work extending the present study is discussed.

# *Chapter 2: Literature Survey*

This chapter presents a detailed literature survey focussed on the corrosion of ferritic stainless steels employed as SOFC interconnect material and the methods adopted to mitigate this. The chapter elaborates on the theory and the mechanisms for metals/alloys oxidation, then discusses the properties of candidate materials that can be used for SOFC interconnect applications. The chapter highlights promising coating materials reported in the literature to reduce stainless steel surface degradation. Moreover, the chapter provides a critical review of different techniques used for the application of the protective layer coatings.

## 2.1. Introduction

Metals, in general, possess common characteristics such as high melting point, good malleability, ductility, thermal, heat, and electrical conductivity. In terms of chemical reactivity, with the exception of noble metals, metals react with oxygen to attain the thermodynamically stable oxide state. The formation of a passive oxide layer on the surface of a metal keeps it unaffected in ambient conditions by protecting the bulk of the metal from further reaction with the oxygen. The diffusion of oxygen or metal ions via the passive layer occurs continuously and can lead to corrosion based on several factors such as the composition of the base metal, temperature of the surroundings, time of exposure, and further surrounding conditions. Corrosion leads to loss of the base metal, affecting the chemical and physical properties of the metal over time.

The corrosion behaviour of metallic interconnects in SOFC's is described as high-temperature corrosion, where metals react with the gaseous phase (air at the cathode side) to form oxides as a product. Though noble metals, such as gold or platinum, are inert to any chemical reactivity or corrosion, they are expensive. Hence, transition metals such as chromium, iron, or nickel have been employed and studied for SOFC interconnect applications. These metals exhibit good physical properties, ease of manufacture, and are cost-effective. Metals of different properties are usually combined to form an alloy to meet the needs of the desired applications. The metal/alloy capable of forming an oxide layer under corrosive conditions offers protection to the base metal, which makes it suitable for applications such as aerospace, car engines, power generation and other high-temperature processes. Despite the benefits of the formed oxide layer, it is susceptible to mechanical stress, volatilisation of its components, and cracking over the time of exposure.

The theory and oxidation mechanism in metals/alloys and the issues related to the oxidation of metallic materials for SOFC interconnect application are discussed in sections, 2.2 to 2.3. The choice for potential metallic material as interconnects, their limiting factors and the steps taken to mitigate the issues are reviewed in sections, 2.4 to 2.7. Finally, the scope and adaptation of inkjet printing techniques in SOFC technology are reviewed in section, 2.8.

## 2.2. Oxidation in metals

### 2.2.1. Thermodynamics

Metals and alloys are thermodynamically unstable in oxygen atmosphere and therefore react with the gas present within their environment. Equation (2.1) presents the interaction between a metal and the oxygen molecule, forming a metal oxide [22]. The feasibility of the chemical reaction at constant temperature and pressure can be determined based on the second law of thermodynamics using Gibb's energy (ΔG) as expressed in Equation (2.2).

$$xM(s) + \left(\frac{y}{2}\right) O_2(g) \rightarrow M_x(s)O_y(g) \quad (2.1)$$

$$\Delta G = \Delta H - T\Delta S \quad (2.2)$$

Where ΔH and ΔS represent the change in enthalpy and entropy of the reaction. The reaction is at equilibrium when ΔG=0, and non-spontaneous, or spontaneous when ΔG is greater or less than zero, respectively. Thus, the change in Gibbs energy for reaction (2.1) is given by Equation (2.3):

$$\Delta G = \Delta G^\circ + RT \ln k_{eq} \quad (2.3)$$

$$\Delta G = \Delta G^\circ + RT \ln \left( \frac{a\,(M_x O_y)}{a\,(M^x) a\,(O_y)^{\frac{y}{2}}} \right) \quad (2.4)$$

Where ΔG° is the change in free energy for all the species in their standard state, R is the universal gas constant, T is the temperature, $k_{eq}$ is the equilibrium constant for the reaction, and *a* is the thermodynamic activity of each species. For pure metals, the thermodynamic activity is equal to 1, and in the case of gases, it is expressed as a function of the partial pressure of the gas, *p*. It must be noted that for a metal in an alloy system the activity of the metal is determined based on its concentration.

Equation 2.4 can be simplified for the oxidation of metals to:

$$\Delta G = \Delta G^\circ + \left(\frac{y}{2}\right) RT \ln\left(p_{O_2}\right) \quad (2.5)$$

At equilibrium conditions, i.e., when ΔG= 0, equation 2.4 can be expressed as

$$p_{O_2\,(\Delta G=0)} = \exp\left(\frac{\Delta G^\circ}{y\,RT}\right) \quad (2.6)$$

Equation 2.5 helps to predict the thermodynamic stability of a metal or an oxide at a given temperature and oxygen partial pressure ($p_{O_2}$). At equilibrium conditions, the partial pressure of oxygen is referred to as dissociation pressure (dp) which denotes the minimum $p_{O_2}$, required to oxidise the metal. Thus, the oxide layer formation is thermodynamically favoured only when the $p_{O_2}$ is higher than the equilibrium partial pressure. Harold L.T Ellingham (1944) introduced the Ellingham/Richardson diagram (Fig. 2.1) to predict the oxide formation of a metal at a certain temperature and oxygen partial pressure. However, the high-temperature corrosion behaviour of metals/alloys in equilibrium conditions cannot be revealed by thermodynamic predictions and is determined by the rate of oxidation based on Wagner's oxidation theory . In terms of life-time analysis, it is significant to understand the oxidation mechanism and the reaction rate at which metal/alloys oxidise.

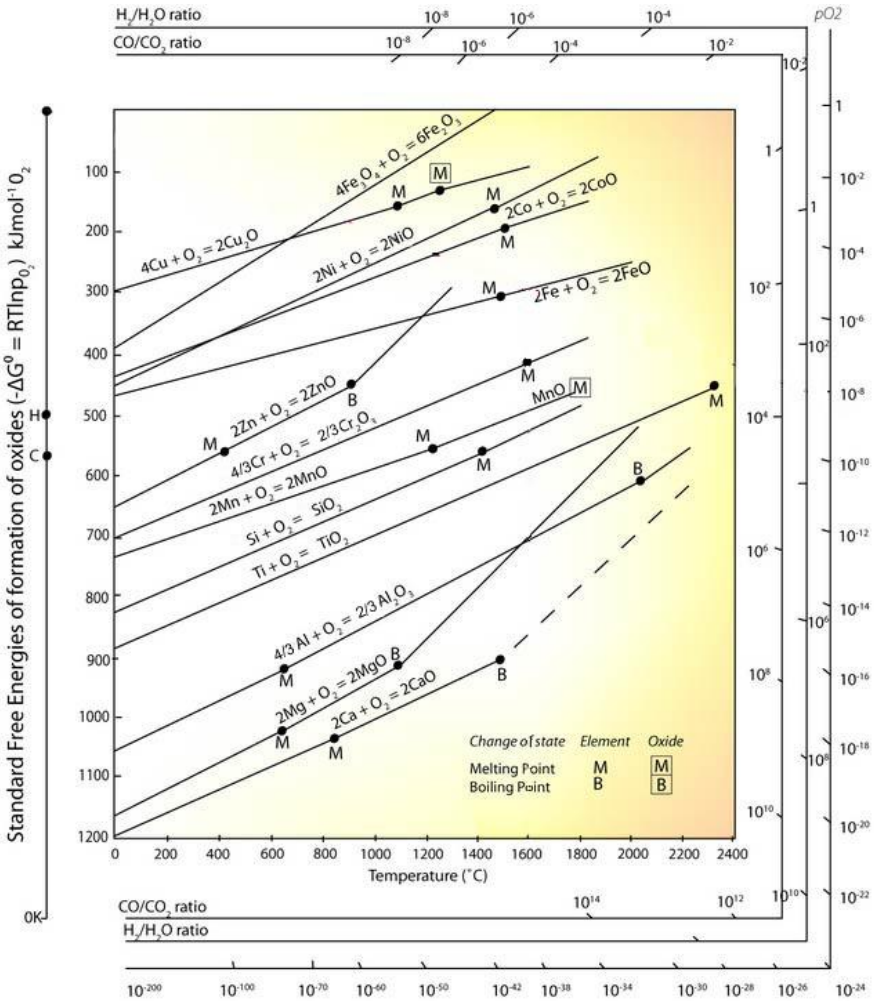


**Figure 2.1:** Ellingham-Richardson diagram illustrating the formation of a stable oxide for a given metal at a given temperature and oxygen partial pressure, taken from [23].

## 2.2.2. Oxidation mechanism

As soon as an oxide layer develops on the surface of the metal, it is evident that the two reactants metal and oxygen, are separated by the metal oxide formed. To sustain the reaction, either one or both reactants must infiltrate the oxide scale. The formation of an oxide layer is shown in Fig. 2.2 and the sequential steps involved in the formation is as follows:

1) Adsorption of oxygen molecules on the surface of the substrate (metal/alloy) - When a metal/alloy is exposed at high-temperature, oxygen molecules from the surrounding atmosphere are adsorbed on the surface as a result of weak Van der Waals interaction.

2) Nucleation of the adsorbed oxygen species across the surface - The adsorbed oxygen molecules, $O_2$, reduces to $O^{2-}$ by forming an ionic bond with the substrate.

3) Growth of oxide scale - The chemisorbed oxygen ions diffuse across the surface of the metal/alloy to form stable nuclei which grow upon further adsorption of oxygen to cover the whole surface of the substrate.

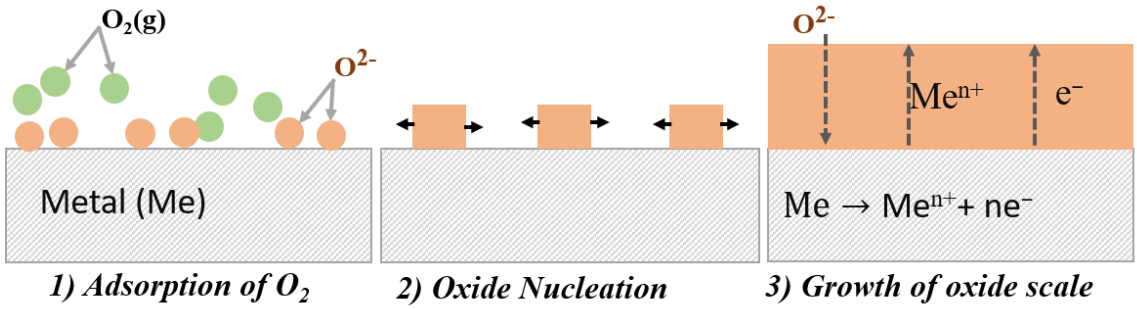


**Figure 2.2:** Sequential steps depicting the oxide layer growth on a metal surface, adapted from [24].

The thermally grown oxide layer prevents any interaction between the metal/alloy and the environment by isolating the two from each other. Further growth of the oxide is governed only by solid-state diffusion; which progresses by the combination of mechanisms such as outward metal ion (cation) diffusion and inward diffusion of oxygen ions (anions) to the metal/alloy interface through the formed oxide scale [9,24].

The developed oxide layer can be either dense or porous with crystalline, vitreous, or amorphous oxide structures. The porous oxide layer forming metals are less resistant to continuous oxidation as they favour the transport of gaseous species through the growing oxide scale. Chromium oxide ($Cr_2O_3$) layers exhibit polycrystalline structure due to the existence of multiple oxygen nuclei in their initial oxidation. The polycrystalline nature gives rise to varying grain boundaries which act as diffusion paths for the reacting species. The transport of ions

which governs the reaction rate of the oxide layer growth is determined by the concentration of defects present in the oxide layer [25]. High-temperature oxidation favours more disorder resulting in more defects.

A defect can be due to an interstitial or substitutional impurity atom or a metal/oxygen vacancy. The oxides are classified based on the nature of point defect [22],[25]. The protective oxides, alumina and chromia, are referred to as stoichiometric oxides as their only one stable oxidation state is III ($Al^{3+}$ and $Cr^{3+}$), also known as slow-growing oxides. Whereas metals such as iron and nickel with two oxidation states create oxygen and metal ion vacancies for ion transport and are referred to as anion (n-type) and cation (p-type) deficit oxide, respectively [26]. Thus, at high temperatures, anion and cation deficit oxide layers tend to grow faster due to more defects than the slow-growing oxides. Also, the diffusion of ions via the formed oxide scale accounts for the diffusion through non-lattice defects such as dislocations, bulk and grain boundaries. The order of diffusivity in polycrystalline materials can be sequenced as [27]:

$$D \ll D_d \leq D_{gb} \leq D_s \qquad (2.7)$$

D = lattice diffusivity

$D_d$ = dislocation diffusivity

$D_{gb}$ = grain boundary diffusivity

$D_s$ = surface diffusivity

Based on the relation (2.7), the fastest diffusion path is grain-boundary diffusion for a dense oxide scale. However, considering the volume where grain-boundary diffusion occurs, it is less compared than volume of lattice diffusion that occurs [26].

## 2.3. Vaporisation of Cr

The protective oxide layer of some metals and alloys is prone to volatilisation at higher temperatures leading to the gradual removal of the oxide layer and subsequently its failure to protect the base metal. In the case of Cr-containing alloys, volatile Cr (VI) species are formed under an oxidising atmosphere which drives a mass transfer of chromium through the oxide layer, away from the metal/alloy surface [28,29]. The higher vapour pressure of $CrO_2(OH)_2$ species compared to $CrO_3$ at temperatures below 1000 °C make it susceptible to evaporation and therefore causes depletion of Cr from the chromia layer, see Fig. 2.3. In dry air or oxygen, $CrO_3$ gaseous species are formed as shown in the reaction (2.8) which does not impose a critical issue of vaporisation of the oxide layer, whereas, in the presence of water vapour, the volatile chromium oxyhydroxide is formed as shown in the reaction, Equation 2.9.

$$Cr_2O_3(s) + \frac{3}{2}O_2\,(g) \rightarrow 2\,CrO_3(g) \qquad (2.8)$$

$$Cr_2O_3(s) + 2H_2O(g) + \frac{3}{2}O_2(g) \rightarrow 2CrO_2(OH)_2(g) \qquad (2.9)$$

Ebbinghaus et al. [30] showed that gaseous $CrO_2(OH)_2$ species is a dominant species in the temperature range 526 °C to 1325 °C at fixed oxygen and water partial pressures of 1.0 kPa and 10 kPa, respectively. Hilpert et al. [31] showed the formation of gaseous $CrO_2(OH)_2$ species even at low water vapour content of 2% below 1000 °C. Cr volatilisation affects the oxidation rate of the metallic interconnect material during SOFC operation. Due to the prolonged oxidation exposure, the oxidation rate shifts from parabolic to linear as a result of the equilibrium attained between the mass gain and mass loss from oxidation and evaporation, respectively. The formed oxide layer thickness can be determined based on both a parabolic

rate constant for the oxide layer formation, $k_p$, and a linear rate constant for the Cr evaporation $k_v$. The mass gain and evaporation processes balance each other with time to yield an oxide layer of a constant thickness ($x_i$) known as maximum scaling or limited oxide scale thickness, expressed as shown in the relations (2.10 and 2.11).

$$\frac{dx}{dt} = \frac{k_p}{2x} - k_v \tag{2.10}$$

$$x_i = \frac{k_p}{2k_v} \ . \tag{2.11}$$

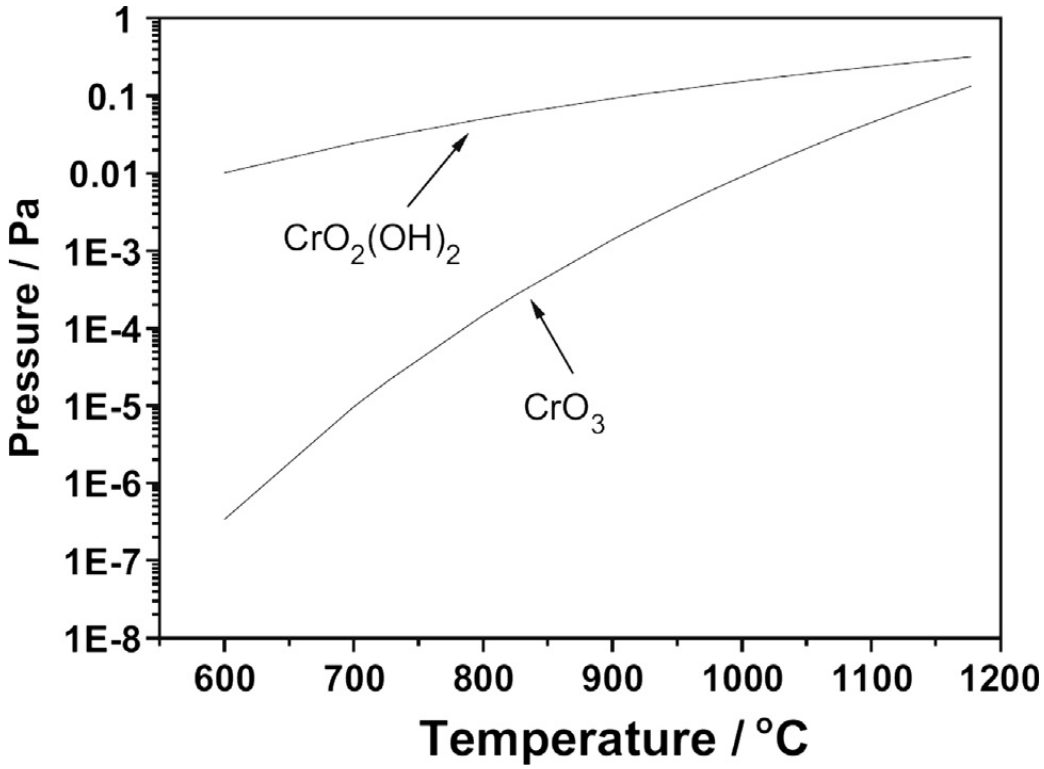


**Figure 2.3:** Partial pressure of $CrO_2(OH)_2$ in wet air (3 volume % $H_2O$) and $CrO_3$ in dry air over chromia at different temperatures [8].

## 2.3.1. Chromium poisoning

The volatilization of Cr species from the oxide scale not only weakens the corrosion resistance of the substrate, but it also leads to the degradation of SOFC. The high vapour pressure of air at the cathode has more affinity for the volatile species than at the fuel side of the interconnect material [28,31,32]. The volatile species from the interconnect react at the cathode by getting reduced chemically or electrochemically at the triple-phase boundary (TPB) and deposit as $Cr_2O_3$. The transportation of chromium species from the alloy substrate to the functional layers of the fuel cell is driven by the partial pressure of the Cr containing gaseous species which also acts as the source for the chromium migration [33,34]. Fig. 2.4 shows the schematic of Cr evaporation and deposition of $Cr_2O_3$ at the TPB of the fuel cell.

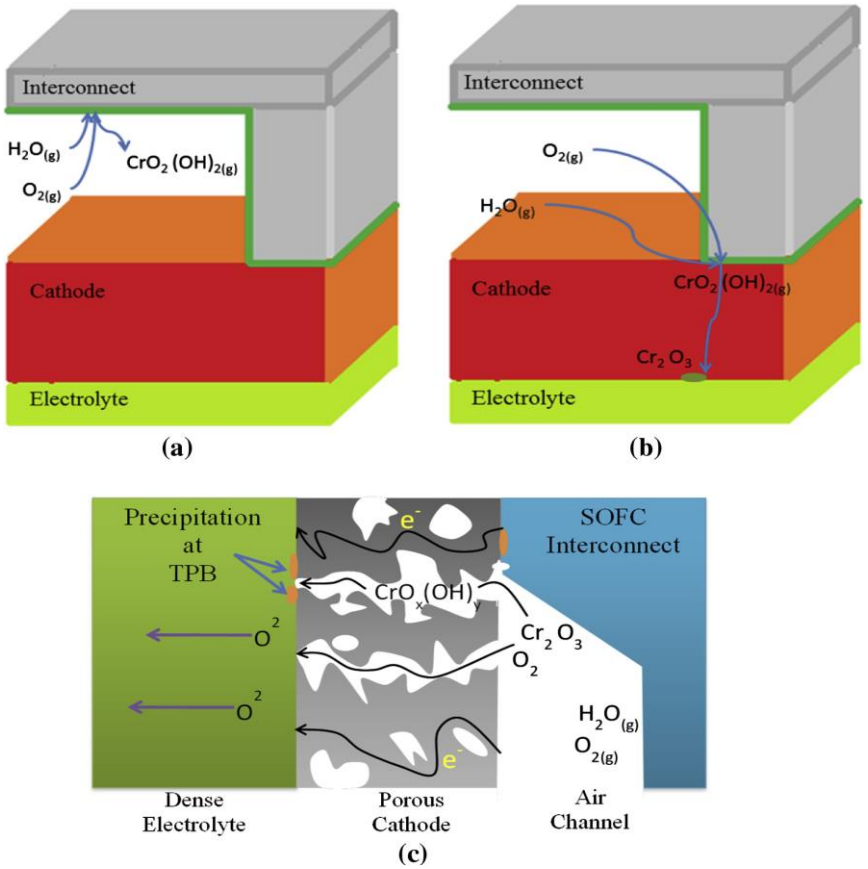


**Figure 2.4:** Schematic representation of Cr evaporation (a) and (b) at the interconnect and (c) deposition of volatile Cr species as chromia at the functional layers [8], [10].

## 2.4. Materials for metallic interconnects

Zhu et al. [9] reviewed the metallic materials for SOFC interconnect applications operating at temperatures above 800 °C. Metallic materials ( in particular, Cr-based and Fe-based alloys) were highlighted as promising candidates to compete with the ceramic interconnects. It was emphasised that the development of materials capable of resisting corrosion by forming a stable oxide scale with reasonable oxide growth rate and high electrical conductivity during the expected SOFC lifetime operation is essential. In 2003, the , (PNNL) carried out an inclusive study to evaluate and identify the alloys suitable for SOFC interconnect application [35]. The developed database has been studied since then to improve the performance of the possible alloy compositions at operating temperatures between 700-850 °C. The study explored transition-based metal alloys, namely Ni-based, Fe- based, and Co-based superalloys, Cr-based alloys, and stainless steels. At high temperatures, based on the oxidation potential of the alloying elements, a stable $Cr_2O_3$ (chromia) or $Al_2O_3$ (alumina) layer is formed which offers protection to the base metal from the environment during high-temperature exposure [24]. However, a thermally growing oxide layer over the metal surface at a high temperature affects the electrical conductivity of the interconnect [36]. For this reason, $Cr_2O_3$ forming alloys are widely chosen over silica and alumina formers irrespective of their superior oxidation resistance compared to chromia formers [35–37].

The critical amount of Cr content in the alloy composition for the formation of a continuous chromia layer, resisting high-temperature corrosion and preventing breakaway oxidation was found to be 20 to 25 % [35]. Bricks and Rickert confirmed the formation of a continuous $Cr_2O_3$ layer when the Cr content was higher than 20% in the alloy [35]. It was considered that the Cr content must be greater than 20 % in Ni, Fe, and Co-based superalloys to overcome high-temperature corrosion. Thus, a minimum of 18 % Cr with appropriate alloy composition (i.e.,

the addition of trace elements) in Ni, or Fe-based alloys significantly improves the corrosion resistance. Alloying trace elements such as La, Ce, Y, Zr also referred to as reactive elements, has shown improved oxidation resistance [5]. The effect of alloying trace elements is discussed in section, 2.4.3. In Co-based alloys, the oxidation resistance is poor due to the properties of pure Co as it mainly forms CoO and an outer thin layer of $Co_3O_4$ [24] . Upon 9% addition of Cr in the composition, its oxidation resistance was found to improve significantly along with the formation of some $CoCr_2O_4$. The optimum content of 25 to 30 % Cr in Co-based alloys favours the formation of a continuous chromia layer, and the oxidation rate can be slowed down by alloying with Ca, B, Zr, and Al. But, high Cr content in the composition is prone to vaporisation of Cr during long time exposures under SOFC conditions.

Wasielewski and Robb, classified Fe - based and Ni - based superalloys into three categories based on the Al and Cr ratio in the alloy composition [35]as follows:

1) NiO scale formers - low Cr and Al content,
2) Chromia scale formers - with high Cr (>15%) and low Al (1-3%) content,
3) α- Alumina scale formers - with high Cr (15%) and high Al (>3%) content.

The oxidation resistance of the mentioned superalloys was evaluated based on the steady-state parabolic oxidation, which is lower for alumina scale formers followed by chromia scale and NiO scale formers. The maximum scaling temperature, a theoretical value at which the thermally grown oxide scale disintegrates for NiO is 850 °C, which is a concern under SOFC operating conditions [9]. Alumina scale formers offer higher oxidation resistance and lower volatilisation rate, but they are limited due to their electrically insulating nature. Thus, Cr based alloys with moderate oxidation resistance and good electrical conductivity were considered as

the promising material for SOFC interconnect applications. The maximum scaling temperature of chromia is 1100 °C, higher than the SOFC operating conditions [9]. Moreover, the coefficient of thermal expansion (CTE) of Cr based alloys ($11\times10^{-6}$ to $12.5\times10^{-6}$ $K^{-1}$) is in the range required for the interconnect applications. Yang et al. [35] classfied group of alloys capable of forming a protective chromia layer based on Cr content and their oxidation resistance for SOFC interconnect application in a Fe-Ni-Cr phase diagram, Fig. 2.5.

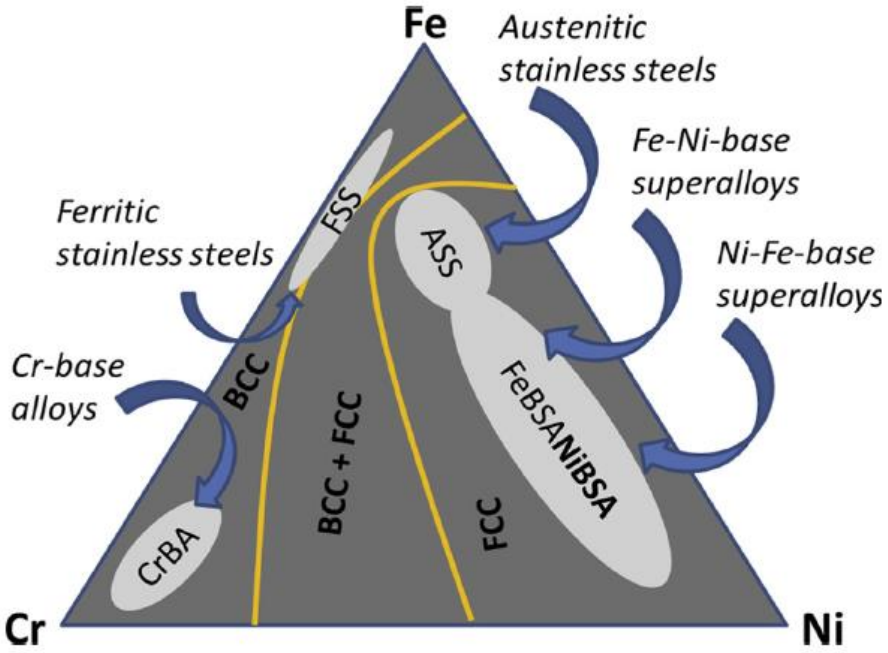


**Figure 2.5:** Schematic of alloy design for SOFC interconnects based on the Fe-Ni-Cr phase diagram, taken from [38].

## 2.4.1. Chromium-based alloys

Linderoth et al. [39] investigated different high-temperature metallic alloys for SOFC interconnect application. 94Cr5FeY$_2$O$_3$ (Plansee), H-230 (Haynes), IN601 (Inco), APM (Kanthal) alloys were assessed based on thermogravimetric and oxidation tests at 1000 °C in dry air. 94Cr5FeY$_2$O$_3$ (CFY) exhibited promising results in terms of oxidation rate, low electrical resistivity, and compatible CTE with other fuel cell components. It is important to

note that Plansee Ducralloy (CFY), an oxide dispersion strengthened alloy, was the first metallic based interconnect to replace lanthanum-based ceramic interconnects at operating temperature greater than 900 °C. The alloy demonstrated good oxidation resistance, compatible CTE ($11.8\times10^{-6}$, 20 to 1000 °C) to Ni/YSZ based anode supported SOFC cells and good mechanical strength. Despite the advantages, the alloy faced a similar challenge as ceramic interconnectors in terms of cost and ease of fabrication. Also, due to the high Cr content (94%), thicker oxide scales and high volatilisation of Cr species from the thermally grown oxide layer imposed concerns for long-time operation. The oxide layer thickness was estimated to be 10µm after one year and 23 µm after 5 years of operation at 900 °C [11]. Cr poisoning and increased electrical resistance due to the thicker oxide scale affected the durability of the stack, and their application was limited to high operating temperature (>900 °C).

Ni-Fe-Cr and Fe-Ni-Cr based superalloys are the other class of chromia forming alloys of interest for interconnect applications. This class of alloys with FCC crystal structure exhibit high mechanical strength and lower scale growth rate at SOFC operating conditions but are largely limited by the CTE of $15\times10^{-6}$ to $20\times10^{-6}$ $K^{-1}$ (room temp to 800°C) and the high cost of fabrication [11,35].

## 2.4.2. Fe-based alloys

Iron-based alloys, Fe-Cr, are widely considered for SOFC interconnect applications due to their oxidation and creep resistance at elevated temperatures in comparison to the other alloys. Fe-based alloys with a minimum of 11wt.% Cr, generally known as stainless steels (SSs), ensure the formation of a thin protective chromium oxide layer. In stainless steels, carbon content is significantly limited to 0.08% and steels with a very low carbon content of < 0.03% are preferred for SOFC interconnect applications due to their improved ductility, being able to

machine to the desired shapes. Also, it minimises the formation of chromium carbides which weakens corrosion resistance by causing chromium depletion in the oxide layer [40]. Stainless steels are classified into four groups based on their microstructure, namely: ferritic, austenitic, martensite, and precipitation-hardening steels.

Pure iron exhibits the transformation of its crystal structure from body centred cubic (BCC) to face centred cubic (FCC) when heated above 910 °C and transforms back to BCC at temperatures beyond 1400 °C. The formation of a duplex structure, i.e., α-ferrite (BCC) to γ-phase (FCC) commonly referred to as austenite structure can be inferred from the Fe-Cr phase diagram, Fig. 2.6. The formation of austenite phase is not preferred for the interconnect application due to their higher CTE. The temperature range at which the austenite phase forms and stabilises is decreased by the addition of chromium beyond 7%. Ferritic stainless steels (FSS) require a minimum of 13% Cr to maintain their BCC structure at all temperatures, and thus Cr is referred to as ferritizer or ferrite stabilizer [35]. Like Cr- based alloys, ferritic alloys maintain BCC structure at all temperatures and are not influenced by any heat-treatment processes. FSS with higher chromium content (>18%) is currently considered as the main material for interconnect applications due to its low-cost fabrication and easy machinability along with reasonable oxidation resistance [14,37,41].

Various studies on different heat resistant alloys for SOFC interconnector applications established FSS as the best performer in comparison to Cr-based alloys [11,35,42–44]. FSS employed for intermediate temperature SOFC's (700- 850 °C), should have more than 17% of chromium content and preferably higher than ~22% to prevent break-away oxidation which results from total depletion of chromium content through chromia layer formation and subsequent failure of the material by Fe- oxide formation. Meanwhile, too much Cr content

will enable the formation of a sigma phase; an inter-metallic phase containing iron and chromium that forms at a higher temperature (560 to 980 °C). Sigma phases decrease the oxidation resistance of the stainless steel and cause embrittlement. The addition of alloying elements like molybdenum (Mo) is known to promote the sigma phase formation [44].

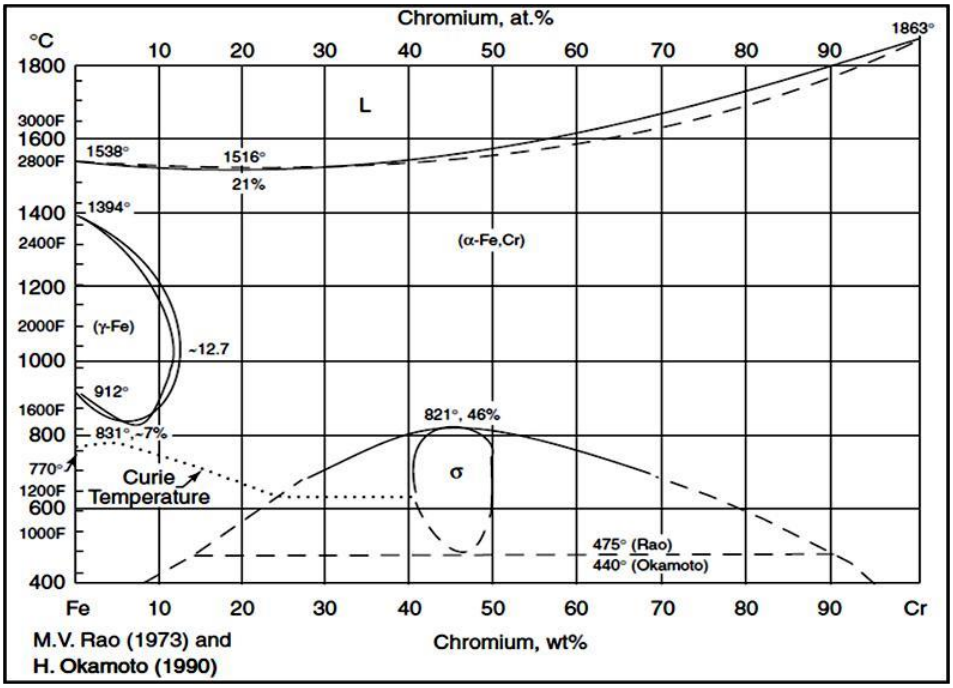


**Figure 2.6:** Fe-Cr phase diagram showing the formation of austenite phase at lower Cr content and formation of sigma phase at higher Cr content, taken from [44].

A higher amount of chromium also increases the CTE of the FSS, which is balanced by the incorporation of Al, Mo, W, and Ti [45]. The addition of 0.3 to 0.5 wt.% of Mn into the Fe-Cr (22 to 23%) matrix favours the formation of a spinel $(MnCr)_3 O_4$ layer on top of the oxide scale which enhances the electrical conductivity of the formed oxide layer and reduces Cr evaporation [46–48]. Extensive research studies has been done on alloying and modification of alloy components in Fe-Cr based stainless steels to improve the performance and lifetime of SOFC interconnects [5,44,49,50].

## 2.4.3. Effect of alloying

Extensive studies and technical research have been performed on both available commercial materials, and specifically designed materials with high Cr content for SOFC interconnect applications. The materials were developed based on CTE match with the other SOFC materials, good electrical conductivity, low Cr vaporization, and easy processability. The desired properties of the materials were achieved by optimising concentration of the alloying elements and reducing the concentration of elements such as Si, Al and other impurities which affect creep resistance at 700 to 900°C [44].

The high yield strength of FSS at higher temperatures prevents deformation during long-time operations. This is enhanced by alloying refractory elements such as Nb, W, and Mo. The refractory elements are capable of forming Laves phases; an intermetallic precipitate composed of $(Fe, Cr)_2$ (Nb, W, Mo) which is known to enhance the creep resistance of the stainless steel at elevated temperature. Increase in hardness and decrease in brittleness of the steel is achieved by alloying elements through a solid solution strengthening process, where alloyed elements are incorporated into the Fe-C matrix imposing a local non-uniformity within the lattice, and consequently, any dislocation process is hindered, improving the yield strength of the material. T. Horita et al. [51] suggested that alloy grain boundaries, with a high concentration of Mn, and Fe along the ridges, act as fast diffusion pathway favouring the transportation of elements for the growth of oxide scales. The addition of Laves phase forming elements (Nb, W, Mo) into the Fe-Cr matrix regulates the cation diffusivity along the grain boundaries under oxidising conditions and slows down the oxidation rate.

Yamamoto K et al. [52] investigated the significance, and the design of the Laves phase ($Fe_2Nb$) based heat-resisting ferritic stainless steels of the Fe-Cr-Nb (-Ni) system. The study

showed the feasibility of designing ferritic steels with good static strength at high temperature and good ductility at room temperature based on Fe- Cr (10 atomic. %)- Nb alloys, with or without Ni. An optimum concentration for Nb of ~ 1 atomic % was reported to achieve an appropriate volume fraction of Laves phase. However, the affinity of Nb towards C and N led to the formation of coarse precipitates of Nb ($Fe_3Nb_3X$, X- C, N) at high temperature leading to the degradation of high-temperature strength and weakening of thermal fatigue resistance.

The addition of Ti and Mo in Nb alloyed stainless steels suppressed the precipitation of coarse $Fe_3Nb_3C$ by forming $Fe_2Nb$ [53]. It has been reported that the addition of Ti favours internal oxidation to form internal $TiO_2$, which enhances the oxide scale strength [5], lowers the contact resistance when doped with chromia [54], and slows down the Cr evaporation rate along with W [55]. Despite the positive effects, the higher concentration of Ti may cause spallation of the oxide scale. Ti concentration of 0.15 wt.% has resulted in drastic internal oxidation at the grain boundaries leading to buckling and plastic deformation of the oxide scale [5]. The effect of Mo addition on the oxidation behaviour of Fe-22Cr-0.5Mn alloys at 800°C was studied and showed that Mo suppresses the inward progression of oxygen species and improves the oxidation resistance [56].

Ferritic stainless steels like Crofer 22 APU (ThyssenKrupp VDM) and ZMG232 (Hitachi Metals) are specially designed for SOFC interconnect applications by a vacuum refining process. The refining process reduces the amount of residual elements such as Si and Al in the alloy composition, [5] thereby eliminating the formation of highly insulating silica and alumina layers during the time of high-temperature exposure. However, the extra refining process led to cost addition in the process. Low ASR and absence of Si sub-layer formation was observed in the alloys, 1.4509 and 1.4016 (similar to AISI 441 and AISI 430 respectively in alloy

composition) with residual Si content of <0.5 wt.%, processed by conventional techniques [35]. The presence of Nb and Ti captured the silica due to the formation of Laves phases and thus allowed the utilisation of alloy modification in conventional steel making to obtain the desired characteristics [35,57].

Froitzheim et al. [44] investigated alloying refractory elements Nb and W, of various concentration of 0.5 to 2 wt. %, into Crofer 22APU and the interaction of Nb with Si and Al. Oxidation tests at 800 and 900 °C showed that 1wt.% of Nb exhibited the highest oxidation rate by forming an Nb rich oxide layer at the metal/scale interface whereas alloys with the minor addition of Si exhibited similar performance to the standard Crofer 22APU steel. The high solubility of Si in Laves phase precipitates ($Fe_2$(Nb, W)) suppresses the effect of Nb on oxidation and also ensures the lower activity of Si in the alloy matrix [58]. The minor alloying of Si and Al in the Laves phase forming alloys have shown enhanced performance in oxidation behaviour and creep resistance on different studies [48,59–62]. The effect of Laves forming alloys under reducing conditions (at 800 °C) also exhibited slower oxide scale growth in comparison to standard ferritic stainless steel (SUS 430) [57].

Elements such as Y, Hf, Ce, La, and, Zr (lanthanide group of elements), referred to as reactive elements (RE), tend to promote selective oxidation at high temperature and favour chromia layer formation even in FSSs with Cr concentrations of less than 18 wt.% [63]. They have shown a significant effect on the oxidation behaviour of chromia forming alloys at high temperatures by enhancing the oxidation resistance of the alloy and improving the adhesion of the thermally grown oxide layer [64]. Moreover, the addition of RE prevents the accumulation of sulfur at the substrate- scale interface, which could weaken the oxide scale-metal adhesion [65].

Different grades of ferritic stainless steels have been studied for SOFC interconnect applications based on the addition of varying alloys. Table 2.1 lists the most studied stainless steel materials for SOFC interconnect applications in recent years.

**Table 2.1:** List of stainless steel grades studied for the SOFC interconnect applications in recent years.

| Alloy | Fe | Cr | Mn | C | Nb | Si | Ti | Al | RE** | Others | Ref |
|---|---|---|---|---|---|---|---|---|---|---|---|
| **Crofer 22 APU (min-max)** | Bal* | 20.0 - 24.0 | 0.3 - 0.8 | 0.03 | | 0.50 | 0.03 - 0.2 | 0.50 | La 0.04 - 2 | P - 0.05 Cu - 0.50 | [5,66,67] |
| **Sanergy HT** | Bal* | 21.2 | 0.3 | 0.04 | 0.71 | 0.12 | 0.09 | 0.017 | Zr | Mo -0.96 | [29,67,68] |
| **Crofer 22H** | Bal* | 20.0 - 24.0 | 0.80 | 0.03 | 0.2-1.0 | 0.1-0.6 | 0.02 - 2 | 0.10 | La 0.04 - 2 | Cu - 0.5; N - 0.04; P - 0.5; W - 1-3; S - 0.006 | [44,48,59] |
| **AISI 441/K41** | Bal* | 18 | 0.3 | 0.12 | 0.45 | 0.35 | 0.17 | - | | | [69,70] |
| **AISI 430** | Bal* | 15.54 | 0.4 | - | - | 0.20 | - | | - | Ni - 0.59; P bal* with Fe | [71] |
| **SUS 430** | Bal* | 16.27 | 0.22 | 0.05 | - | - | - | - | - | Ni - 0.08; P - 0.016; S - 0.001 | [72] |

* Bal- Balance; ** RE- Reactive elements

## 2.5. Mitigating degradation in FSS

To overcome the degradation mechanisms in FSS, mitigation methods such as the development of conductive and protective coatings, surface treatment/ modification, and alloy development are continuously being studied [13,14]. Alloy modification is considered to be a tedious approach, and materials often do not solve all degradation issues simultaneously. For instance, specially designed alloy Crofer 22APU which is capable of forming (Cr, Mn) spinel layers exhibited high degradation rates. Bare Crofer 22 APU as an interconnector with LSM as cathode displayed a degradation rate of 21%/ 1000hrs whereas the targeted degradation rate for a SOFC system is <2%/1000hr (lifetime of 5000-10,000 hours) for mobile applications [73]

and <0.3%/1000h (lifetime of maximum 80,000 hours) for stationary applications [74]. Hence, the application of protective coatings and surface modification have been suggested as a low-cost approach to increase the lifetime of interconnect materials and also provides opportunity to utilise available commercial heat-resistant alloys for SOFC interconnector applications [37,41,75–80].

## 2.5.1. Protective Coatings

Various coating materials have been developed and studied as a protective layer based on the following requirements:

(a) low area-specific resistance (>$10^{-3}$ Ω $cm^2$),

(b) low diffusion coefficients for Cr and O within the coating,

(c) good thermal stability and matching CTE with the alloy substrate under thermal cycling,

(d) chemical and thermodynamic stability under SOFC operating conditions,

(e) inhibiting Cr migration and evaporation from the oxide layer,

(f) facile and low-cost application.

Shaigan et al. [13] and Mah et al. [81] have discussed different materials used as protective coatings for SOFC interconnects. The following sections (2.5.2 to 2.5.4) discusses the most widely studied coating materials for the SOFC interconnects.

## 2.5.2. Reactive Element Oxides

Alloying with reactive elements is known to enhance the oxidation resistance at high temperature and improve the adhesion of the oxide layer/substrate. Oxides of reactive elements are considered as the first generation of protective layer coatings for metallic interconnects [82]. Reactive Element Oxide (REO) coatings reduce the contact area of the metal/oxide layer.

Consequently, the thickness of the oxide layer is reduced, which results in a lower ASR. However, REO coatings are limited to thin layers (< 0.2 µm) which fail to sufficiently inhibit Cr migration [13,81]. The most used deposition methods for REO coatings are metal-organic chemical vapour deposition (MOCVD) [83] and the sol-gel process [84].

### 2.5.3. Rare earth perovskites

Rare earth perovskites with the regular formation of $ABO_3$ display p-type electronic conduction in oxidizing conditions and are known for their stability in low oxygen partial pressure conditions. They are composed of large trivalent rare-earth cations occupying A sites (e.g., Y, La or Sr) and generally a trivalent transition metal cation (e.g., Ni, Cr, Co, Fe, Co, Mn or Cu) on the B site. Doping with electron acceptors like Fe, Cu, Ni are known to improve the electrical conductivity and CTE of the rare earth perovskites.

Fontana et al. [85] fabricated and studied the performance of conductive perovskites on three different steels, Crofer 22 APU, Haynes 230, and AL453, by utilising reactive element oxides. A conductive perovskite was formed by applying binary oxides ($La_2O_3$, $Y_2O_3$, and $Nd_2O_3$) over the steels and allowing them to react with Cr from the developed chromia layer. The interaction between the $La_2O_3$ and Cr led to the formation of a conductive perovskite ($LaCrO_3$), which exhibited a low ASR of 0.004 Ω $cm^2$ after 100 hours. ASR value was estimated an increase to 0.035 Ω $cm^2$ after 40,000h.

The effective perovskite coatings found in the literature are lanthanum chromite ($LaCrO_3$). However, due to the low conductivity of pure $LaCrO_3$, it is often doped with alkaline earth elements to improve its performance [86]. The most used perovskites in literature are lanthanum strontium manganite ($La_{1-x}Sr_x MnO_3$), lanthanum strontium ferrite ($La_{1-x}Sr_x FeO_3$),

and lanthanum strontium chromite ($La_{1-x}Sr_x CrO_3$). The presence of reactive elements such as La enhances the oxidation behaviour of the substrate material by promoting selective oxidation behaviour at high temperature. Despite enhancing oxidation behaviour, oxide scale adhesion and lowering ASR, their innate ionic conducting nature fails to inhibit diffusion of oxygen ions and volatile Cr species [13,81].

Radiofrequency magnetron sputtering is the most established deposition technique for perovskite coatings which enables to achieve the desired deposition rate. Other techniques like sol-gel [87], pulsed laser deposition [88] and screen printing [70,89] have also been employed.

## 2.5.4. Spinel oxides

Fig. 2.7 represents the unit cell structure of a spinel oxide represented by the formula of $AB_2O_4$. A and B are usually occupied in octahedral and tetrahedral sites by divalent, trivalent or quadrivalent cations, whereas the face-centred cubic lattice is occupied by oxygen anions. Studies in the past decade have shown that based on the physio-chemical nature and ratio of A and B cations, spinels have exhibited good electronic conductivity and displayed good CTE match with the FSS and other components in the SOFC stack [13,90,91]. In comparison to perovskites, spinels are efficient in inhibiting Cr species migration and minimising Cr poisoning.

Larring and Norby [92] proposed a Cr-free spinel $(Mn, Co)_3O_4$ (Mn-Co = MCO) as the promising candidate for the protective layer application for metallic SOFC interconnects (CFY alloy). MCO coatings on CFY alloy showed promising results in inhibiting Cr migration and achieved an estimated ASR of 0.24 $m\Omega\ cm^2$ after10000 hours. Yang et al. [93] studied Mn-Co spinels with the nominal composition of $Mn_{1.5}Co_{1.5}O_4$ as protective layer coating over FSS

with varying Cr percentage. $Mn_{1.5}Co_{1.5}O_4$ displayed excellent electrical conductivity, good thermal stability, CTE match, and lower contact resistance between FSS and the cathode material, lanthanum strontium-ferrite (LSM). The applied slurry coating also demonstrated good performance in inhibiting Cr migration. The same study demonstrated the two-stage heat treatment for the spinel coatings to achieve densified coating applied via wet chemical processing methods. The coating was initially heat-treated in reducing atmosphere and then oxidized. The densification of the coating was thus achieved by the reactive-sintering procedure. During the reduction process, the composition is reduced to cobalt and manganese oxide, as shown in the reaction (Equation 2.15), and during the subsequent oxidation step, the spinel phase is reformed.

$$MnCo_2O_4 \rightarrow MnO + 2Co + \frac{3}{2}O_2 \qquad (2.15)$$

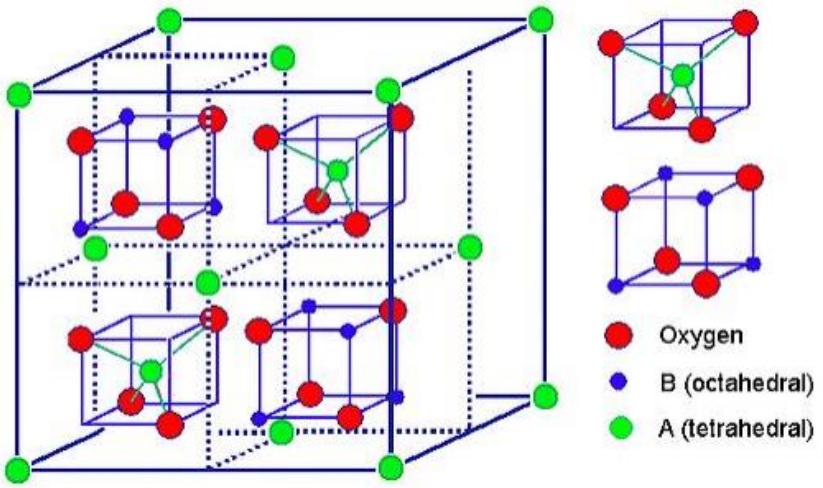


**Figure 2.7:** Unit cell of spinel structure [94].

Yang et al. [95] in another study screen-printed $Mn_{1.5}Co_{1.5}O_4$ on Crofer 22 APU stainless steels. The coatings displayed an ASR of 0.01 mΩ $cm^2$ post 1000h of oxidation in air at 800 °C in comparison to the uncoated substrates, which showed an ASR of 0.04 mΩ $cm^2$ post 400 h under similar testing conditions. The widely studied spinels are $Mn_{0.5}Co_{2.5}O_4$, and $MnCo_2O_4$

representing cubic spinel structure, where Mn occupies tetrahedral sites and Co occupies both tetrahedral and octahedral interstitial positions in the FCC cubic oxygen ion lattice.

$Mn_{1+x}Co_{2-x}O_4$ (x= 0.3-0.9) based spinel materials exhibit dual-phase (cubic and tetragonal) during heating/cooling. The phase transformation of the respective spinels was found to occur at 400 °C.

The thermal and electrical conductivity of different binary spinels comprising Mg, Mn, Cr, Co, Ni, Fe, and Cu at 800 °C was reviewed and studied by Petric and Ling [96]. The study revealed spinels with Fe had a CTE of $11\times10^{-6}$ $°C^{-1}$, closest matching to ferritic stainless steel, whereas other spinels had an estimated CTE between 7 to 9 $\times10^{-6}$ $°C^{-1}$. In terms of electrical conductivity, $MnCo_2O_4$ and $Cu_{1.3}Mn_{1.7}O_4$ displayed the highest conductivity of 60 S $cm^{-1}$ at 800 °C and 225 S $cm^{-1}$ at 750 °C respectively. It was highlighted that $Mn_xCo_{3-x}O_4$, $Cu_xMn_{3-x}O_4$ ($1<x<1.5$), $CuFe_2O_4$ and $Co_3O_4$ as suitable materials for protective layer application for SOFC interconnect, yet there is no ideal composition. Recent studies have shown that doping of Cu into MCO spinel enhances sinterability, electrical conductivity and matching of CTE with other fuel cell components [97,98].

The conductivity in spinels $(Mn, Co, M)_3O_4$ (M=Fe, Cu, Cr) exhibits electrical conductivity by the polaron hopping model [99]. The conduction of electrons in semiconductors such as spinel oxides is slowed down significantly due to the presence of a very narrow band, i.e., the bandgap in between the valence and conduction band and thus band theory is not applicable to elucidate the conduction mechanism in spinel oxides. The slower motion of electrons interacts with the surrounding lattice and generates a polaron which creates a deformation (distorts/polarise) and sustains along its path. A polaron is classified as small when the spatial extent is in the order of the lattice constant and large when it extends beyond the lattice constant. The transfer of

charge in the small polaron hopping model is a thermally activated process and is directly proportional to the temperature [100].

Belma et al. [101] studied electrical conductivity and thermal behaviour of Fe and Cu doped $MnCo_2O_4$ spinel materials proposed in Petric and Ling study [96]. The study investigated the properties of $MnCo_{2-x}M_xO_4$ (M= Cu, Fe; x= 0.1, 0.3, 0.5) at 800 °C under oxidising conditions. The study revealed $MnCo_{1.7}Fe_{0.3}O_4$ had an average CTE of $12.0\times10^{-6}$ °$C^{-1}$ and the closest match to Crofer 22 APU ($11.9\times10^{-6}$ °$C^{-1}$). Thermal behaviour of Cu doped materials was reported to be complicated and attributed to the precipitation of CuO in materials with a high amount of Cu. The electrical conductivity was found to increase with the substitution of Cu and decrease with the addition of Fe as a dopant. The highest electrical conductivity for Fe and Cu doped candidates were 31 S $cm^{-1}$ for $MnCo_{1.7}Fe_{0.3}O_4$ and 168 S $cm^{-1}$ for $MnCo_{1.5}Cu_{0.5}O_4$. The effect of doping was reported to be insignificant at 800 °C. It was suggested that it is more significant to reduce the oxidation rate of interconnect materials rather than improving the conductivity of the coating materials to achieve the optimum ASR [102].

The increase in chromium content is known to decrease the electrical conductivity of the spinels due to the strong affinity of $Cr^{3+}$ ions towards the octahedral sites thereby forming Cr rich reaction layers [76]. Thus, as the Cr content increases in the spinel composition, it reduces the available sites for the conduction mechanism. Recent studies have shown that the doping of Cu to the spinel compositions exhibited enhanced electrical conductivity by limiting the formation of poorly conducting Cr-rich reaction layers at the oxide scale/spinel coating interface [97,98,103]. Also, doping of Cu has shown significant contribution in inhibiting Cr evaporation and reducing oxidation of FSS materials. Spinel coatings have exhibited promising

outcomes in Cr retention, thereby minimising the Cr poisoning along with reducing the oxidation rate of the base metal by forming Cr-rich spinels and low ASR.

The most common deposition methods for spinel oxide coatings are sol-gel, wet chemical spraying, magnetron sputtering, slurry coating, electroplating, and electrodeposition.

## 2.6. Outlook on deposition techniques

The application of protective layers for SOFC interconnects depends on the physical and chemical nature of the starting material, desired surface morphology and effectiveness in terms of cost and time. This section explains different coating methods used in the deposition of spinel oxide layers. The coating techniques employed can be broadly classified into 1) thermal spray techniques, 2) wet chemical methods, 3) electrodeposition, and 4) physical or chemical vapour deposition (PVD or CVD) techniques.

Vacuum deposition processes, for instance, such as physical vapour deposition (PVD), atomic layer deposition (ALD), metal oxide chemical vapour deposition (MOCVD), radiofrequency and magnetron sputtering have been experimentally employed for SOFC interconnect applications. Each of these different coating techniques has its advantages and disadvantages [13]. Vacuum deposition processes produce dense coating layers, but the limitation is in the thickness of the layer produced. Due to low thickness, the layers fail to form a complete barrier against Cr species migration. Moreover, the batch nature of processing hinders industrialisation (with one exception [104]). The coating process is considered to be expensive, time-consuming and also requires masking while coating 3D interconnectors. The process demands heavy investment to set-up for large scale manufacturing which also adds to the cost of the SOFC stack production. Electrodeposition is one of the widely used approaches in recent years and has shown promising results in terms of oxidation resistance and Cr inhibition [37] but is

limited due to the interdiffusion of coating components into the substrate during oxidation, resulting in breakaway oxidation. The process also requires intensive sequential steps during the coating process [81].

Wet chemical methods such as slurry coating, wet powder spraying, and screen printing are well-known conventional processes in ceramics processing. These techniques are inexpensive and capable of coating large structures of varying thickness in short periods. However, they produce porous coating layers with non-uniformity across the layers. They also require masking, and a large amount of coating materials are wasted during the process, for example, by overspray. Efforts are being made to reduce the porosity by indulging the coated samples into heat-treatment processes, reactive- sintering, or infiltration of porous microstructures. Techniques like sol-gel or dip-coating are relatively simple and cost-effective approaches. The coating adhesion in these cases largely depends on the surface property of the base metal and is susceptible to the heat- treatment process. The Atmospheric Plasma Spraying (APS) technique, capable of producing coatings of a thickness between 20 and 200 μm has been employed for protective layer application in several studies [105–110]. Hu et al. [109] showed that the use of APS in deposition of $Mn_{1.5}Co_{1.5}O_4$ along with preheating and reactive sintering produces gas-tight protective layers and prevents Cr outward migration. Though APS produces dense layers in comparison to the conventional plasma spraying technique, it requires masking and is considered to be an expensive approach.

The primary challenges associated in most of the coating methods are the requirement of masking, reproducibility, time consumed, wastage of materials in wet chemical methods, and influence of porosity in simple approaches like wet powder spraying, sol-gel, dip coating techniques. Kendall et al. [37] highlighted that most of the techniques employed are irrelevant

in terms of technological aspects by accounting the limitation of coating area, applicability on 3D interconnect structures, the expense of starting materials and coating process in terms of cost and time consumption. In the same study, a tentative parameter based on the thickness '*t*' was stated to indicate the homogeneity of the coating over the 3D interconnect material.

$$t = \frac{t_{top}}{t_{wall}} \tag{2.12}$$

When $t = 1$, this represents uniform coating over walls and valleys of a 3D ribbed structure, if $t > 1$, this indicates uneven coating between the walls and valleys and $t = \infty$ represents void, no coating at all, on the 'wall' elements.

**Table 2.2:** Characteristics of various deposition techniques, technological relevance and thickness ratio of the respective coating processes, taken from [15], [44], [53], [37].

| **Coating technique** | **Advantages** | **Drawbacks** | **Technological relevance.** | **Thickness ratio** [37] **$t = t_{top}/t_{wall}$** |
|---|---|---|---|---|
| PVD* | • Dense and defect-free | ▪ Expensive set-up<br>▪ Thin coating layers | - | ~ 4-10 |
| MOCVD** | • Effective for ceramic coatings | ▪ Expensive set-up<br>▪ Thin coating layers | -- | ~ 2-5 |
| PLD*** | • Effective for ceramic coatings | ▪ Expensive set-up<br>▪ Limited coating area | -- | ~ 4-10 |
| RF-magnetron sputtering | • Effective for ceramic coatings | ▪ Porous coatings<br>▪ Difficult processability | -- | -- |
| Sol-gel | • Easy processing<br>• Cost-effective | ▪ Thin, porous and non-uniform coatings<br>▪ Requires masking | - | ~ 3-10 |
| Screen printing | • Easy processing<br>• Cost-effective | ▪ Porous and non-uniform coatings<br>▪ Requires masking | + | ~ 3-10 |
| Slurry coating, WPS | • Simple process<br>• Cost-effective | ▪ Porous and non-uniform coatings<br>▪ Requires masking | ++ | ~ 3-10 |
| Plasma spraying | • Effective for ceramic coatings | ▪ Expensive approach | + | ~ 2-8 |
| Electrodeposition | • Easy<br>• 3D shapes | ▪ Wastage of materials<br>▪ Laborious sequential steps | ++ | 1 |

*PVD -Physical Vapour Deposition;
**MOCVD- Metal Oxide Chemical Vapour Deposition;
******* PLD- Pulsed Laser Deposition

## 2.7. Surface modifications

Oxidation kinetics and oxide scale formation at high temperature are significantly affected by the surface, thermo-mechanical, and electrochemical properties of the metal substrate [24]. The presence of defects such as dislocations in the metal/alloy surface offers rapid pathways for outward progression of Cr to the surface of the metal rapidly in a homogenous manner for the formation of the oxide scale during the early stages of the oxidation process.

In general, alloys used for interconnect applications are processed by cold working (cold rolling) to yield homogenous thickness and to increase the yield strength by strain hardening. The surface finishing process generates mechanical deformation within the crystal structure via defects and reduces the grain size [111]. The deformed surface grains recrystallise during the high-temperature operation, which in turn results in abundant grain boundaries. Grain boundaries prevent the dilution of Cr on the alloy surface by supplying enough oxide-forming elements from the base alloy to its surface. Cooper et al. [112] confirmed the formation of parabolic oxidation behaviour on cold-rolled FSS, AISI-SAE 434/430 and ZMG 232.

Belogolovsky et al. [113] investigated the adhesion of a chromia scale on FSS based on various surface treatment processes such, sandblasting, heat treatment in reducing conditions, application of yttrium nitrate coatings, grinding, electropolishing, and pickling in HCl and $HNO_3$. The adhesion of the oxide with the metal substrate was evaluated by tensile pull testing for the oxidised samples at 800 °C/ 458h. Sandblasted, and reduced samples displayed higher performance amongst different surface treatment. Heat treatment in reducing atmosphere is believed to eliminate the impurities such as sulphur and improve the adhesion. Sandblasting creates surface deformation at room temperature, which recrystallises and supplies oxide-forming elements via newly formed grain boundaries.

The surface of the ferritic stainless steel can be nitrided to increase its surface hardness. The formation of chromium nitrides during the gas nitriding process has been shown to affect the corrosion resistance of the stainless steels [114]. Studies have shown that the formation of Cr nitrides can be eliminated using plasma nitriding at temperatures below 450 °C [115]. Bergamo [114] studied the effect of nitridation on high-temperature ferritic steels by plasma nitriding process. The study reported that nitrided AISI 444 steels had developed thicker oxide scale and exhibited a slower oxidation rate in comparison to surface unmodified AISI 444 steels. The formation of $Cr_2N$ precipitates was observed in oxidising conditions at 600 °C with rich manganese at the outer layer of the thermally grown oxide layer. The effect of nitridation is widely studied on austenite steels [116–119], and only few studies were reported on ferritic stainless steels [120].

Though surface modifications can improve the oxidation resistance in FSS and in reducing ASR, Cr poisoning is still a concern which could only be limited by applying additional, efficient protective layer coatings.

## 2.8. Inkjet printing

Inkjet printing works on the principle-based on Lord Rayleigh's 'Instability of the Jets', which states that "liquid of constant radius traces the vertical fall under gravity" [121]. Fig. 2.8 represents the instability of the jet, where the formed jet loses its cylindrical shape after it reaches a critical length and breaks down into droplets.

A conventional inkjet printer consists of nozzles, charging electrode, deflecting plates, Gutter screen, ink supply, pump**,** and other components. The ink is forced to pump out of the nozzle into tiny droplets. Generated ink droplets are guided using different techniques such as the

deflection of drops by charged plates, piezo-electric force, thermal energy, and laser. Ink droplets fall out in precision and are capable of producing a small volume of liquid in the range of femtoliter to a microliter.

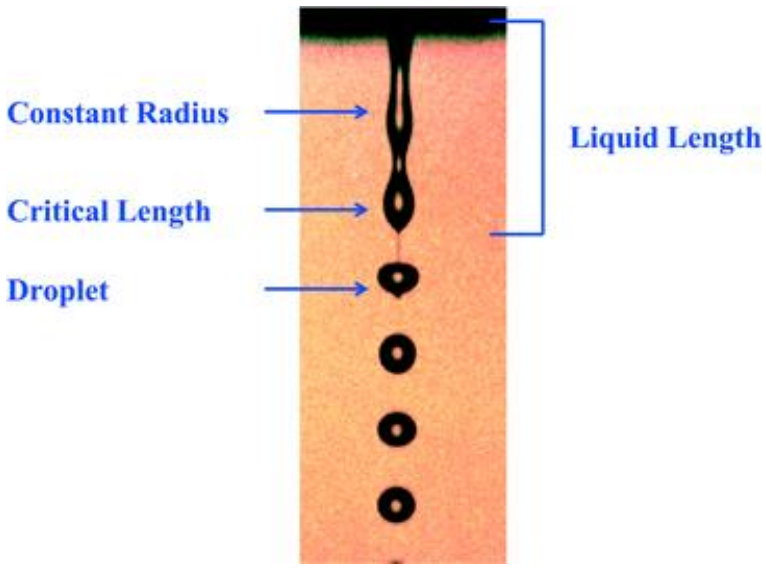


**Figure 2.8:** Schematic illustration of Rayleigh's instability of the jets [75].

A conventional inkjet printer consists of nozzles, charging electrode, deflecting plates, Gutter screen, ink supply, pump**,** and other components. The ink is forced to pump out of the nozzle into tiny droplets. Generated ink droplets are guided using different techniques such as the deflection of drops by charged plates, piezo-electric force, thermal energy, and laser. Ink droplets fall out in precision and are capable of producing a small volume of liquid in the range of femtoliter to a microliter.

Inkjet printers are classified into different types based on their mode of operation, namely Continuous Inkjet printing (CIJP) and Drop-on- Demand inkjet printing (DOD) [122], as shown in Fig. 2.9. DOD mode ejects ink droplets on need and eliminates the complexity of drop charging and ink recirculation systems as in the continuous ink-jet technology therefore also reducing cost. Drop generation is aided by the generation of acoustic pulses, either

thermally or piezoelectrically. DOD is more precise in terms of smaller drop generation than continuous mode printing. The accuracy in placement and versatile drop generation favours the Drop-on-Demand mode in research and development sectors.

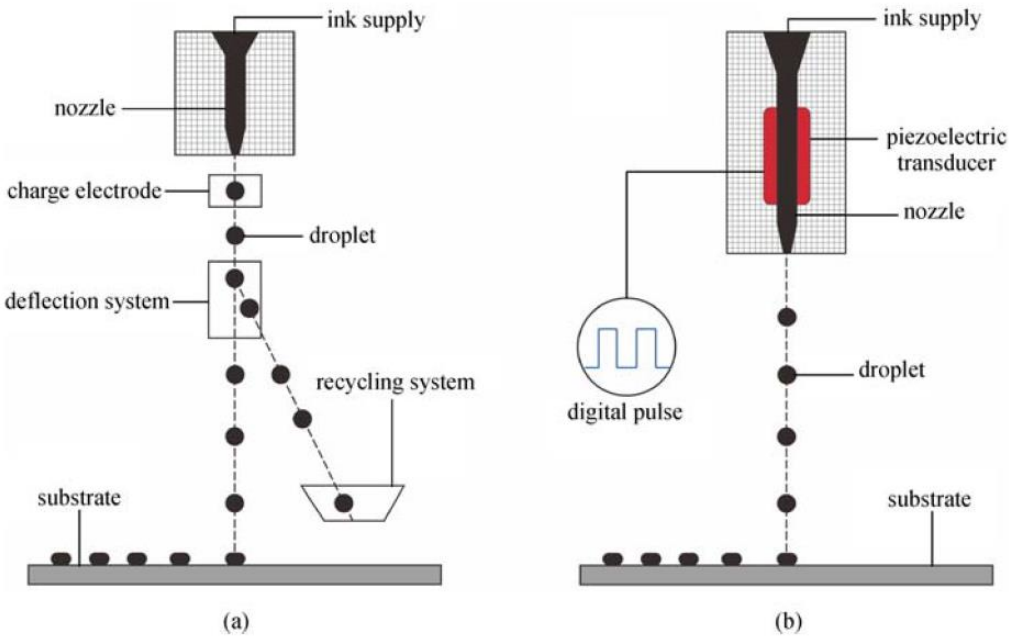


**Figure 2.9:** Schematic illustration of the inkjet printing process (a) CIJ mode - transducer generates pressure waves resulting in the formation of identical droplets. Deflector plate defines the path of droplets to the substrate, (b) DOD mode- a transducer expands under the application of voltage, thereby causes volume change in the nozzle resulting in droplets formation, taken from [123].

The inkjet process is being used in various fields such as material coating, electronic circuits, drug delivery, the printing of electronics and biomaterials, DNA arranging, fabricating Micro-Electro-Mechanical System (MEMS) components, and manufacturing of particles and microcapsules [124]. The prime challenge with inkjet technology is the formulation of ink that suits any selected mode of printing. The right choice of additives is significant to meet the rheological requirements of the ink, such as viscosity and surface tension for efficient printing [125]. The most widely used inkjet printers based on research applications are DOD based piezo-electric and electro-magnetic printers [126]. The electromagnetic printers have the

advantage of printing both solution and suspension-based inks in comparison to piezoelectric. The general characteristics comparison of both piezoelectric and electromagnetic printer is shown in Table 2.3.

**Table 2.3:** General characteristics of piezoelectric and electromagnetic inkjet printers [80].

| Specifications | Piezoelectric | Electromagnetic |
|---|---|---|
| Nozzle orifice size | 10-60 µm | 60-150 µm |
| Drop volume | 1-100 pL | 10-50 nL |
| Pressure regime | Vacuum (~50 mbar) | Positive (100-600 mbar) |
| Jetting distance | 1 mm | ~5 mm |
| Jetting range | 10 – 50 kHz | 0.5 – 3 kHz |
| Advantages | ▪ High resolution<br>▪ High Jetting rate | ▪ Ink compatibility<br>▪ Low cost |
| Disadvantages | ▪ High throughput<br>▪ Expensive | ▪ Maintenance<br>▪ Low resolution |
| Applications | ▪ Solutions, thin layers<br>▪ Patterns | ▪ Suspensions<br>▪ Coatings |

## 2.8.1. Significance of ink formulation

Table 2.4 represents the general characteristics, requirements, and challenges of the inkjet inks. Inkjet inks are a crucial factor for an effective printing process. The generation of ink droplets and their interaction with the substrate followed by drying are determined by the physical and chemical properties of the inkjet ink used. In general, inkjet inks are classified into four major types: solvent-based, aqueous-based, phase-change and UV curable [127]. Solvent-based and aqueous-based inks are widely used in the research applications, whereas the other two types are mostly in commercial aspects such as the printing industry and media applications. Solvent-based inkjet inks are prone to clogging of the nozzle due to their rapid evaporation, and they tend to release volatile organic compounds. Despite the high surface tension, aqueous-based

inks have gained attention as they are environmentally friendly and have the feasibility of using co-solvents such as alcohols to match the inkjet printer requirements [128–130].

**Table 2.4:** General characteristics of inkjet inks [76].

| Features | Requirements | Challenges |
|---|---|---|
| • Additive technique<br>• Variable layer thickness<br>• Less time consuming<br>• High material efficiency<br>• Eliminates the need for masking<br>• Precise and less wastage of materials | • Printable inks<br>• Ink viscosity<br>• Ink surface tension<br>• pH of the inks<br>• Particle size matching nozzle requirements<br>• Substrate nature | • Clogging of nozzle<br>• Ink composition<br>• Wetting behaviour<br>• Film homogeneity |

The ink formulation and selection of ink components is merely dependent on the mode of inkjet printer used. The selection of ink components must consider factors like pH, the stability of the ink, viscosity, surface tension, solid loading, and foaming agents. The essential components of inkjet inks are functional material, carrier medium, and the additives as shown in Table 2.5. Functional materials are the components to be transferred over the substrate. The carrier medium is the solvent in the system which determines the drying rate, surface tension, and viscosity of the ink system. Other additives such as a binder, plasticiser, surfactant, wetting modifiers are used in case of colloidal suspension inks to regulate the stability and rheology of the ink system.

The most common methods adopted for the formulation of suspension-based inkjet inks are chemical methods: a sol-gel, hydrothermal, polyol, reverse microemulsions, and mechanical grinding [131]. Liu et al. [17] reviewed different ink formulation approaches for the inkjet

deposition of functional metal oxide systems namely: colloidal suspensions, sol-gel inks, and, metal salt solutions. Colloidal suspensions were widely used for the formulation of metal oxide inkjet inks as the system allows to achieve high solid loading (up to 30%) and decreases structural changes following the sintering process [17,131].

**Table 2.5:** General components used in the inkjet inks.

| Component | Function |
|---|---|
| **Solvent** | Carrier vehicle – acts as the carrier medium |
| **Powders** | Functional material- the material to be deposited |
| **Dispersant** | Stability of the suspension- disperses the particles in the suspension |
| **Binder** | Viscosity modifier and to provide sufficient strength |
| **Plasticisers** | acts as a lubricant and retains moisture to overcome clogging at the nozzle |
| **Surfactant** | Surface tension regulator – reduces the surface tension of the suspension |
| **De-foaming agent** | Removal of air bubbles in the suspension |

Sol-gel based inks are the widely used approach, and successful inkjet deposition has been reported in the literature [132–134]. In recent years, IJP has been scarcely used for the deposition of inorganic materials in comparison to the organic materials mainly due to the challenges in the synthesis of the respective inkjet inks. Metal oxide inks are in general colloidal systems with the typical composition of functional materials (1-30 wt.%), solvent (50-60 wt.%), and additives (1-10 wt.%).

To achieve effective inkjet deposition of aqueous-based colloidal suspensions following considerations must be taken into account [17]:

- For micron-sized metal oxide particles, an inkjet printer with a nozzle size of 50 to 140 µm should be preferred,

- Chemical methods such as sol-gel processing, hydrothermal or microwave synthesis or mechanical methods such as ultrasonic mixing or ball milling should be used to formulate metal oxide inks.

The major challenge with colloidal suspensions is their particle size and distribution of the suspended particles. The tendency of a suspended particle to flocculate may lead to sedimentation and as a consequence inks result in clogging of the nozzle. As a rule of thumb, the particle size must be maintained below 10% of the nozzle diameter of the inkjet printer used, the estimated optimal value is less than 2% [20], and should have narrow size distribution [17]. Also, the stability of the colloidal suspension must be met to prevent particles from flocculation with respect to time.

## 2.8.2. Printability

Derby [135] elucidated the fluid property requirements for successful inkjet printing of structural and functional materials. Based on the physical property of inkjet inks, IJP can be summed up into the following three steps: 1) droplet generation, 2) interaction of droplets over the substrate and accuracy of the interaction, and 3) solidification to form a solid deposit. During the process of inkjet printing, four significant forces act on the inks, namely; gravity, inertia, surface tension, and viscous force. These forces are grouped into independent dimensionless parameters such as Reynolds number (Re), Weber number (We), Ohnesorge (Z) to assess the printability or jet-ability of the inkjet inks. The dimensionless parameters are described as follows,

$$Re = \frac{v\rho a}{\eta} \tag{2.13}$$

$$We = \frac{v^2 \rho a}{\gamma} \tag{2.14}$$

$$Oh = \frac{\sqrt{We}}{Re} = \frac{\eta}{(\gamma \rho a)^{\frac{1}{2}}} \quad (2.15)$$

Where $\rho$, $\eta$, and $\gamma$ are the density, dynamic viscosity and surface tension of the fluid respectively, v is the velocity, and a is a characteristic length (size of the inkjet nozzle used for the printing).

Fromm et al. [136] defined the parameter Z, the inverse of the Ohnesorge number, that rates inertial and surface tension force with viscous force. Fromm proposed that for stable droplet generation in DOD systems, Z must be greater than 2 (Z >2), which was further investigated by Reis and Derby using numerical simulation. In their work, inkjet printing of ceramic suspensions with high solid loading showed that the value of Z must lie in the limits 1< Z <10 for satellite free drop generation, where the lower limit represents high viscosity, and the upper limit relates to surface tension force and formation of satellite droplets [137,138].

Further work has been done to investigate the effect of rheological properties and drop formation. Drop generation is restricted by the influence of inertia and by surface tension at the air/fluid interface. The minimum velocity for droplet formation was suggested by Duineveld et al. [139] (Equation 2.16) and reformulated in terms of Weber number (Equation 2.17):

$$v_{min} = \left(\frac{4\gamma}{\rho a}\right)^{\frac{1}{2}} \quad (2.16)$$

$$We_{min} = v_{min} \left(\frac{\rho a}{\gamma}\right)^{\frac{1}{2}} > 4 \quad (2.17)$$

The onset of splashing occurs when the generated drops interact with the substrate, which largely depends on the velocity of the drops. Stowe and Hadfield, based on Re and We number, proposed the critical threshold limit (Equation 2.18) beyond which splashing is bound to occur.

$$We^{\frac{1}{2}} Re^{\frac{1}{4}} > f(R) \qquad (2.18)$$

*F (R)* is a function of surface roughness for a flat and smooth surface, *f(R)~ 50*. The relation is based on various reported values for smooth and flat surfaces [140]. Based on the equations (2.13- 2.18), Derby illustrated the space parameter defined by Re and We numbers as co-ordinates to evaluate the jet-ability of the formulated inkjet inks [135], shown in Fig. 2.10. The Re and We space parameters have been reported in the literature to predict the jet-ability of the ceramic suspension inks for piezoelectric, DOD mode printers [137].

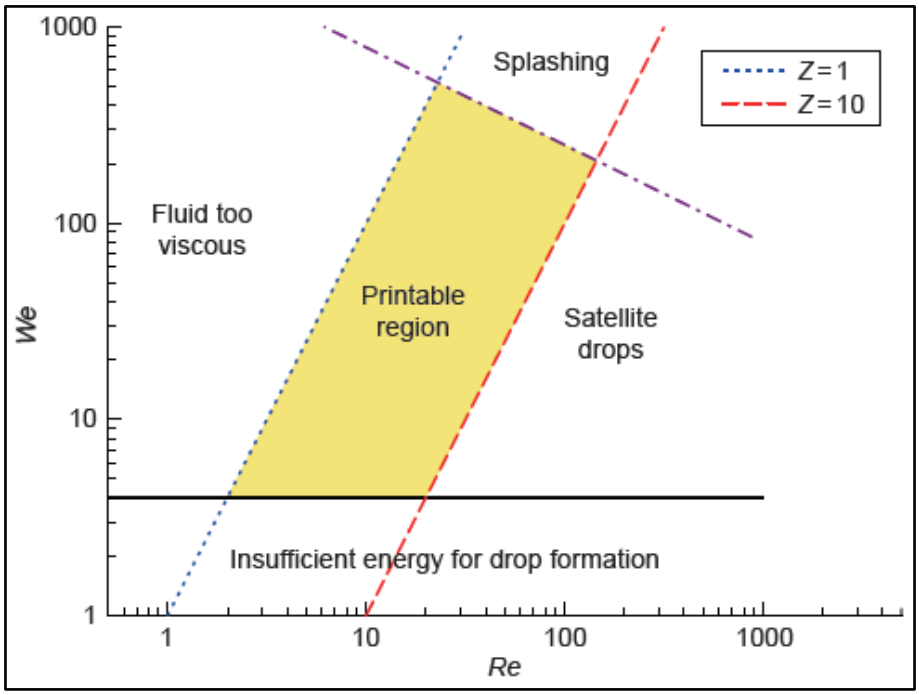


**Figure 2.10:** Illustration of fluid properties based on Re and We numbers to evaluate the printability for DOD inkjet printing, taken from [135].

## 2.8.3. Inkjet printing in SOFC

Young et al. [141] employed the inkjet printing process to fabricate Yttria- stabilised zirconia (YSZ)/ NiO/ $La_{0.8}Sr_{0.2}MnO_3$ based SOFC functional layers. The study highlighted the potential of IJP processes on tailoring the morphology of materials and their impact on fuel cell

performance. Sukeshini et al. [124] explored IJP in the fabrication of SOFC functional layers and stressed the significance of ink formulation and their optimisation along with the printing parameters to obtain the desired surface morphology on the ink-jet printed layers.

Tomov et al. [18] fabricated thin (~6µm), dense YSZ electrolyte layers for anode supported SOFC using an electromagnetic inkjet printer. The fabricated cells exhibited a power density of 170 $mWcm^{-2}$ at 800 °C. The study demonstrated the use of inkjet printing technology to obtain dense layers by multiple coatings, and the flexibility in the fabrication of functional layers of desired thickness by optimising printing parameters such as nozzle opening time, pressure and droplet formation to achieve desired surface properties.

Wang et al. [133] reported successful inkjet deposition of dense gadolinium- doped ceria (>10 µm of thickness) using an electromagnetic inkjet printer with sol-gel based inks. Esposito et al. [20] adapted a commercial desktop printer (HP Deskjet 1000) to fabricate dense electrolyte layers of 1.2 µm thickness using water-based YSZ inks. Inks were prepared based on dispersion ball milling, and the printability was assessed. The electrolyte deposited over the single cell (area of 16 $cm^2$) exhibited an open circuit voltage close to the theoretical value with a power density greater than 1.5 $Wcm^{-2}$ at 800 °C.

Han et al. [142] applied a commercial printer (HP inkjet printer) to fabricate cathode layers, using water-based LSCF inks, on anode- supported single cells. A maximum peak power density of 377mW $cm^{-2}$ at 600 °C was achieved, and the study demonstrated the scope in evaluating different cathode materials by rapid selection using IJP. Chen et al. [143] developed aqueous-based LSCF suspension inks and its characteristics such as stability, rheology, surface tension, and the printability of the inks were characterised along with the drying and sintering

methods. Tomov et al. [144] developed electrodes by two-step production of the functional coatings using inkjet printing infiltration to reduce the polarisation losses at the electrodes. The porous scaffold layer of the electrode was inkjet printed, followed by the infiltration in the form of nano-grid decoration to minimise the porous nature of the inkjet deposited layers. Drop-on-Demand based printers have been used for the fabrication of functional layers in SOFC manufacturing. Table 2.6 lists the different inkjet printers and their nozzle specifications used in the fabrication of SOFC functional layers.

**Table 2.6:** List of different inkjet printers employed for the fabrication of SOFC functional layers in recent years.

| Material | Inkjet printer used | Printer specs | Ref |
|---|---|---|---|
| 3Y-TZP[1] | HP DeskJet 850c ® | ~30 µm | [145] |
| LSCF[2]-GDC[3] | Pico Jet-1000, MICROJET Co., Ltd. | ~50 µm | [146] |
| NiO[4], YSZ[5], LSM[6] | Fujifilm Dimatix printer - DMP 2831 series | 21 µm | [147] |
| NiO-GDC | Domino MacroJet printer | 90 µm | [148] |
| YSZ | Domino MacroJet print | 90 µm | [18,134] |
| YSZ | HP Deskjet 1000 | ~20 µm | [20] |
| Composite cathode (SSC-SDC)[7] | HP Deskjet 2668 | - | [149] |
| GDC | Domino MacroJet printer | 90 µm | [133] |
| NiO, YSZ, and GDC | Domino MacroJet printer | 90 µm | [144] |
| LSCF | HP Deskjet 1010 | - | [142] |
| LSCF | Dimatix DMP-2850 | 21µm | [143] |

[1]Y-TZP: Yttria – Tetragonal Zirconia Polycrystal
[2]LSCF- Lanthanum Strontium Cobalt Ferrite
[3]GDC- Gadalonium doped Ceria
[4]NiO- Nickel Oxide
[5]YSZ- Yttria Stabilised Zirconia
[6]LSM- Lanthanum Strontium Magnetite
[7]SSC- SDC: Samarium Strontium Cobalt oxide – Samarium doped Ceria.

## 2.9. Summary

Metallic interconnects, in particular, ferritic stainless steels are currently considered as the standard metal interconnect material. Ferritic stainless steels are prone to high-temperature corrosion under SOFC operating conditions and results in degradation of the material. Several steps such as alloy modifications, surface treatments and application of protective/ conductive coatings have been studied as mitigation methods to overcome the degradation mechanisms in metallic interconnects. Application of protective and conductive coatings have shown significant results in mitigating volatile chromium species from the oxide layer and along with improved electrical conductivity by decelerating the growth of the oxide layer.

With regards to the coating materials, spinel coatings have shown significant results, and various spinel compositions are being analysed to find optimal protective-conductive layers for SOFC interconnects. Different coating techniques such as Vacuum Deposition techniques and Wet Chemical methods have been studied for the application of protective coatings. Wet chemical methods are inexpensive and capable of coating large structures of varying thickness in short periods in comparison to the vacuum deposition techniques. The primary challenges encountered in most of the coating methods are the requirement of masking, reproducibility, time consumed, integration into continuous industrial manufacturing, wastage of materials, and reducing the porosity in the layers applied. Inkjet printing technique, as a deposition technique has been scarcely used for the deposition of inorganic materials. The scope and challenges associated with the inkjet printing technique have been discussed. Thus, application of spinel based protective coatings by inkjet printing and evaluation of the inkjet printed coatings is subject of interest.

# *Chapter 3: Materials and Methodology*

This chapter details the stainless steel substrates and coating materials used in this study. The general composition of the inkjet inks is taken as a reference point to formulate spinel based aqueous inkjet inks. Each component used in the ink composition is listed, and the reason for the selection is discussed. The ink formulation route adopted for the two-stage ball milling method was developed and the techniques used to determine the optimal formulation with respect to the electromagnetic inkjet printer used in the study are explained. The working principle and the inkjet deposition process of the electromagnetic printer are discussed. The evaluation of the performance of the inkjet-printed protective layers is assessed based on the high-temperature tests and characterisation techniques developed for SOFC interconnect application.

# 3.1. Materials

Two stainless steels, K41 and Crofer 22H from KARA and VDM metals respectively were used as the interconnect substrates in the current study. The alloy composition of the stainless steel substrates is shown in Table 3.1. K41 ferritic stainless steels have been designed for high-temperature applications to achieve good corrosion and oxidation resistance at temperatures up to 980 °C and have been extensively studied for SOFC interconnect applications [15]. K41 stainless steels are dual stabilised with titanium and niobium which makes them favour the formation of laves phase precipitates at SOFC operating conditions. It has been shown that laves phase precipitates capture insulating silica ($SiO_2$) present in the alloy composition at high temperatures, thereby suppressing those as mentioned earlier electrically insulating scales on the interconnect [15,70]. Crofer 22H is a specially designed high-temperature stainless steel for SOFC interconnect applications. The selected ferritic based stainless steels are capable of forming protective chromia ($Cr_2O_3$), and spinel $(Mn, Cr)_3O_4$ dual-layers and prevent excessive oxidation under SOFC operating conditions [44,48,59].

**Table 3.1:** Composition of the stainless steel substrates (in wt.%) as specified by the manufacturers.

| Steel | Fe | Cr | C | Si | Mn | Nb | Ti | S | P |
|---|---|---|---|---|---|---|---|---|---|
| **K41** | bal. | 17.8 | 0.015 | 0.35 | 0.30 | 0.45 | 0.17 | 0.001 | 0.023 |
| **Crofer 22H** | Bal. | 20-24 | 0.05 | 0.24 | 0.8 | 0.51 | 0.06 | - | - |

In the SCoReD 2.0 project, Teer Coating. Ltd (TCL), introduced a nitriding technology as a surface modification process to enhance the physical properties of the steel substrates such as high hardness, resistance to wear, and plastic deformation. TCL reported the effect of the nitriding process in the austenitic 316 stainless steel, the nitridedsubstrates displayed low interfacial contact resistance (~0.01 Ω $cm^2$) at room temperature in comparison to as received

substrates (0.2 to 0.5 Ω $cm^2$). Based on the report from TCL, surface nitrided K41 was used, and its performance in comparision to K41 unmodified surface stainless steel (virgin K41) was studied.

## 3.2. Coating materials

Manganese Cobalt Oxide, $MnCo_2O_4$ (MCO), Manganese Cobalt Ferrite, $MnCo_{1.8}FeO_4$ (MCF), $Cu_{1.3}Mn_{1.6}Fe_{0.1}O_4$ (CMF) powders from Kceracell, South Korea were used as the starting material. The physical properties of the powders are listed in Table 3.2. Copper doped MCF, $MnCo_{1.6}Fe_{0.2}Cu_{0.2}O_4$ (MCFC) from ENEA, Italy, were used instead of CMF in batch I samples. (explained in Chapter 5, section 5.1).

Mn-Co based spinels ($(Mn, Co)_3O_4$) are considered as a promising material to mitigate oxide scale growth and chromium migration in interconnects at oxidising conditions (cathode side) of a solid oxide fuel cells. The Mn-Co spinel interacts with the thermally growing chromia layer at the oxide scale/coating interface to form a Cr rich $(Mn, Co, Cr)_3O_4$ reaction layer. The reaction layer slows the oxide layer formation and inhibits the Cr migration to the cathode layer [89]. The enhanced performance of MCO spinels substituting the Co with Cu and Fe have been reported [150–152]. Doping MCO spinels with Fe and Cu has shown beneficial effects in reducing CTE [9] and in increase of electrical conductivity respectively [10]. Recent studies have suggested that the doping of copper in Mn-Co based coatings can enhance the coating density [103,154]. The evaluation of the selected stainless steel substrates and the coating materials have been investigated in several studies at the operating temperature 800 °C or above. In the present study, the performance of the substrates and the effect of doping has been studied at 700 °C.

**Table 3.2:** Physical properties of the spinel powders as provided by the supplier.

| Powder | Particle size ($d_{50}$) (µm) | Specific surface area ($m^2/g$) |
|---|---|---|
| **$MnCo_2O_4$ (MCO)** | 0.54 | 6.31 |
| **$MnCo_{1.8}FeO_4$ (MCF)** | 0.55 | 7.60 |
| **$Cu_{1.3}Mn_{1.6}Fe_{0.1}O_4$ (CMF)** | 0.71 | 8.27 |

## 3.2.1. Overview of the methodology

Fig. 3.1 shows the sequential steps adopted for the ink production, inkjet deposition and finally, performance assessment. The first step is to produce an ink formulation that satisfies the requirements of the inkjet printer used for the deposition process. In this step, the particle size of starting powder and ink components were selected and prepared as shown in Fig. 3.2. To achieve a printable ink, ink properties were optimised by varying a number of composition parameters. The prepared inks were characterised and assessed for the printability based on the Re-We space parameter as discussed in Chapter 2, section 2.8.2

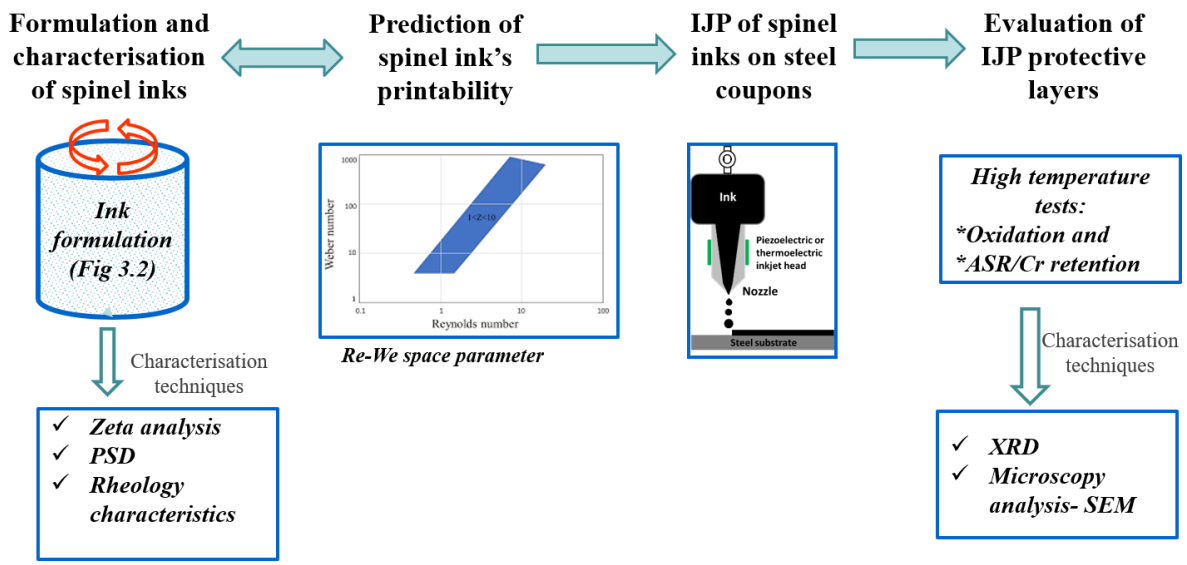


**Figure 3.1:** General overview of the study.

Initially, aqueous-based trial inks were prepared to assess the inks jet-ability. Ink components were then further optimised based on the test observations. Inks with optimal formulation were then printed onto the stainless steel substrate, and their performance as protective layers was evaluated in high-temperature exposure tests. The preparation of the ink suspensions and different ink components used for the ink formulation will be discussed in the following section.

### 3.2.2. Formulation of inks

Aqueous based inkjet inks with the selected spinel powders were prepared by a two-stage milling process in a PET bottle with zirconia beads of 0.3mm diameter as grinding media. A comminution process ball milling technique was employed to break down the soft agglomerates and to attain a homogenous mixture of the different ink components, as shown in Fig. 3.2.

In the first milling stage, spinel powders suspended in the DI water along with the dispersant and grinding media were ball milled for 24 hours at 400rpm. Before the addition of powder, DI water and dispersant were milled for 10-15 minutes to ensure the dissolution of the water-soluble dispersant molecules. Binder solution was freshly prepared before the second milling stage. Along with the binder solution, other additives such as plasticiser, surfactant, and, anti-foaming agent were added. The mixture was then subjected to slow milling at 200rpm for 4 hours to achieve homogenous mixing. Inks were filtered and stored for further experimental studies. The step by step optimisation process of the ink components will be discussed in Chapter 4 and is summarised in Fig. 4.1.

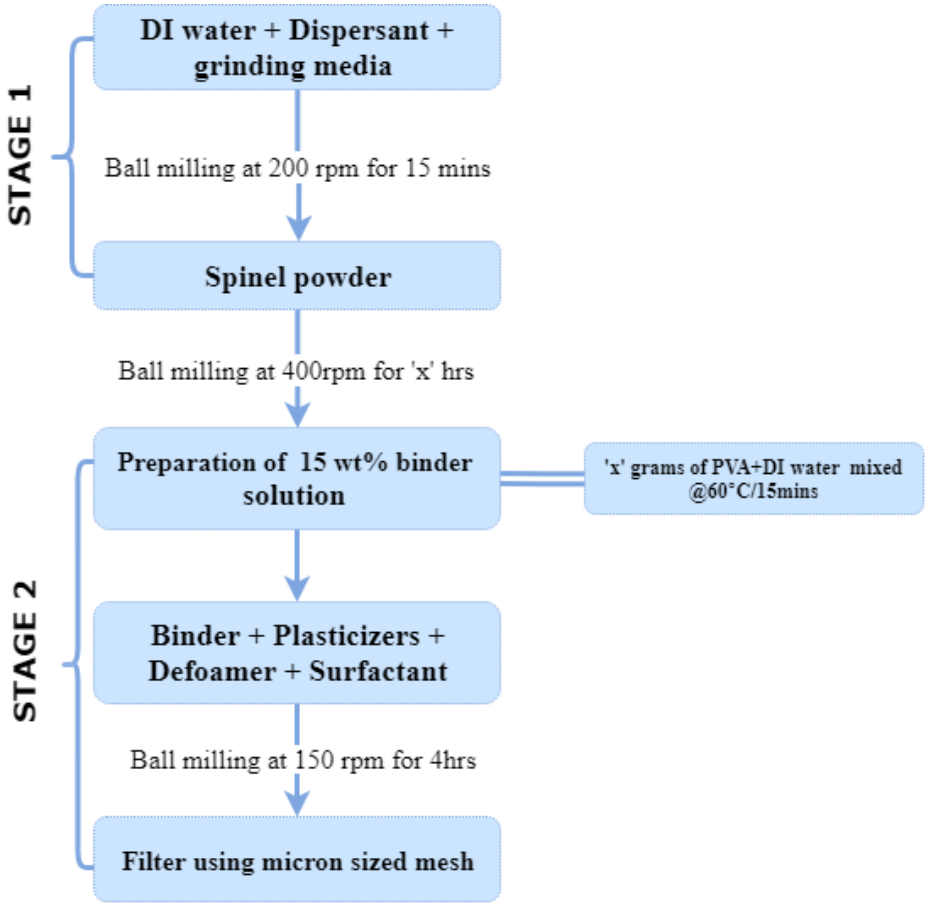


**Figure 3.2:** Schematic of the ink formulation route.

## 3.2.3. Inkjet deposition process

Prior to the coating process, stainless steel substrates were polished with silicon carbide sandpaper of grit size 1200 µm and cleaned in an ultrasonic bath with acetone for 30 minutes. Further, the samples were wiped with ethanol to ensure the removal of any impurities. The nozzle head with a 90µm ruby orifice was mounted approximately 5 mm above the substrate. The inks were fed into the print head compartment through a 3µm glass-fibre filter membrane to avoid dust contamination. The prepared inks were diluted with methanol in 2:1 volume proportion and printed over the stainless steel coupon in three layers in the x-y direction along the substrate with the optimal inkjet processing parameters.

The inkjet coated samples were then subjected to heat treatment in air at 800 °C for 10 hours with a heating and cooling rate of 5 °C/min to dry and sinter the inkjet-printed layers. To study the effect of sintering procedure, reactive sintering was also carried out to improve the densification of the coating layers. Anticipating the porous microstructure of the as-prepared coatings, an additional sol-infiltration process over the coated layers was carried out in few coated samples. Cobalt Manganese nitrate with 0.75 M solution was prepared with citric acid as a gelling agent and deposited over the heat-treated samples. The infiltrated sample was then heat-treated at 500 °C for an hour at the heating/cooling rate of 10 °C/min to remove the organics.

## 3.2.4. Ink components

Table 3.3 lists the different components used in the ink formulation and their physical properties. The essential components of inkjet inks are functional material, carrier medium, and other additives. De-ionised water (DI) was used as the carrier medium for the formulation. Aqueous based suspension systems pose severe challenges in terms of the stability of the inks (due to their high polarity), wettability of the powders (due to their high surface tension) and drying of the inks (due to the high vapour pressure). To overcome these challenges, components like dispersant, binder, plasticiser, surfactant, wetting modifiers and other additives were used in the formulation. The properties and selection criteria of the dispersant, binder and other additives will be discussed in the following sections.

### 3.2.4.1. Dispersant

Inorganic materials suspended in water tend to form soft agglomerates due to the existing attractive Van der Walls forces. This leads to a flocculated suspension which in the case of

inkjet inks leads to increase in viscosity and as a consequence clogging of the inkjet printer nozzle during the deposition process. Thus, it is crucial to obtain agglomerate free systems (dispersed systems) which can be attained by tailoring the surface charge of the dispersed particles in the suspension by adding dispersants. The most widely used dispersants, which offer chemical stability in the colloidal dispersion systems, are ionic surfactants and polymeric dispersants. Fig. 3.3 represents the effect of dispersant on the particles, where flocculates are dispersed in the presence of a polymeric dispersing agent.

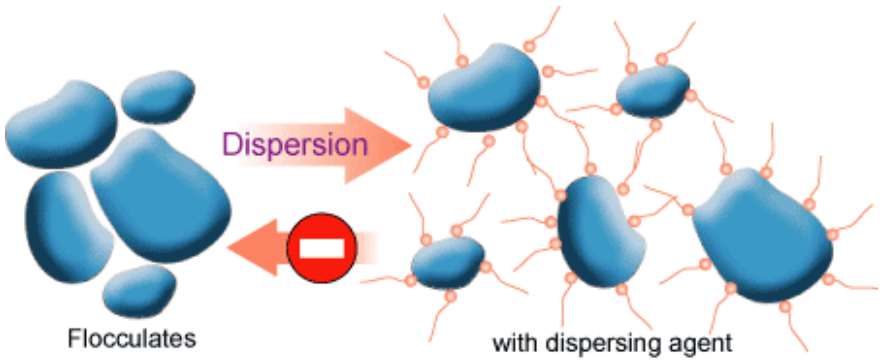


**Figure 3.3:** Dispersion of flocculates upon the addition of a dispersing agent [155].

The addition of dispersants eliminates the interaction between the particles mainly based on three mechanisms, namely; electrostatic, steric, and electro-steric. The particles in the aqueous suspension may carry electrical charges. When an electro-static dispersant is added to the suspension medium, it dissociates and adsorbs onto the particles in the suspension. As a result, a charge develops in the vicinity of particles and generates repulsive forces amongst them. Polyelectrolytes are high molecular weight compounds and are the most effective form of dispersant for this mode of stabilisation. Electrostatic stabilisation is effective in media with a high dielectric constant such as water-based systems. Whereas, in low dielectric constant media such as organic solvent systems, charge stabilisation is not adequate. In such cases, steric stabilisation is preferred, where the polymeric dispersant molecules adhere to the surface of the particles and their polymeric chain extends into the continuous medium (carrier medium).

When the particles approach each other, the polymeric chains intermingle and minimises the degree of freedom and keeps them apart. The significant aspect in the stabilisation is that the polymeric chain of dispersant molecules should be fully solvated in the medium, enabling them to extend freely in the suspension. The electro-steric mode of stabilisation is the combined effect of electrostatic and steric hindrance effect. Fig. 3.4 represents the schematic of the electrostatic and steric modes of stabilisation.

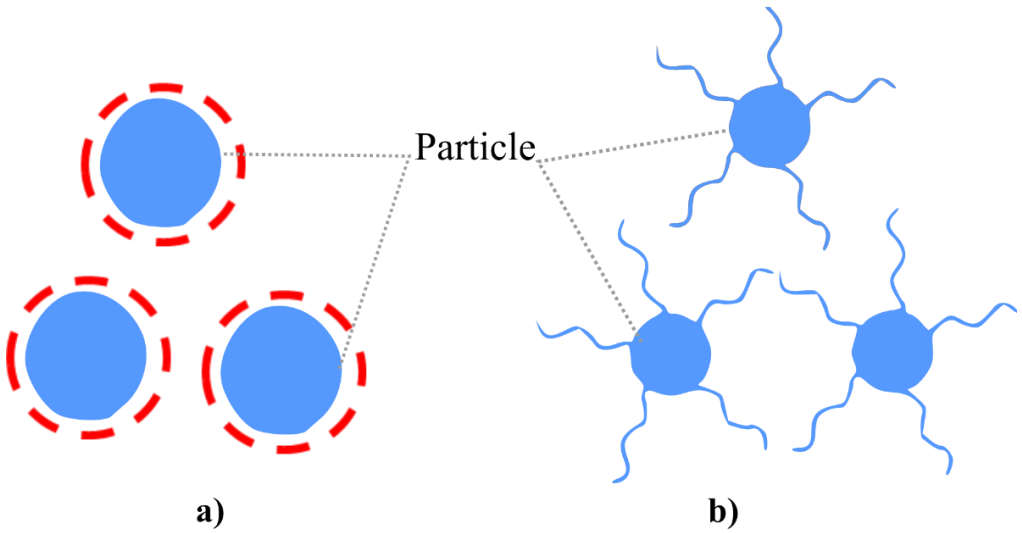


**Figure 3.4:** Illustration of the dispersion mechanism of particles in a suspension a) Electrostatic stabilisation- repulsion of particles due to the developing charges in their vicinity, b) Steric stabilisation- extended polymeric chains entangle, and the particles lose the degree of freedom of movement thereby keeping them apart.

In this study, Darvan C-N (R.T Vanderbilt Company, Inc. USA), ammonium polymethacrylate (PMMA-$NH_4$) solution was used as the dispersant. Darvan C-N is a water-soluble dispersant which is stable in the presence of alkalis over a broad range of pH (7.5-9.0) [156]. It has been used as an active dispersing agent for oxides in water-based suspensions in several studies [157–161]. The dispersion was performed in three stages: wetting, grinding and stabilisation. Wetting and grinding happens in the first milling stage. During wetting, the dissolved dispersant and powder particles are mixed as such to remove any air molecules in the interface and ensure adsorption of the dispersant molecules onto the suspended particles. In the grinding

stage, the uniform distribution is achieved by breaking down any agglomerates or any particle clusters by shear milling force.

### 3.2.4.2. Binder

The binder used in the suspensions must be compatible with the solvent, the dispersant and other additives, to deliver the desired properties such as viscosity of the suspension, reasonable green-strength, and dense coating when applied on the substrate. The most commonly used water-based soluble binders in slurry processing are cellulose-based materials, starches, and polyvinyl alcohol (PVA) [162]. The water-soluble binder eliminates the effect of pH variations in the ink composition during formulation and also satisfies the pH requirement (pH < 9) for the inkjet inks. In this study, PVA (Sigma Aldrich, UK) was used as the binder in the ink formulations. PVA comprises of polar -OH groups which have higher affinity and interaction with polar solvents, i.e., they are highly soluble in polar solvents such as water.

Adding the binders to the system in the liquid phase enhances the homogenous dispersion of its molecules. As the water in the suspension system evaporates, residual -OH side groups of the PVA form a hydrogen bond with the surface of the particles and form interparticle bridges to provide adhesion strength [163]. The degree of hydrolysation and the molecular weight of the polymer have a significant influence on its solubility, viscosity and surface tension [162]. Although fully hydrolysed PVA yields higher density and good packing fraction of particles, the increased hydrogen bonding leads to cracks due to the high stress developed during the drying stage of the green layers [163]. Considering the inkjet droplets are bound to dry quicker, partially hydrolysed PVA (87-90%) with molecular weight (avg. 30,000-70,000) was chosen due to its ease of solubility, lower viscosity, and lower surface tension. Finally, to, reduce the gel formation temperature ($T_g$) of the binder, plasticisers were added with the PVA [164,165].

In this work, 12.5 wt% PVA solution was prepared by adding PVA to the DI water using a magnetic stirrer heated up to 50 °C. The optimal amount of binder and plasticisers were determined based on the viscosity values of the ink composition obtained by flow curve analysis. The details of the optimisation process will be discussed in Chapter 4, section 4.1.

### 3.2.4.3. Other additives

Polyethylene glycol (PEG) and Glycerol (Sigma Aldrich, UK) were used as plasticisers in the ink formulations. The compatibility of PEG with PVA in slurry processing has been reported in the literature [166]. PEG provides the flexibility for the ink droplets during the inkjet printing process by breaking the alignment and polymer chains in the binder molecules [167]. Glycerol was to retain moisture and to prevent drying of the inks at the ink nozzle. A surfactant, 2,4,7,9-Tetramethyl-5-decyne-4,7-diol ethoxylate (Sigma Aldrich, UK), was added in the ink composition to lower the surface tension of the water-based inks. Antifoam 204 (Sigma Aldrich, UK), a mixture of organic non-silicone-based polyether dispersions were added to the ink compositions to eliminate air bubbles forming during the milling stage. The concentration of surfactant and antifoaming agent were adjusted between 0.005 and 0.01 wt.% with respect to the powder content, as specified by the supplier. Table 3.3 lists the physical properties of the ink components used in the formulation process.

**Table 3.3:** Physical properties of ink components as provided by the suppliers [14].

| Component | Function | Molecular weight (Mn) | Density (g/mL) at 25 °C) | Viscosity | pH |
|---|---|---|---|---|---|
| **Darvan C-N** | Dispersant | 10,000 -16,000 | 1.11 ± 0.02 | 75 mPa.s | 7.5-9.0 |
| **PVA** | Binder | 30,000-70,000 | 1.269 | 4-6 cps in water | |
| **PEG** | Plasticizer | 190-210 | 1.12 | ~60 cps | 4.5-7.5 |
| **Glycerol** | Plasticizer | 92.09 | 1.26 | - | - |
| **Surfactant** | Surfactant | 670 | 1.04 | - | 6-8 |
| **Antifoam 204** | Antifoaming agent | - | 1.01 | 400 | - |

The optimal concentration of different ink components to obtain printable ink was determined based on the pH, particle size, viscosity, and surface tension. The techniques used to achieve the desired ink properties are described in the following section.

## 3.2.5. Ink characterisation

### 3.2.5.1. Zeta Potential analysis

Zeta sizer Nano Z (Malvern Panalytical) was used to determine the Iso-Electric Point (IEP) of the spinel powders, and to identify the optimal pH range for ink formulations. The effect of milling time on dispersion at different dispersant concentrations was studied by observing the zeta potential.

The physical stability of the formulated ink is determined based on the charge carried by the dispersed particle in the continuous medium (distilled water). The dispersed particles in distilled water (polar medium) acquire surface electrical charge, which is influenced by conditions such as pH and ionic strength. The charge formation results in a surface potential due to the adsorption of ions from the suspension/solution or as a consequence of reaction

between the functional group on the particle surface and the surrounding medium [168]. The charge formation of a negatively charged in a liquid and its interaction with surrounding liquid is shown in Fig. 3.5, based on the electrochemical double layer (EDL) model. Based on the surface charge carried by the particles, molecules or ions with counter charge occupy the space next to the surface of the particle developing an electrical double layer. The EDL comprises of two layers, an immobile layer nearby the particle surface (stern layer) and an outer layer (diffuse) layer, that allows the diffusion of ions which are dispersed under the influence of electrical forces and random thermal motions. The overall net charge of the particle is characterised by the shear plane, the boundary layer between the stern and outer diffuse layer. The electrical potential at the shear plane is quantified by the zeta potential.

The zeta potential ($\zeta$) is defined as the electro-kinetic potential difference between the dispersed particle and the surrounding medium, usually expressed in millivolts. The magnitude of the zeta potential indicating the strength of repulsive force between the individual particles in the suspened medium, represents the stability of the suspension, i.e., $\zeta$ above $\pm$ 30 mV representing a stable dispersion and below $\pm$ 30 mV indicating unstable dispersion [169].

**Sample preparation:**

To determine IEP, 0.1 g of powder was added to 50mL distilled water in a beaker and agitated using a magnetic stirrer plate to obtain the base sample. 10mL from the base sample was extracted, and its pH was modified by varying the amount of a 0.1M solution of nitric acid and ammonia solution. The pH was monitored using the pH meter. The titrated sample was then fed into a DTS070 folded capillary cell for zeta analysis. To understand the effect of dispersant concentration with respect to milling time, inks were extracted and diluted with 10mL of distilled water; the inks were diluted due to their opaque nature. The IEP of the spinel powders

and zeta values of different dispersant dosages with respect to the milling time will be reported in Chapter 4, section 4.2.

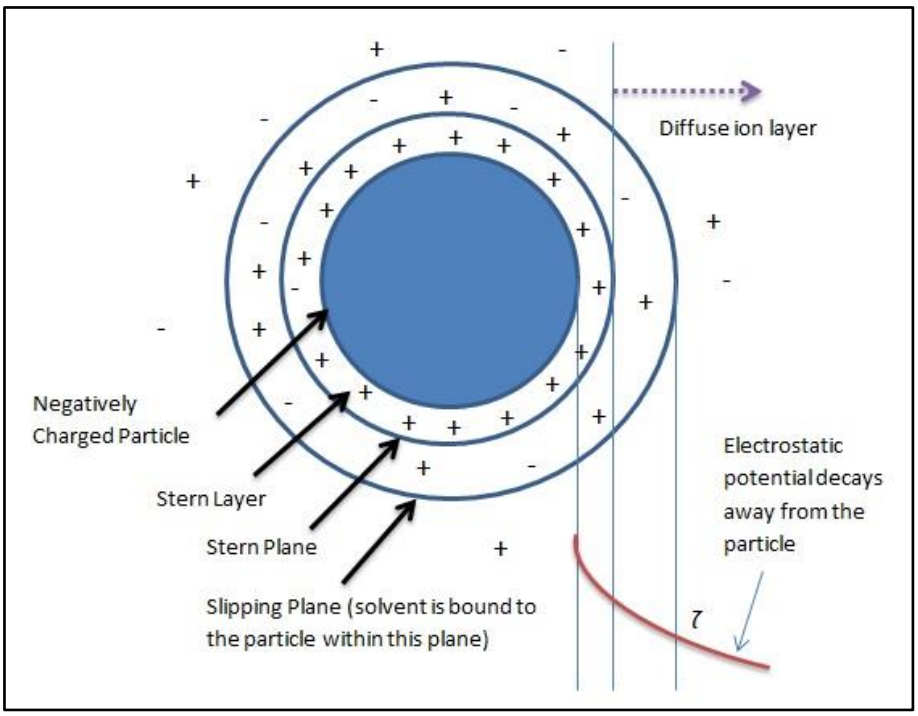


**Figure 3.5:** Schematic representation of a negatively charged particle at the solid-liquid interface based on the electrochemical double-layer model, taken from [170].

### 3.2.5.2. Particle Size Distribution (PSD)

The effect of varying milling time (24, 48, and 72, hours) at different dispersant concentrations on PSD was studied using a Mastersizer 2000 (Malvern Panalytical).

The Mastersizer 2000 is capable of measuring particle size in the range 0.02-2000 µm based on the laser diffraction method using an He-Ne laser. The samples were extracted from the inks using a pipette and added to the dispersion unit, Hydro2000 G, comprised of (distilled water). The dispersion unit was set to stir at 2000 rpm for all the measurements. The sample was added to the dispersion unit within the set obscuration range. The laser was then turned on to pass via the dispersed particles, and as a consequence, the dispersed particles diffracted the laser beam

at varying intensity and angle. Large particles scatter light at smaller angles relative to the laser beam, whereas small particles scatter at a large angle [171]. The particle size distribution of the particles was determined using the intensity and angle of the scattered light and was correlated to the PSD based on Mie theory [171].

The refractive index of 2.4 with the absorption value of 0.1 was set to specify the optical properties for all the sample measurements. The obscuration range, which defines the ratio of light lost from the source when the particles are dispersed, was set between 5 and 10%. Volume-based distributions are reported in this study, and the specification of different diameter analyses are defined in Table 3.4.

**Table 3.4:** Parameters and their specifications derived from the PSD analysis, taken from [171]. The particle size is represented in microns.

| Parameter | Definition |
|---|---|
| D (v, 0.5) – $d_{50}$ | represents particle size where 50% of the sample is smaller, and 50% is larger in the PSD- known as mass median diameter |
| D (v, 0.9) – $d_{90}$ | denotes the size of the particle below which 90% of the sample lies in the PSD – referred to as maximum particle size |
| D (v, 0.1) – $d_{10}$ | denotes the size of the particle below which 10% of the sample lies in the PSD – referred to as minimum particle size |
| D [4, 3] | represents the volume-weighted mean value |
| Span= $\frac{d_{90}-d_{10}}{d_{50}}$ | Specifies the distribution width of the sample. |

### 3.2.5.3. Rheology measurements

Understanding the rheological behaviour of ink suspensions aids in achieving the desired fluidity, to determine the maximum solid content, to understand the effect of additives on viscosity, and to attain kinetic stability in order to avoid or slow down the sedimentation. In colloidal suspension systems, the rheological nature is determined by the microstructure of the

dispersed phase, which depends on factors such as Brownian motion, viscous forces, and interparticle interactions [172].

In general, fluids are categorised based on the flow behaviour, namely; Newtonian and non-Newtonian fluids. Fig. 3.6 represents different types of flow behaviour based on the relationship between applied shear force (γ) and its response, shear stress ($\tau$), and viscosity (η). In Newtonian fluids, shear stress grows linearly with shear rate where viscosity is more or less constant in response to the applied shear force. This is most commonly observed in water, alcohol and dilute dispersions. Various materials, namely; suspensions, emulsions, and polymer solutions exhibit non- Newtonian behaviour due to their complex microstructure, i.e., viscosity either decreases (shear thinning) or increases (shear-thickening) in response to the applied shear force. Suspension based inkjet inks mostly exhibit shear-thinning behaviour due to their ink compositions and the suspended particulate matter [172].

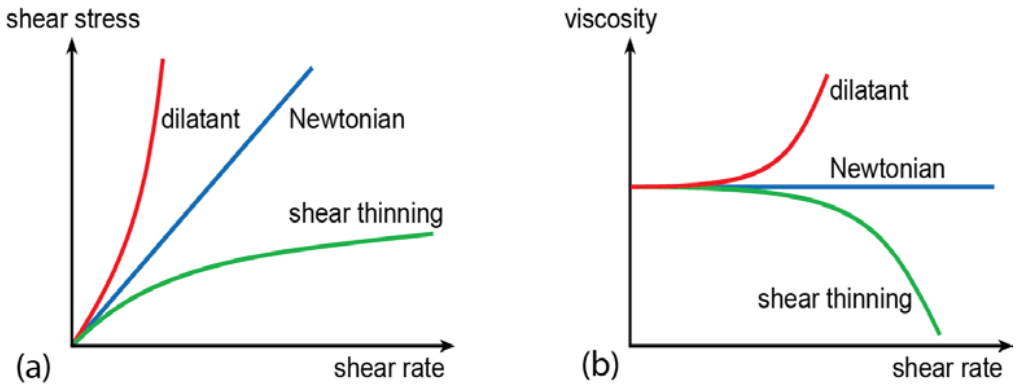


**Figure 3.6:** Different types of fluid behaviour a) shear rate vs shear stress, b) shear rate vs viscosity, taken from [173].

In the present study, flow curve analysis was performed to comprehend the flow behaviour of inkjet inks and to determine the dynamic viscosity, which is a function of time, shear rate, pressure, and temperature. For an efficient inkjet deposition process in DOD printers, the

recommended viscosity for the fluids is 10 to12 mPa.s. However, fluids with viscosity up to 30 mPa.s can also be printed based on the printhead specifications. The simulated shear force experienced by the inks at different steps of the inkjet printing process is shown in Fig. 3.7.

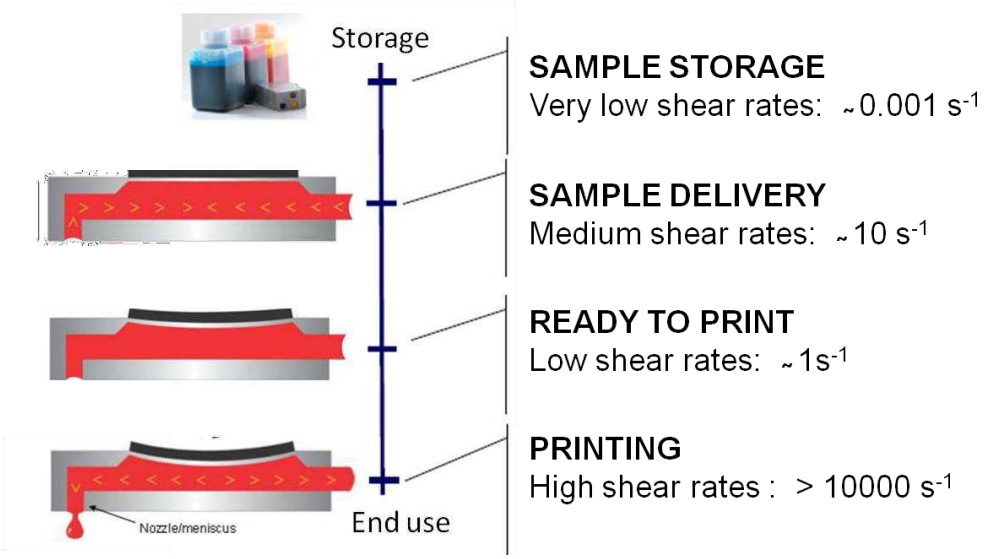


**Figure 3.7:** Evolution of ink during the inkjet printing process estimated at different shear rates, taken from [174].

For DOD mode inkjet printing, the characterisation of the ink at lower shear rates ($<10^3$ $s^{-1}$) is insufficient for assessing the jet-ability of the fluids as the shear force during the jetting process is in the range $10^5$ to $10^6$ $s^{-1}$ [175]. Moreover, the viscoelastic property of the inkjet ink which influences the droplet formation and droplet breakup during the deposition process, cannot be evaluated using conventional rheometers due to their limitations of reaching higher shear force ($10^5$ to $10^6$ $s^{-1}$ ) [176]. Studies have analysed the complex viscosity and linear viscoelastic properties of the inkjet fluids for piezoelectric printers using a Piezo-Axial Vibrator (PAV) which operates in the frequency range, 1to 10,000 Hz [177–179].

A Discovery HR-2 rheometer (TA Instruments, United Kingdom) was used to determine the rheological behaviour of the inks. Flow curve analysis was carried out to identify optimal dispersant dosage, and binder and solid content with respect to the requirement of the inkjet

printer used in the study. The measurements were performed using a sandblasted 40mm parallel-plate geometry in the shear interval of 0.1 to 1000 $s^{-1}$ (logarithmic ramp profile) at steady shear flow. Before the measurements, samples were subjected to pre-shear of 100 $s^{-1}$ for 60 seconds to maintain the same shear history for all the samples. The linear viscoelastic behaviour and complex viscosity of the inks with the final compositions were analysed using the Piezo-Axial Vibrator (PAV) dynamic squeeze flow rheometer at Rheology centre, Department of Chemical Engineering and Biotechnology, University of Cambridge.

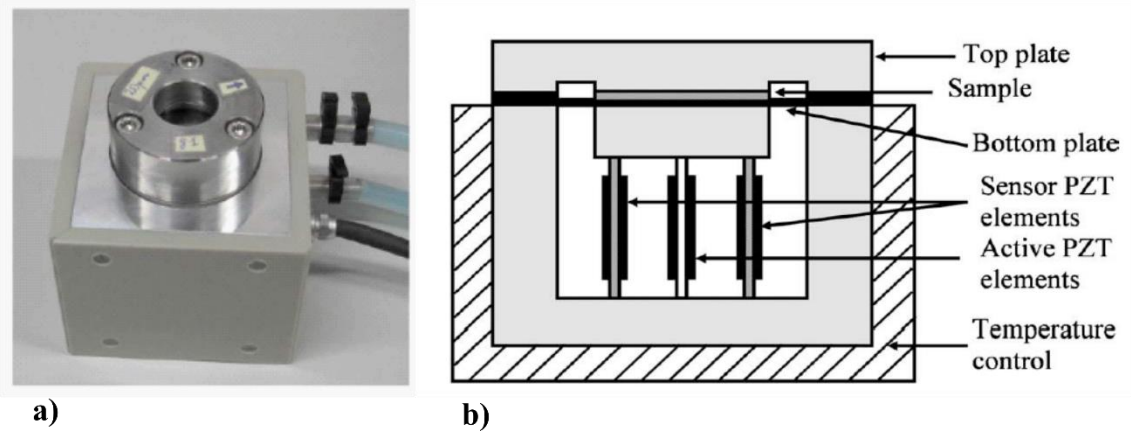


**Figure 3.8:** Photograph (a) and (b) schematic of PAV at Department of chemical engineering, University of Cambridge, taken from [176].

The Piezo Axial Vibrator (PAV) operates at frequencies between 1 to 10,000 Hz. Fig. 3.8 shows the schematic of the PAV set-up; it consists of a dynamic press with a thin gap (d<200 μm) where the test fluid is confined. The fluid sample is perturbed by an oscillatory squeeze flow generated by the piezoelectric drive, and the response is measured by piezo sensors. The K*, complex spring constant of the device is determined initially without and later with the sample fluid. The difference between the two gives the fluid. The test yields shear modulus ($G^* = G' + iG''$) and complex viscosity ($\eta^* = G^*/i\omega$, $\omega$ is in rad/s ) where G' and G'' represent storage and loss modulus respectively. Thus, the viscoelastic behaviour of the tested fluid can be understood.

### 3.2.5.4. Surface tension

The surface tension of the formulated inks was measured using the Wilhelmy plate method. The schematic of the Wilhelmy plate method is shown in Fig. 3.9. A plate made of roughened Platinum, attached to the tensiometer, was immersed into the ink sample (~15 ml) vertically and the force exerted on the plate was used to measure the surface tension of the ink, as given by Equation 3.1.

$$\gamma = \frac{F}{l.cos\theta} \tag{3.1}$$

Where γ is the Surface tension; F the Force exerted on the plate (mN/m); l the wetted length of the plate in mm, and cos θ represents the contact angle of the plate with the sample fluid.

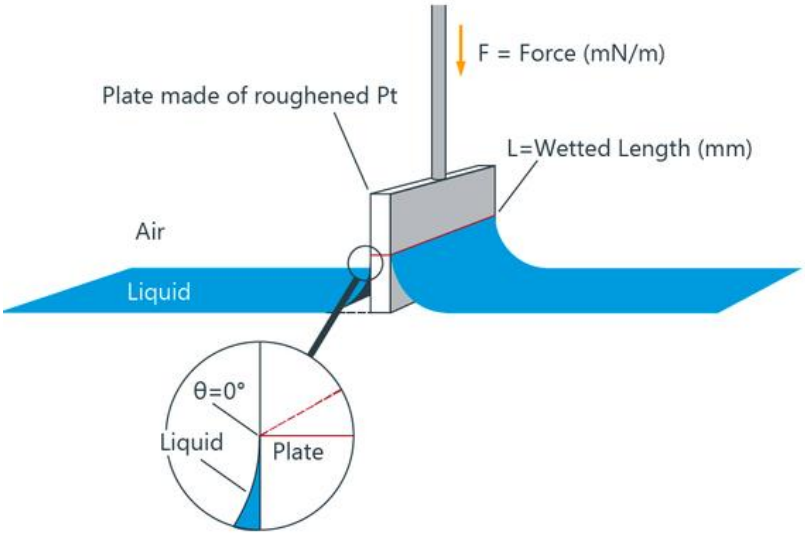


**Figure 3.9:** Schematic of Wilhelmy plate method, taken from [180].

### 3.2.5.5. Surface roughness and wettability

The surface roughness of the stainless steel substrates was measured using Bruker's Focus-Variation Microscopy (FVM) (InfiniteFocus®, Alicona )at x20 magnification. FVM is similar to confocal microscopy, where the image of the samples is acquired based on the analysis of the depth of the field – focus variation. Fig. 3.10 shows the schematic of FVM illustrating its

principle of operation. The light from the light source is introduced into the system's optical path and projected on to the surface of the sample using a beam splitter. Based on the sample's topography, the projected light is reflected in different directions which are then focused by the beam splitter to the photoelectric detector to obtain geometric and photometric details of the specimen surface. The sample surface was scanned at different locations to obtain an average surface roughness value.

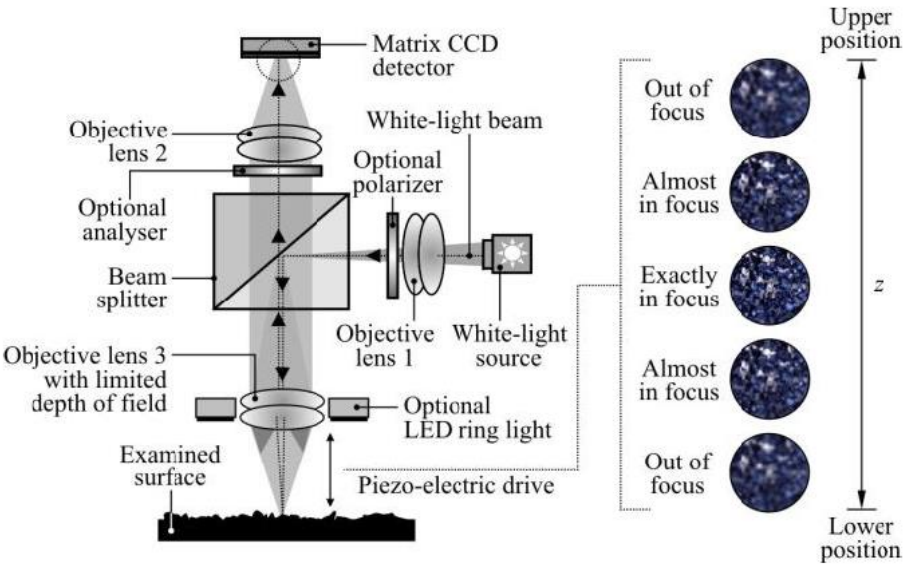


**Figure 3.10:** Illustration of focus variation microscopy representing the principle of operation, taken from [36].

The interaction between the formulated spinel inkjet inks with the stainless steel substrates can be either attractive or repulsive and are quantified by contact angle measurements. The contact angle is the angle where the three-phase boundary liquid/solid/air interface intersects. The contact angle is given by Young' equation; Equation (3.2). The wettability of the stainless steel substrate can be understood based on the contact angle obtained from the measurements, as shown in Fig. 3.11. The solid substrate is hydrophilic if the contact angle formed is less than 90° and hydrophobic when the angle formed is greater than 90°.

The contact angle was measured using an Attension Optical Theta Tensiometer, Biolin Scientific. The measurements were done using a static sessile drop method. The formulated inks were fed into the syringe, and a droplet was generated manually on to the stainless steel substrate which was then recorded by a camera. The recorded image was analysed using One Attension software to obtain the contact angle.

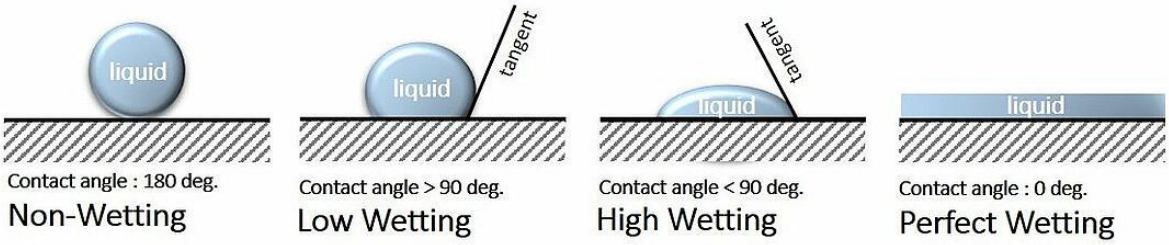


**Figure 3.11:** Wetting behaviour of the substrate based on the measured contact angle [181].

$$\gamma_{SA} = \gamma_{SL} + \gamma_{LA}Cos\theta \qquad (3.2)$$

Where $\gamma_{SA}$, $\gamma_{SL}$, $\gamma_{LA}$ are the interfacial surface tensions between solid-air, solid-liquid and liquid-air respectively. $\theta$ is the contact angle.

### 3.2.5.6. Thermo-gravimetric analysis (TGA)

TGA was used to observe the thermal characteristics of the spinel inkjet inks before the heat-treatment process. TGA measurements were carried out using a TG209 F1, NETZSCH instrument (UK). The instrument contains a crucible supported by a precision balance. The crucible that holds the sample material is placed inside in a furnace and heated or cooled during the experiment. Whilst the change in mass of the crucible due to the loss of sample material is recorded during the experiment. The environment of the sample is controlled by a purge gas controls. The purge gas flows across the sample and it can be chosen as per the need, it can be either inert or reactive gas such as oxygen, air or hydrogen.

The ink samples were weighed, placed in a Pt crucible and heated up to 850 °C at the heating and cooling rate of 5 °C/min in air atmosphere. The change in mass of the ink samples was recorded with respect to the temperature. The thermal stability of the sample is directly correlated to change in weight measured. The change in weight occurs as a consequence of sample degradation or due to its volatile nature. In the present study, TGA data were used to quantify the loss of water, solvent, dispersant, binder and other organic additives.

## 3.3. Inkjet Printing

### 3.3.1. Inkjet Printer

The inkjet printer used for the deposition process was based on electromagnetic printing technology, referred to as valve-jet technology. The printing facility at the Department of Materials Science and Metallurgy, University of Cambridge was used for the deposition process. The custom-made inkjet printer was composed of an electromagnetic single nozzle printhead with the opening of 90 μm mounted directly above the substrate on a Roland pen plotter. As can be seen in Fig. 3.12, the electromagnetic solenoid valve was connected to the ink reservoir closed by a rubber-tipped piston. The piston was driven up and down (opening and closing the orifice) as the effect of the magnetic field generated in the solenoid when a pulse of current was applied. The period of the pulse, termed as “opening time”, controls the time for which the orifice was left open and thereby ensuring the controlled volume of the ink is ejected through the nozzle to form the droplet [144]. The ink reservoir was separated from the external solenoid, and thus the heat generated at the solenoid did not affect the inks assuring that the viscosity of the ink suspension remained constant.

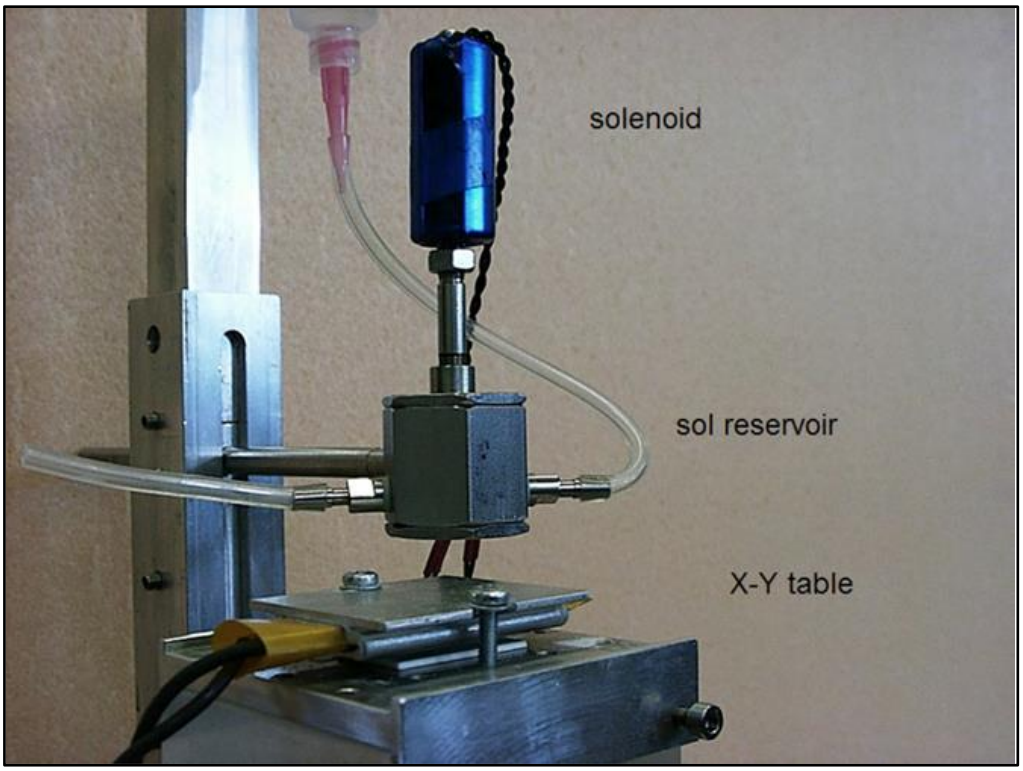


**Figure 3.12:** Custom built DOD electromagnetic inkjet print head used in the inkjet deposition process, taken from [19].

## 3.4. Evaluation of stainless steels and IJP layers

### 3.4.1. High-temperature oxidation

The stainless steel samples (uncoated and coated) were cut into small coupons (dimensions of the cut coupons are mentioned in Chapter 4, seciton 4.1), placed on an alumina plate in a tubular furnace and exposed to a continuous airflow of 1 L/minute with 3% relative humidity at 700 °C, simulating SOFC operating conditions at the cathode for 1000 hours. Fig. 3.13 illustrates the schematic of the experimental set-up. The samples placed in the furnace were heated to the target temperature at 5 °C/min and held at that temperature for 1000hrs by the furnace controller. The air mass flow rate with the desired relative humidity at the inlet was controlled using a Mini CORI-Flow (Bronkhorst, UK) and Controlled Evaporator Mixer (Bronkhorst, UK). The air supply line was heated using a ribbon heater to prevent condensation

in the line. The exposed samples were also weighed at regular time intervals to monitor the mass-gain.

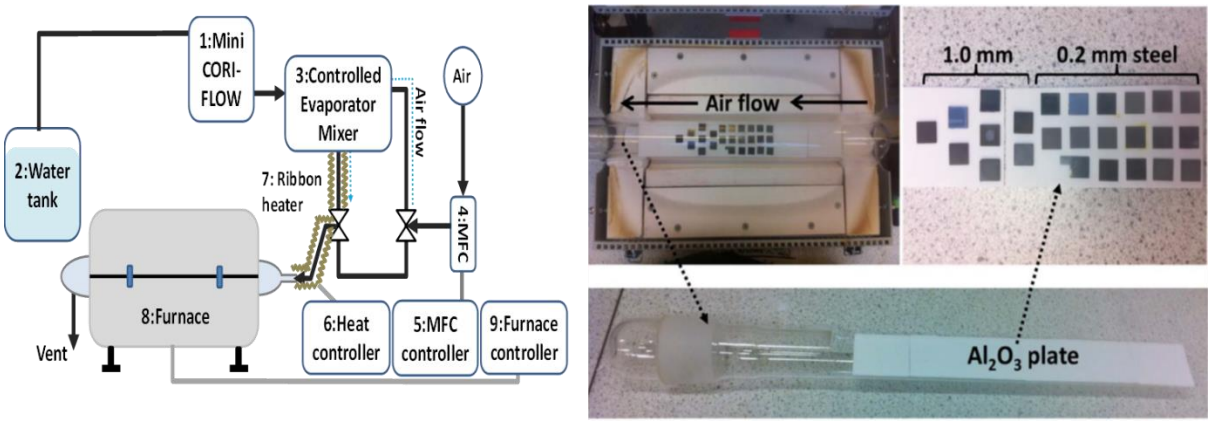


**Figure 3.13:** Schematic (left) of the high-temperature oxidation test. The test setup (right) with stainless steel samples placed inside the furnace under the test conditions: 700 °C: 1 L/ minute air with 3 volime % humidity.

The rate of oxidation in metals is measured based on the number of reactants, i.e., metal and oxygen consumed, and the amount of oxide formed. The change in the sample mass is attributed to the sum of oxygen uptake and metal consumed to form an oxide, provided it remains stable without any spallation or volatilisation during the exposure time. The nature of thermally grown oxide layers varies based on the oxidation process that takes place. From the mass gain measurements, the nature of the oxide scale growth mechanisms can be classified as linear, logarithmic or parabolic [24], as shown in Fig. 3.14.

The *Linear rate law* refers to a constant oxidation rate over time. The linear rate behaviour is controlled by a surface- reaction step or a phase boundary process or diffusion via the gas phase. The behaviour is commonly observed in porous or very thin oxide layer formation, and similarly in cases where the oxide layer thickness remains constant. The mass gain as a function of time can be expressed as in Equation 3.3

$$\Delta m = K_1 t \quad (3.3)$$

Where Δm represents the mass gain, $K_1$ is the linear rate constant, and t is the exposure time.

The *Logarithmic rate law* is usually detected at temperatures (>400 °C) and in cases of very thin thermally grown oxide layers (2 to 4 nm). At low temperatures, transfer of electrons from the metal substrate to the gas-oxide interfaces occurs by quantum mechanical tunnelling via the oxide scale [22]. This mechanism is limited after a time period where the thickness of the oxide layer increases. There are other proposed rate-determining steps such as chemisorption or formation of cavities within the oxide layer or ion/electron transport due to an electric field [22].

$$\Delta m = K_{log}(t + t_0) + A \quad (3.4)$$

Where $\Delta m$ is the mass gain, $t$ is the exposure time, $K_{log}$ is the parabolic rate constant, A is the integration constant.

With the *Parabolic rate law*, the reaction rate is inversely proportional to the square root of time. This behaviour is observed when the formed oxide layer is dense, which is also known as a protective layer.

$$\frac{dx}{dt} = \frac{k_p}{x} \rightarrow x^2 = 2k_p' t + C \quad (3.5)$$

Where kp is the parabolic rate constant, t is the time and, C is an integration constant.

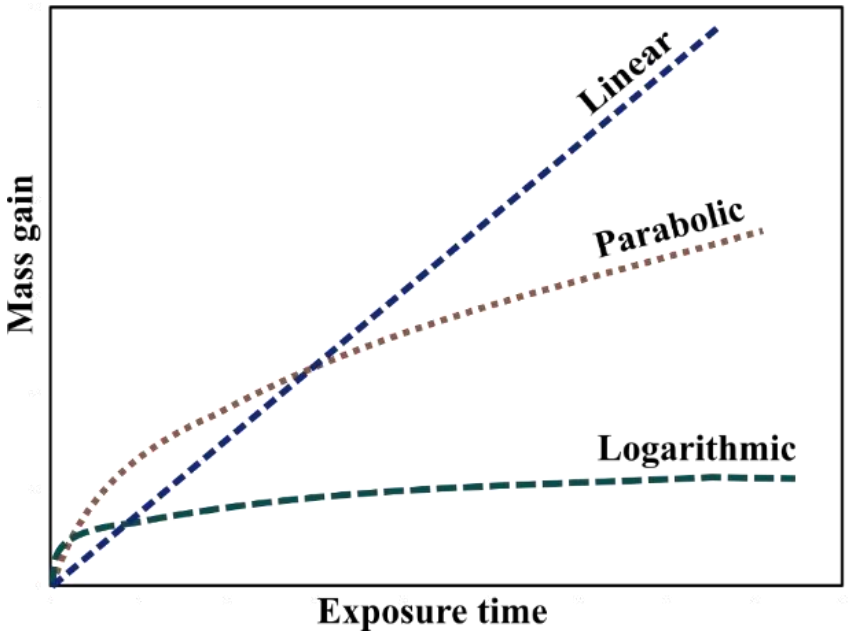


**Figure 3.14:** Oxidation growth mechanism based on the evolution of the mass-gain measurements.

Carl Wagner introduced a theory based on parabolic oxidation based on the following assumptions: dense, continuous and well-adhered oxide layer is formed; thermodynamic equilibria exist at the metal/oxide and gas/oxide interfaces and within the oxide layer; solubility of oxygen in the metal is insignificant. The oxidation rate in parabolic regime occurs by solid-state diffusion within the oxide layer, and the reaction rate decreases with time due to the continually growing oxide layer, which prolongs the diffusion path for the reacting species. The difference in the oxygen partial pressure between the oxide surface and oxide-metal interface develops a gradient in the chemical potential. The developed gradient acts as the driving force for the charged species across the oxide layer. Wagner's oxidation model was found to be accurate in elucidating the oxide layer growth kinetics of various metals and alloys [22].

Uncoated and coated stainless steel substrate (inkjet coated) samples were subjected to continuous and discontinuous oxidation to evaluate and compare the performance of protective

layers in this study. In continuous oxidation, samples were left in the furnace for 1000 hours under the reference test conditions undisturbed, whereas in discontinuous experiments, samples were taken out at defined intervals of time and their change in mass was recorded. The post-mortem analysis of the tested samples was characterised by XRD and microscopy analysis.

### 3.4.2. ASR/Cr retention

Area Specific Resistance for the uncoated and coated stainless steel substrates was measured using a modified version of a 4-wire probe test set-up. Fig.3.15 shows the illustration of the test set-up carried out at EPFL as part of the SCORED 2:0 project [182]. The samples were stacked in a sandwich assembly adjacent to thick palladium foils (0.5mm) screen printed with the SOFC cathode material, $La_{1-x}Sr_xCoO_3$, with the thickness 20 ± 2µm. In the experiment, SOFC operating conditions were replicated by maintaining compressive stress of 0.4 MPa on the samples and supplying a current of 0.4 $A.cm^{-2}$ throughout. Palladium was selected as the contact material due to its matching CTE (13.9 µm $m^{-1}$ $K^{-1}$, 0 to 1000 °C) with other SOFC materials, low electrical resistivity ($32.2\times10^{-8}$ Ω m at 727 °C), chemical stability at high temperatures and low chromium content [183].

The ASR was then calculated, as a function of time, from the measured voltage drop between the samples and palladium foils. ASR measurements were carried out at 700 °C in 1L/min air with 3% humidity. The ASR values were derived from the relation, Equation, 3.6.

$$ASR = \frac{VA}{I} \tag{3.6}$$

Where V is measured voltage, I is the applied current, and A is the area of the sample (steel substrate). The tested samples were later investigated using microscopy analysis.

The set-up replicating planar SOFC testing condition also enabled the observation of the chromium retention of the applied coating layers. The diffusion of chromium from the stainless steel substrate through the coating and the reaction with the cathode layers was investigated using a cross-section of the samples in microscopy analysis.

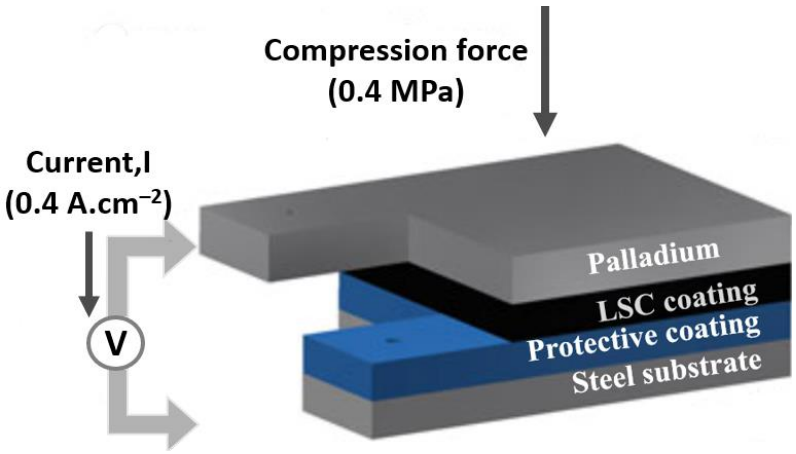


**Figure 3.15:**Schematic of ASR measurement test set-up; the coated stainless steel substrate was placed in contact with the palladium-coated with LSC coating, reproduced from [183].

## 3.5. Characterisation of the stainless steels and inkjet printed substrates

### 3.5.1. X-ray diffraction

X-ray diffraction (XRD) was used to identify any phase changes on the coated and uncoated stainless steel samples, prior and post the high-temperature tests in this study. X-rays are part of the electromagnetic spectrum with short wavelengths ($10^{-8}$ to $10^{-12}$ m) interact with the atoms and gets diffracted in all directions. William Henry Bragg proposed a general relationship for the occurrence of constructive interference patterns to occur when X-rays interact with the sample. Bragg's law defines the geometric conditions for the diffraction to occur, given by Equation (3.7)

$$n\lambda = 2dsin(\theta) \quad (3.7)$$

Where n- is an integer, λ is the characteristic wavelength of x-rays interacting with the sample, d is the interplanar distance between the atoms, and θ is the incident angle. An individual crystalline phase is represented by its respective peak positions and diffraction patterns. The measured peak position and diffraction patterns are compared with the reference database to analyse any changes on stainless steel samples post high-temperature tests.

In this study, the uncoated and coated samples were characterised using a diffractometer (Bruker D2 Phaser) with Co Kα radiation=1.79 Å source, an applied voltage of 30 kV and 10 mA current flow. The samples were analysed at a scanned 2θ range of 15 to 85° using the detector LYNXEYE_XE_T.

## 3.5.2. Microstructural analysis

Scanning Electron Microscopy (SEM) was used to observe the microstructure of the inkjet-printed layers post-deposition and high-temperature tests. SEM images were obtained using a Hitachi TM3030 Plus with an electron beam of 15kV. The electron beam interacts with the electron shells in the atoms on the sample surface and results in different emissions such as secondary electrons (SE), auger electrons, back-scattered electrons (BSE) and X-ray emissions. The excited emissions are transformed into a signal to produce the microstructural image of the samples. For the thesis work, sample images were recorded on SE and BSE mode to investigate the topography and compositions of the samples, respectively. A Quantax 70 was used to perform electron dispersive spectrum (EDS) analysis based on the x-ray emissions to characterise and quantify the elements in the samples. The analysis was performed on the surface and cross-section of the samples. For cross-section analysis, post-test samples were

embedded in epoxy resin and polished using silica carbide sandpapers of different grit sizes, as shown in Fig. 3.16.

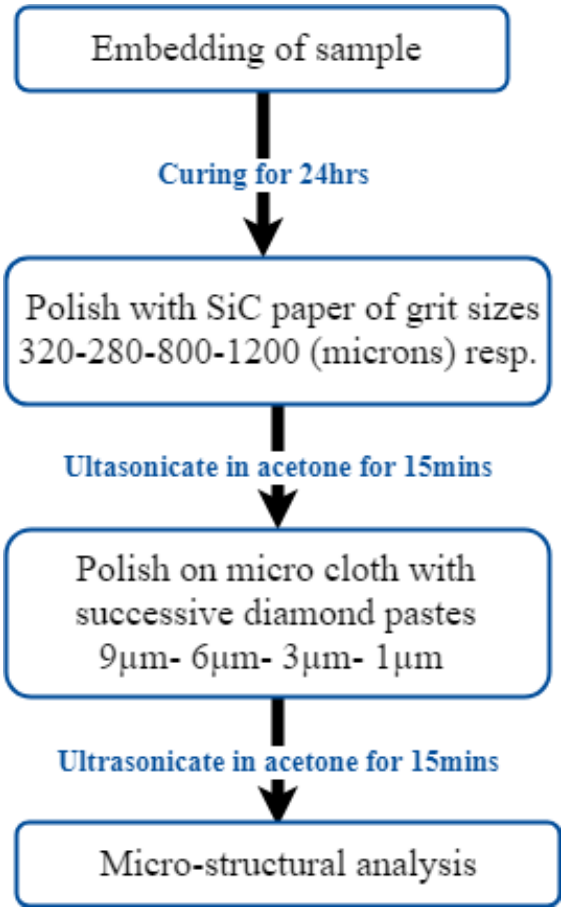


**Figure 3.16:** Polishing procedure for SEM cross-section analysis.

### 3.5.2.1. Microstructural analysis of inkjet coatings

The microstructure of the inkjet-printed coatings was assessed using image processing tool; Image J. Image J analysis has been in used in the different research field for the microstructural analysis to measure the particle size, pore size and porosity area [184]. The porosity and the average pore size were estimated on the surface SEM micrographs as shown in Fig.3.17. The steps adopted for the estimation of pore volume and pore size on SEM micrographs of ink-jet coatings are described below:

1. SEM micrographs were converted into 8-bit binary images.

2. The surface SEM micrographs were classified into different regions using image segmentation. Image segmentation classifies a digital image into distinct categories or regions by grouping pixels of similar characteristic with similar greyscale value. In the context of the present study, image segmentation was used to measure the voids (pores) in inkjet-printed surface SEM micrographs. Image segmentation was done by K-means algorithm using Python coding (given in Appendix I) to highlight the voids and distinguish them with the particles.

3. The images obtained after clustering were then thresholded using Otsu's thresholding algorithm in Image J analysis. Otsu thresholding has been previously utilised to analyse the microstructure of inkjet-printed layers [185] and in SOFC microstructural analysis. Thresholding transformed the images into a binary data set enabling to perform 2D measurements such as measuring particle size, area fraction, particle length, diameter and other binary measurements. The thresholded image was then used to measure the highlighted objects (voids), the analysis excluded objects from the edges and the noise in the image were removed by applying a built-in tool (despeckle) in Image J. Another built-in tool, Watershed, was used to break bigger objects into single binary data. Fig. 3.16 represents the illustration of each step used in estimating the porosity of inkjet-printed coatings.

**1. SEM 8 binary image**

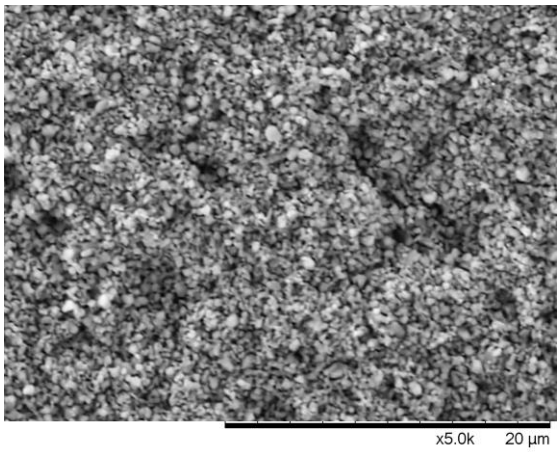


Conversion of SEM micrograph to 8-bit image.

**2. K- means clustering**

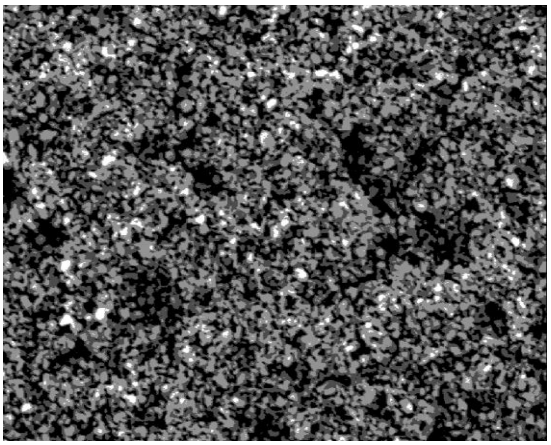

Clustering of the image to highlight particles and voids

**3. Otsu's thresholding**

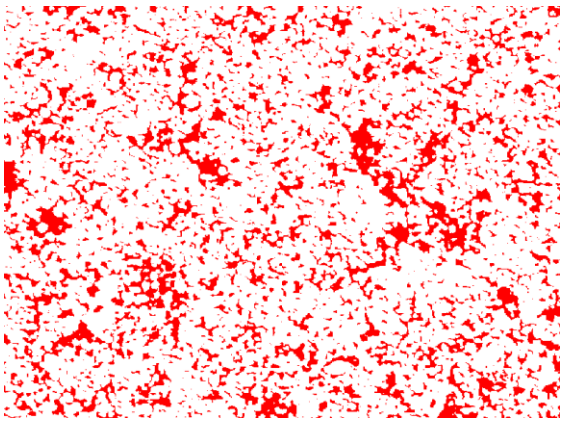

Otsu thresholding to select the voids for the measurements using Image J

**4. Watershed-Analyse**

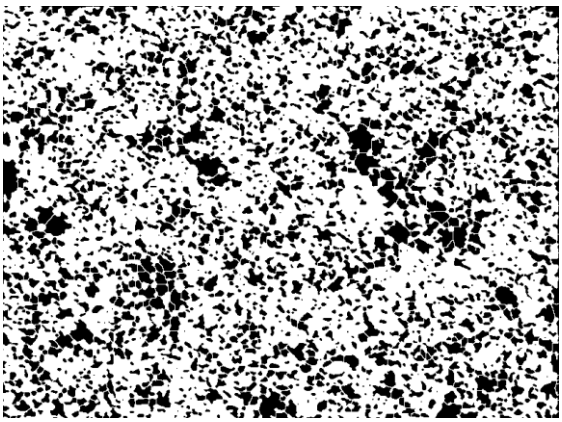

Watershed process – to separate large objects.

**Figure 3.17:** Illustration of porosity volume estimation in surface SEM micrographs of inkjet coated layers by K-means clustering and using Image J analysis tool.

# *Chapter 4: Formulation and Printability of Aqueous based Spinel Inkjet Inks*

The inkjet deposition process requires identification of the right inkjet printer for the selected particle size and the compatibility of ink. The requirement and selection of the nature of the ink nature are solely dependent on the mode of the inkjet printer to be used. In this chapter, the formulation of spinel particulate inks for the electromagnetic printer based on the pH, particle size, viscosity, and surface tension is discussed. The optimal concentration of each component was determined based on the one-factor-at- a time method.

# 4.1. Introduction

Fig. 4.1 shows the step by step procedure of the optimisation process for the different ink components. Initially, the pH range for the ink formulation was determined using zeta analysis, as a pH greater than 9 are prone to corrode the inkjet nozzles. In order to avoid agglomeration of particles in the ink suspension, iso-electric point of the spinel powder suspensions were determined using Zeta analysis, and the pH value was maintained in a defined range during the optimisation of each ink component. The optimal dispersant dosage to maintain ink stability and to understand the effect of milling time for different dispersant dosage was analysed using particle size distribution data. The effective dispersant dosage was further investigated using a sedimentation test. With the optimal pH, milling time and dispersant dosage, the effect of different binder concentration was determined using flow curve analysis. Also, to understand the interaction between the dispersant and binder molecules, binder concentration was varied at low and high dispersant dosages. The effective binder content was determined based on the target viscosity values. The solid content was then varied, and the optimal content was determined based on viscosity values. Based on the optimal dispersant, binder, and solid content, final inks were formulated, and their physical properties were found to assess the printability of the inks using dimensionless numbers. The rheological behaviour of the formulated spinel inks during the inkjet printing process was studied using a piezo-axial vibrator rheometer.

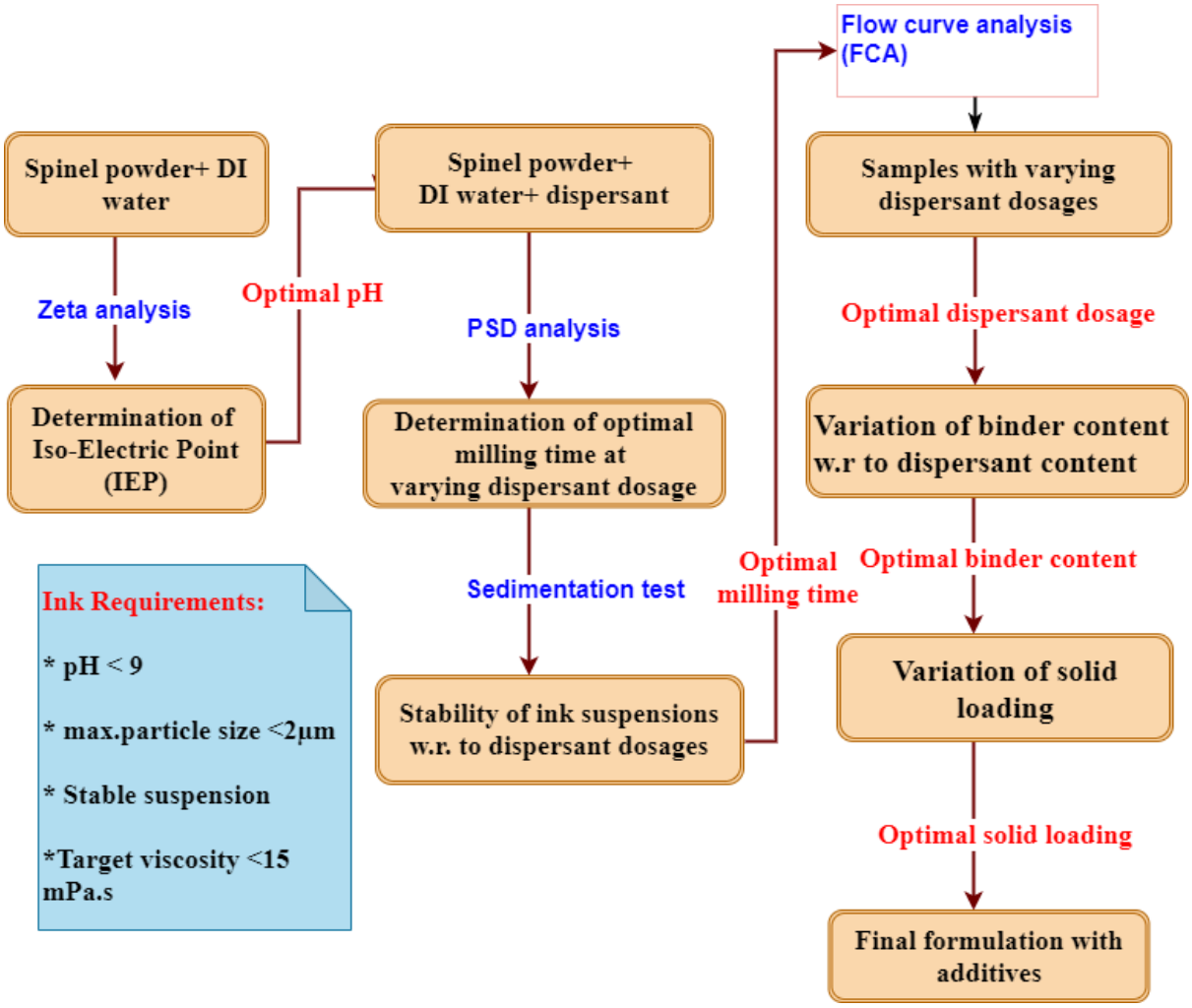


**Figure 4.1:** Optimisation of ink components based on the requirements of ink properties. The optimal values for each ink component were determined based on the inkjet printer requirements.

## 4.2. Optimisation of ink components

### 4.2.1. Iso-Electric point of spinel powders

The isoelectric point (IEP) of the spinel powders in aqueous suspension is the point at which the surface charge of the particle is neutral. At IEP, suspended particles tend to attain the thermodynamic equilibrium state resulting in an onset of flocculation and leading to sedimentation with time [186]. Also, it is crucial to determine IEP and define pH range, corresponding to the inkjet printer requirement, as pH greater than 9 are prone to corrode the

inkjet nozzles. The IEP value for MCO and MCF powders suspended in distilled water was found to be in the pH range 2.5 to 3.0, as shown in Fig. 4.2.

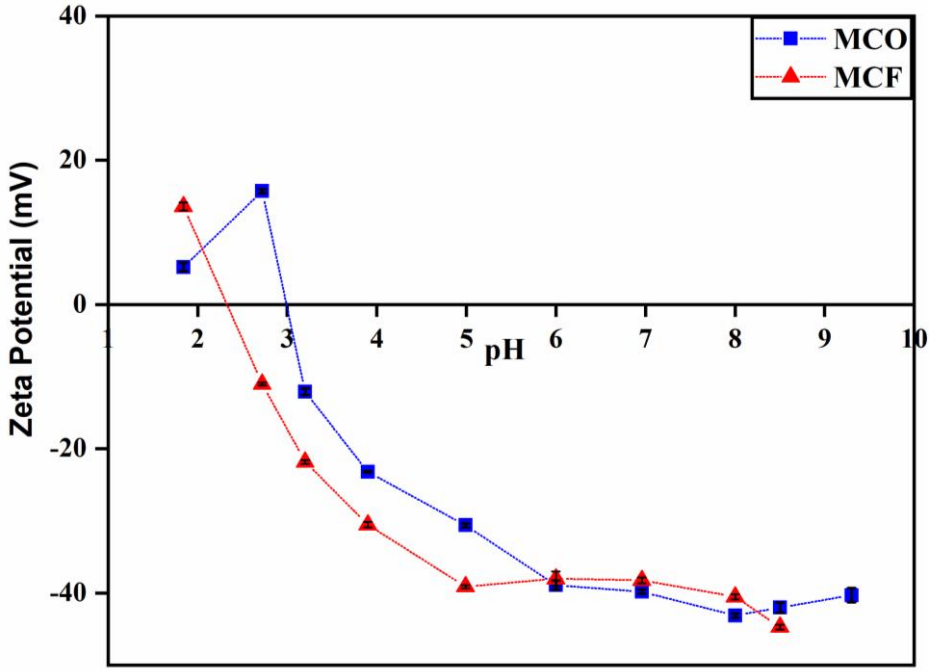


**Figure 4.2:** IEP curves for MCO and MCF inks. The iso-electric point of both the spinel inks was in the pH range 2.5-3.0.The connecting lines do not represent any model fitting data.

Metal oxides dispersed in an aqueous medium, due to their amphoteric nature, dissociate as weak bases or acids resulting in the formation of $H^+$ and $OH^-$ ions as shown in Equations (4.1 and 4.2). MCO and MCF powders exhibit positive Zeta values in acidic conditions below the IEP and negative Zeta values above the IEP, due to the protonation and deprotonation of the hydroxy group in acidic and basic conditions, respectively. The observed amphoteric nature of the spinel powders is a common characteristic of metal oxides as reported in the literature [159,187,188].

$$MeOH + H^+ \leftrightarrow MeOH_2^+ \text{ (in acidic conditions)} \quad (4.1)$$

$$2MeOH^- \leftrightarrow 2MeO^- + H_2O \text{ (in basic conditions)} \quad (4.2)$$

Me represents the metal component.

The ion concentration, which acts as a function of pH in the suspension, directly influences the surface charge of the dispersed particles, the Zeta potential [169], signifying the pH as a critical factor in dispersion stability of the suspension. Thus, the pH for the inks formulated was maintained within the pH range 8.0 to 8.5, to ensure that the pH operating range was away from the IEP and also to enhance the dissociation of the selected anionic dispersant.

### 4.2.2. Determination of optimal dispersant concentration

The dissociation of the polyelectrolyte dispersant, Darvan C-N is shown in Equation 4.1; the fraction of dissociation for the dispersant increases with the pH [189,190]. Thus, as the pH increases, the number of anions in the polyelectrolyte dispersant increases. The natural pH of the suspended powder particles in distilled water was around 6.2 to 6.5 and increased with the addition of the dispersant, 8 to 8.5, due to the adsorption of negatively charged polyelectrolyte molecules onto the suspended particles.

$$[C_3\,H_4COONH_4]\,n + H_2O \rightarrow [C_3\,H_4COO^-]\,n + [NH^+{}_4]n \qquad (4.3)$$

The dissociated polyelectrolyte extends into the DI water and the $COO^-$ functional groups, interact with the surface of the particles, thereby creating an electrostatic force of repulsion between the particles. Darvan C-N is known to dissociate in aqueous media before being absorbed into the surface of the dispersed particles. The polymer chain in the dispersant molecules forms a compact coil and transforms a stretched conformation in acidic and basic conditions, respectively [191]. The dispersion in slurries or suspensions is achieved based on electro-steric stabilisation to obtain a dispersed system with minimal viscosity [192,193]. The optimal dispersant dosage for the ink formulation is determined based on the effect of milling time and viscosity values, as discussed in the following sections.

## 4.2.3. Effect of milling time vs dispersant concentration

The optimal dispersant concentration and milling time for the ink formulation were determined by studying the effect of different milling time on Particle Size Distribution (PSD) at varying amounts of dispersant dosage. Dispersant dosage of 0.25 ml for 5 gram of powder is represented as 5 wt.%. The optimal milling time was determined based on the evolution of $d_{50}$ (mean particle size) and $d_{90}$ (maximum particle size) values from the PSD data. The analysis was done on day 0, and after ageing for a week (day 7), samples were not agitated or stirred during this time.

Fig. 4.3 shows the $d_{50}$ and $d_{90}$ values obtained from PSD analysis of MCO suspensions measured each after 24, 48 and, 72 hrs milling time at varying dispersant dosage. After 24hrs of milling time, the $d_{50}$ value was comparable to the manufacturer value (0.5434 µm). Fig. 4.4 shows the $d_{50}$ and $d_{90}$ values of MCF suspensions measured after each 24, 48 and, 72 hrs milling time at varying dispersant dosage. After 24hrs of milling time, the $d_{50}$ value at dispersant dosages above 10 wt.% was less than 0.45 µm, less than the manufacturer value (0.5521 µm). There was no significant trend observed after 48hrs and 72hrs milling, where $d_{50}$ and $d_{90}$ were less the 0.4 and 1.0 microns, respectively. For both ink suspensions (MCO and MCF), the maximum decrease in particle size, $d_{50}$ and $d_{90}$, was seen after 72 hrs at the dispersant dosage above 20 wt.%. The best reduction in PSD was achieved with a maximum milling time of 72 hrs. However, the effect of varying dispersant dosage after storage (day 7), an increase in PSD was seen in both the inks for the samples milled 48 and 72 hrs whereas 24 hrs milled samples remained consistent. The observed increase in PSD can be attributed to the increase in surface area of particles after 48 and 72 hrs milling at day 0, demanding more dispersant concentration to prevent them from flocculating. Thus, the effect of dispersant dosage was evaluated for 24 hrs milled based on the evolution of $d_{90}$ on each sample after 7 days of ageing.

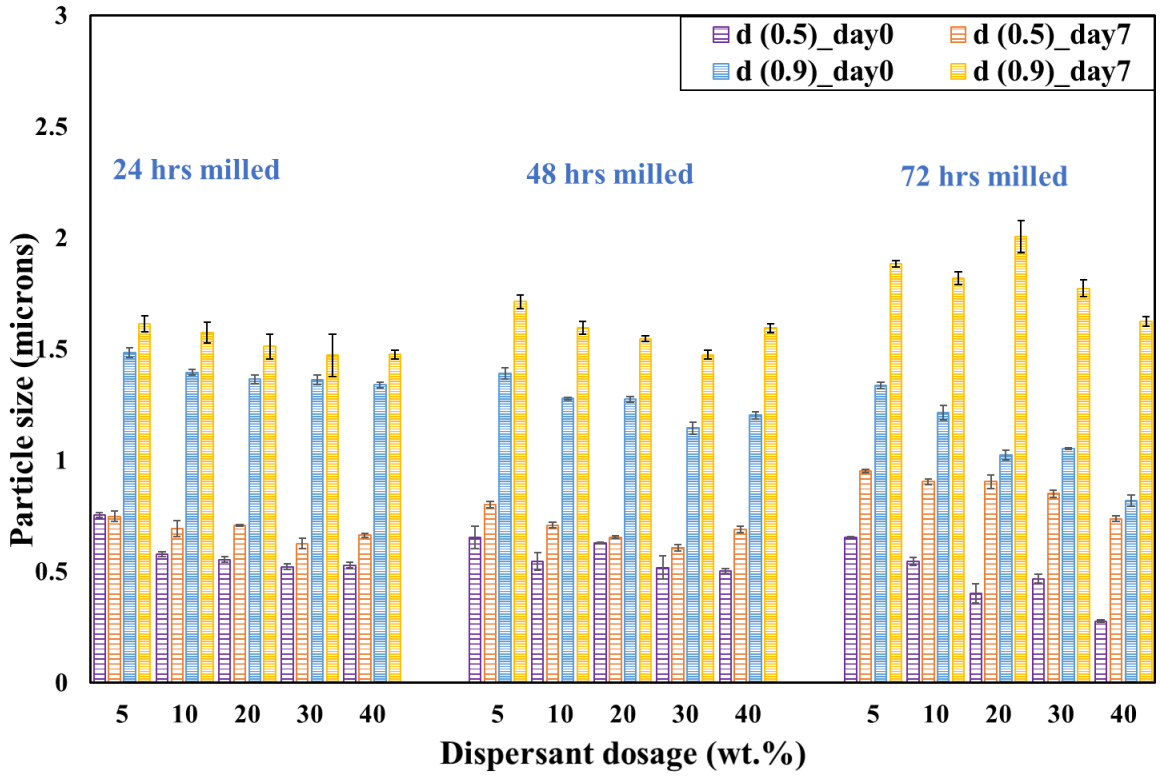


**Figure 4.3**: Evolution of $d_{50}$ and $d_{90}$ values of MCO ink suspension milled for 24,48 and 72 hrs, at different dispersant dosages.

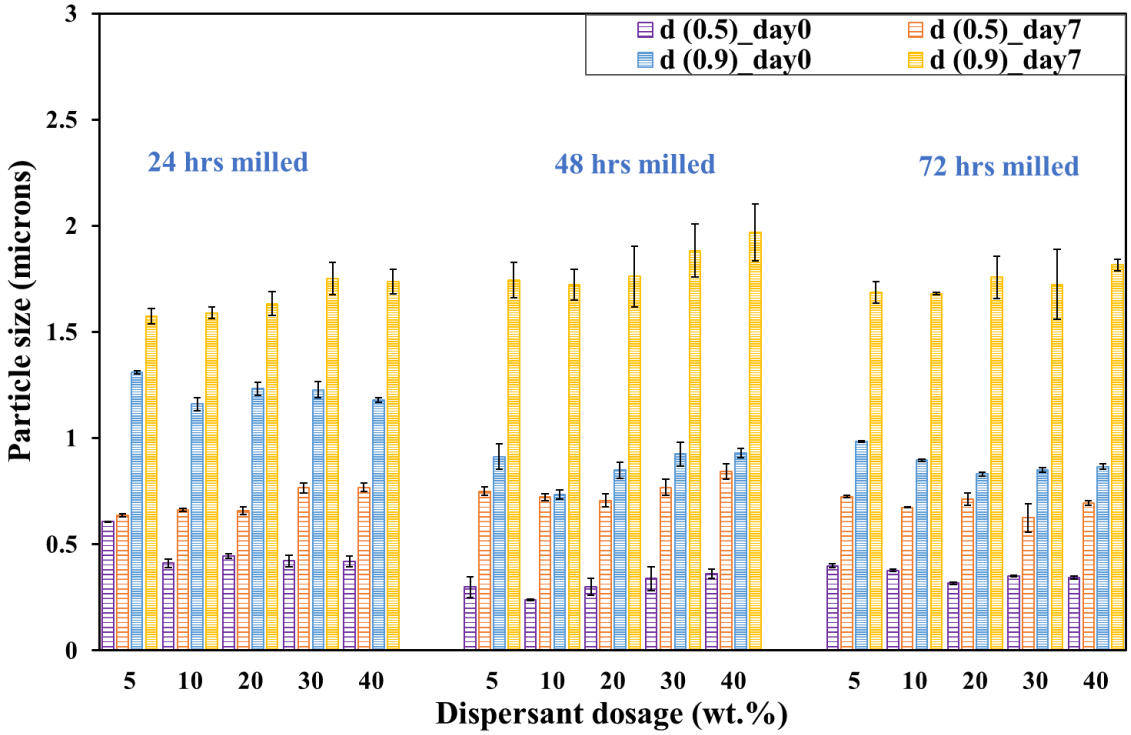


**Figure 4.4:** Evolution of $d_{50}$ and $d_{90}$ values of MCF ink suspension milled for 24,48 and 72 hrs, at different dispersant dosages.

Fig. 4.5 shows the ink suspensions left for sedimentation test on day 0 and day 7. At low dispersant dosages (10 and 20 wt.%) apparent settling of particles can be seen for both the inks, where MCF suspensions showed quicker settling than the MCO suspensions. In the case of MCO ink suspensions, supernatant showed the presence of particles at the dispersant dosage 30 and 40 wt.% after ageing whereas in MCF ink suspensions it was observed at 40.wt% dispersant dosage.

MCO and MCF ink suspensions milled for 24 hrs displayed the maximum particle size within the requirements of the inkjet printer (less than 2 µm). Based on the PSD, and sedimentation test, 40 wt% dispersant dosage to the solid content for the further formulation was selected.

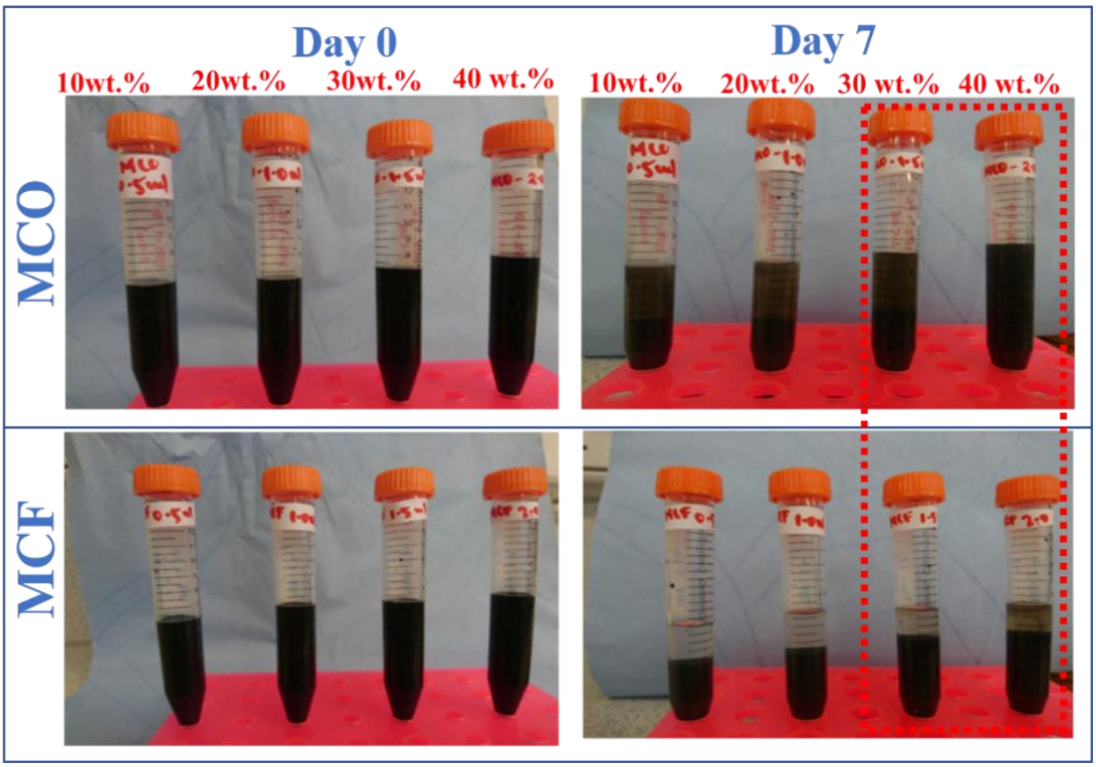


**Figure 4.5:** Sedimentation test- MCO and MCF ink suspensions milled for 24 hours at varying dispersant dosages. 30 and 40wt.% suspensions displayed better stability in relative to other dosages, and turbid supernatant shows the dispersed particles in the suspension.

## 4.2.4. Optimal dispersant dosage based on flow curve analysis

The dynamic viscosity of the ink suspensions milled for 24 hours at different dispersant dosage is shown in Fig. 4.6 and Fig. 4.7. The viscosity of the ink suspensions decreased with the applied shear rate, as expected, due to the presence of polymer molecules and flocculation. The observed shear-thinning behaviour is a typical characteristic of the suspension-based systems. Similar behaviour has been reported in ceramic and metal-oxide suspension systems [160,194–196]. MCO and MCF inks showed a decrease in viscosity with respect to the increase in dispersant dosage as a general trend. The observed lower viscosity reflects the lower resistance to flow, indicating less flocculation as the dispersant dosage was increased from 5 to 40 wt.%. In both cases, viscosity values were less than 5 mPa.s at the shear rate 1000 $s^{-1}$, and the rate of increase was of small magnitude.

The degree of flocculation at different dispersant dosages was determined by fitting the measured flow curves with the Herschel-Bulkley equation to obtain the apparent yield stress. The presence of flocs or network structure in the suspension requires higher yield stress relative to the less flocculated suspension. A similar approach was adopted to estimate the effect of polyelectrolyte on the flocculation [197,198]. The best rheological fit was obtained by the Herschel-Bulkley model equation with an $R^2$ value above 0.99 for each sample. Table 4.1 shows the obtained yield stress values for MCO and MCF inks at different dispersant dosages. The low yield stress values for MCO and MCF inks were above 30 wt.% highlighting the less flocculation in the ink suspensions, which agrees well with the viscosity values and the sedimentation stability results.

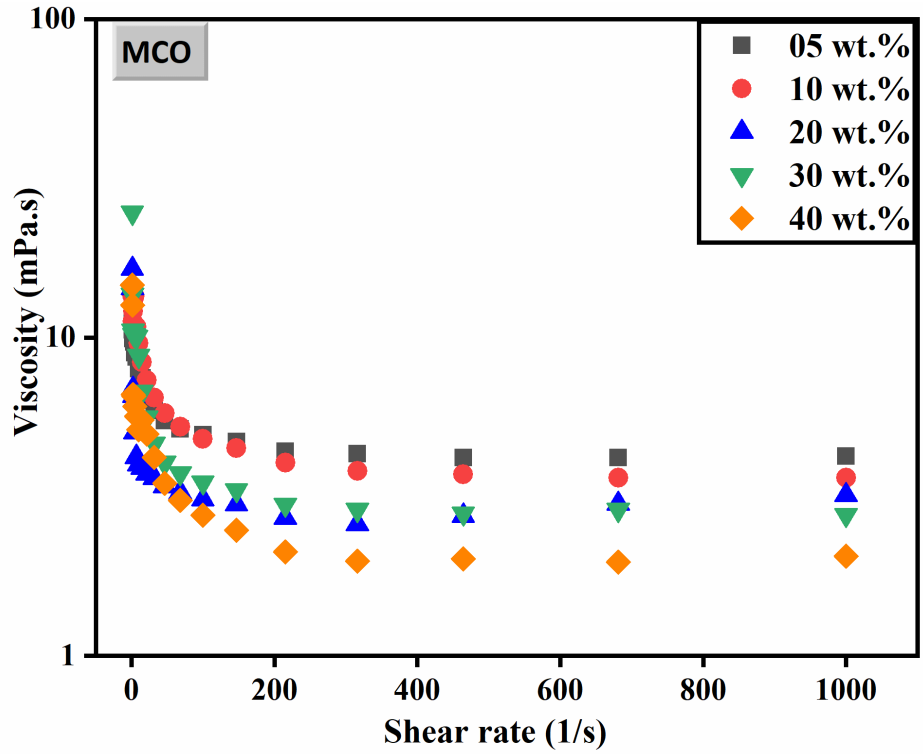


**Figure 4.6:** Flow curve of MCO ink suspensions with varying dispersant dosages at the shear rate (1-1000 $s^{-1}$).

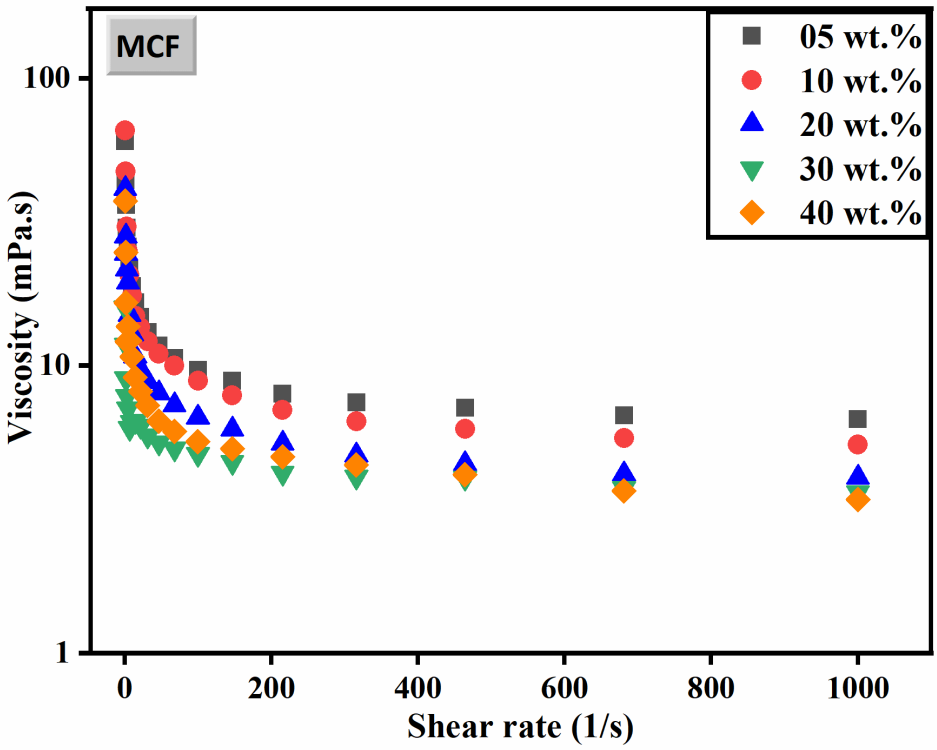


**Figure 4.7:** Flow curve of MCF ink suspensions with varying dispersant dosages at the shear rate (1-1000 $s^{-1}$).

**Table 4.1:** Yield stress values of MCO and MCF ink suspensions at different dispersant dosages obtained by fitting the measured data with the Herschel-Bulkley model.

| Ink | Dispersant dosage (wt.%) | Yield stress | Rate index | $R^2$ |
|---|---|---|---|---|
| MCO | 5 | 0.050 | 1.100 | 0.99 |
| | 10 | 0.055 | 0.960 | 0.99 |
| | 20 | 0.038 | 1.160 | 0.99 |
| | 30 | 0.037 | 0.980 | 0.99 |
| | 40 | 0.052 | 0.970 | 0.99 |
| MCF | 5 | 0.085 | 0.894 | 0.99 |
| | 10 | 0.073 | 0.840 | 0.99 |
| | 20 | 0.053 | 0.854 | 0.99 |
| | 30 | 0.007 | 0.888 | 0.99 |
| | 40 | 0.013 | 0.805 | 0.99 |

## 4.2.5. Optimisation of the binder content

The addition of binder acts as a viscosity modifier and primarily affects the rheology of the suspension. It is crucial to determine the optimal binder concentration that maintains the viscosity within the desired value for the inkjet deposition process. Having set the optimal pH, dispersant dosage and milling time, varying binder concentrations were analysed based on the flow curve analysis with a target viscosity value of less than 15 mPa.s. To understand the interaction of the binder and the dispersant, low dispersant dosage (LD=5wt.% dispersant) and high dispersant dosage (HD=40wt.%) were taken, and the concentration of the PVA solution was varied. The PVA concentration was limited to 15wt.% as higher loading yielded a viscosity beyond the target viscosity (15 mPa.s).

Fig. 4.8 and Fig. 4.9 shows the flow curve analysis of varying binder concentrations for the different dispersant dosages for MCO and MCF ink suspensions, respectively. Table 4.2 shows

the viscosity measured at lower and higher shear rates for varying binder concentrations at the respective lower and higher dispersant dosages. It can be seen that the viscosity increased when binder content was varied at lower dispersant dosage whereas, in the case, of high dispersant dosage, the variation of viscosity with respect to binder content was minimal for both the inks. 10 wt.% binder with 40 wt.% dispersant yielded a lower viscosity value for both the inks as shown in the Table 4.2.

The increase in viscosity with respect to the increase in binder content is due to the presence of Darvan C-N molecules. Darvan C-N, a polymer of high molecular weight, extends into the suspending medium with tail-loop configuration and causes entanglement with the binder molecules and exhibits shear-thinning behaviour [172], as observed in the case of ink suspension. Khan et al. showed that the addition of PVA in the presence of dispersant, Darvan C, significantly affects the rheology of aqueous-based alumina suspensions [199]. However, a less pronounced effect on viscosity at higher dispersant concentration can be due to the weakened lubricant characteristics of Darvan C-N. The excess of Darvan C-N molecules at higher dispersant dosage easily breaks down into smaller chains during the milling a stage and acts as lubricant between the polymeric chains of binder molecule thereby reducing the flow resistance [195]. Nampi et al. [165] showed that the effect of PVA binder is less pronounced with the addition of the stearic acid which acts as an internal lubricant in alumina-based suspensions prepareed for spray coating application. The interaction between the binder and the suspended particles is considered to be lower at the optimal pH, and dispersant concentration [200].

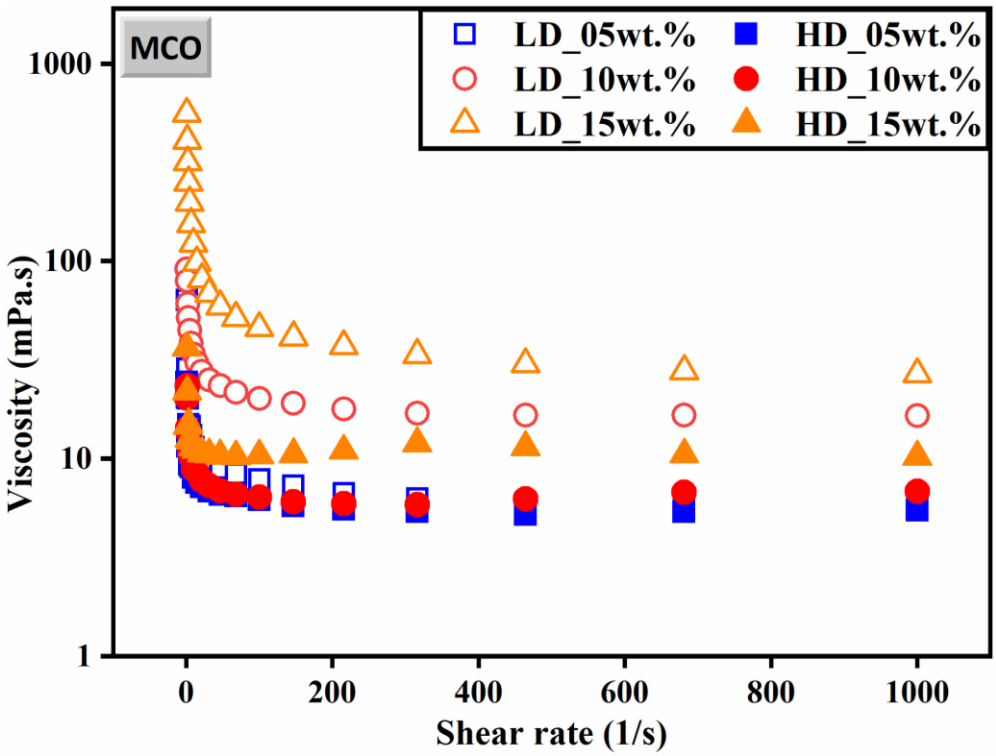


**Figure 4.8:** Flow curve of MCO ink suspensions in the shear range (1 to 1000 $s^{-1}$) with varying binder concentration at low and high dispersant dosage.

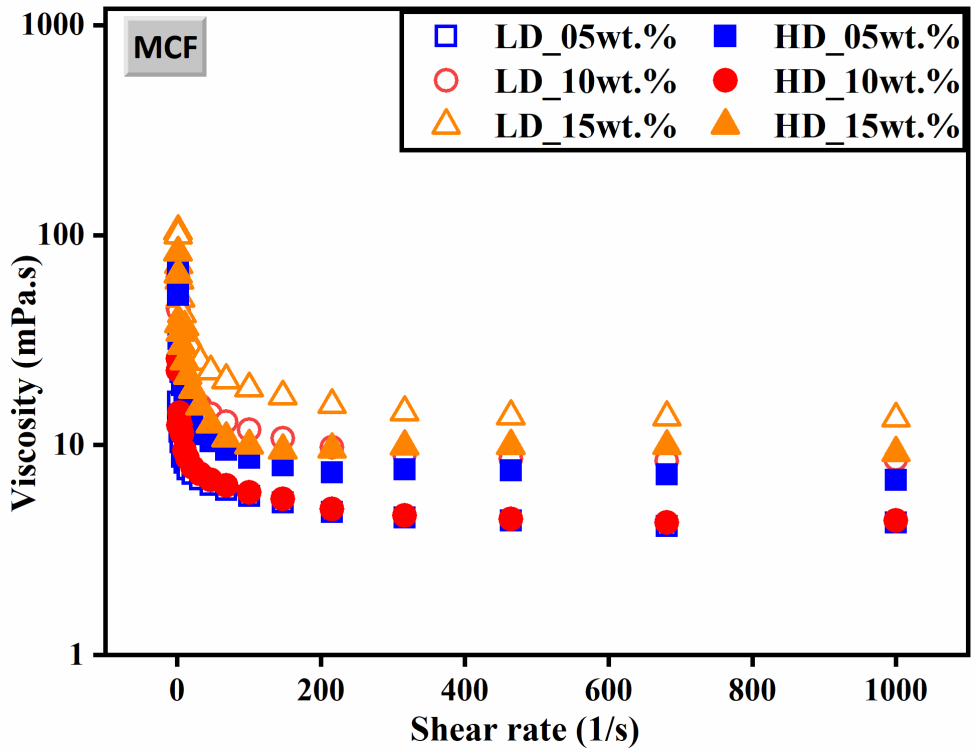


**Figure 4.9:** Flow curve of MCF inks in the shear range (1 to 1000 $s^{-1}$) with varying binder concentration at low and high dispersant dosage.

**Table 4.2:** The viscosity of the inks at low and high dispersant dosage with varying binder concentration.

| Ink | Shear rate (1/s) | Viscosity (mPa.s) | | | | | |
|---|---|---|---|---|---|---|---|
| | | Low dispersant dosage (5 wt.%) | | | High dispersant dosage (40 wt.%) | | |
| | | 5wt.% B | 10wt.%B | 15wt.%B | 5wt.%B | 10wt.%B | 15wt.%B |
| MCO | 1.00 | 63.94 | 91.44 | 560.29 | 24.42 | 20.26 | 36.43 |
| | 1000 | 6.09 | 16.56 | 26.81 | 5.48 | 6.86 | 10.26 |
| MCF | 1.00 | 16.12 | 62.87 | 104.45 | 25.88 | 69.57 | 82.65 |
| | 1000 | 4.26 | 8.54 | 13.39 | 4.37 | 6.83 | 9.21 |

## 4.2.6. Optimal solid loading

Fig. 4.10 (a-b), shows the effect of varying solid content on the viscosity of the ink suspensions. The optimal solid loading was investigated with reference to the target viscosity to attain maximum possible dense layers post inkjet deposition process. The viscosity of both the MCO inks remained less than 10 mPa.s at 30 and 35wt.% whereas, in the case of the MCF ink, the viscosity value was higher than the target viscosity at 35wt.%. The increase in solid content led to the increased volume fraction of the particles in the suspension. As a consequence, the particle-particle interaction became dominant and higher resistance to flow was observed in the form of an increase in the viscosity.

Table 4.3 shows the viscosity of MCO and MCF ink suspensions of different solid content at lower and higher measured shear rates. MCF ink displayed a viscosity greater than 15mPa.s at 35 wt.% whereas MCO ink showed comparatively lesser viscosity. At 30 wt.% solid loading, both the inks had a viscosity within the target value, and this was chosen as the optimal value for the final ink compositions.

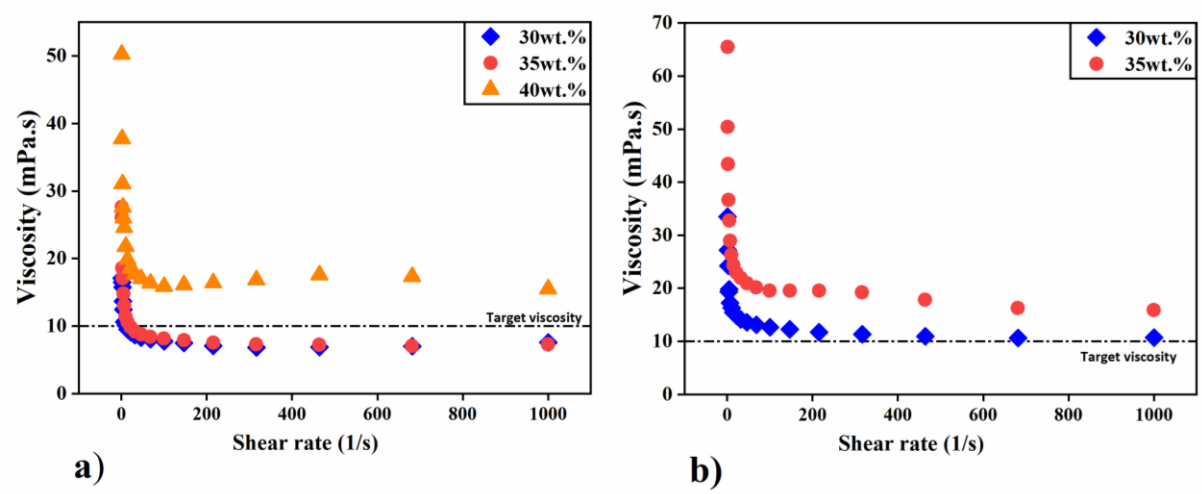


**Figure 4.10:** Flow curve of spinel inkjet inks (a) MCO and (b) MCF at varying solid content with optimal pH, dispersant dosage and binder concentration.

**Table 4.3:** The viscosity of spinel inkjet inks at varying solid loading.

| Ink | Shear rate (1/s) | Solid loading | | |
|---|---|---|---|---|
| | | 30 wt% | 35 wt.% | 40 wt.% |
| MCO | 1.00 | 17.09 | 27.60 | 50.27 |
| | 1000 | 7.58 | 7.26 | 15.51 |
| MCF | 1.00 | 33.50 | 65.50 | - |
| | 1000 | 10.75 | 15.89 | - |

## 4.3. Characterisation of the final inks

The final composition of the MCO and MCF inks with optimal milling time of 24 hrs, dispersant, binder, solid content, and other additives based on the adapted ink formulation route is shown in Table 4.4. The physical properties and jet-ability of the inks were assessed prior to the inkjet deposition process. Wettability of the inks with the stainless steel substrate was analysed using contact angle measurements, and the thermo-gravimetric analysis was done before the heat-treatment step of the inkjet-printed samples.

**Table 4.4:** Final composition of the spinel inks with the optimal amount of dispersant, binder, solid loading and other additives.

| Component | Amount (wt.%) |
|---|---|
| **DI** | 35.53 |
| **Powder** | 25.38 |
| **Dispersant** | 10.15 |
| **Binder (solution)** | 18.27 |
| **PEG +Glycerol** | 10.15 |
| **Surfactant** | 0.25 |
| **Antifoam** | 0.25 |

## 4.3.1. PSD analysis

The inks displayed monomodal distribution without any agglomeration or secondary peak, as shown in Fig 4.11. The measured $d_{90}$ values for MCO and MCF inks were 1.29 ±0.017 and 1.05 ±0.003 µm, respectively. The maximum particle size observed was less than 2% of the nozzle size of the inkjet printer, this PSD was well within the range of inkjet printer requirements used for the deposition process in the present study. The stability of the inks was assessed based on the PSD data measured on day 0 and after 7 days (day 7). Table 4.5 shows the PSD data of the spinel inks on day0 and day 7. The increase in $d_{50}$ and $d_{90}$ on day 7 signifies the onset of flocs, yet the maximum particle size did not exceed 2 microns. Thus, inks could be stored and used for the inkjet deposition process at a later date.

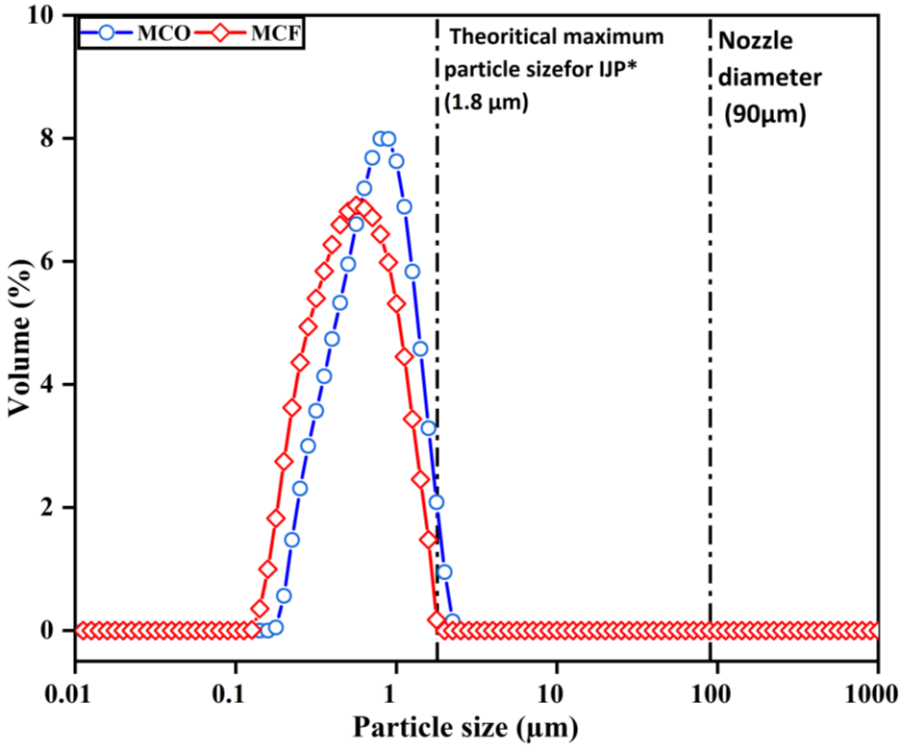


**Figure 4.11:** PSD of the final composition of the MCO and MCF ink composition.

**Table 4.5:** PSD of MCO and MCF final ink composition measured on day 0 and day 7.

| Ink | Day 0 | | | Day 7 | | |
|---|---|---|---|---|---|---|
| | **$d_{50}$ (µm)** | **$d_{90}$ (µm)** | **Span** | **$d_{50}$ (µm)** | **$d_{90}$ (µm)** | **Span** |
| MCO | 0.68 ±0.010 | 1.29 ± 0.017 | 1.44 ±0.001 | 0.87 ±0.005 | 1.50 ±0.012 | 1.24 ±0.002 |
| MCF | 0.50 ±0.002 | 1.05± 0.003 | 1.64±0.003 | 0.78 ±0.002 | 1.47 ± 0.006 | 1.46 ±0.004 |

## 4.3.2. Flow curve analysis

The flow curve analysis for both inks is shown in Fig 4.12. The inks exhibited shear-thinning behaviour, a characteristic behaviour for ceramic suspensions [192,200,201]. The change in viscosity with respect to the shear force in the formulated inks can be attributed to the structural alignment of polymers in the suspension and the particulate matter. Whereas, at the low shear rate, the observed high viscosity is the reflection of more resistance exerted by the smaller

particles which are in constant Brownian motion [172]. The MCO and MCF inks had a viscosities of 72.1 and 53.32 mPa.s at the shear rate, $0.01s^{-1}$, and 9.98 and 11.26 mPa.s at the shear rate, $1000s^{-1}$ respectively. The high viscosity at the low shear rate ($<1s^{-1}$) offers kinetic stability to the suspended particles against the gravitational force during storage and ensures better stability. Although, the measured viscosity was high at low shear rate ($0.1\ s^{-1}$), both the inks attained the viscosity value of ~15mPa.s at the medium shear rate ($10\ s^{-1}$) which was equal to shear force at the time of sample delivery. The viscosity was well within the requirements for the printing process.

The rheological parameters for the inks were determined by fitting the measured data of shear rate against viscosity with available rheological models, shown in Fig. 4.12. The best fit was shown by the Carreau-Yasuda model with an $R^2$ value of 0.98 and 0.99 for MCO and MCF inks, respectively, is shown in Table 4.6. The model used was a generalised form of Carreau's model describing the characteristics of the shear-thinning fluids. The Carreau-Yasuda model is represented by the equation 4.2,

$$\frac{\eta-\eta_\infty}{\eta_o-\eta_\infty} = [1 + (k\gamma)^a]^{\frac{n-1}{a}} \qquad (4.2)$$

Where $\eta_o$ is zero shear viscosity, $\eta_\infty$ is the infinite rate viscosity, $k$ is the consistency, $n$ is the power-law index representing the transition between the $\eta_o$ and power-law region. The power-law index is used to elucidate the flow behaviour of the fluids, $n$ less than unity signifies the shear-thinning characteristic of the inks.

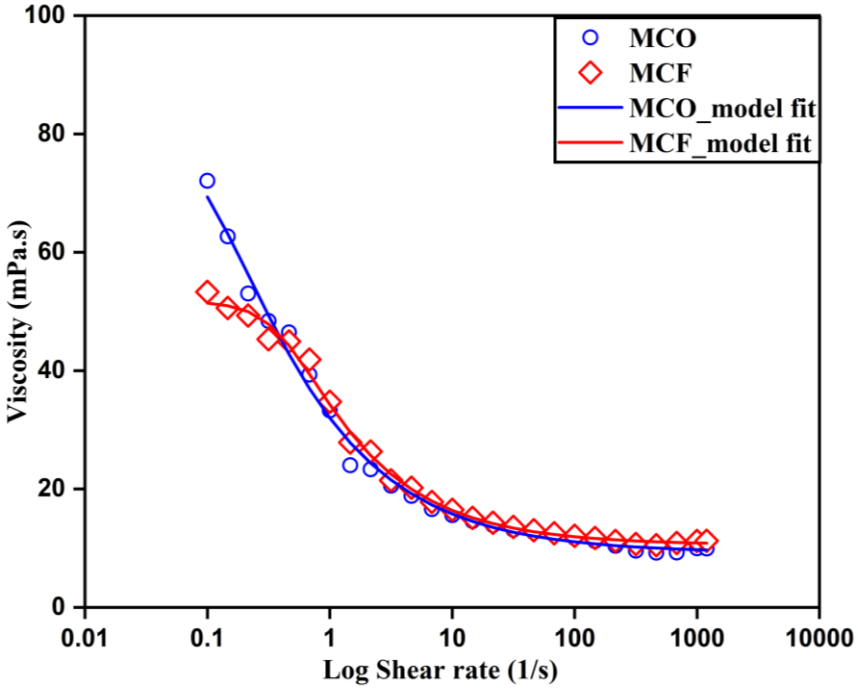


**Figure 4.12:** Flow curve of MCO and MCF inks with the final composition. The model fitting for both the inks is represented in a line plot, where $R^2$ values for MCO and MCF inks are 0.98 and 0.99.

**Table 4.6:** Parameters for MCO and MCF inks based on the Carreau-Yasuda model.

| Parameter | MCO | MCF |
|---|---|---|
| Zero-rate viscosity (mPa.s) | 86.04 | 51.73 |
| Infinite rate viscosity (mPa.s) | 9.92 | 10.57 |
| Consistency (s) | 8.79 | 2.30 |
| Rate index (n) | 0.45 | 0.38 |
| Transition index | 1.37 | 2.41 |

## 4.3.3. Viscoelastic properties

In general, inkjet inks are characterised based on the flow curve analysis to understand the rheological behaviour and the resistance to flow. Practically, the test conditions do not reflect the real-time printing process where the shear force experienced by the inks are in the order of ~$10^{-6}$ $s^{-1}$. Also, the viscoelastic properties of the inkjet inks determine the droplet formation and break-up during the printing process. The stability of the formulated ink suspensions was

assessed PAV rheometer at the frequency ~5Hz replicating the shear force during the inkjet process. The viscoelastic moduli, storage modulus (G') and loss modulus (G''), measured in the frequency range, 30- 5KHz, as shown in Fig. 4.13. G' and G'' represents the measure of elastic and viscous resistance to deformation, respectively [175]. It is evident that both the inks exhibit viscoelastic liquid nature, with dominant G'' throughout the measured frequency. This behaviour indicates the suspension is stable where particles are separated from each other irrespective of the frequency applied. Similar characteristics were reported for stable aqueous-based silver ink suspensions at higher frequencies [202]. The drop seen in G' at high frequency in MCO ink is due to the artefact during the testing process. Fig. 4.14 shows the plot of complex viscosity against the shear rate for the inks with and without the methanol added to the ink suspensions. The measured complex viscosity is slightly higher than the dynamic viscosity (Fig 4.12) with slight shear-thinning behaviour.

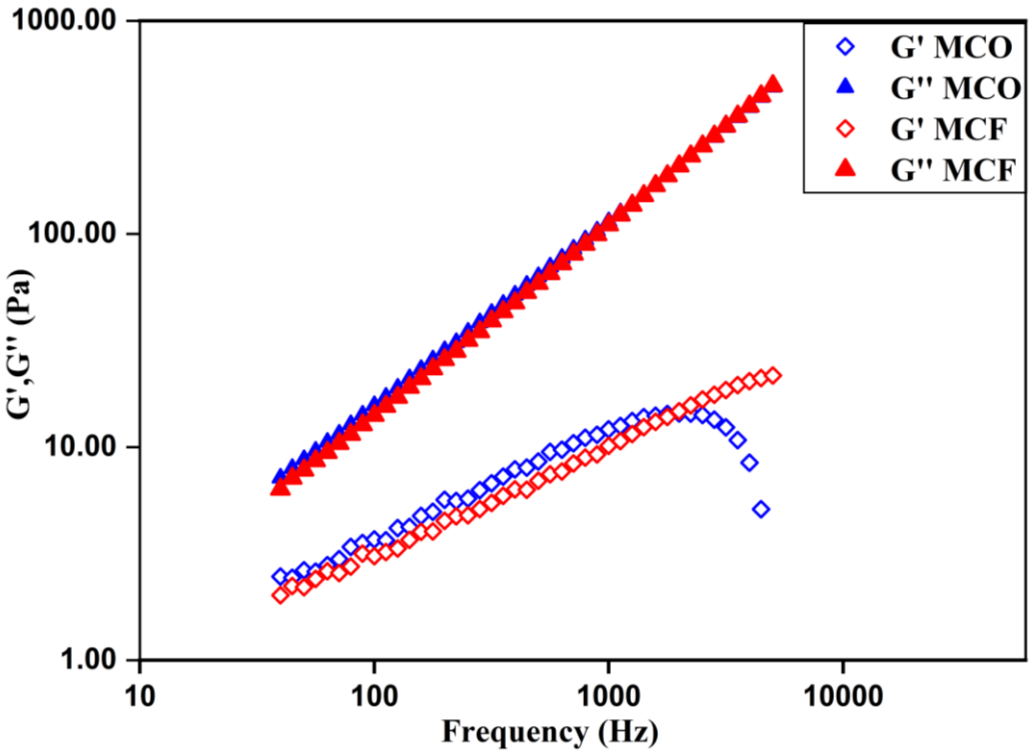


**Figure 4.13:** Storage and loss moduli of MCO and MCF inks measured at the frequency (30-5K Hz). Both the inks were displaying viscoelastic liquid nature with dominant G''.

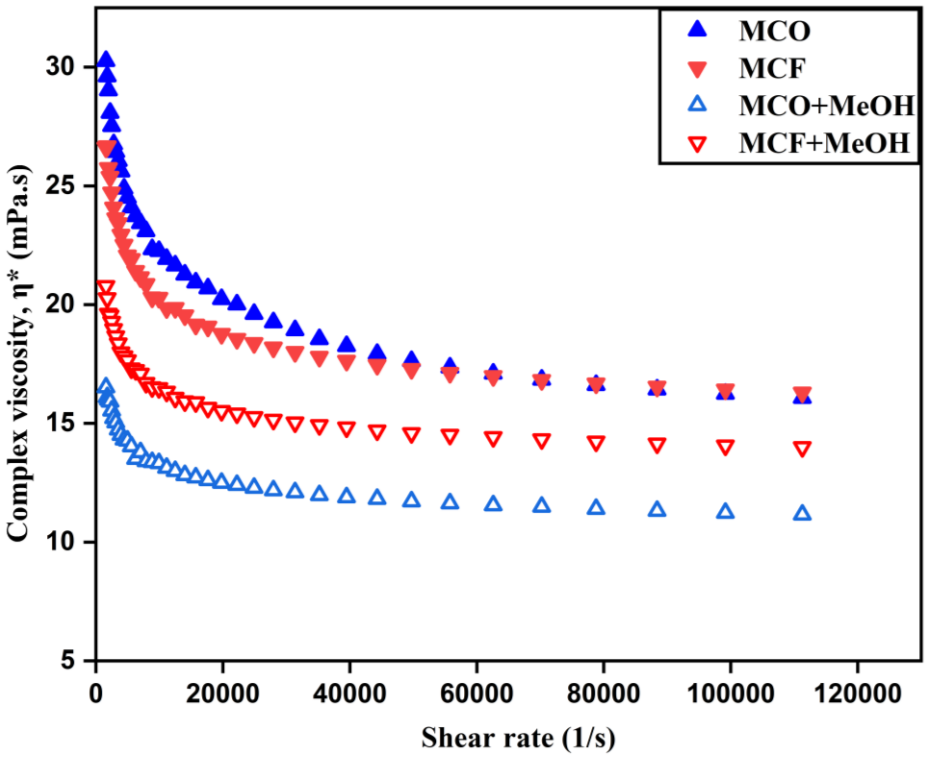


**Figure 4.14:** Complex viscosity of MCO and MCF inks with and without methanol at higher shear rates.

## 4.3.4. Printability of the inks

The printability of the inks was assessed based on the Re-We space parameter. Table 4.7 lists the measured physical properties of the formulated spinel inks. The printability of the formulated inks was established based on the semi-empirical models, Re-We space parameter. The inverse Ohnesorge number (Z) is plotted against the Re-We space parameters in Fig. 4.15. It can be seen that the inks fall well within the printable region.

**Table 4.7:** Physical properties of the final ink compositions and the dimensionless numbers for the respective inks.

| Ink | η (mPa.s) | γ (dyne/cm) | ρ (g/cc) | Re | We | Oh | Z=1/Oh |
|---|---|---|---|---|---|---|---|
| **MCO** | 10 | 35.2 | 1.2 | 38.9 | 39.8 | 0.16 | 6.17 |
| **MCF** | 13 | 32.9 | 1.3 | 32.4 | 46.0 | 0.21 | 4.77 |

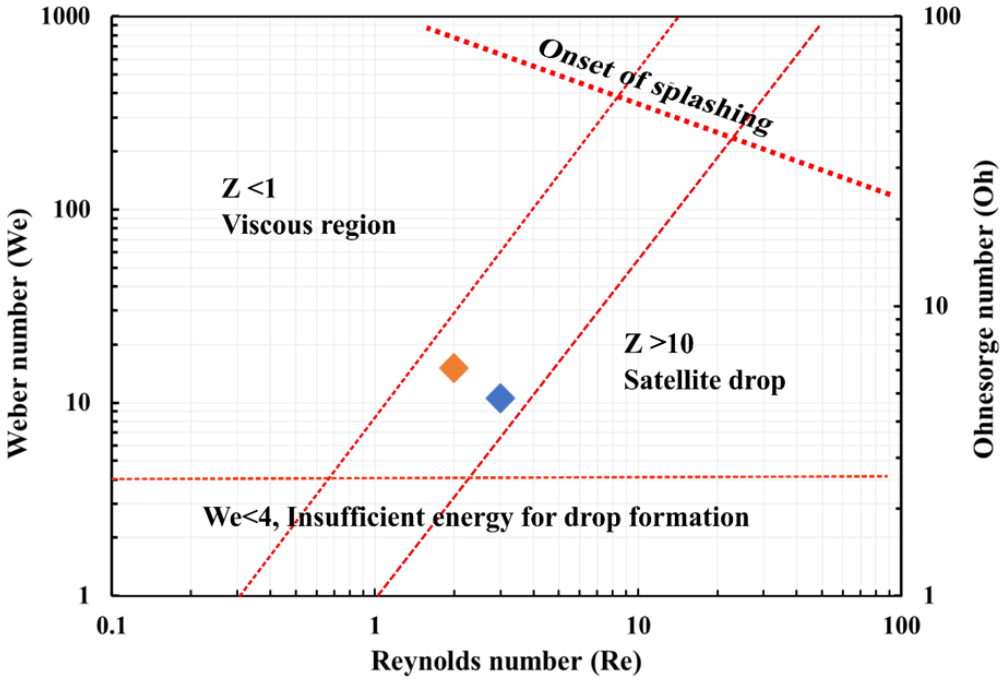


**Figure 4.15:** Re-We space parameter that defines the printing characteristics of the formulated spinel inks. The Z value for MCO (orange diamond) and MCF (blue diamond) inks are 6.17 and 4.77, respectively.

## 4.3.5. Thermal analysis of the inks

Fig. 4.16 shows the TGA curve of MCO and MCF inks. The dominant mass loss was observed in the first 100 °C and a gradual loss in the temperature regime 100 °C to 450 °C, marked as 1 to 4 in Fig. 4.16. The initial mass loss was due to the evaporation of the carrier medium (distilled water) and the co-solvent (methanol) present in ink. The gradual mass loss (marked as 1-2-3-4 zones) observed was due to the burn out of the organics from the dispersant, binder and additives. The residual mass obtained for MCO and MCF inks are 33.55% and 27.14 % respectively. Based on the thermal analysis, the sintering temperature ramp was set to 5 °C/ min for the burn out of the organics. Table 4.8 highlights the mass change and reason for the mass loss in different zones as marked in the TGA curve.

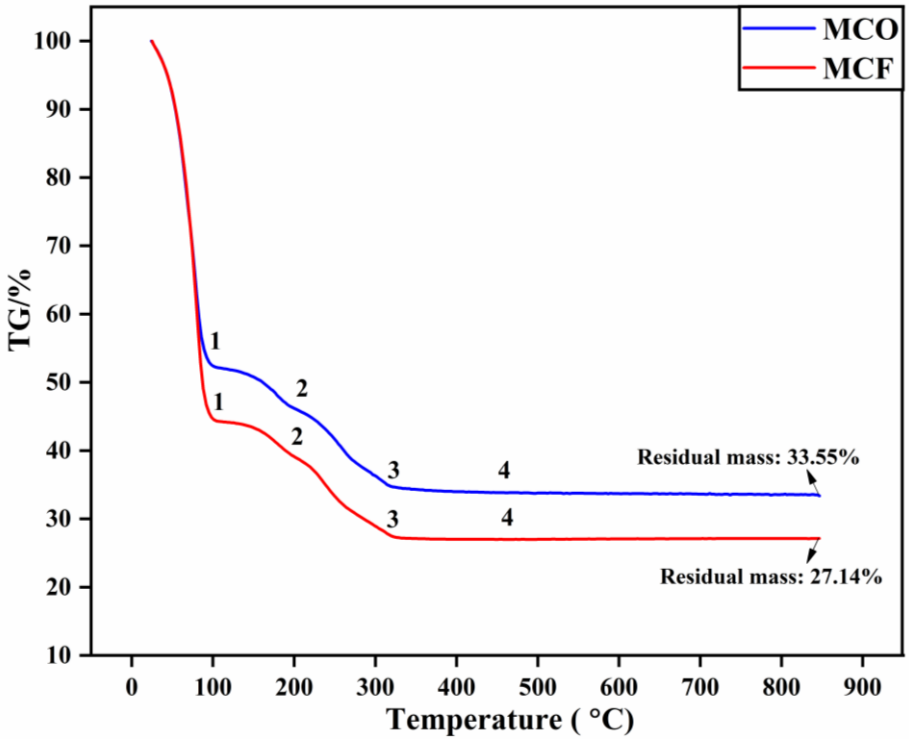


**Figure 4.16:** TGA curves of MCO and MCF ink suspensions. The major mass-loss events between 100 to 450 °C are marked (1-4) for both the inks. Standared error calcualted for the obtained residual mass MCO and MCF inks are ± 0.42 and ± 0.71 respectively.

**Table 4.8:** The observed mass change and reason for the mass loss observed in different zones (1-4) in the TGA curve.

| Ink | Zones | Mass change | Temperature (°C) | Reason for the mass loss |
|---|---|---|---|---|
| **MCO** | 1 | 47.02 | 25- 100 | DI water+ solvent evaporation |
| | 2 | 6.23 | 100- 200 | Removal of plasticisers |
| | 3 | 11.24 | 200-450 | Removal of binder |
| | 4 | 1.02 | 450-500 | Removal of organics |
| **MCF** | 1 | 55.38 | 25- 100 | DI water+ solvent evaporation |
| | 2 | 5.49 | 100- 200 | Removal of plasticisers |
| | 3 | 11.68 | 200-450 | Removal of binder |
| | 4 | 0.45 | 450-500 | Removal of organics |

### 4.3.6. Wettability of the inks

K41 and Crofer 22H stainless steel substrates had a surface roughness of 0.17 ± 0.01 µm and 0.13 ± 0.002 µm, respectively, after polishing with 1200 grit sandpaper. The K41 polished substrates were used as the sample material for contact angle measurement with the formulated inks. Table 4.9 lists the measured contact angle for the MCO and MCF inks with the K41stainless steel substrate. Both the inks exhibited a contact angle of less than 45°, thus representing the good wettability of the inks with the substrates [135].

**Table 4.9:** Average values of MCO and MCF inks from Contact Angle measurements.

| Ink | Contact angle left [°] | Contact angle right [°] | Contact angle mean [°] |
|---|---|---|---|
| **MCO** | 39.98 | 41.27 | 40.62 |
| **MCF** | 43.58 | 33.95 | 38.76 |

## 4.4. Inkjet deposition

The wettability of the formulated inks was tested using an electromagnetic printer. The printing controlling parameters were – (i) pressure; (ii) opening time, and (iii) line spacing (distance between the centres of two adjacent drops). The ejection of the ink droplets through the nozzle was controlled by the pressure applied to the ink reservoir, and the volume of the droplets was determined by the nozzle opening time. The printing parameters were adopted based on previous work for the inkjet deposition of ceramic suspensions using the same electromagnetic printer [18,133,144]. Table 4.10 lists the inkjet printing parameters used for the deposition of the spinel inks. The line length, pattern width and the number of points control the drop spacing and the interaction of adjacent droplets by allowing the adjacent droplets to coalesce in their liquid state.

**Table 4.10:** Ink jetting parameters of the inkjet printer used for the deposition process.

| **Printing parameters** | **Protective layer coating** |
|---|---|
| Nozzle opening time | 300 µs |
| Pressure | 350 mbar |
| Print speed | 40 mm/s |
| Line length | 25 mm |
| Number of points | 25 |
| Pattern width | 40 mm |
| Step size | 1 mm |

Fig. 4.17 shows images of K41 substrate inkjet printed using the formulated spinel inks. Fig. 4.17 (a) shows the deposition of MCO trial ink (without methanol). The ink tended to spread ink outwards over the substrate resulting in ink seepage, and the coffee-ring effect was observed, possibly due to loss of carrier medium (rapid evaporation at the edges). The interaction between the droplet and the substrate determined the drop spreading and the formation of the solid layer upon drying. The solidification of the droplets was dominated by the evaporation of the solvent and spreading of the ink suspension over the substrate. When the droplet impinged on the substrate, it deformed spread and tended to achieve mechanical equilibrium and surface tension [137].

In the case of suspensions, evaporation of the solvent is faster at low contact angles (ink droplet close to the contact line) resulting in particles to flow outwards and segregation of particles in the form of a ring around the corner termed as a coffee-ring effect [203,204]. To overcome these effects, the substrates were heated during the deposition process. However, the ink droplets impinging on the substrate at a given temperature (100 °C) resulted in uneven spreading due to the partial premature evaporation of the carrier medium and also leading to a gradient in drying from centre to edge of the droplet. The use of two solvents of different vapour

pressure and surface tension was shown to suppress the coffee ring effect, can be seen in the Fig. 4.17 (b-d). In the present study, DI water and methanol were used as the solvent. The presence of high vapour pressure solvent (methanol) evaporating quickly at the drop edge, created local surface tension gradient. Fig. 4.17 (d) shows the inkjet-printed stainless steel substrate with MCO and MCF inks post to heat-treatment; no visible defects were observed.

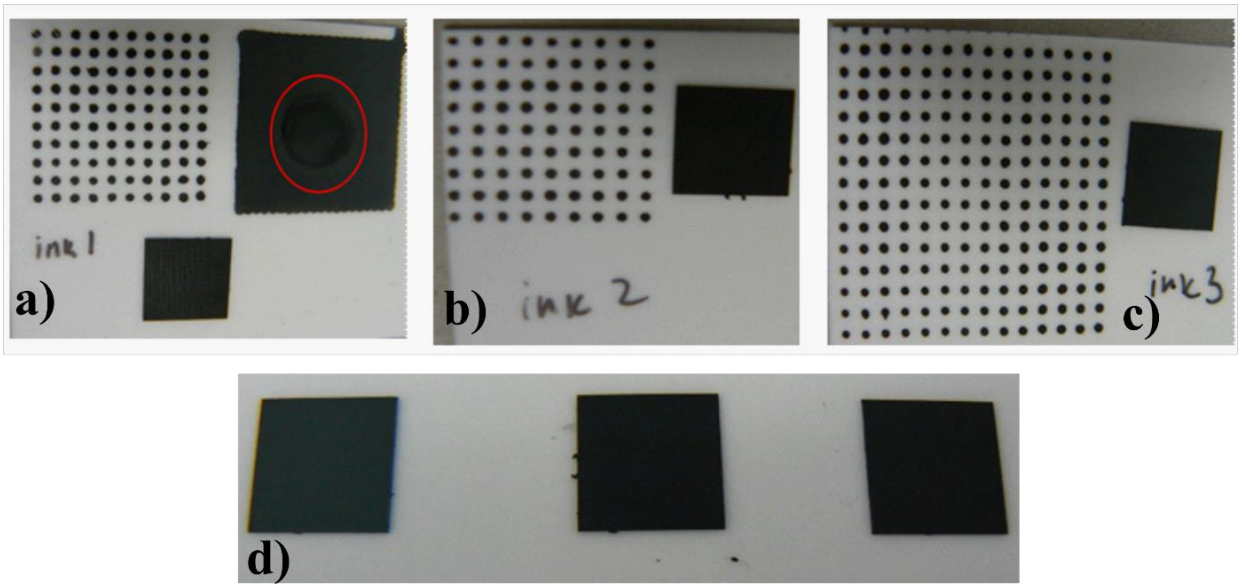


**Figure 4.17:** Inkjet-printed stainless steel substrates with the formulated inks, a) the substrate printed without the co-solvent in the ink composition, red marking shows the uneven drying of the inks, b) c) the substrates printed on a hot plate with the addition of co-solvent methanol in ink, d) K41 substrates post inkjet deposition and heat-treatment.

## 4.5. Summary

Aqueous based spinel inks were successfully formulated, and the printability of the inks was assessed based on the Re-We parameter. The effect of milling time and different dispersant dosage for the sub-micron sized spinel powders showed that samples beyond 24 hours milling time required additional dispersant addition due to the increase in surface area of the particles. The optimum dispersant dosage was evaluated based on the apparent viscosity, and the presence of flocs was estimated by fitting the results into the Herschel-Bulkley equation. Based

on the results from PSD, sedimentation test and flow curve analysis, 40wt.% dispersant with respect to the powder was chosen as the optimal dosage. The optimum solid content of 30wt.% was found to achieve the target viscosity of less than 10mPa.s.

The final formulation for both the MCO and MCF inks exhibited shear thinning behaviour with the maximum particle size within the limits of the inkjet printer requirements (< 2µm). The rheological behaviour of the inks at higher frequencies, during the jetting process, was assessed using the PAV rheometer and revealed the visco-elastic liquid nature of the inks with the complex viscosity less than 15 mPa.s. The formulated inks with the Z values 6.17 and 4.77 for MCO and MCF inks, respectively, fell within the printable regime for DOD mode of printing based on the Re-We space parameter. The formulated inks were printed over the stainless steel substrate successfully without visible defects. Thus, spinel-based suspension inks with DI water as the carrier medium was successfully formulated and printed over the stainless steel substrates.

# *Chapter 5: Evaluation of Inkjet-Printed Protective Layer Coatings*

This chapter evaluates the performance of the inkjet-printed spinel coatings MCO, MCF and MCFC deposited over K41 virgin and K41 nitrided substrates. To understand the effect of nitriding on the stainless steel substrates, uncoated K41 virgin and K41 nitrided samples were exposed to an oxidation test for 1000 hours. The inkjet-printed samples were subjected to oxidation and area-specific resistance tests at 700 °C for 1000 hours. The chromium retention in each coating layer and the influence of the surface nitriding modification process are discussed. Sol-gel infiltration was introduced to develop a scaffold layer over the porous microstructure, and its performance was analysed.

# 5.1. Introduction

The inkjet deposition of spinel coatings was carried out in two batches. Initially, the formulated inks were deposited on K41 virgin and nitrided stainless steel substrates, and their performance was analysed in Batch I. Based on the inference from the results, Batch II samples were prepared with similar ink formulation. Table 5.1 lists the details of the stainless steel substrates, coating, and tests performed in Batch I and II. The description of the two batches are as follows:

### IJP batch I:

K41 virgin and surface nitrided stainless stainless steel substrates of dimension ($10\times10\times1$ $mm^3$) were inkjet printed with the formulated spinel inks, the composition of the inks was shown in Chapter 4, section 4.3, Table 4.4. The spinel inks refer to the coating materials $MnCo_2O_4$, $MnCo_{1.8}FeO_4$, and $MnCo_{1.6}Fe_{0.2}Cu_{0.2}O_4$ and henceforth, spinel coatings are mentioned as MCO, MCF, and MCFC respectively. The MCFC powder procured from ENEA (SCORED: 2:0 project partner) was used in this batch. The printed samples were heat-treated in air for 10 hours at 800 °C at the heating and cooling rate of 5 °C/min. The samples were exposed to isothermal oxidation and an Area-Specific Resistance (ASR) measurement for 1000 hours with the testing conditions as described in Chapter 3, section 3.5.

Anticipating the porous microstructure of the as-prepared coatings, an additional infiltration process over the coated layers was carried out on MCO and MCF coatings prior to tests for oxidation and ASR characterisation, respectively. A 0.5 M solution of Co $(NO_3)_2$ and Mn $(NO_3)_2$ was prepared with citric acid (1M solution) as a gelling agent and inkjet deposited over heat-treated coatings with two pass printing. The infiltrated sample was then heat-treated at 500 °C for an hour at the heating rate of 10 °C/min to remove the organics used in the sol-gel ink.

## IJP batch II:

K41 (20×20×0.2mm$^3$) and Crofer 22H (20×20×0.3mm$^3$) stainless steel substrates were inkjet printed with three spinel inks. The coating was applied with two pass printing in order to obtain a thinner coating compared to Batch I. The deposited samples were subjected to a reactive sintering process to achieve denser coatings. The coated samples were subjected to reducing conditions (Ar/ 3%$H_2O$ / 3% $H_2$) at 900 °C for 3 hours followed by oxidation in stagnant air at 800 °C for 4 hours. $Cu_{1.3}Mn_{1.6}Fe_{0.1}O_4$ (CMF) powders from Kceracell, South Korea, was used for this batch of samples.

**Characterisation:**

The surface SEM micrographs of the inkjet-printed samples from both batches were used to estimate the average pore size and volume after the different heat-treatment processes, before and after the oxidation test. The performance of the inkjet-printed layers was analysed based on Cr migration identification from the stainless steel/coating interface to the surface of the coatings.

**Table 5.1:** Details of the stainless steel substrate, coatings, and high-temperature tests performed in two batches.

| Batch | Steel substrate | Coating | Sintering procedure | High-temperature tests | |
|---|---|---|---|---|---|
| | | | | Oxidation | ASR |
| I | K41 | MCO | Air | ✓ | ✓ |
| | | MCF | Air | ✓ | ✓ |
| | | MCFC | Air | ✓ | ✓ |
| | K41 Nitrided (K41 N) | MCO | Air | ✓ | ✓ |
| | | MCF | Air | ✓ | ✓ |
| | | MCFC | Air | ✓ | ✓ |
| | K41 infiltrated (K41 INF) | MCO | Air | ✓ | - |
| | | MCF | Air | - | ✓ |
| II | K41 | MCO | Reactive | ✓ | - |
| | | MCF | Reactive | ✓ | - |
| | | CMF | Reactive | - | - |
| | Crofer 22H | MCO | Reactive | ✓ | - |
| | | MCF | Reactive | ✓ | - |
| | | CMF | Reactive | - | - |

## 5.2. XRD of the materials

Fig. 5.1 (a-b) shows the XRD patterns of the spinel powders and the stainless steel substrates. The diffractogram of the spinel powders exhibited a cubic spinel structure with the peak positions revealing $MnCo_2O_4$ (ICSD: 201314) well-matched with $Co_3O_4$ phase (ICSD: 36256). The peaks identified in the MCFC powder belong to the $Cu_{0.5}Mn_{0.5}Fe_2O_4$ spinel group. Two peaks matching with the stainless steel substrate, Fe-Cr (ICSD: 102751) were observed, as shown in Fig 5.1 (b). It can be seen that the nitrided substrate displayed a ferritic phase with broadened peaks which can be associated with the presence of nitrogen in the ferritic structure after the nitriding process.

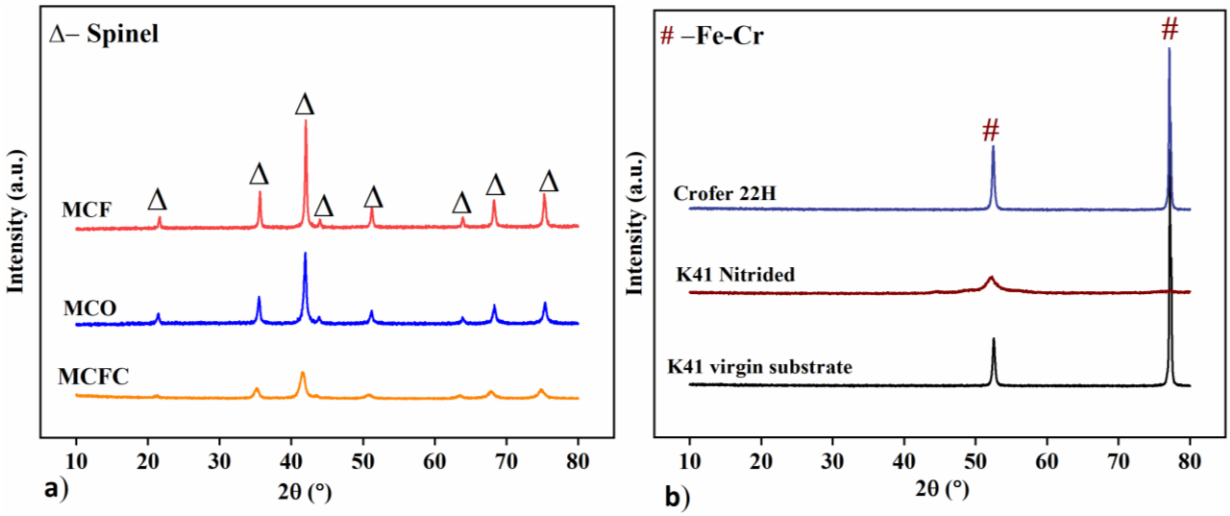


**Figure 5.1:** XRD data of (a) spinel powders- MCO, MCF, and MCFC, (b) stainless steel substrates - K41, Crofer 22H and K41 nitrided used in the study.

Fig. 5.2 (a-c) shows the surface SEM micrographs of inkjet-printed layers on stainless steel substrate K41 after deposition. The inkjet-printed layers were free of any significant cracks or defects after drying, with well-packed particles. The surface micrographs of the three spinel coatings revealed homogenous grain distribution with a porous nature. MCFC coatings exhibited a relatively larger grain size which can be attributed to the coarser particle size of the starting material (0.70µm) in comparison to the MCO and MCF powders (~0.55µm).

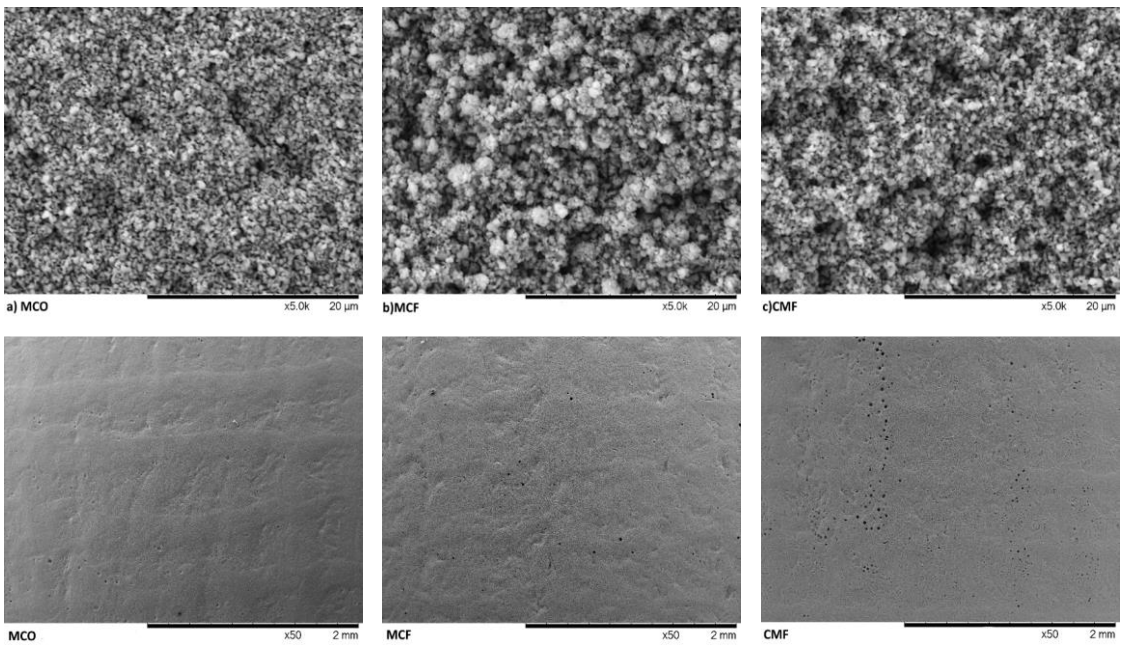


**Figure 5.2:** Surface SEM micrographs of spinel coatings after the inkjet deposition process; top row: high magnification of the printed layers; bottom row: overall surface impression.

# IJP Batch I

## 5.3. High-temperature oxidation

### 5.3.1. Oxidation of uncoated K41 stainless steel substrates

A virgin and surface nitrided substrate of K41 stainless steel with dimension 20×20×0.2 $mm^3$ were exposed to cyclic oxidation for 1050 hours at 700 °C with 3% relative humidity in the air. The mass gain of the samples was recorded after 50, 150, 250, 500, 750, 850, 950 and 1050 hours. Fig 5.3 shows the mass gain of virgin and nitrided K41 substrates against the exposure time. After 1050 hrs of exposure, nitrided substrates had twice the total amount of mass gain of 0.30 $mg.cm^{-2}$ in comparison to the virgin stainless steel substrates with the total mass gain value of 0.15 mg $cm^{-2}$. The high mass gain by the nitrided substrates compared to the unmodified surface in stainless steels has also been reported in other studies [114],[205].

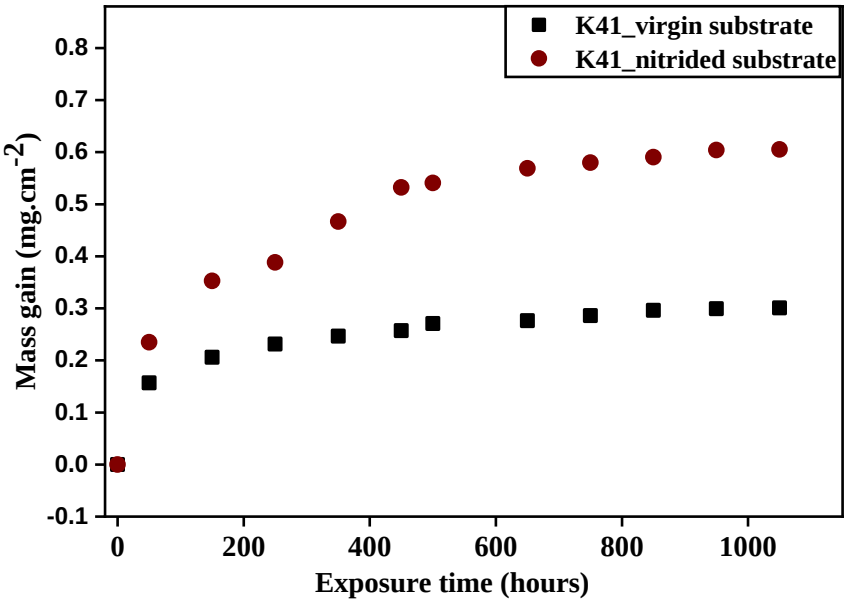


**Figure 5.3:** Mass gain of K41 virgin and nitrided substrates at 700 °C over 1000 hours.

Fig. 5.4 shows the diffractogram of the virgin and nitrided substrates after 1000 hours of the oxidation test. The low-intensity peaks confirming the presence of chromia formation (ICSD: 75577) were seen in both the substrates. The nitrided substrates exhibited the presence of $Cr_2N$ (ICSD: 67400) with low-intensity peaks after the oxidation test. No presence of Cr nitride phase was seen in as-received nitrided substrates as the formation and growth of nitrides is limited at low temperature ( about 400 °C), processing temperature during the nitriding process [120]. The removal of nitrogen from the ferritic phase was evident from the narrowing of ferritic phase peaks after the oxidation test, shown in Fig. 5.4. Thus, the formation of Cr nitride in the exposed sample can be accounted for the interaction between the nitrogen and Cr, also due to the strong affinity of Cr to N [115,116].

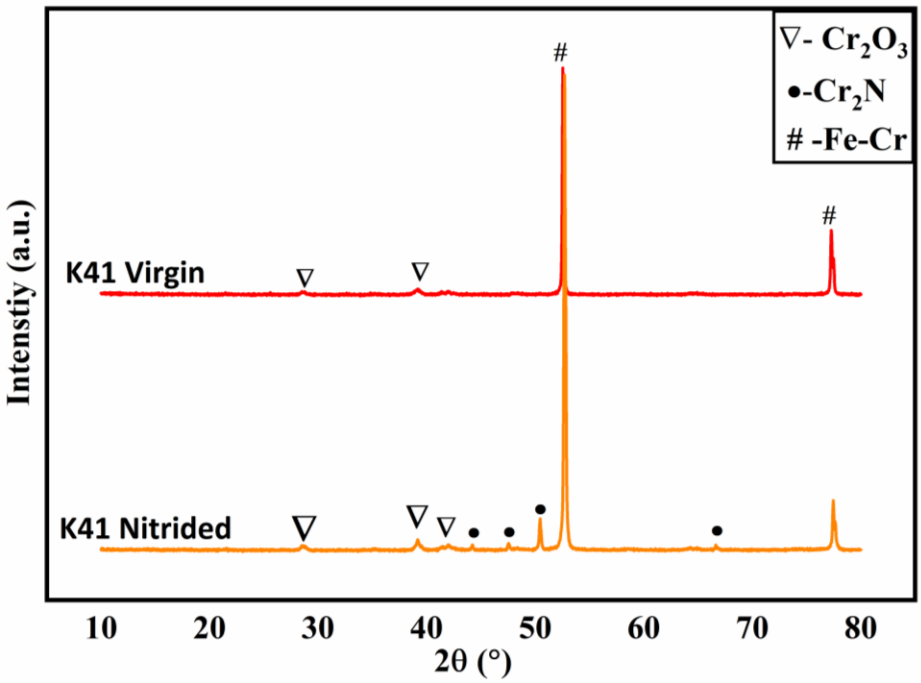


**Figure 5.4:** XRD data of the uncoated K41 virgin and surface nitrided K41 stainless steel substrates after 1000 hours of oxidation at 700 °C.

The surface SEM micrographs and elemental quantification of the uncoated samples after oxidation test are shown in Fig. 5.5 and 5.6, respectively. Both substrates were free of any spallation after 1000 hours of oxidation. An increase in Mn content was detected at the surface of nitrided (5.25 atomic%), and virgin substrate (3.47 atomic%), signifying the formation of a spinel layer $(Mn, Cr, Fe)_3O_4$. The EDS quantification on the surface of both substrates confirmed the presence of Mn, Cr, Fe, and O in both sample types. It is interesting to note the difference in Si content at the surface of the virgin and nitrided substrates. The virgin substrate had a higher Si content, and the nitrided substrate showed suppressed Si content at the surface even before the test, which can be associated with the presence of the nitrided layer. The inset images shown in Fig 5.5 reveal the capture of Si due to the formation of Laves phases. A high amount of Mn was seen over the nitrided substrate. The presence of Mn resists corrosion by forming a spinel layer during high-temperature exposure.

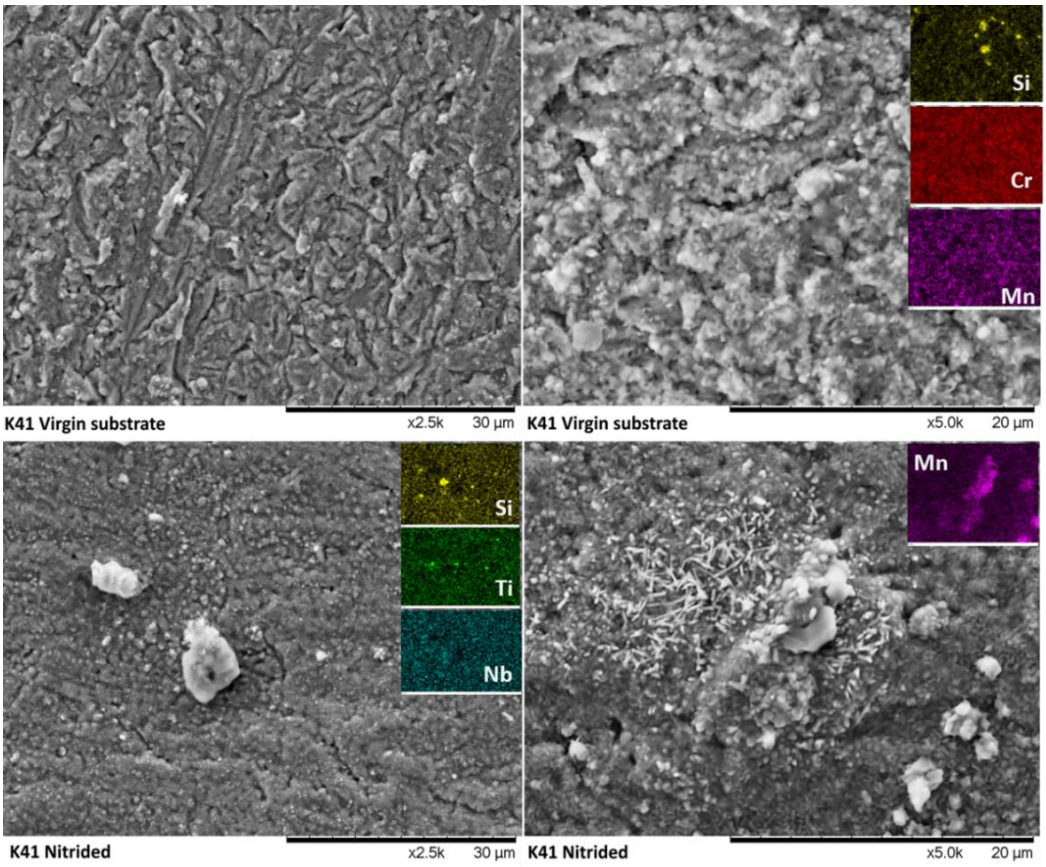


**Figure 5.5:** Surface SEM micrographs of K41 virgin (top row) and nitrided substrates (bottom row) after 1000 hours of oxidation test. The insets within the micrographs highlight the presence of Si, Ti, Nb.

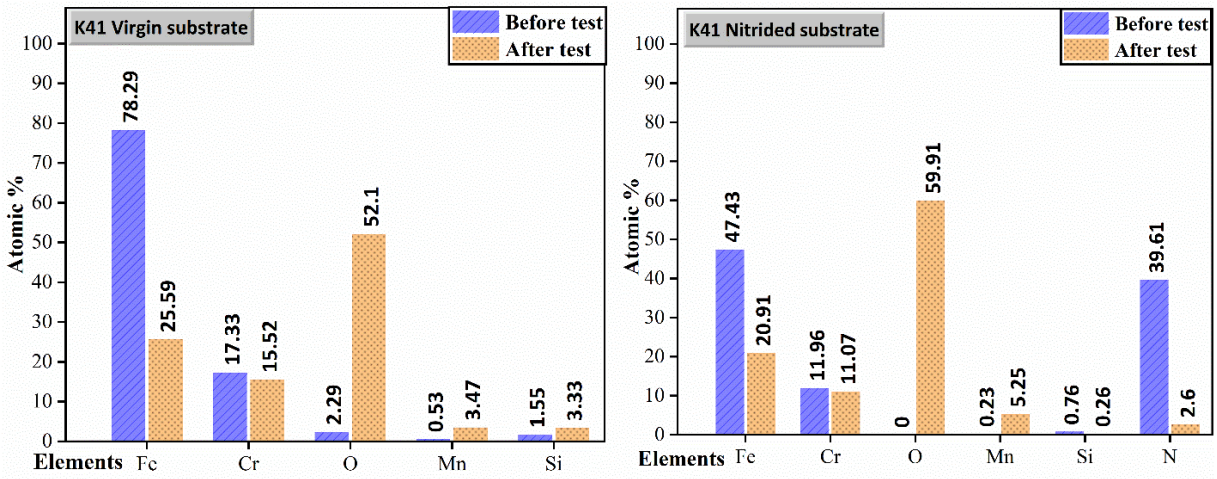


**Figure 5.6:** Elemental quantification of the uncoated virgin and nitrided K41 stainless steel substrate before and after the oxidation test.

## 5.3.2. Oxidation of IJP spinel coatings over K41 virgin substrate

The samples heat-treated in air were subjected to isothermal oxidation at 700 °C for 1000hrs. The XRD analysis of the samples after the test is shown in Fig. 5.7. No significant phase change was observed, with all samples showing the cubic structure of $MnCo_2O_4$ (ICSD: 201314). Fig. 5.8 shows the surface SEM micrographs of the three spinel coatings after 1000 hours of oxidation test. No cracks or significant defects were seen on the surface post oxidation test. The coating layers exhibited particles of homogenous nature with well-connected grains. The MCO layer had developed a prism-like spinel crystal microstructure confirming the formation of the single cubic spinel phase. The microstructure of MCF and MCFC layers transformed into a connected grain network, signifying the occurrence of further densification of particles during the test.

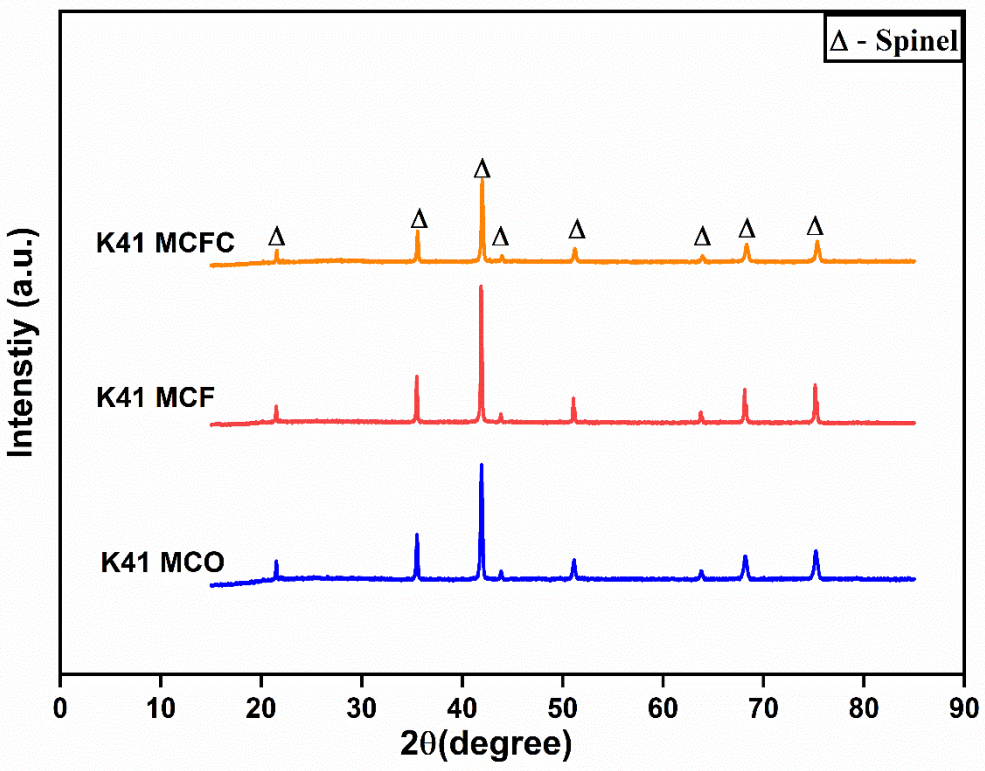


**Figure 5.7:** XRD data of the inkjet-printed spinel coatings over K41 substrate after 1000 hours of oxidation test.

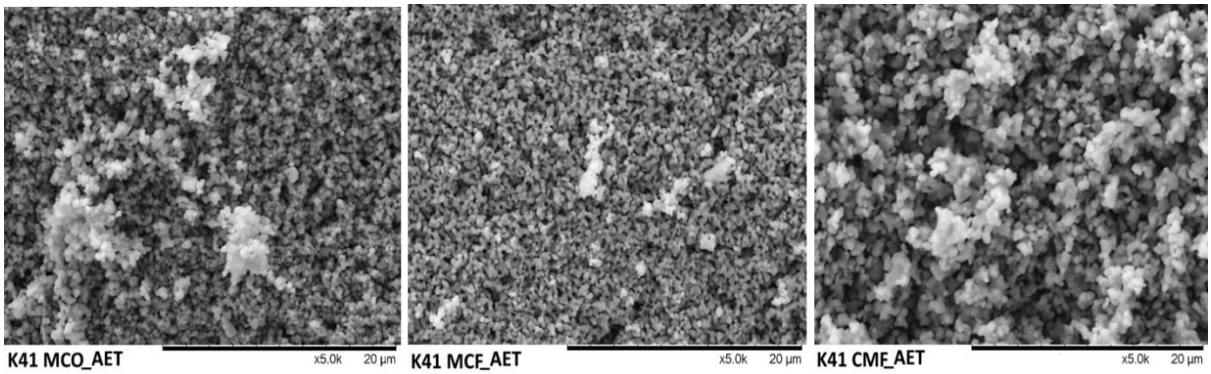


**Figure 5.8:** Surface SEM micrographs of MCO, MCF and MCFC coatings over K41 substrates after the oxidation test for 1000 hours.

The line scan analysis over the white clusters seen on the microstructure of the deposited layers post-oxidation revealed the presence of an oxide with cobalt-rich phase and confirmed the high stability of Mn-Co based coatings as observed in similar oxide mixtures [99,153,206,207]. EDS quantification analysis on the surface of all the samples before and after the oxidation test is shown in Table 5.2. The distribution of elements, Mn, Co, and Fe over the surface did not vary much before and after the oxidation test confirming the stability of the coatings over 1000hours of exposure. The MCO coating displayed a Cr content of more than 1 atomic % even before the oxidation test. The observed Cr presence may be due to the failure of coatings to suppress the Cr migration during the heat-treatment process. The MCF coating displayed least Cr at the surface, followed by the MCFC coating.

**Table 5.2:** EDS quantification of inkjet-printed spinel coatings on K41 virgin substrate before and after the oxidation test. EDS analysis performed over the sample surface (shown in Fig. 5.8)

| Coating layer | Before oxidation test in (at%) | | | | | | After the oxidation test in (at%) | | | | | |
|---|---|---|---|---|---|---|---|---|---|---|---|---|
| | O | Co | Mn | Fe | Cr | Cu | O | Co | Mn | Fe | Cr | Cu |
| **MCO** | 51.98 | 31.74 | 14.74 | 0.14 | 1.40 | | 51.37 | 28.89 | 13.68 | 0.08 | 5.98 | |
| **MCF** | 52.68 | 29.70 | 13.91 | 3.32 | 0.40 | | 52.01 | 30.09 | 14.30 | 3.54 | 0.06 | |
| **MCFC** | 54.12 | 22.18 | 16.93 | 3.81 | 0.89 | 2.7 | 44.13 | 27.88 | 18.94 | 4.75 | 1.39 | 2.06 |

The cross-section analysis of the samples after the test is shown in Figs. 5.9 to 5.12. The average coating thickness measured across the coating layer in two different SEM micrographs for MCO, MCF and MCFC coatings were 49.76 ±1.3 µm, 48.39 ± 1.20 µm, and 33.16 ± 1.21 µm, respectively. All the coatings displayed good adhesion to the stainless steel substrate. The presence of a chromia layer was not seen distinctly in the cross-section analysis, yet the chromia layer was evident from the elemental mapping and line scan analysis displaying high Cr and O presence at the stainless steel/ coating interface in all three coatings. The MCO coating displayed a high Cr gradient and the presence of a silica layer throughout the coating, starting from the steel substrate was observed. The elemental mapping of MCO coating (Fig. 5.9) showed a silica layer at the stainless steel/ coating interface. Trace amount of Si was also seen across the MCF and MCFC coatings. The line scan profile of MCO, MCF and MCFC coatings shown in Figs. 5.9 to 5.12 revealed the presence of phases rich in Co, Mn, and O with inclusions of Fe and Cr in the protective layer. The concentration of Cr decreased from the stainless steel substrate towards the coating surface as a general trend in all three coatings, indicating the inhibition of Cr diffusion to an extent.

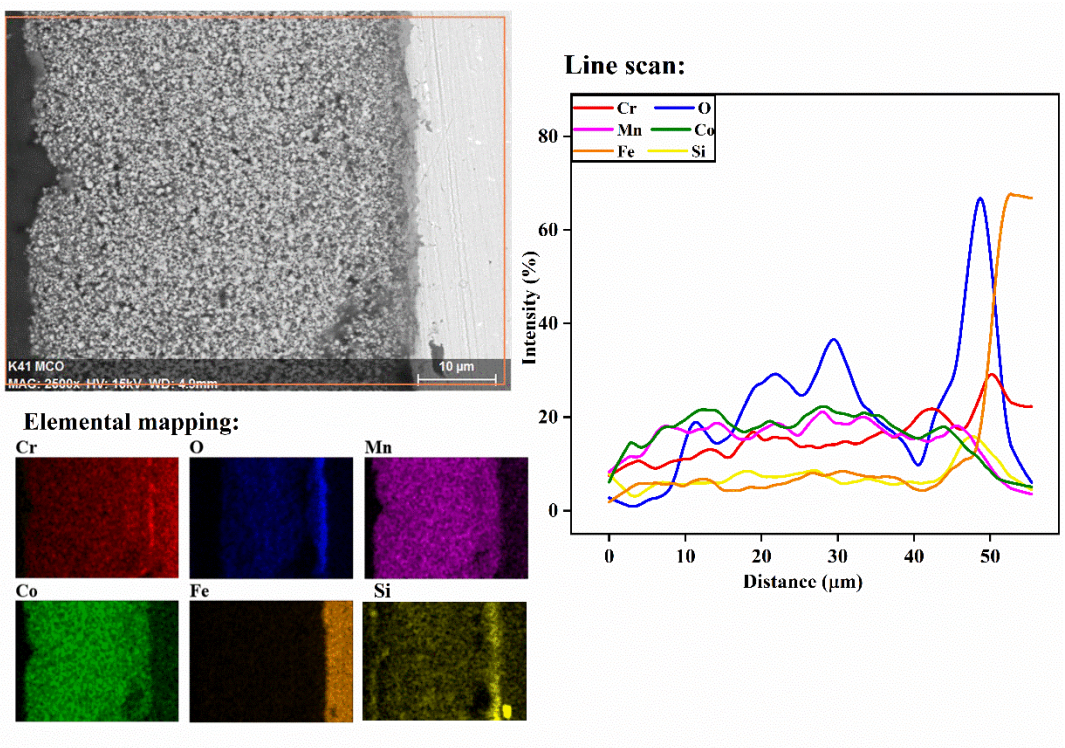


**Figure 5.9**: Cross-sectional analysis of the K41 substrate with an MCO coating post 1000 hours of oxidation test. Elemental mapping and line scan analysis on the sample represents the concentration of elements across the stainless steel/coating bilayer.

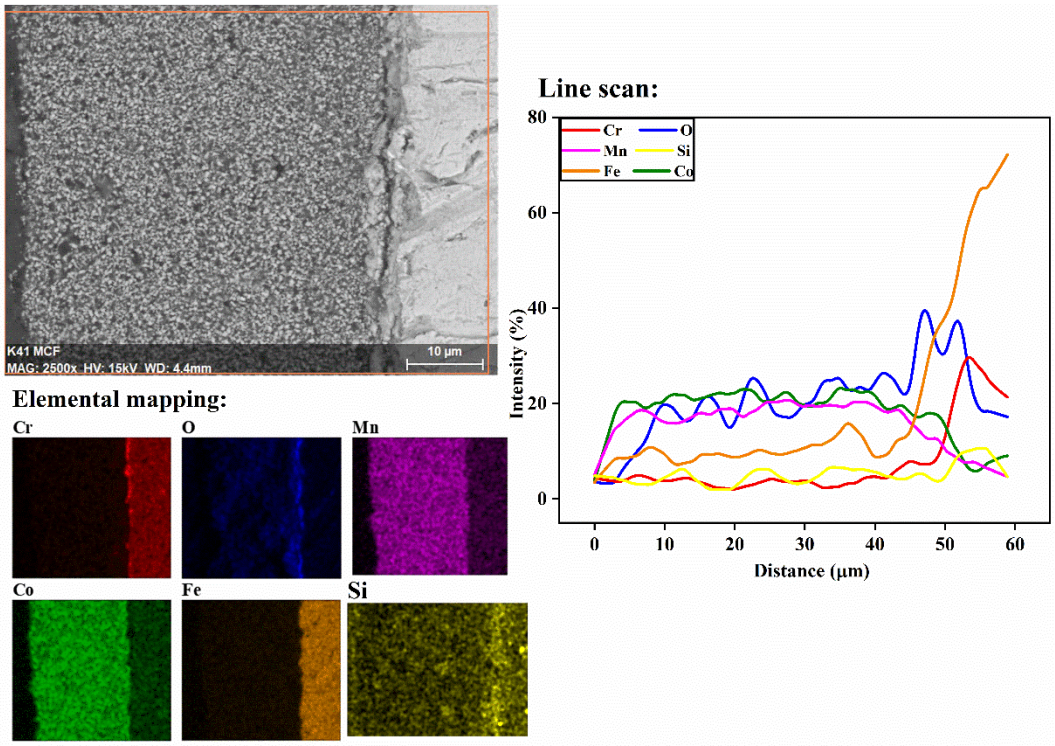


**Figure 5.10:** Cross-sectional analysis of the K41 substrate with an MCF coating post to 1000 hours of oxidation test. Elemental mapping and line scan analysis on the sample represents the concentration of elements across the stainless steel/coating bilayer.

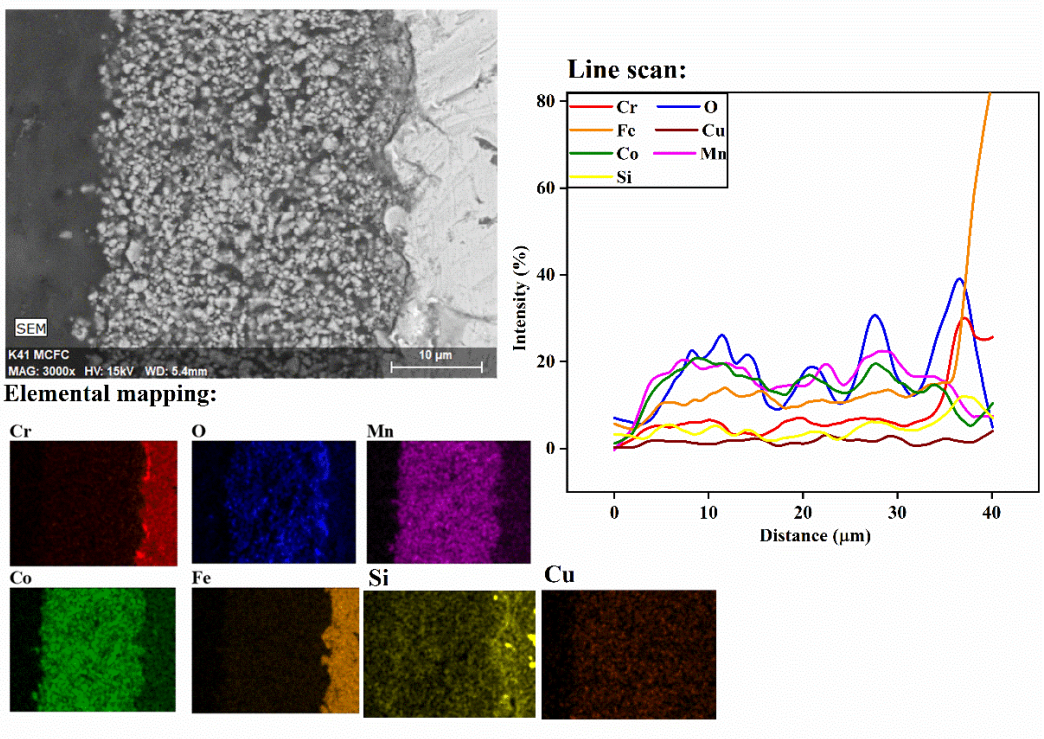


**Figure 5.11:** Cross-sectional analysis of the K41 substrate with an MCFC coating post 1000 hours of oxidation test. Elemental mapping and Line scan analysis on the sample representing the concentration of elements across the steel/coating bilayer.

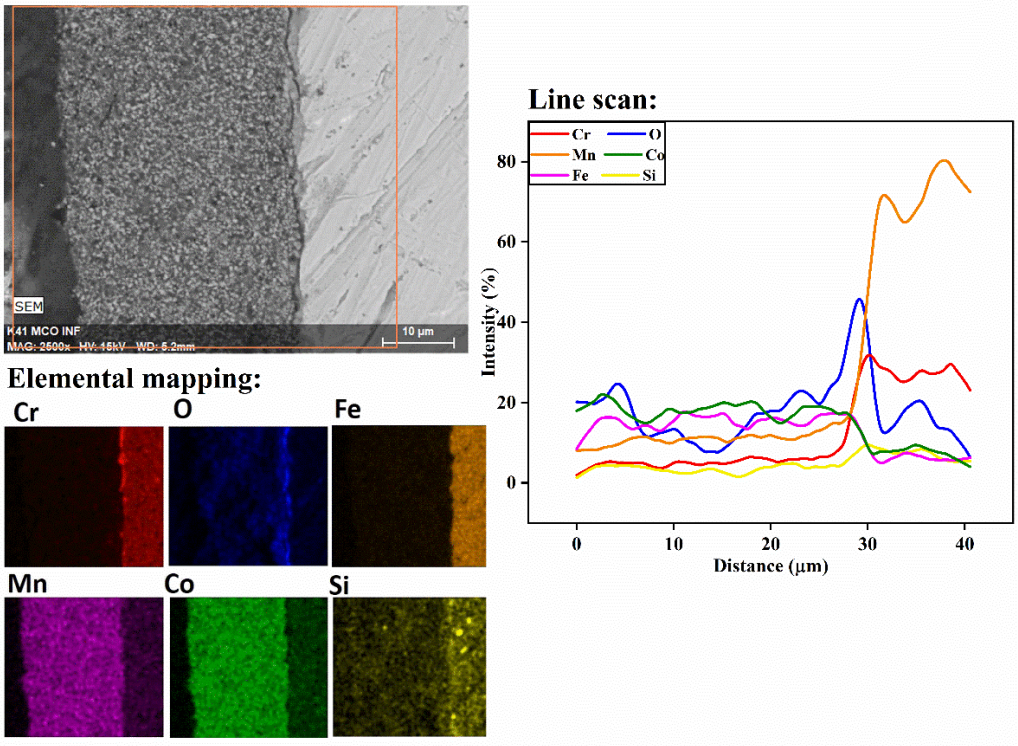


**Figure 5.12:** Cross-sectional analysis of with K41 infiltrated MCO coating post-1000 hours of oxidation test. Elemental mapping and Line scan analysis on the sample represents the concentration of elements across the stainless steel/coating bilayer.

The quantitative analysis of elemental distribution measured across the protective coatings with the spot size of 30 µm before and after the oxidation test is shown in Table 5.3. The higher Cr content of 8.56 atomic % after the test was observed in the MCO coating layer and a value of 2.94 atomic % in the MCFC coating. The high concentration of Cr in the MCO coating was due to the presence of pits and voids, as shown in Fig. 5.13. The observed defects in the deposited coating could have arisen from the inkjet printing process itself or were due to the fast removal of organics; similar defects on inkjet printed layers have been reported before [208]. Thus, the failure of the coating explains the higher Cr gradient across the MCO coating. The defects must have favoured inward diffusion of O at an early stage of oxidation, leading to the formation of a silica sub-layer. No such defects were seen in MCF and MCFC coatings. The least amount of Cr across the coating was seen in MCF coating, 1.31 atomic %, and a Cr content of 1.40 atomic% in the MCFC coating.

**Table 5.3:** EDS quantification of the spinel coating composition after the oxidation test. The analysis of each coating was done using the cross-section images shown in Fig. 5.9 to 5.12.

| **Coating** | **Amount of chromium (atomic %)** | | | | | | |
|---|---|---|---|---|---|---|---|
| | O | Co | Mn | Fe | Cr | Si | Cu |
| **MCO** | 48.67 | 24.61 | 11.55 | 3.88 | 8.56 | 2.72 | - |
| **MCF** | 49.23 | 27.11 | 13.7 | 7.73 | 1.31 | 0.93 | - |
| **MCFC** | 41.58 | 25.15 | 16.4 | 10.8 | 2.94 | 0.64 | 2.49 |
| **MCO INF** | 44.00 | 28.65 | 13.99 | 9.84 | 2.94 | 0.58 | - |

The trend observed in the Cr detection across the protective layer was in line with the amount of Cr detected at the surface of the coatings post oxidation test, signifying the migration of Cr from the stainless steel interface/oxide layer to the surface of the coatings. Based on the Cr

migration to the surface of the coating layer, the best-performing inkjet printed spinel coatings can be sequenced as MCF > MCFC > MCO.

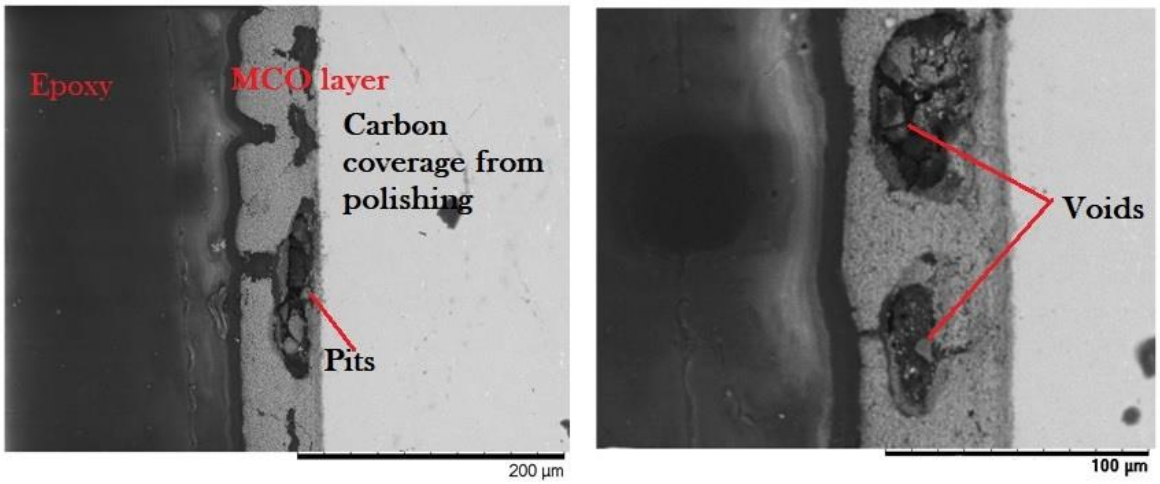


**Figure 5.13:** Cross-sectional SEM micrographs of exposure tested K41 MCO with defects.

## 5.3.3. Oxidation of Nitrided samples

The XRD analysis did not show any significant phase changes, and identified peaks showed cubic spinel phase, $MnCo_2O_4$ (ICSD: 201314), shown in Fig. 5.14. No Cr nitride peaks were seen in nitrided substrate possibly due to the thickness of the coating layer. Fig. 5.15 shows surface SEM micrographs of the three spinel coatings over the surface nitrided K41 substrates after 1000 hours of the oxidation test. The microstructure of the samples was similar to the spinel coatings over the virgin substrate.

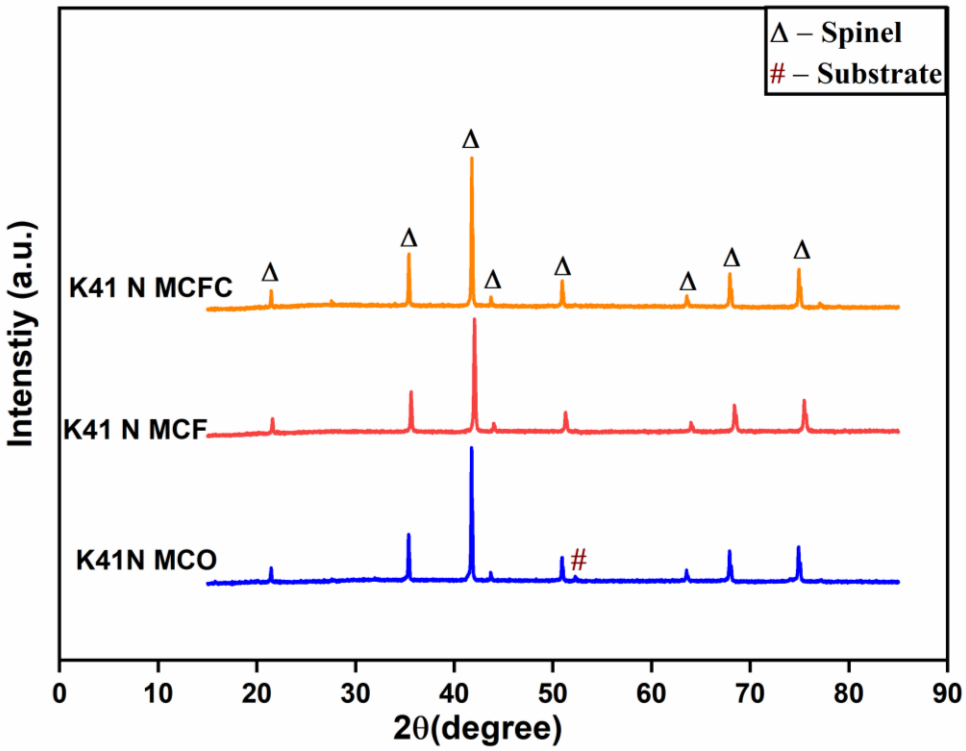


**Figure 5.14:** XRD patterns of spinel coatings over the nitrided substrate after 1000 hours of oxidation test.

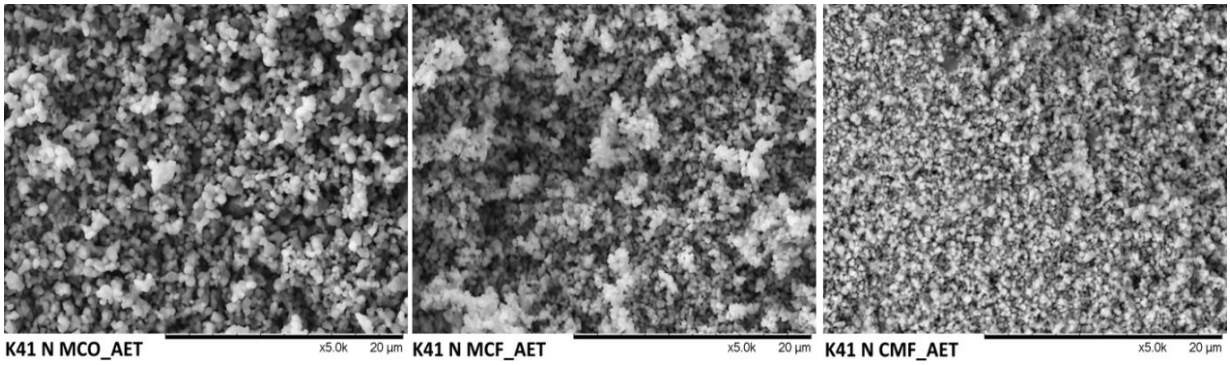


**Figure 5.15:** Surface SEM micrographs of three spinel coatings over the nitrided substrate after 1000 hours of oxidation.

The average thickness was measured across the coatings in two different SEM micrographs for the MCO, MCF and MCFC were 53.81 ± 1.36 µm, 55.02 ± 1.00 µm, and 36.40 ± 1.9 µm, respectively. The standard deviation was above 1 due to the uneven coverage of epoxy on the coating edges. The coatings displayed good adhesion with the stainless steel substrate. The elemental quantification on the surface of the coatings before and after the oxidation test is shown in Table 5.4. The amount of Cr detected was higher in the MCO coating in comparison

to MCF and MCFC coatings. It is interesting to note the presence of nitrogen at the surface of all the coatings post oxidation, with MCFC coatings displaying higher nitrogen presence at the surface followed by MCO and MCF coating.

**Table 5.4:** EDS characterisation of the spinel coating surfaces of after the oxidation test. The analysis of each coating was done using the SEM images shown in Fig. 5.14.

| Coating | Before oxidation test in (at%) | | | | | | After the oxidation test in (at%) | | | | | |
|---|---|---|---|---|---|---|---|---|---|---|---|---|
| | O | Co | Mn | Fe | Cr | N/ Cu | O | Co | Mn | Fe | Cr | N/Cu |
| **MCO** | 38.95 | 38.06 | 20.78 | 0.89 | 0.47 | N:0.86 | 42.07 | 34.87 | 16.81 | 0.42 | 3.83 | N:2 Cu:- |
| **MCF** | 52.24 | 28.71 | 13.45 | 3.21 | 0.38 | N: 2.01 | 52.52 | 30.72 | 14.19 | 0.24 | 0.04 | N: 2.25 |
| **MCFC** | 48.86 | 35.54 | 17.53 | 0.39 | 0.16 | N: 1.88 Cu:2.6 | 48.8 | 24.23 | 16.95 | 4.3 | 0.22 | N: 3.1 Cu: 2.4 |

The cross-sections of three spinel coatings are shown in Figs 5.16 to 5.18. The presence of chromia at the stainless steel/coating interface was confirmed by line scan and elemental mapping of the respective coatings. The elemental quantification performed across the coatings with the spot size of 30µm revealed high Cr content in the MCO coating followed by MCF and MCFC. The elemental distribution as observed in virgin substrates is shown in Table 5.5. In comparison to the virgin substrate, observed Cr at the surface was less even in the case of MCO coating. Diffusion of nitrogen across the coatings was observed, with MCFC displaying a high amount of nitrogen both at the surface and across the coatings.

**Table 5.5:** EDS quantification of the spinel coatings after the oxidation test. The analysis of each coating was done using the cross-section images shown in Fig. 5.16 to 5.18.

| Coating | Amount of chromium (atomic %) | | | | | | | |
|---|---|---|---|---|---|---|---|---|
| | O | Co | Mn | Fe | Cr | Si | N | Cu |
| **MCO** | 49.64 | 27.02 | 12.83 | 3.48 | 3.80 | 0.41 | 2.83 | |
| **MCF** | 42.18 | 31.11 | 14.69 | 5.67 | 1.56 | 0.53 | 3.98 | |
| **MCFC** | 51.32 | 18.36 | 12.44 | 8.63 | 1.6 | 0.31 | 5.5 | 1.84 |

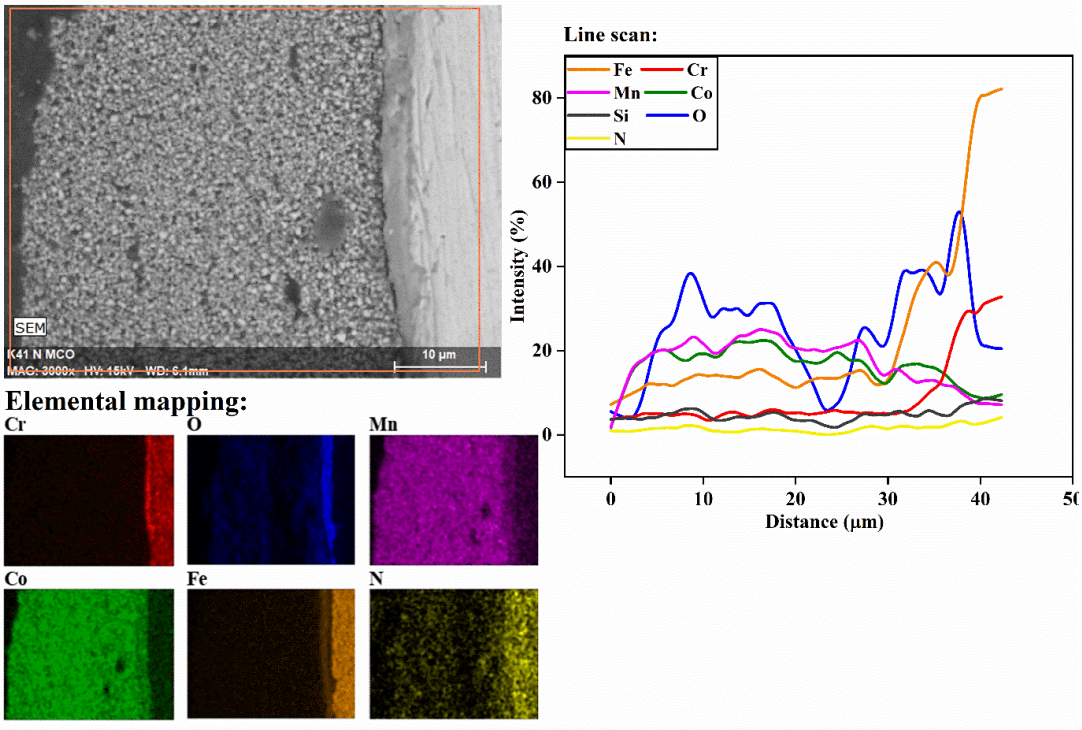


**Figure 5.16:** Cross-sectional analysis of surface nitrided K41with MCO coating after 1000 hours of oxidation. Elemental mapping and line scan analysis on the sample represents the concentration of elements across the stainless steel/coating layers.

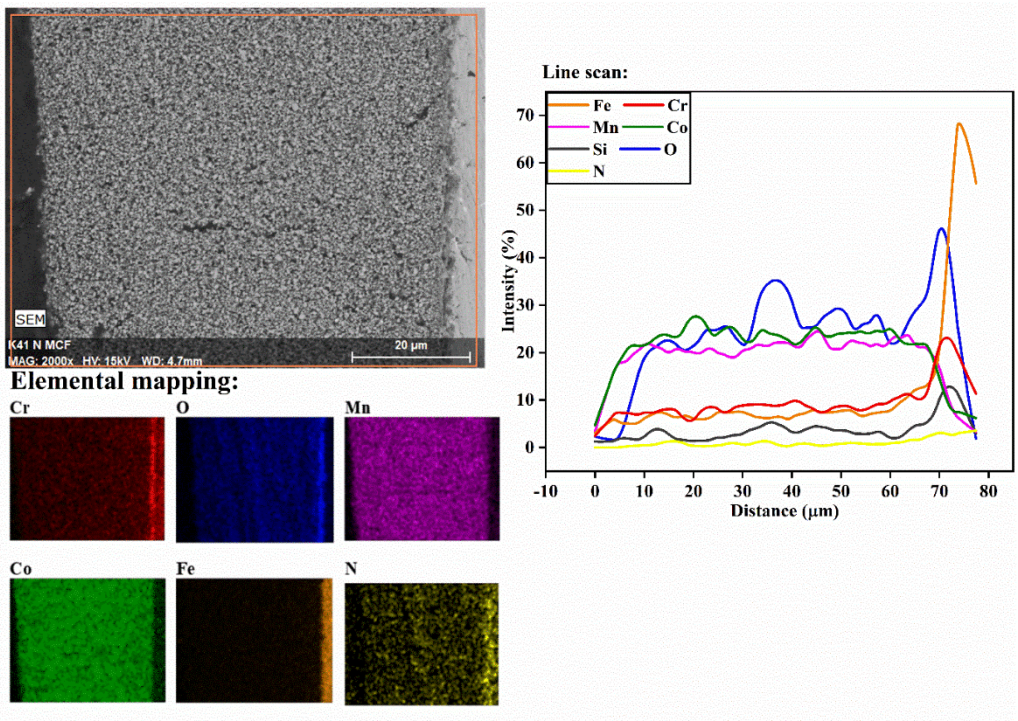


**Figure 5.17:** Cross-sectional analysis of surface nitrided K41 substrate with MCF coating post to 1000 hours of oxidation. Elemental mapping and line scan analysis on the sample representing the concentration of elements across the stainless steel/coating layers.

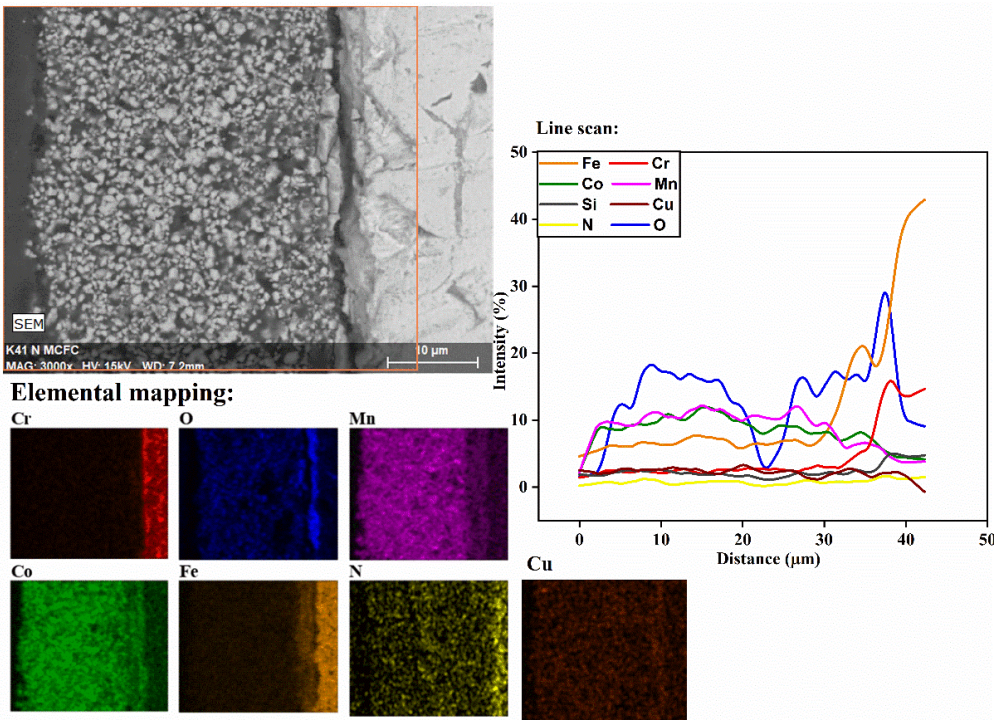


**Figure 5.18:** Cross-sectional analysis of surface nitrided K41 substrate with MCFC coating after 1000 hours of oxidation. Elemental mapping and line scan analysis on the sample represents the concentration of elements across the stainless steel/coating layer.

## 5.3.4. Discussion

Fig. 5.19 represents the amount of Cr detected at the surface and across the cross-section of the spinel coatings over virgin and nitrided substrates after the oxidation test. MCO coatings displayed high Cr content at the surface and across the coating layer after the oxidation test. Though the high Cr diffusion in the case of K41 virgin stainless steel substrate was due to the observed defects in the coating layer, MCO deposited over nitrided substrate exhibited Cr presence of more than 3 atomic% at the surface and across the coatings. MCF coatings on both the substrates displayed the least amount of Cr after the oxidation test. MCFC coatings over nitrided substrate displayed less Cr at the surface and across the layers, in contrast to the virgin substrate. The better performance in inhibition of Cr diffusion towards the surface was observed with MCF and MCFC coatings in comparison to the MCO coating. The outward migrating Cr from the alloy/oxide layer reacted with the spinel coatings, and the detection of Co, Mn, O, Fe and Cr on the coatings confirm the formation of an (Mn, Co, Fe, Cr)$_3$O$_4$ reaction layer next to the oxide layer [206] in all the coatings on both the substrates. The formation of an (Mn, Co, Fe Cr)$_3$O$_4$ reaction layer at the outer surface of the oxide layer is known to slow down the Cr diffusion [206]. The presence of Fe in MCF and MCFC overtakes Cr as the diffusion rate of Fe is faster than Cr, and forms the inhibiting spinel surface, as a consequence slowing down Cr diffusion. A similar effect of doping Fe and Cu in Mn-Co spinels has been reported [47,103,153,154,209,210] and hence the better performance of Cr inhibition of these coatings in comparison to the pure MCO coatings.

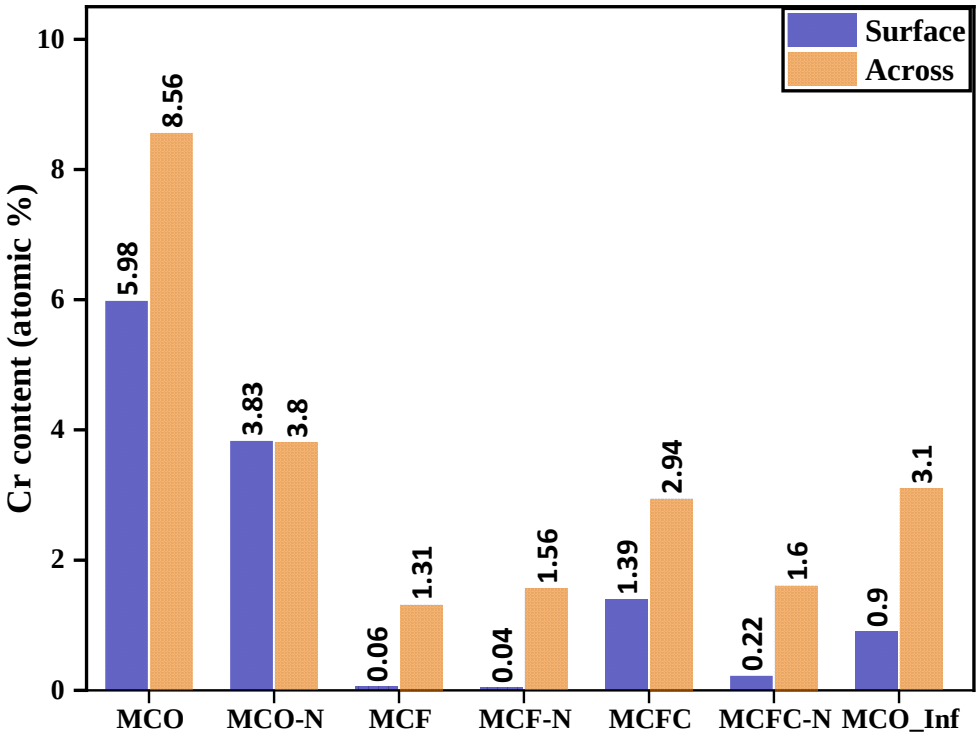


**Figure 5.19:** Comparison of Cr content at the surface and across the spinel coatings of K41 virgin and nitrided substrates after 1000 hours of the oxidation test at 700 °C.

The spinel coatings over the nitrided substrates showed drastically less Cr amount than their respective counterparts (virgin substrate). MCF and MCFC coatings displayed a Cr content less than 1 atomic % at the surface and around 1.5 atomic % across the coatings. A thicker oxide scale was expected based on the results from the uncoated (virgin and nitrided) substrate, but no difference in the oxide layer was seen on the coated nitrided substrates. Fig. 5.20 shows the presence of chromium nitride observed within the stainless steel after 1000 hours of oxidation in cross-sectional analysis. The better Cr inhibition displayed by the nitrided substrate could be due to the strong affinity of Cr to nitrogen present within the substrate. According to a study by Cao et al. [116], regarding the oxidation of nitrided austenitic stainless steels, the interaction between N and Cr decreases the activity of chromium thus inhibiting the diffusion of chromium towards the surface.

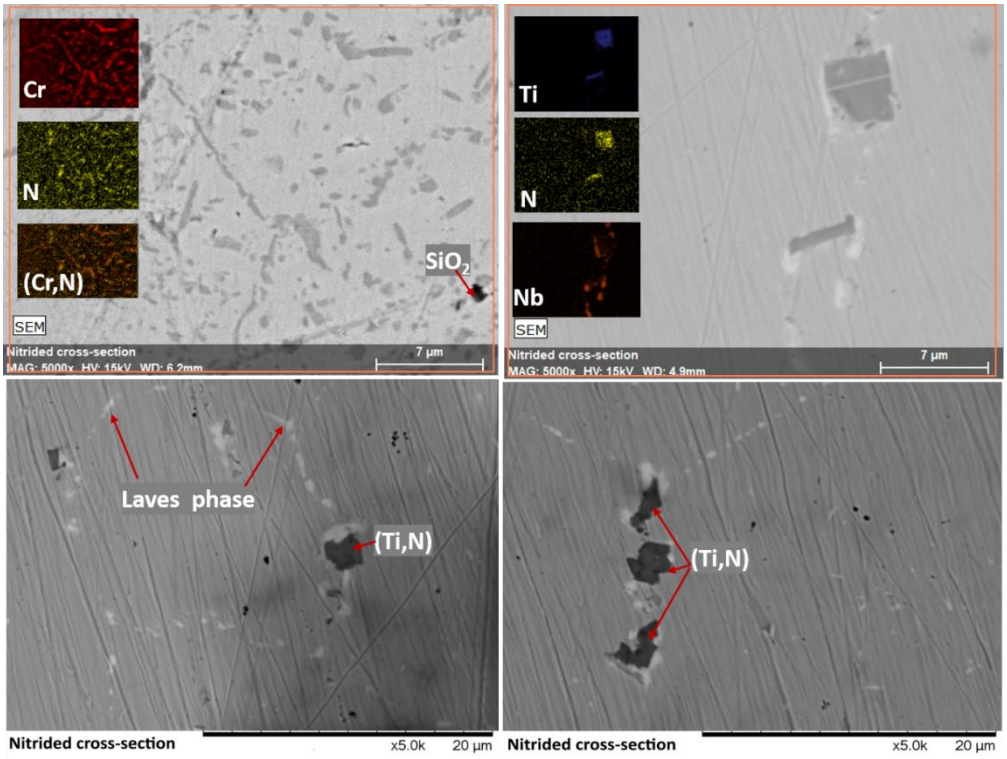


**Figure 5.20:** SEM images of nitrided stainless steel observed in a cross-sectional analysis showing the formation of CrN and precipitates of TiN. Formation of a Laves phase rich in Nb and $SiO_2$ was also seen.

The porous microstructure of the inkjet-printed coatings dominated their performance with respect to inhibition of Cr diffusion towards the surface from the substrate/coating interface. The porosity volume and pore sizes were estimated using Image J analysis (as described in Chapter 3, section 3.5.2). Table 5.6 lists the estimated pore volume and average pore size of the coatings after inkjet deposition, after heat treatment, and after 1000 hours of the oxidation test.

The estimated pore volume in surface SEM micrographs of MCO, MCF, and MCFC after deposition were 28.01, 27.80, and 32.10%, respectively. After the heat-treatment, a major decrease in the pore volume of 60 % was seen in MCFC coatings, followed by MCF and MCO coatings with a decrease of ~ 45 and 33% respectively. Based on the pore volume fraction, well-sintered coatings can be ordered as MCFC > MCF > MCO. Thus, during the initial hours

of the oxidation test, the coatings with higher pore volume and pore size must have favoured higher Cr diffusion, as the applied coatings remain porous at this stage. An increase in pore size and volume was observed after 1000 hours of oxidation test. The aqueous-based coatings tend to attain a minimal porosity after the initial heat treatment, which highly depends on annealing temperature, particle size of the starting material, and the coating process. The high-temperature exposure leads to further oxidation processes where cobalt ions move to the surface by solid-state diffusion and tend to react with the oxygen to form $Co_3O_4$, as can be seen in the XRD (Fig.5.15) and EDS analysis (Table 5.3). This diffusion process generates a counterflow of vacancies and accumulates as pores in the coating to facilitate the transfer of electrons necessary for the reaction to occur. A similar increase in pore size after oxidation in iron-doped Mn-Co based spinel coatings has been reported [211].

**Table 5.6:** Estimated average pore size and volume on the inkjet coated layers after deposition, heat-treatment, and 1000 hours of oxidation. The surface SEM micrographs (shown in Fig. 5.2, 5.8 and 5.14) were used for this analysis.

| Sample | Estimated pore size (µm) | | | Estimated pore volume in % (area fraction of pores) | | |
|---|---|---|---|---|---|---|
| | As coated | Heat-treated | After oxidation | As coated | Heat treated | After oxidation |
| **K41 MCO** | 0.087 | 0.089 | 0.134 | 28.01 | 18.60 | 21.62 |
| **K41 MCF** | 0.079 | 0.052 | 0.122 | 27.80 | 15.26 | 16.26 |
| **K41 MCFC** | 0.071 | 0.071 | 0.208 | 32.10 | 12.59 | 18.00 |

The performance of the MCO coating is dominated by the porous microstructure, whereas in MCF and MCFC coatings, the presence of dopants enhanced their performance in terms of Cr inhibition. In general, MCF coating performed better in Cr diffusion inhibition from the stainless steel/coating interface to the surface in both the substrates. A similar trend of

chromium diffusion (more than 1 atomic%) across the protective layer to the surface, applied through wet chemical methods, under the same testing conditions, was reported in [182].

## 5.4. Area Specific Resistance

Fig. 5.21 depicts the time-dependent evolution of ASR of spinel coatings inkjet printed on virgin K41 and onto nitrided substrate. The experiment planned for 1000 hours was disrupted towards the end, and the readings were finally reported after effectively 925 hours of exposure. The measured electrical resistance stems from the sum of palladium, stainless steel, protective coating, cathode layer (LSC), oxide layer and contact resistance between the cathode and the protective coating. The resistance from the bulk palladium and the stainless steel are negligible due to their high electrical conductivity. The resistance from the LSC layer at 700 °C was 0.25 mΩ $cm^2$ [183]. Thus, reported area-specific measurements values come from the contact resistance between the cathode, protective coating and the thermally grown oxide layer [183]. Goebel et al. [212] showed that measured ASR is contributed primarly from the chromium-containing oxides, and the influence from the protective coating is negligible.

The ASR values of all the samples, along with the average coating and oxide layer thickness, are listed in Table 5.7. The decrease in ASR within the initial time frame of ~200 hours can be attributed to the recrystallisation of electronically conductive Co-oxide in coating layers into spinel phases [16]. The nitrided substrate with MCFC coating and the infiltrated MCF coated sample exhibited an ASR of 0.055 and 0.062 Ω $cm^2$ after 925 hours. Also, the nitrided samples with MCO and MCFC coatings displayed a lower contact resistance value than their virgin counterparts.

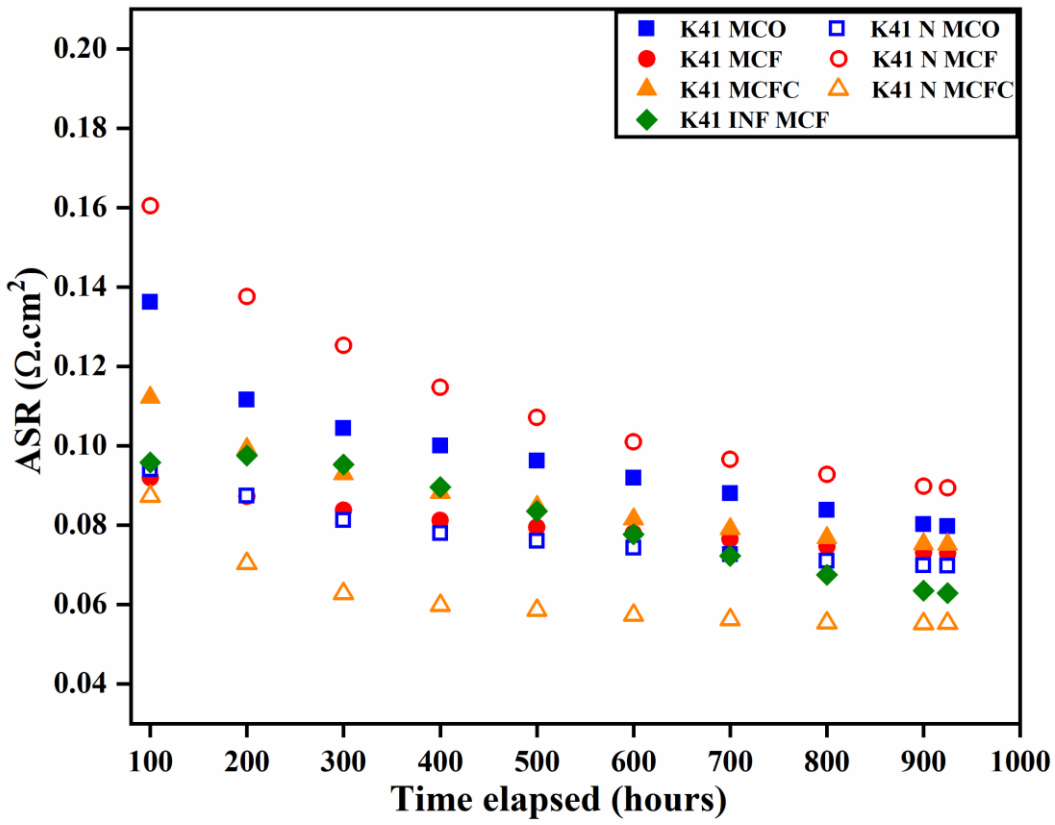


**Figure 5.21:** Evolution of ASR in inkjet-printed samples exposed at 700 °C for 925 hours.

**Table 5.7:** ASR values of the spinel coating after 925 hours of exposure at 700 °C with their respective average thickness of coating and oxide scale. The error values are the measure of standard deviation.

| Sample | Average coating thickness (µm) | Average oxide scale thickness (µm) | Measured ASR after 925 hours. ($\Omega.cm^2$) |
|---|---|---|---|
| **K41 MCO** | 44.42 ± 1.10 | 1.25 ±0.46 | 0.080 |
| **K41 MCF** | 43.68 ±1.17 | 1.25 ±0.14 | 0.073 |
| **K41 MCFC** | 30.98 ±1.10 | 1.55 ± 0.38 | 0.075 |
| **K41 N MCO** | 47.98 ± 0.78 | 2.8 ± 0.76 | 0.070 |
| **K41 N MCF** | 48.64 ± 1.21 | 4.5 ± 0.84 | 0.089 |
| **K41 N MCFC** | 30.28 ± 0.44 | 2.0 ± 0.42 | 0.055 |
| **K41 MCF INF** | 67.12 ± 1.30 | 1.8 ± 0.55 | 0.063 |

Figs. 5.22 to 5.27 show the cross-sections of the three spinel coatings along with their respective cathode layer over virgin and nitrided substrates. The formation of the thermally grown oxide scale at the stainless steel/coating interface is seen in all three coatings as a dense grayscale at the stainless steel/coating interface and is evident from the elemental mapping images shown. The formation of the dual-layer, oxide layer ($Cr_2O_3$) with outer spinel layer $(Mn, Co, Fe, Cr)_3O_4$, can be seen in the elemental mapping and line scan profiles. Nitrided samples had a thicker oxide layer formation than the un-modified substrates in line with the observation from the mass gain measurement of uncoated K41 substrates, where nitrided substrates had double the mass gain. The formation of Cr nitride precipitates similar to the nitrided samples in the oxidation test was observed over the surface of stainless steels as grey patches, clearly seen in the elemental mapping, Fig 5.27.

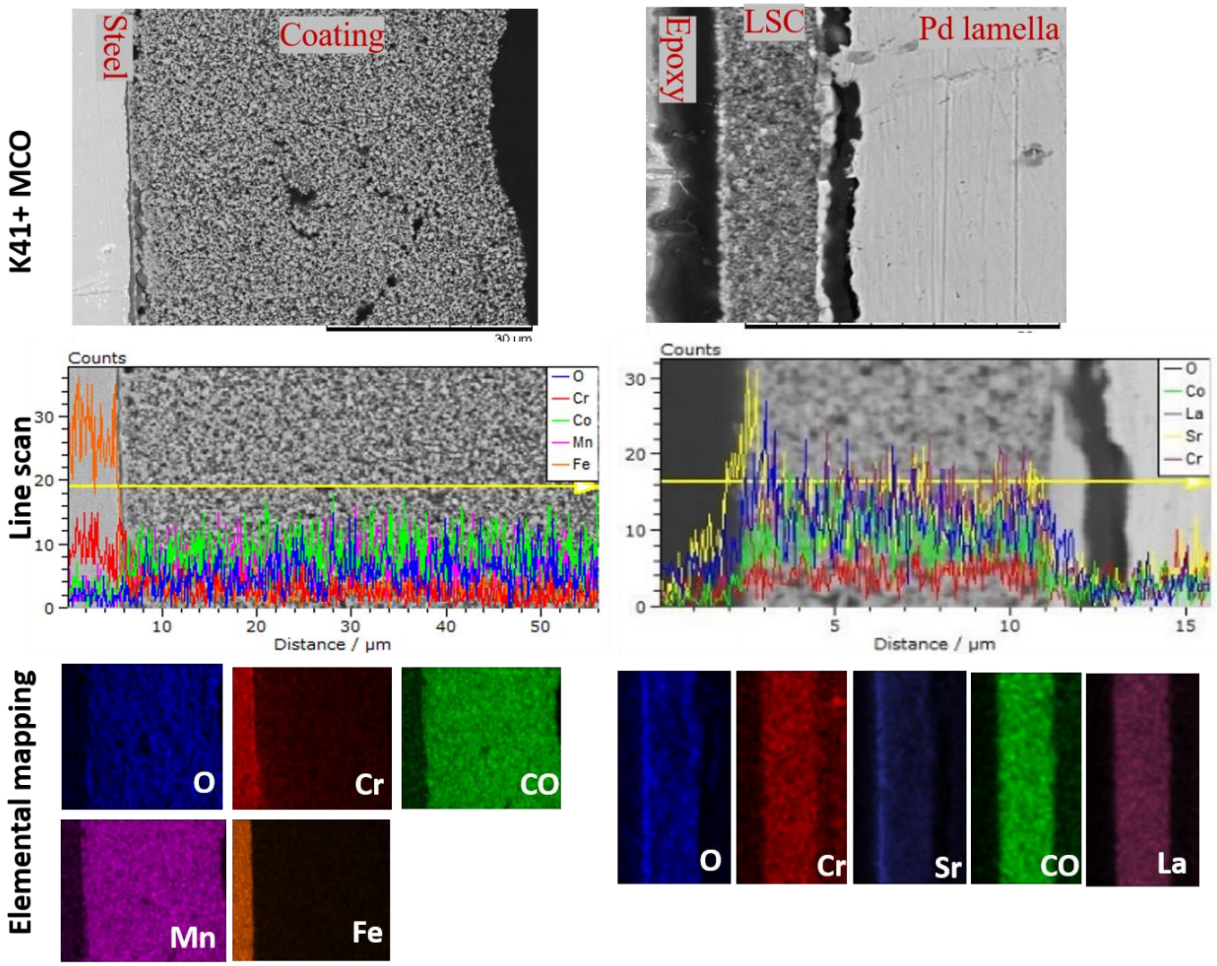


**Figure 5.22**: Cross-sectional analysis of K41 MCO after 1000 hours of ASR test. The elemental mapping and line scan of the respective protective layer and cathode layer are shown beneath the SEM images.

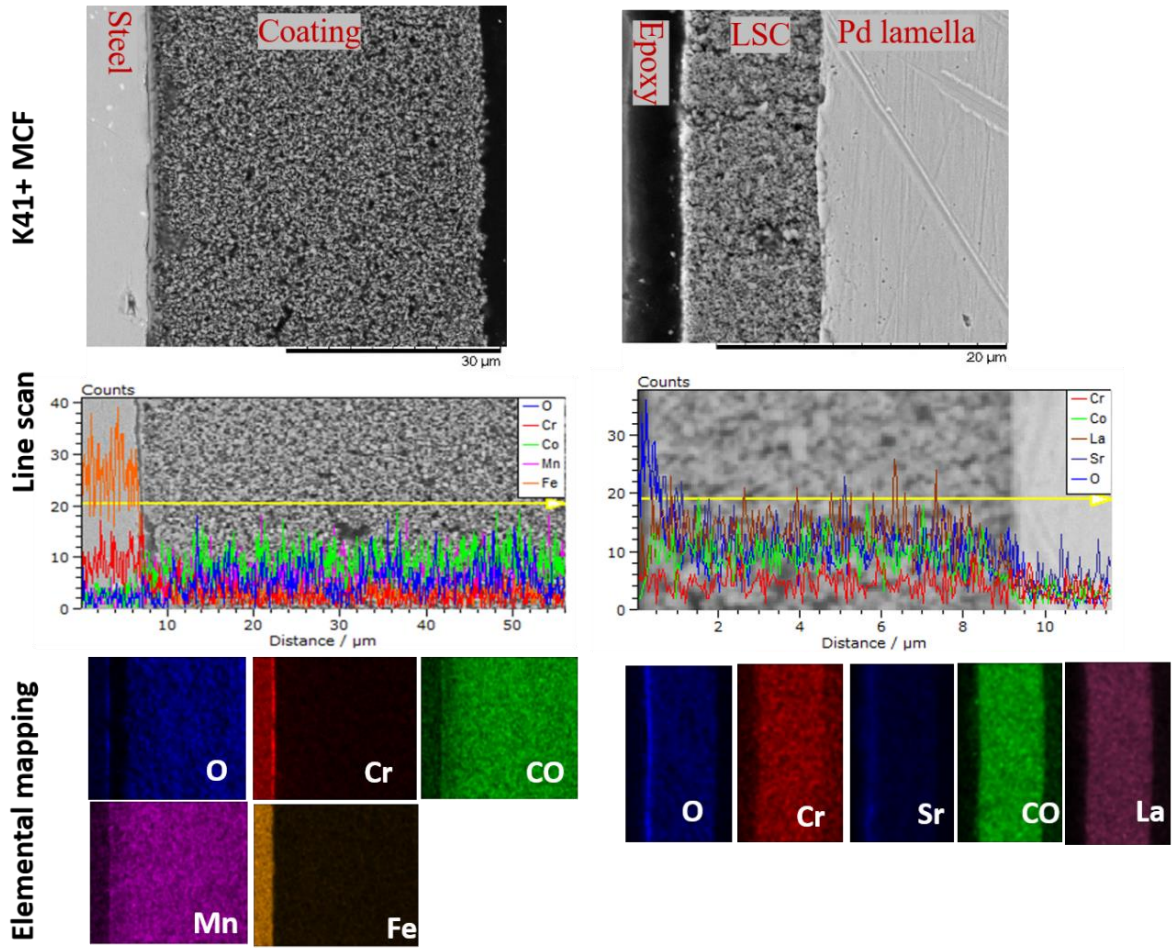


**Figure 5.23:** Cross-sectional analysis of K41 MCF after 1000 hours of ASR test. The elemental mapping and line scan of the respective protective layer and cathode layer are shown beneath the SEM images.

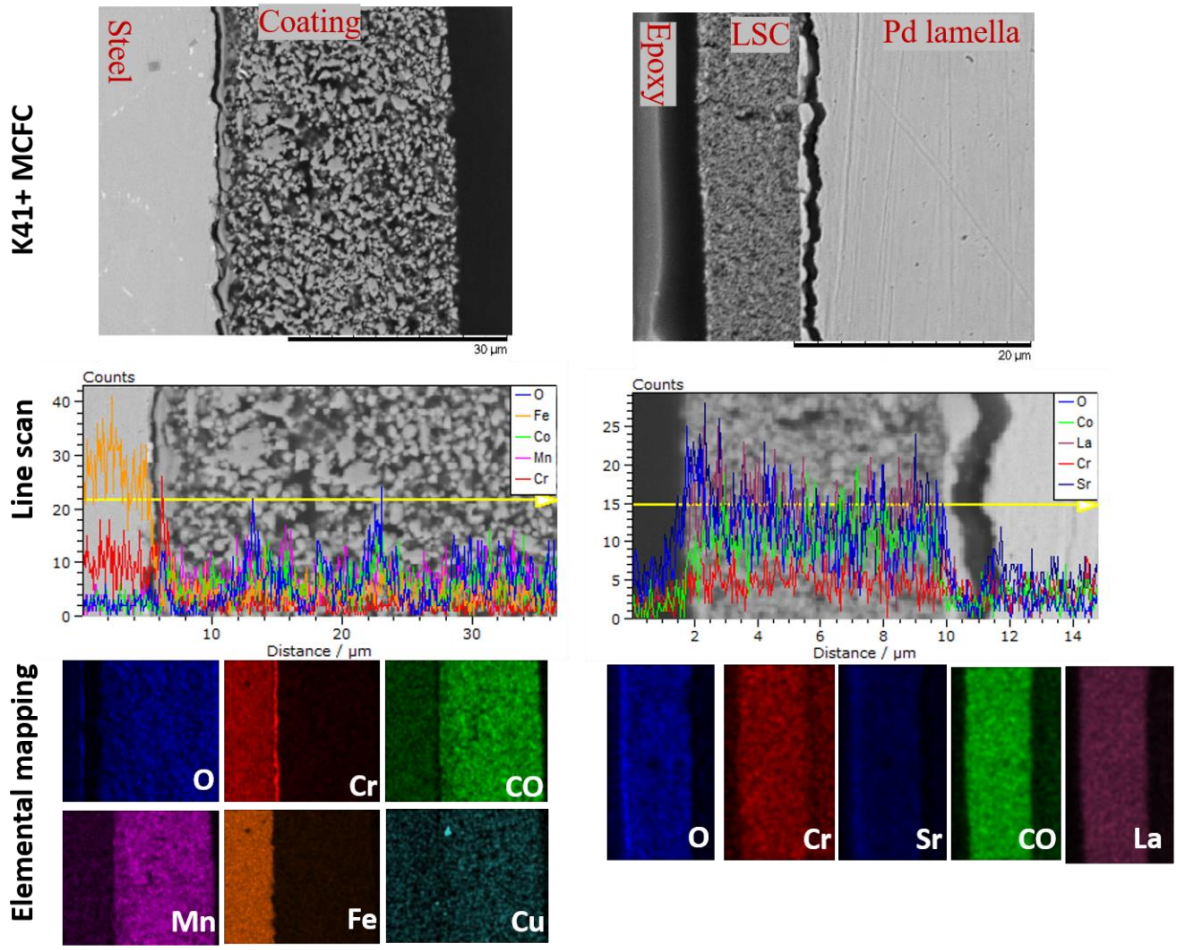


**Figure 5.24:** Cross-sectional analysis of K41 with MCFC coating after 1000 hours of ASR test. The elemental mapping and line scan of the respective protective layer and cathode layer are shown beneath the SEM images.

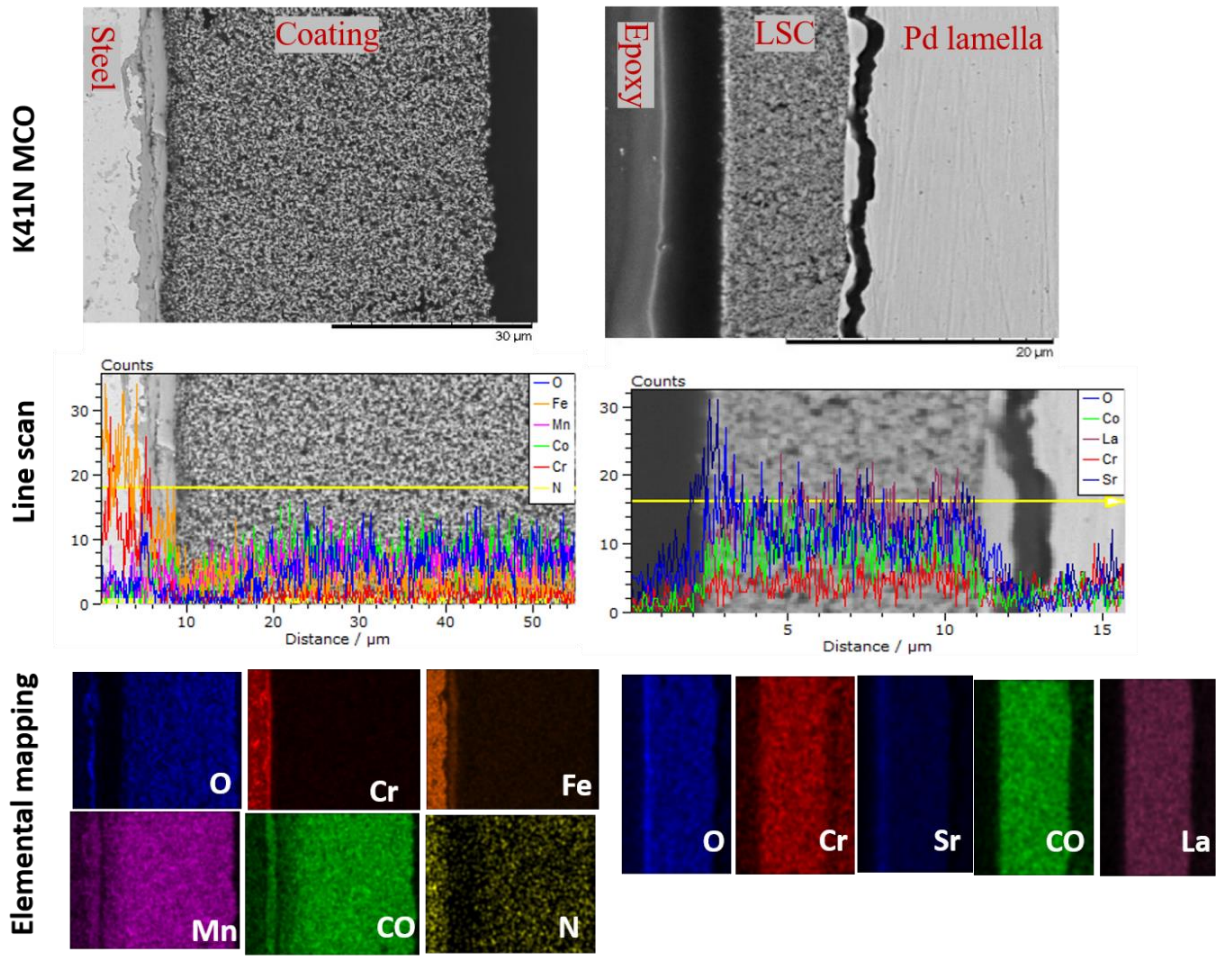


**Figure 5.25:** Cross-sectional analysis of surface nitrided K41 with MCO coating after 1000 hours of ASR test. The elemental mapping and line scan of the respective protective layer and cathode layer are shown beneath the SEM images.

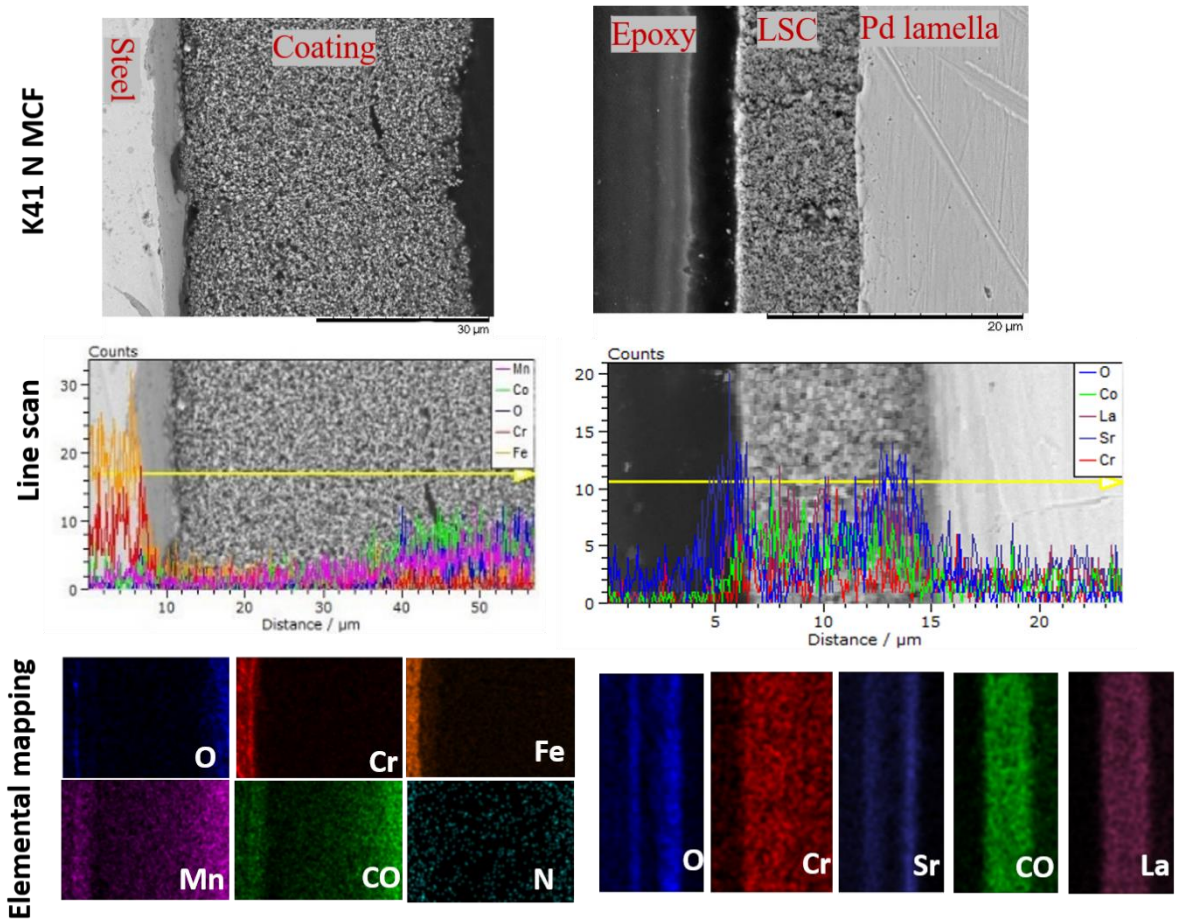


**Figure 5.26:** Cross-sectional analysis of surface nitrided K41 with MCF coating after 1000 hours of ASR test. The elemental mapping and line scan of the respective protective layer and cathode layer are shown beneath the SEM images.

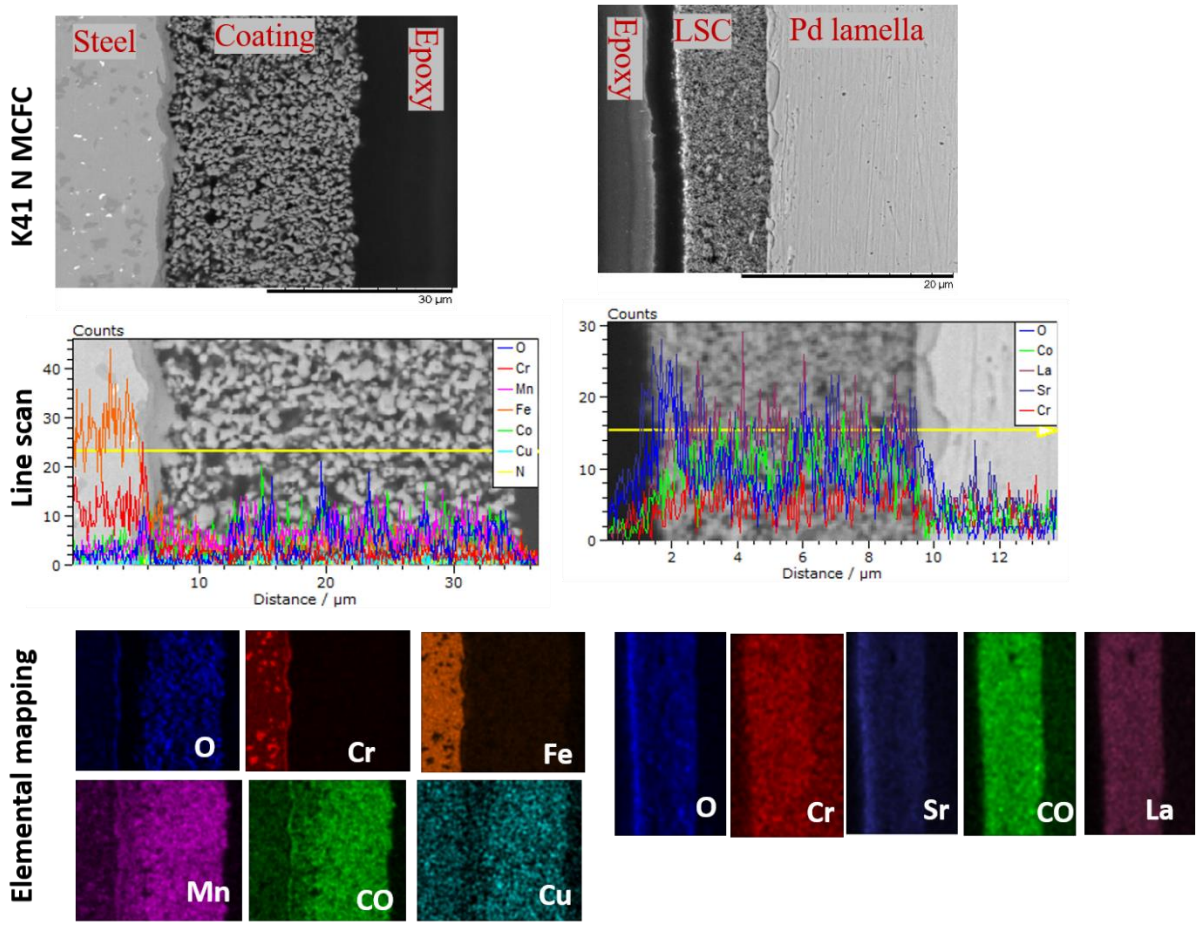


**Figure 5.27:** Cross-sectional analysis of surface nitrided K41 with MCFC coating after 1000 hours of ASR test. The elemental mapping and line scan of the respective protective layer and cathode layer are shown beneath the SEM images.

## 5.4.1. Discussion

As a summary, the ASR values did not significantly depend on the stainless steel substrates, and the effect of doping in the Mn-Co spinels on ASR was very less pronounced, at least at 700 °C. The nitrided substrates with MCFC and MCO showed the lowest ASR of 0.055 and 0.070 Ω $cm^2$, respectively. MCF coating on surface-nitrided substrates did not perform so well, due to the defects observed in the coating layer as seen in MCO coating in oxidation tests. The application of an additional, infiltrated surface layer on the K41 material with MCF protective coatings served to fill voids and inhomogeneities in the coating and was very effective in

inhibiting the chromium migration through the protective layer. These samples showed the least amount of chromium across the protective layer and in the cathode.

Migration of chromium across the protective layers was measured at three different spots with a spot size of 5 µm covering the whole layer; their average values are reported in Fig 5.28. The measurement was performed to observe the diffusion of Cr within the protective coatings. Line scan and EDS quantification displayed a trend of higher Cr content closer to the stainless steel-coating interface and reducing with the distance from the substrate in all the samples.

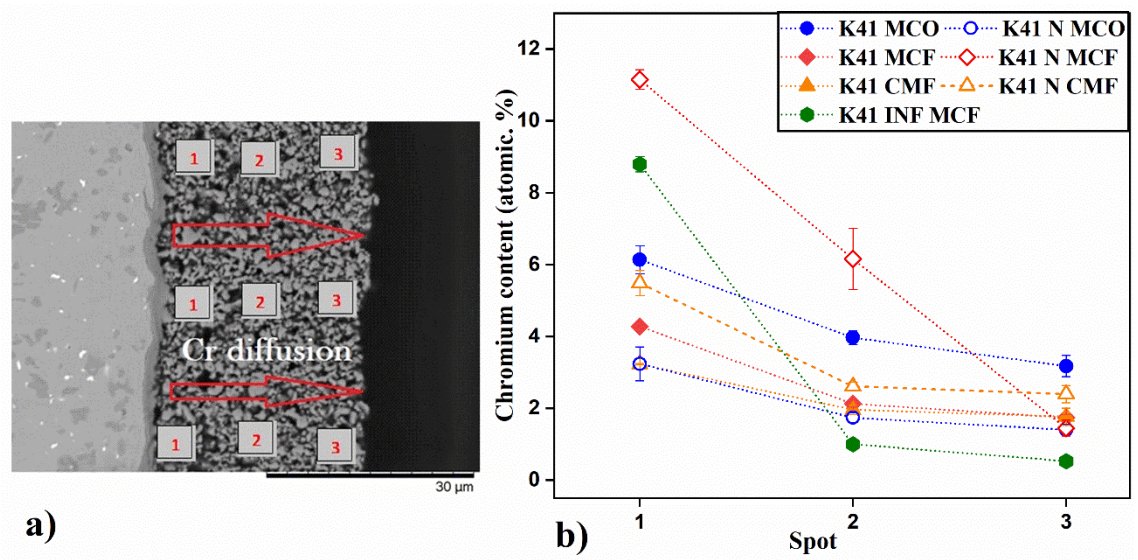


**Figure 5.28:** Plot representing the average distribution of Cr content, measured across the protective layer at three different spots, as shown in the micrograph for ASR tested samples.

A high concentration of manganese and cobalt was observed closer to the oxide layer, indicating the likely formation of an $(Mn, Co, Cr)_3O_4$ spinel layer formation at the oxide scale and coating interface. However, the porous microstructure of the deposited layers failed to stop the inward diffusion and outward progression of oxygen and chromium ions, respectively. The amount of Cr detected across each protective layer with their respective cathode layer is shown in Table 5.8. The Cr migrating from the protective layer reacted with the LSC cathode layer to

form $SrCrO_4$, a light grey oxide layer at the interface between protective and cathode layer. Similar observations on spray-coated samples have been reported in [182]. Tallgren et al. reported that $SrCrO_4$ might contribute to the increase in ASR due to its high resistivity (316.2 Ωm) at 700 °C [183]. Also, formation of $SrCrO_4$ at the cathode causes Sr depletion which can lead to higher polarisation resistance of the fuel cell [213].

**Table 5.8:** Amount of Cr detected across the protective layer and their respective cathode layer. The values reported are analysed from the micrographs shown in Fig.5.22 to 5.27.

| **Sample** | **Average Cr content (atomic. %)** | |
|---|---|---|
| | Protective layer | Cathode layer |
| **K41 MCO** | 4.4 ±0.35 | 1.7 ±0.02 |
| **K41 MCF** | 2.0 ±0.19 | 1.66 ±0.02 |
| **K41 MCFC** | 2.22 ±0.18 | 1.40 ±0.09 |
| **K41 N MCO** | 1.69 ±0.1 | 1.11 ±0.04 |
| **K41 N MCF** | 2.66 ± 1.8 | 0.65 ±0.15 |
| **K41 N MCFC** | 2.50 ±0.2 | 1.9 ±0.15 |
| **K41 Inf MCF** | 0.79 ±0.16 | 0.55 ±0.06 |

# IJP batch II

The $Cu_{1.3}Mn_{1.6}Fe_{0.1}O_4$ (CMF), samples were omitted due to the failure of coatings after the heat-treatment process. Fig. 5.29 (a) shows the image of CMF inks printed on K41 samples after the heat-treatment process. CMF inks were prepared with a similar composition, as mentioned in Chapter 4, section 4.3 (Table 4.4). The failure of coatings can be attributed to the lower solid content (~23 wt%), ~ 5-6% less solid content than MCO and MCF inks, which is further confirmed from the TGA analysis (Fig. 5.32 (b)). The starting particle of CMF (0.7067 µm) is higher than the MCO and MCF (~ 0.55 µm) which requires higher milling time or varying dispersant concentration or lack of binder content. To avoid inconsistency, CMF printed samples were omitted for further analysis.

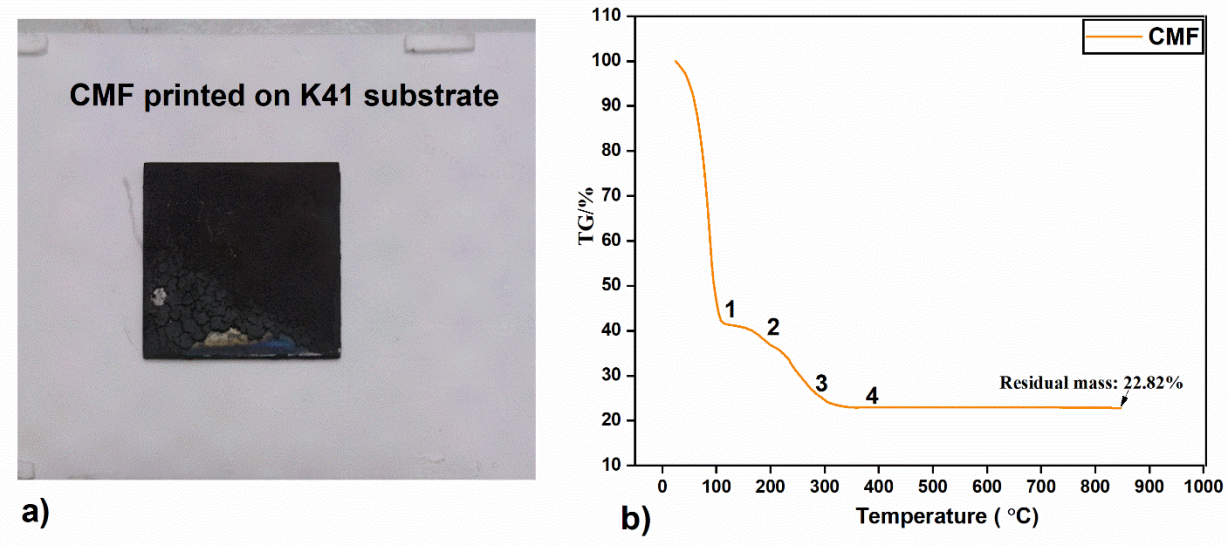


**Figure 5.29:** a) Image of failed CMF coating printed on K41 stainless steel substrate after the heat-treatment process. b) represents the TGA performed on CMF inks, markings 1, 2, 3, and 4 show the major loss events due to the removal of solvent, plasticiser, binder and other organics respectively. The lower solid loading combined with two-pass printing must have led to coating failure. Standared error calcualted for the obtained residual mass, ± 0.66.

## 5.5. Reactive sintering

The spinel inkjet inks were printed onto K41 substrate for the reactive sintering process. During the reactive sintering process, the spinel coatings were reduced to metallic Co and MnO phases during the reduction step and reformed into a single spinel cubic phase when re-oxidised. Fig. 5.30 shows the XRD data of reactive sintered samples confirming the reduction and reformation of the spinel phase during the reactive-sintering process. The identified peaks revealed that Mn-Co spinel coatings reduced to Co (ICSD: 42684) metallic phase and MnO (ICSD:9864) during the reduction step, and upon oxidation they recombined to form a single cubic spinel structure $MnCo_2O_4$ (ICSD: 201314). The MnO phase formed during the reduction step was of defective nature with internal voids and smaller lattice parameter than expected for the stoichiometry which favoured the diffusion of cobalt ions to the surface and reduction to the metallic form [214].

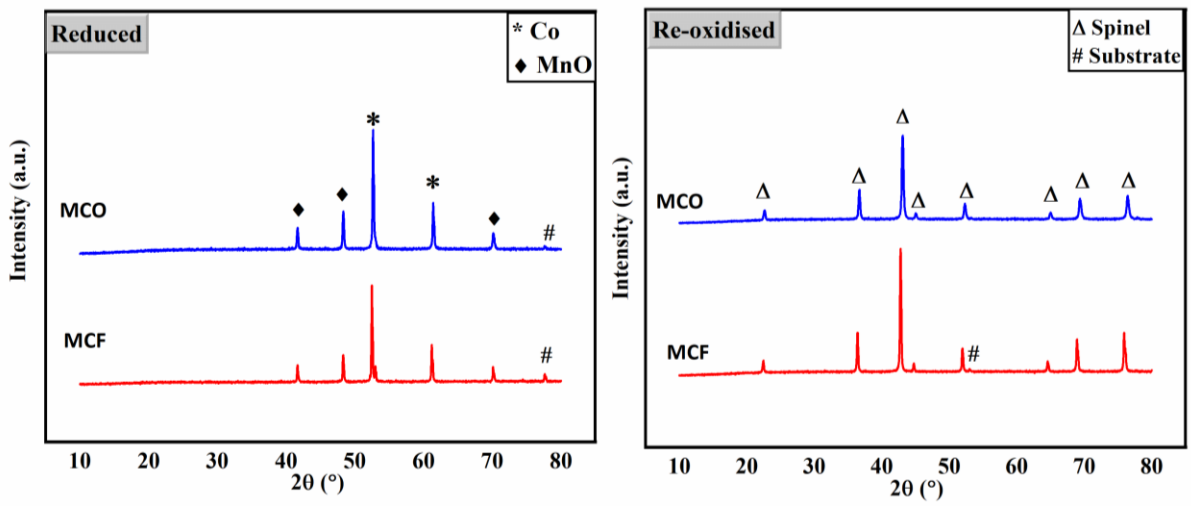


**Figure 5.30:** XRD patterns of three spinel coatings after subsequent reduction and re-oxidation steps.

Fig. 5.31 shows the SEM micrographs of the surface MCO and MCF coatings before and after the reactive sintering process. The elemental quantification at the surface before and after

reactive sintering is shown in Fig. 5.32. The amount of Cr detected at the surface after the reactive sintering step was less than 1 atomic %. Similar to Batch I samples, the MCF coating was more efficient in Cr inhibition, displaying only 0.10 atomic % of Cr, whereas MCO and MCFC layer revealed 0.60 and 0.52 atomic% at the surface post reactive sintering.

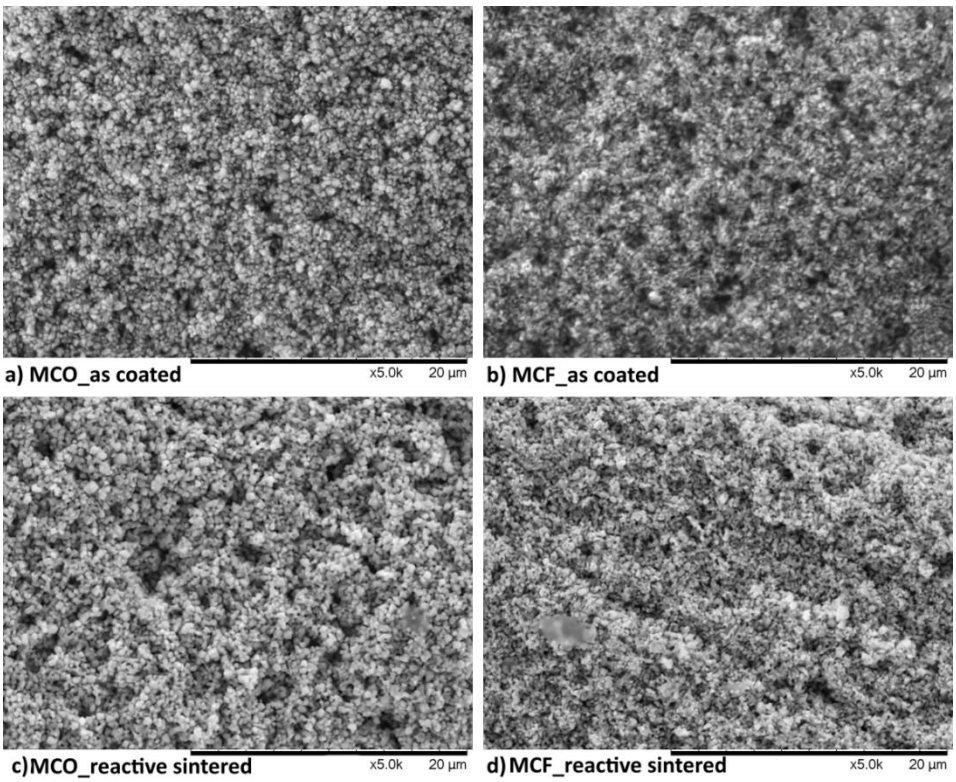


**Figure 5.31:** Surface SEM micrographs of Batch II spinel coatings after deposition (a and b) and after the reactive- sintering process (c and d).

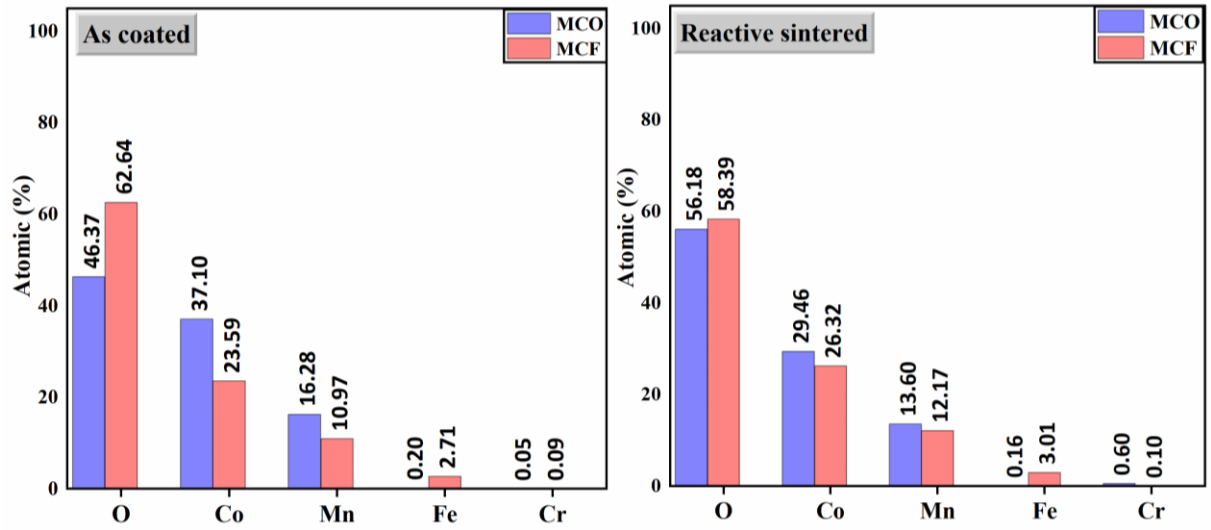


**Figure 5.32:** Elemental quantification of inkjet coated spinel layers before and after the reactive sintering process.

## 5.5.1. High-temperature oxidation

The reactive sintered samples were subjected to isothermal oxidation test at 700 °C for 1000 hours. The XRD analysis for the samples after the test is shown in Fig. 5.33. No significant phase change was observed, with all samples showing the cubic structure of $MnCo_2O_4$ (ICSD: 201314). Figs. 5.34 and 5.35 shows surface SEM images of the MCO and MCF coatings before and after 1000 hours of oxidation for inkjet-printed over K41 and Crofer 22H stainless steel substrates, respectively. The MCO coating after the oxidation test had a dense layer in comparison to the Batch I MCO coating and exhibited the prism-like crystal structure confirming the presence of spinel phase as seen in Fig. 5.8. MCF coating appeared to be realtively denser in comparision to the Batch I MCF coating, it exhibited closed pores as can be seen in the SEM micrograph, Fig 5.31(d). The surface of the MCF coating appeared to be rough and quite non-homogenous in both the substrates which could have arisen during the inkjet printing process. The elemental quantification of the spinel coatings after 1000 hours of exposure shown in Fig. 5.36 and 5.37, revealed less than 1 atomic % of Cr at the surface on both the substrates, indicating the better Cr inhibition than air sintered samples.

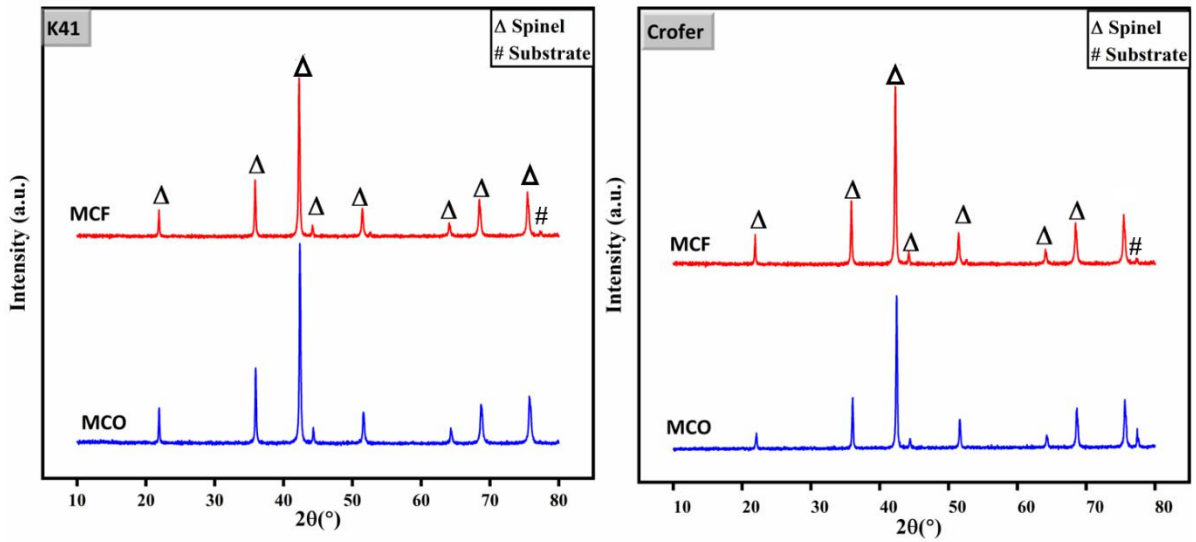


**Figure 5.33:** XRD pattern of spinel coatings deposited on K41 and Crofer stainless steel substrates after 1000 hours of the oxidation test.

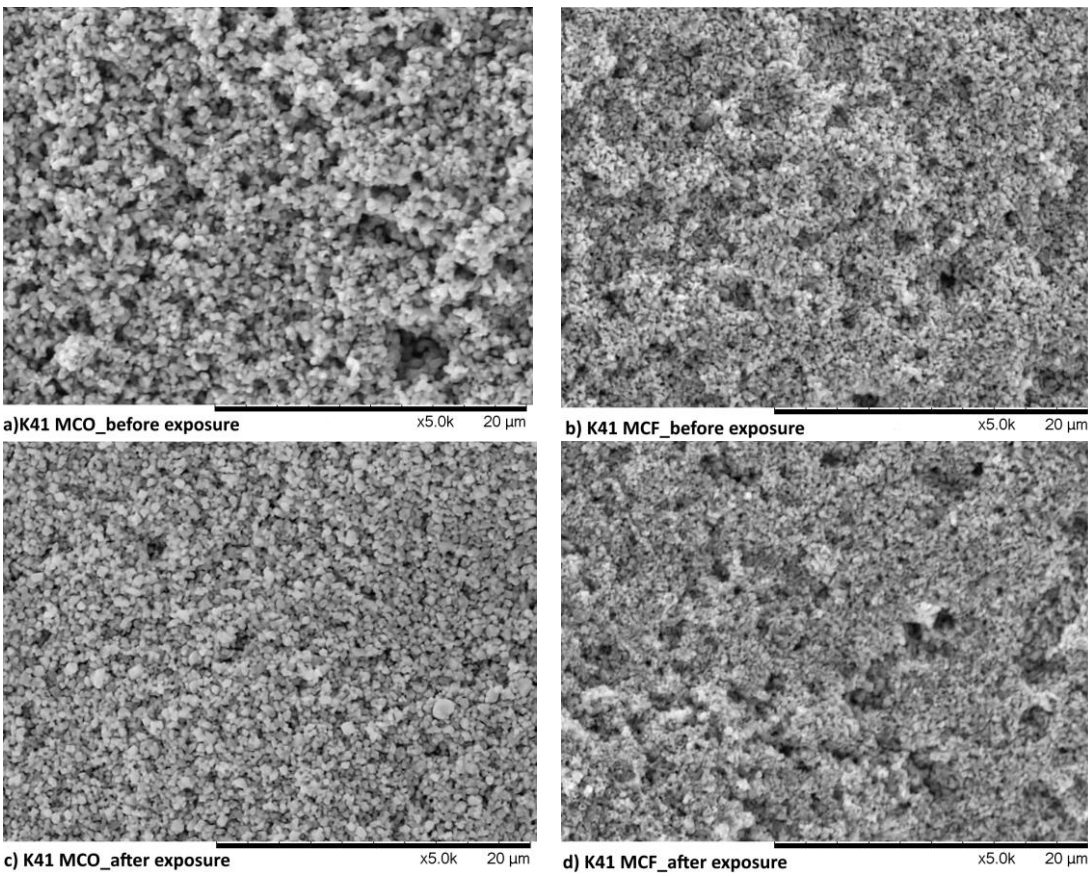


**Figure 5.34:** Surface SEM micrographs of MCO and MCF coatings on K41substrate before and after the oxidation test of 1000 hours exposure at 700 °C.

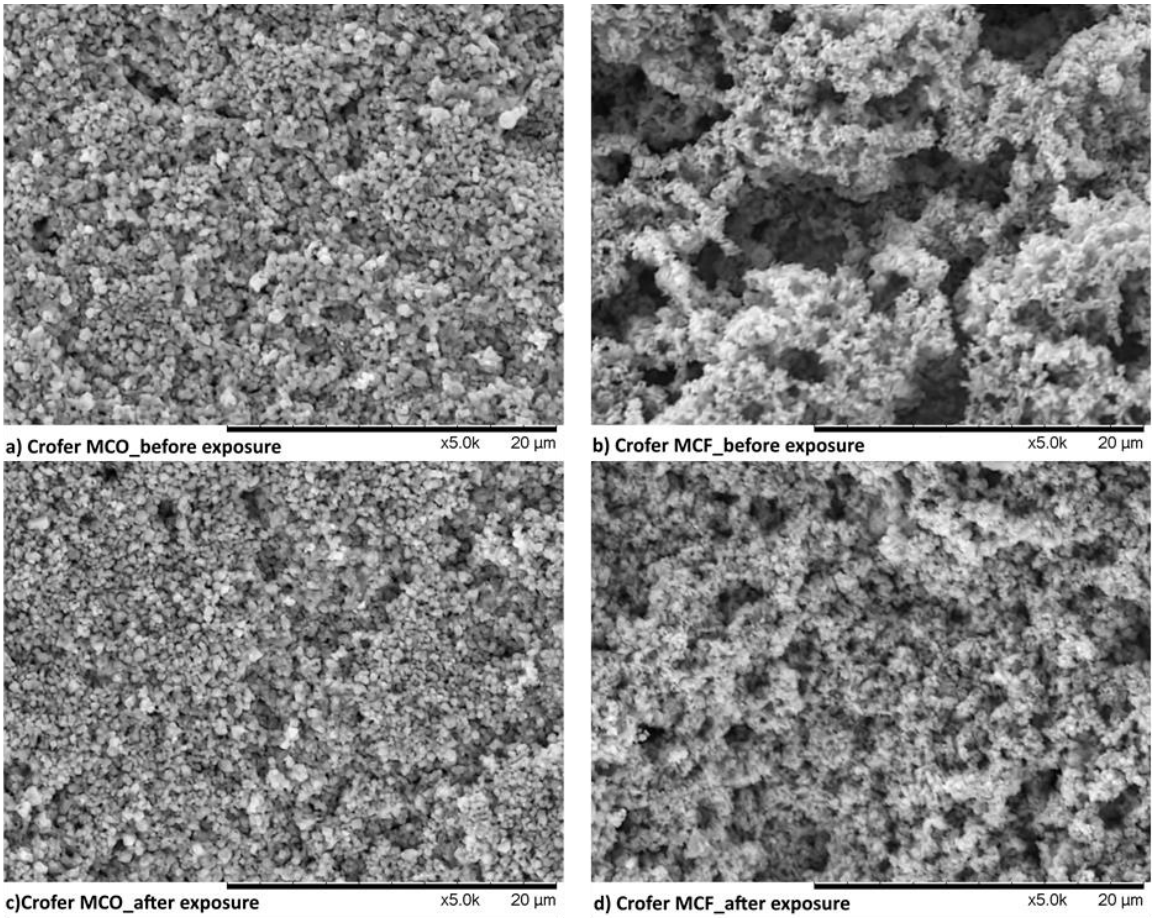


**Figure 5.35:** Surface SEM micrographs of MCO and MCF coatings on Crofer before and after the oxidation test of 1000 hours exposure at 700 °C.

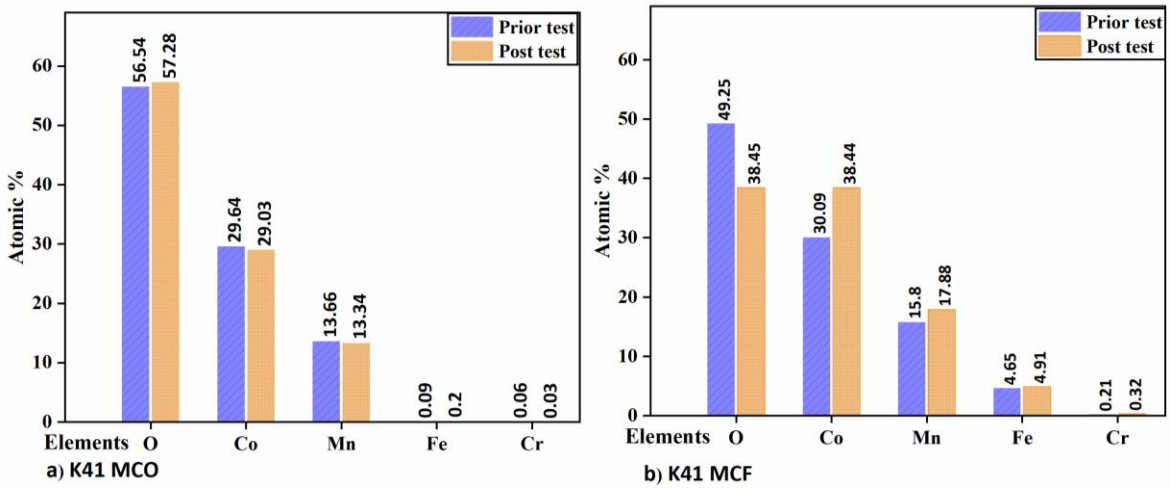


**Figure 5.36:** EDS quantification performed on surface SEM micrographs of coatings inkjet printed over K41 substrate before and after 1000 hours of the oxidation test.

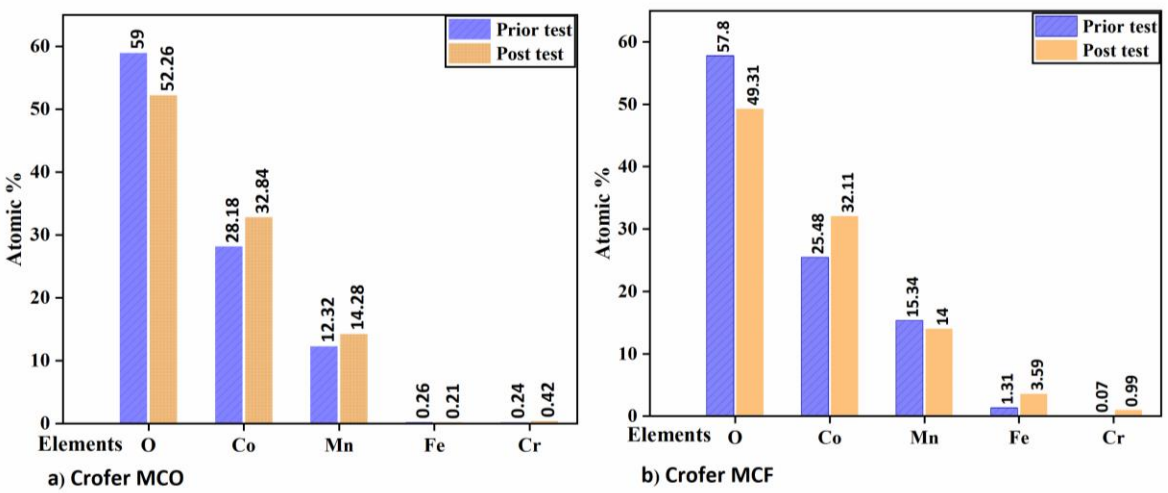


**Figure 5.37:** EDS quantification performed on surface SEM micrographs of coatings inkjet printed over Crofer substrate before and after 1000 hours of the oxidation test.

The cross-sectional analysis of the Batch II samples was attempted. Fig 5.38 (a) shows the K41 substrate with the MCO coating, after 1000 hours of oxidation. The coating was denser in comparison to the air sintered MCO coatings. Fig. 5.38 (b) shows the elemental mapping performed on the same micrograph. The micrograph showed less Cr presence in the coating layer, an EDS analysis performed on the coating layer revealed only 0.87 atomic % Cr across the coating.

The analysis was not able to be completed in other samples as the coating layer had epoxy coverage across the samples. Fig. 5.39 shows the micrograph of K41 substrate with MCF coating. The epoxy was seen over the coating and stayed on with further polishing. The epoxy presence could have arisen during polishing steps or any failure in the coatings. Based on the Cr content at the surface of the samples, failure of coatings can be ruled out. In the case of coating failure, high Cr must have been detected as observed in K41with MCO coating in Batch I. Thus, the observed epoxy presence can be due to the polishing steps.

However, based on the surface analysis, the reactive-sintered samples exhibited better microstructure and less Cr presence at the surface of the printed samples in comparison to the normal air sintered counterparts.

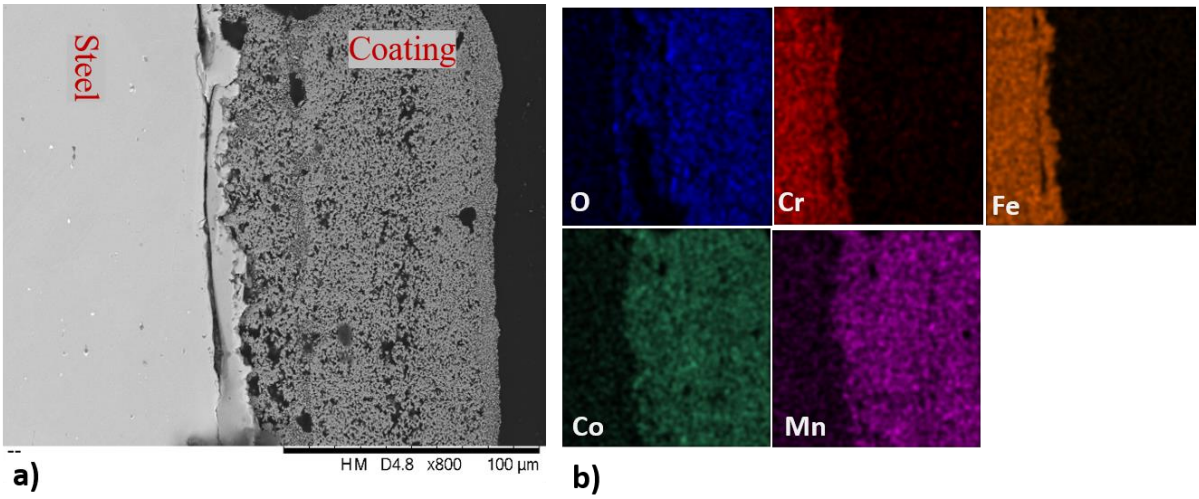


**Figure 5.38:** Cross-sectional micrograph of reactive sintered K41 MCO after 1000 hours of exposure test. Image (a) shows the denser coating observed across the sample, (b) shows the elemental mapping performed.

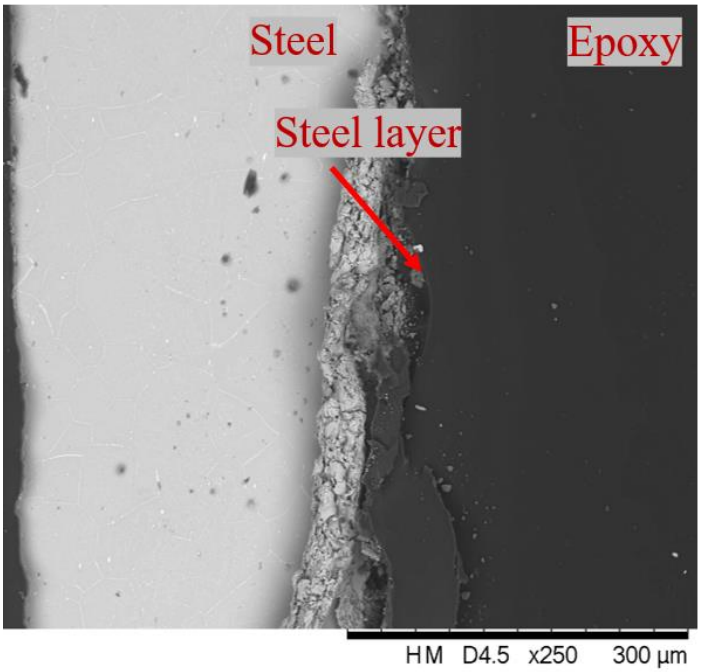


**Figure 5.39:** Cross-section of K41 substrate with MCF coating. The presence of epoxy on covering the coating can be seen.

Table 5.9 shows the estimated pore size and volume on reactive sintered MCO and MCF coating over K41 virgin substrates. The surface SEM micrographs are shown in Fig. 5.31 (a and b– as coated), ( c and d- reactive sintered) and Fig. 5.34 (c and d – after oxidation) were used for the analysis. K-clustered images of the selected SEM micrographs were shown in Appendix II. The coatings over K41 substrate was considered to keep consistent with the batch I samples. The area fraction of pore volume estimated after the reactive sintering step for MCO and MCF inks indicated ~ 45% decrease. The change in pore size observed post reactive sintering step had no major increase in pore size as seen in similar coatings from Batch I after 1000 hours of the oxidation test. Thus, it can be inferred that the reactive sintered coatings had denser microstructure after the heat-treatment step and must have limited the diffusion of elements to the surface of the coatings. However, the pore volume calculation was just an estimation to understand the nature of inkjet-printed layers. The accurate analysis of porosity requires characterisation techniques like Focused ion beam scanning electron microscopy.

**Table 5.9:** Estimated average pore size and volume on the Batch II inkjet coated layers after deposition, heat-treatment, and 1000 hours of oxidation.

| Sample | Estimated pore size (µm) | | | Estimated pore volume in % (area fraction of pores) | | |
|---|---|---|---|---|---|---|
| | As coated | Reactive sintered | After oxidation | As coated | Reactive sintered | After oxidation |
| **K41 MCO** | 0.041 | 0.045 | 0.038 | 24.80 | 13.64 | 14.19 |
| **K41 MCF** | 0.073 | 0.108 | 0.082 | 21.26 | 11.64 | 13.74 |

## 5.6. Summary

Aqueous based inks with spinel powders were formulated and successfully inkjet-printed on virgin (un-modified) and surface-modified (nitrided) K41 ferritic stainless-steel substrates. The applied protective layers displayed good adhesion, and no delamination was observed before and after high-temperature oxidation and ASR measurements performed over 1000 hours. High-temperature oxidation showed 1.2 atomic% migration of chromium from the stainless steel into the protective layers. In terms of coating materials, MCO coating displayed higher Cr diffusion in both oxidation and ASR measurements. The best performing coating layer based on Cr inhibition can be sequenced as MCF >MCFC> MCO.

In ASR measurements, the ASR reduced to a level around 0.05 Ω $cm^2$ and chromium concentration in the getter (cathode) material below 1 atomic%, close to the detection threshold. The protective layers produced would qualify for SOFC applications. The surface-modified K41 substrates by nitriding process showed better performance in Cr inhibition by forming Cr nitride precipitates during the high-temperature exposure. The effect of doping Mn-Co spinels with Fe and Cu was not pronounced in ASR values which could be due to the formation of $SrCrO_4$ at the cathode surface, as a result of interaction between the LSC and migrated Cr from the stainless steel/coating interface.

The nitrided stainless steel substrates with MCFC and MCO showed the lowest ASR of 0.055 and 0.069 Ω $cm^2$, respectively. The layers with MCF coating on surface-nitrided stainless steels did not perform so well; these experiments need further verification since the failure of these coatings may be due to the printing process. The application of an additional, infiltrated surface layer of MCF on the K41 material with protective coatings served to fill voids and inhomogeneities in the coating and was very effective in inhibiting the chromium migration

through the protective layer. These samples showed the least amount of chromium across the protective layer and in the cathode. The microstructural defects observed in some samples, e.g., K41 MCO and K41 N MCF could be prevented by applying the infiltrated surface layer. The performance of the printed spinel layers was dominated by their porous microstructure. Adapting reactive sintering procedure in batch II samples showed Cr presence of less than 1 atomic % (close to the detection limit). The reactive sintering procedure performed to obtain denser microstructure displayed promising results in terms of Cr inhibition to the surface after 1000 hours of oxidation, however, the cross-sectional analysis on the exposed samples was not able to complete due to the presence of epoxy across the coating after polishing steps.

The Inkjet deposition process applied to SOFC interconnect protective coatings has shown promising results. Since the printing process can be easily scaled to real 3D interconnect structures, this procedure promises substantial advantages in obtaining highly effective protective SOFC interconnect coatings at low costs.

# *Chapter 6: Conclusions and Future work*

This chapter highlights the development of spinel based suspension inks and presents the conclusions based on the performance of the inkjet printed spinel coatings. Also, it lists out the scope for future work.

The presented thesis was part of the project SCORED 2:0, which involved investigating different coating materials and coating processes for the application of a protective layer coating on ferritic stainless steel-based SOFC interconnects. In the present work, inkjet printing technology was employed for the protective layer application on metallic interconnects for the first time. The performance of the inkjet-printed coatings in SOFC cathode environment was assessed based on high-temperature oxidation and area-specific resistance tests. The main objective of the work was to develop aqueous-based spinel inkjet inks for a Drop-On-Demand mode inkjet printer and to evaluate the performance of inkjet-printed layers. The work also attempted to investigate the effect of a nitriding surface modification process on low cost K41 ferritic stainless steel. Furthermore, sol-gel infiltration was examined to develop a scaffold layer over the porous microstructure in order to minimise Cr migration.

## 6.1. Formulation and Printability of the spinel inkjet inks

- Formulation of suspension-based inks for inkjet printing is quite challenging due to the stability factor which marks them as more prone to nozzle clogging and an inefficient inkjet printing process. Spinel powders with sub-micron sized particles were used to formulate aqueous based suspension inks by adopting a systematic approach based on one-factor-a time optimisation.

- The optimisation of the ink components was carried out with respect to the inkjet printer requirements, i.e., maximum particle size, target viscosity and optimal surface tension. Ink suspension prepared by comminution process, a two-stage ball milling technique, enabled to study the effect of milling time and the effect of different dispersant dosage on suspended particles during the optimisation process. The printability of the

formulated suspension inks was assessed using dimensionless numbers, specifically the Re-We space parameter before the inkjet process.

- Aqueous based spinel inkjet inks were successfully formulated, and inkjet printed over the ferritic stainless steels using an electro-magnetic printer. It can be proposed that the adopted ink formulation route and optimisation steps employed can be used as a base to formulate suspension-based inks of any particle size with respect to the selected inkjet printer requirements.

- The spinel inks were applied over a three dimensional interconnect substrate to demonstrate the printability. The image of the printed 3D interconnect is shown below. Seepage of the ink into the valleys during printing was observed thus leaving ridges void, Fig. 6.1 (a and b). The substrate displayed good coverage with multiple pass printing, 5 pass prints, Fig.6.1 (c). To achieve uniform thickness could be a challenge but can be achieved by optimising ink properties and printing parameters.

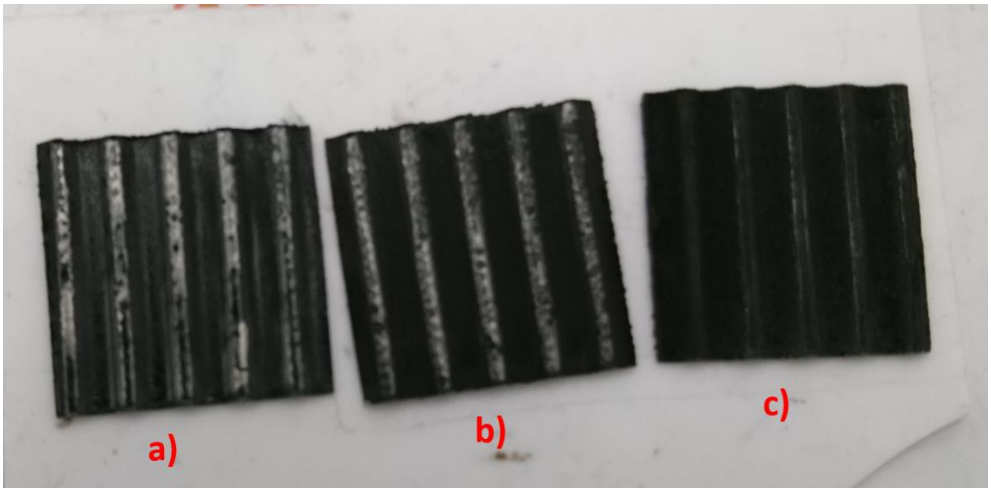


**Figure 6.1:** Images of 3D interconnect substrate with MCO coating. a) and b) represents the initial attempt of printing. c) shows the coverage of the substrate with multiple pass prints.

## 6.2. Evaluation of the inkjet coatings

- The formulated spinel inkjet inks were successfully inkjet printed onto un-modified (virgin) and surface-modified (nitrided) K41 ferritic stainless-steel substrates. The nitrided substrates displayed better performance in Cr diffusion inhibition from the substrate to the surface of the coatings. However, the effect of nitriding on ASR measurements was not pronounced at 700 °C.

- The applied protective layers displayed good adhesion, and no delamination was observed prior and post high-temperature tests of 1000 hours, except in MCO coating on K41 virgin substrate and MCF coating on surface nitrided K41 substrate from Batch I. The high-temperature oxidation test showed ~1 to 2 atomic% migration of chromium into the protective layer from the substrates.

- With the ASR reduced to a level around 0.05 Ω $cm^2$ at 700 °C and chromium concentration in the getter (cathode) material below one atomic%, (close to the detection threshold), the protective layers produced would qualify for SOFC applications.

- The application of an additional, infiltrated surface layer of MCO and MCF on the K41 material with protective coatings served to fill voids and inhomogeneities in the coating and was very effective in inhibiting the chromium migration through the protective layer. These samples showed the least amount of chromium across the protective layer and in the cathode. The observed performance of inkjet coatings in terms of ASR and Cr retention was on par with other wet chemical methods. Thus, it can be inferred that

the coating microstructure is a crucial parameter in Cr retention and low ASR, regardless of the stainless steel and coating composition when operating at 700°C.

- To improve the porous microstructure of the inkjet coatings, a two-step reactive sintering process was employed. The surface analysis of the reactive sintered coatings better performance in Cr inhibition, displaying less than 1 atomic %.

## 6.3. Future work

- The two-stage ball milling method allows to study the combination of different ink components in tandem, and thus different combinations of dispersant, binder and additives can be studied to obtain inks with higher solid loading and printable characteristics. An extensive study on drop formation and jettability based on ink components will provide insights for more controlled deposition.

- The reactive sintering approach showed better microstructure in the study. The best conditions for reactive sintering can be explored by trying a different combination of temperature and time for the heat-treatment process.

- Thus, with identification of optimal heat-treatment, spinel inks can be printed onto the 3D interconnects and evaluated.

- The inkjet coated samples can be further investigated by Cr evaporation test using the Denuder technique. The technique allows to evaluate the Cr migration and in tandem mass- gain measurements can be performed to identify the oxidation rate of the coated substrate.

# *Bibliography*


[1] A.B. Stambouli, Fuel cells: The expectations for an environmental-friendly and sustainable source of energy, Renew. Sustain. Energy Rev. 15 (2011) 4507–4520. doi:10.1016/J.RSER.2011.07.100.

[2] B.C. Steele, A. Heinzel, Materials for fuel-cell technologies., Nature. 414 (2001) 345–352. doi:10.1038/35104620.

[3] Hannah Ritchie and Max Roser, $CO_2$ and Greenhouse Gas Emissions. https://ourworldindata.org/co2-and-other-greenhouse-gas-emissions.

[4] A. Choudhury, H. Chandra, A. Arora, Application of solid oxide fuel cell technology for power generation—A review, Renew. Sustain. Energy Rev. 20 (2013) 430–442. doi:10.1016/J.RSER.2012.11.031.

[5] F.J.P. Abellan, W.J. Quadekkers, Development of Ferritic Steels for Application as Interconnect Materials for Intermediate Temperature Solid Oxide Fuel Cells (SOFCs), Forschungszentrum Jülich, 2005.

[6] Solid oxide fuel cells (SOFCs), University of Cambridge.

https://www.doitpoms.ac.uk/tlplib/fuel-cells/high_temp_sofc.php (accessed March 12, 2019).

[7] S. Badwal, Stability of solid oxide fuel cell components, Solid State Ionics. 143 (2001) 39–46. doi:10.1016/S0167-2738(01)00831-1.

[8] S. Elangovan, S. Balagopal, M. Timper, I. Bay, D. Larsen, J. Hartvigsen, Evaluation of Ferritic Stainless Steel for Use as Metal Interconnects for Solid Oxide Fuel Cells, J. Mater. Eng. Perform. 13 (2004) 265–273. doi:10.1361/10599490419153.

[9] W.Z. Zhu, S.C. Deevi, Development of interconnect materials for solid oxide fuel cells, Mater. Sci. Eng. A. 348 (2003) 227–243. doi:10.1016/S0921-5093(02)00736-0.

[10] K. Wang, Y. Liu, J.W. Fergus, Interactions between SOFC interconnect coating materials and chromia, J. Am. Ceram. Soc. 94 (2011) 4490–4495. doi:10.1111/j.1551-2916.2011.04749.x.

[11] W.-Z. Zhu, M. Yan, Perspectives on the metallic interconnects for solid oxide fuel cells., J. Zhejiang Univ. Sci. 5 (2004) 1471–503. doi:10.1631/jzus.2004.1471.

[12] M.C. Tucker, H. Kurokawa, C.P. Jacobson, L.C. De Jonghe, S.J. Visco, A fundamental study of chromium deposition on solid oxide fuel cell cathode materials, J. Power Sources. 160 (2006) 130–138. doi:10.1016/j.jpowsour.2006.02.017.

[13] N. Shaigan, W. Qu, D.G. Ivey, W. Chen, A review of recent progress in coatings, surface modifications and alloy developments for solid oxide fuel cell ferritic stainless steel interconnects, J. Power Sources. 195 (2010) 1529–1542. doi:10.1016/j.jpowsour.2009.09.069.

[14] J. Wu, X. Liu, Recent development of SOFC metallic interconnect, J. Mater. Sci. Technol. 26 (2010) 293–305. doi:10.1016/S1005-0302(10)60049-7.

[15] Z. Yang, G. Xia, C. Wang, Z. Nie, J. Templeton, J. Stevenson, P. Singh, Investigation of AISI 441 Ferritic Stainless Steel and Development of Spinel Coatings for SOFC Interconnect Applications, Top. Report, Pacific Northwest Natl. Lab. PNNL-17568. (2008).

[16] S. Molin, A.G. Sabato, M. Bindi, P. Leone, G. Cempura, M. Salvo, S. Cabanas Polo, A.R. Boccaccini, F. Smeacetto, Microstructural and electrical characterization of Mn-Co spinel protective coatings for solid oxide cell interconnects, J. Eur. Ceram. Soc. 37 (2017) 4781–4791. doi:10.1016/j.jeurceramsoc.2017.07.011.

[17] X. Liu, T.J. Tarn, F. Huang, J. Fan, Recent advances in inkjet printing synthesis of functional metal oxides, Particuology. 19 (2015) 1–13. doi:10.1016/j.partic.2014.05.001.

[18] R.I. Tomov, M. Krauz, J. Jewulski, S.C. Hopkins, J.R. Kluczowski, D.M. Glowacka, B.A. Glowacki, Direct ceramic inkjet printing of yttria-stabilized zirconia electrolyte layers for anode-supported solid oxide fuel cells, J. Power Sources. 195 (2010) 7160–7167. doi:10.1016/j.jpowsour.2010.05.044.

[19] C. Wang, S.C. Hopkins, R.I. Tomov, R.V. Kumar, B.A. Glowacki, Optimisation of CGO suspensions for inkjet-printed SOFC electrolytes, J. Eur. Ceram. Soc. 32 (2012) 2317–2324. doi:10.1016/J.JEURCERAMSOC.2012.03.001.

[20] V. Esposito, C. Gadea, J. Hjelm, D. Marani, Q. Hu, K. Agersted, S. Ramousse, S.H. Jensen, Fabrication of thin yttria-stabilized-zirconia dense electrolyte layers by inkjet printing for high performing solid oxide fuel cells, J. Power Sources. 273 (2015) 89–95. doi:10.1016/J.JPOWSOUR.2014.09.085.

[21] Y. Yan, R. Bateni, J. Harris, O. Kesler, Fabrication of reactive element oxide coatings on porous ferritic stainless steel for use in metal-supported solid oxide fuel cells, Surf. Coatings Technol. 272 (2015) 415–427. doi:10.1016/J.SURFCOAT.2015.03.041.

[22] N. Birks, G.H. Meier, F.S. Pettit, Introduction to the High-Temperature Oxidation of Metals, Cambridge University Press, Cambridge, 2006. doi:10.1017/CBO9781139163903.

[23] University of Cambridge, The Ellingham diagram. https://www.doitpoms.ac.uk/tlplib/ellingham_diagrams/ellingham.php (accessed January 20, 2019).

[24] P. Kofstad, R. Bredesen, High temperature corrosion in SOFC environments, Solid State Ionics. 52 (1992) 69–75. doi:10.1016/0167-2738(92)90092-4.

[25] P. Kofstad, Defects and Transport Properties of Metal Oxides, 44 (1995) 3–27.

[26] H.F. Windisch, Cr Vaporization and Oxide Scale Growth on Interconnects in Solid Oxide Fuel Cells, CHALMERS UNIVERSITY OF TECHNOLOGY, 2015.

[27] W.J. Tseng, K.-C. Lin, Rheology and colloidal structure of aqueous TiO2 nanoparticle suspensions, Mater. Sci. Eng. A. 355 (2003) 186–192. doi:10.1016/S0921-5093(03)00063-7.

[28] S.P. Jiang, X. Chen, Chromium deposition and poisoning of cathodes of solid oxide fuel cells – A review, Int. J. Hydrogen Energy. 39 (2014) 505–531. doi:10.1016/J.IJHYDENE.2013.10.042.

[29] H. Falk-Windisch, J.E. Svensson, J. Froitzheim, The effect of temperature on chromium vaporization and oxide scale growth on interconnect steels for Solid Oxide Fuel Cells, J. Power Sources. 287 (2015) 25–35. doi:10.1016/J.JPOWSOUR.2015.04.040.

[30] B.B. Ebbinghaus, Thermodynamics of gas phase chromium species: The chromium oxides, the chromium oxyhydroxides, and volatility calculations in waste incineration processes, Combust. Flame. 93 (1993) 119–137. doi:10.1016/0010-2180(93)90087-J.

[31] K. Hilpert, Chromium Vapor Species over Solid Oxide Fuel Cell Interconnect Materials and Their Potential for Degradation Processes, J. Electrochem. Soc. 143 (1996) 3642. doi:10.1149/1.1837264.

[32] C. Sun, R. Hui, J. Roller, Cathode materials for solid oxide fuel cells: A review, J. Solid State Electrochem. 14 (2010) 1125–1144. doi:10.1007/s10008-009-0932-0.

[33] C. Gindorf, L. Singheiser, K. Hilpert, Chromium vaporisation from Fe,Cr base alloys used as interconnect in fuel cells, Steel Res. 72 (2001) 528–533. doi:10.1002/srin.200100163.

[34] S.P. Jiang, J.P. Zhang, X.G. Zheng, A comparative investigation of chromium deposition at air electrodes of solid oxide fuel cells, J. Eur. Ceram. Soc. 22 (2002) 361–373. doi:10.1016/S0955-2219(01)00280-1.

[35] Z. Yang, K.S. Weil, D.M. Paxton, J.W. Stevenson, Selection and Evaluation of Heat-Resistant Alloys for SOFC Interconnect Applications, J. Electrochem. Soc. 150 (2003) A1188. doi:10.1149/1.1595659.

[36] W.Z. Zhu, S.C. Deevi, Opportunity of metallic interconnects for solid oxide fuel cells: A status on contact resistance, Mater. Res. Bull. 38 (2003) 957–972. doi:10.1016/S0025-5408(03)00076-X.

[37] K. Kendall, M. Kendall, L. Niewolak, F. Tietz, W.J. Quadakkers, Interconnects, Academic Press (second edition), 2016. doi:10.1016/B978-0-12-410453-2.00007-5.

[38] N. Mahato, A. Banerjee, A. Gupta, S. Omar, K. Balani, Progress in material selection for solid oxide fuel cell technology: A review, Prog. Mater. Sci. 72 (2015) 141–337. doi:10.1016/J.PMATSCI.2015.01.001.

[39] N. Linderoth, S., Hendriksen, P.V., Mogensen, M., & Langvad, Investigations of metallic alloys for use as interconnects in solid oxide fuel cell stacks, J. Mater. Sci. 31 (1996) 5077-5082.

[40] L. Jian, J. Huezo, D.G. Ivey, Carburisation of interconnect materials in solid oxide fuel cells, J. Power Sources. 123 (2003) 151–162. doi:10.1016/S0378-7753(03)00535-4.

[41] P.E. Gannon, V.I. Gorokhovsky, M.C. Deibert, R.J. Smith, A. Kayani, P.T. White, S. Sofie, Z. Yang, D. McCready, S. Visco, C. Jacobson, H. Kurokawa, Enabling inexpensive metallic alloys as SOFC interconnects: An investigation into hybrid coating technologies to deposit nanocomposite functional coatings on ferritic stainless steels, Int. J. Hydrogen Energy. 32 (2007) 3672–3681. doi:10.1016/J.IJHYDENE.2006.08.012.

[42] I. Antepara, I. Villarreal, L.M. Rodríguez-Martínez, N. Lecanda, U. Castro, A. Laresgoiti, Evaluation of ferritic steels for use as interconnects and porous metal supports in IT-SOFCs, J. Power Sources. 151 (2005) 103–107.

doi:10.1016/j.jpowsour.2005.02.084.

[43] P. Gannon, M. Deibert, P. White, R. Smith, H. Chen, W. Priyantha, J. Lucas, V. Gorokhovsky, Advanced PVD protective coatings for SOFC interconnects, Int. J. Hydrogen Energy. 33 (2008) 3991–4000. doi:10.1016/j.ijhydene.2007.12.009.

[44] J. Froitzheim, G.H. Meier, L. Niewolak, P.J. Ennis, H. Hattendorf, L. Singheiser, W.J. Quadakkers, Development of high strength ferritic steel for interconnect application in SOFCs, J. Power Sources. 178 (2008) 163–173. doi:10.1016/J.JPOWSOUR.2007.12.028.

[45] Z. Yang, P. Singh, J.W. Stevenson, G.-G. Xia, Investigation of Modified Ni–Cr–Mn Base Alloys for SOFC Interconnect Applications, J. Electrochem. Soc. 153 (2006) A1873. doi:10.1149/1.2239582.

[46] Z. Yang, J.S. Hardy, M.S. Walker, G. Xia, S.P. Simner, J.W. Stevenson, Structure and Conductivity of Thermally Grown Scales on Ferritic Fe-Cr-Mn Steel for SOFC Interconnect Applications, J. Electrochem. Soc. 151 (2004) A1825. doi:10.1149/1.1797031.

[47] M. Stanislowski, E. Wessel, K. Hilpert, T. Markus, L. Singheiser, Chromium Vaporization from High-Temperature Alloys, J. Electrochem. Soc. 154 (2007) A295. doi:10.1149/1.2434690.

[48] R. Sachitanand, M. Sattari, J.-E. Svensson, J. Froitzheim, Evaluation of the oxidation and Cr evaporation properties of selected FeCr alloys used as SOFC interconnects, Int. J. Hydrogen Energy. 38 (2013) 15328–15334. doi:10.1016/J.IJHYDENE.2013.09.044.

[49] H.S. Seo, D.W. Yun, K.Y. Kim, Effect of Ti addition on the electric and ionic property of the oxide scale formed on the ferritic stainless steel for SOFC interconnect, Int. J. Hydrogen Energy. 37 (2012) 16151–16160. doi:10.1016/j.ijhydene.2012.08.073.

[50] H.S. Seo, D.W. Yun, K.Y. Kim, Oxidation behavior of ferritic stainless steel containing Nb, Nb-Si and Nb-Ti for SOFC interconnect, Int. J. Hydrogen Energy. 38 (2013) 2432–2442. doi:10.1016/j.ijhydene.2012.12.073.

[51] T. Horita, K. Yamaji, Y. Xiong, H. Kishimoto, N. Sakai, H. Yokokawa, Oxide scale formation of Fe–Cr alloys and oxygen diffusion in the scale, Solid State Ionics. 175 (2004) 157–163. doi:10.1016/J.SSI.2004.09.045.

[52] K. Yamamoto, Y. Kimura, F.-G. Wei, Y. Mishima, Design of Laves phase strengthened ferritic heat resisting steels in the Fe–Cr–Nb(–Ni) system, Mater. Sci. Eng. A. 329–331 (2002) 249–254. doi:10.1016/S0921-5093(01)01586-6.

[53] N. Fujita, K. Ohmura, A. Yamamoto, Changes of microstructures and high temperature properties during high temperature service of Niobium added ferritic stainless steels, Mater. Sci. Eng. A. 351 (2003) 272–281. doi:10.1016/S0921-5093(02)00831-6.

[54] A. Holt, P. Kofstad, Electrical conductivity of Cr2O3 doped with TiO2, Solid State Ionics. 117 (1999) 21–25. doi:10.1016/S0167-2738(98)00244-6.

[55] A. Safikhani, M. Aminfard, Effect of W and Ti addition on oxidation behavior and area-specific resistance of Fe–22Cr–0.5Mn ferritic stainless steel for SOFCs interconnect, Int. J. Hydrogen Energy. 39 (2014) 2286–2296. doi:10.1016/J.IJHYDENE.2013.11.100.

[56] D.W. Yun, H.S. Seo, J.H. Jun, J.M. Lee, K.Y. Kim, Molybdenum effect on oxidation resistance and electric conduction of ferritic stainless steel for SOFC interconnect, Int. J. Hydrogen Energy. 37 (2012) 10328–10336. doi:10.1016/J.IJHYDENE.2012.04.013.

[57] T. Horita, H. Kishimoto, K. Yamaji, Y. Xiong, N. Sakai, M.E. Brito, H. Yokokawa, Evaluation of Laves-phase forming Fe–Cr alloy for SOFC interconnects in reducing atmosphere, J. Power Sources. 176 (2008) 54–61. doi:10.1016/j.jpowsour.2007.10.041.

[58] Z. Yang, G.-G. Xia, C.-M. Wang, Z. Nie, J. Templeton, J.W. Stevenson, P. Singh, Investigation of iron–chromium–niobium–titanium ferritic stainless steel for solid oxide fuel cell interconnect applications, J. Power Sources. 183 (2008) 660–667. doi:10.1016/j.jpowsour.2008.05.037.

[59] B. Kuhn, M. Talik, L. Niewolak, J. Zurek, H. Hattendorf, P.J. Ennis, W.J. Quadakkers, T. Beck, L. Singheiser, Development of high chromium ferritic steels strengthened by intermetallic phases, Mater. Sci. Eng. A. 594 (2014) 372–380. doi:10.1016/J.MSEA.2013.11.048.

[60] B. Kuhn, C.A. Jimenez, L. Niewolak, T. Hüttel, T. Beck, H. Hattendorf, L. Singheiser, W.J. Quadakkers, Effect of Laves phase strengthening on the mechanical properties of high Cr ferritic steels for solid oxide fuel cell interconnect application, Mater. Sci. Eng. A. 528 (2011) 5888–5899. doi:10.1016/J.MSEA.2011.03.112.

[61] P.D. Jablonski, J.S. Sears, The impact of alloy chemistry on the formation of a silicon-rich subscale on two classes of ferritic steels, J. Power Sources. 228 (2013) 141–150. doi:10.1016/J.JPOWSOUR.2012.11.107.

[62] Z.-W. Hsiao, B. Kuhn, D. Chen, L. Singheiser, J.-C. Kuo, D.-Y. Lin, Characterization of Laves phase in Crofer 22 H stainless steel, Micron. 74 (2015) 59–64. doi:10.1016/j.micron.2015.04.007.

[63] H.S. Seo, G. Jin, J.H. Jun, D.-H. Kim, K.Y. Kim, Effect of reactive elements on oxidation behaviour of Fe–22Cr–0.5Mn ferritic stainless steel for a solid oxide fuel cell interconnect, J. Power Sources. 178 (2008) 1–8. doi:10.1016/J.JPOWSOUR.2007.12.026.

[64] P.Y. Hou, J. Stringer, The effect of reactive element additions on the selective oxidation, growth and adhesion of chromia scales, Mater. Sci. Eng. A. 202 (1995) 1–10. doi:10.1016/0921-5093(95)09798-8.

[65] S. Chevalier, What did we learn on the reactive element effect in chromia scale since Pfeil ' s patent ?, Mater. Corros. (2014) 109–115. doi:10.1002/maco.201307310.

[66] K.H. Jo, J.H. Kim, K.M. Kim, I.-S. Lee, S.-J. Kim, Development of a new cost effective Fe–Cr ferritic stainless steel for SOFC interconnect, Int. J. Hydrogen Energy. 40 (2015) 9523–9529. doi:10.1016/J.IJHYDENE.2015.05.125.

[67] P. Alnegren, M. Sattari, J. Froitzheim, J.-E. Svensson, Degradation of ferritic stainless steels under conditions used for solid oxide fuel cells and electrolyzers at varying oxygen pressures, Corros. Sci. 110 (2016) 200–212. doi:10.1016/J.CORSCI.2016.04.030.

[68] A.W.B. Skilbred, R. Haugsrud, Sandvik Sanergy HT – A potential interconnect material for LaNbO4-based proton ceramic fuel cells, J. Power Sources. 206 (2012)

70–76. doi:10.1016/J.JPOWSOUR.2012.01.101.

[69] H. Falk-Windisch, J. Claquesin, M. Sattari, J.-E. Svensson, J. Froitzheim, Co- and Ce/Co-coated ferritic stainless steel as interconnect material for Intermediate Temperature Solid Oxide Fuel Cells, J. Power Sources. 343 (2017) 1–10. doi:10.1016/J.JPOWSOUR.2017.01.045.

[70] J.W. Stevenson, Z.G. Yang, G.G. Xia, Z. Nie, J.D. Templeton, Long-term oxidation behavior of spinel-coated ferritic stainless steel for solid oxide fuel cell interconnect applications, J. Power Sources. 231 (2013) 256–263. doi:10.1016/J.JPOWSOUR.2013.01.033.

[71] Z. Ranjbar-Nouri, M. Soltanieh, S. Rastegari, Applying the protective CuMn2O4 spinel coating on AISI-430 ferritic stainless steel used as solid oxide fuel cell interconnects, Surf. Coatings Technol. 334 (2018) 365–372. doi:10.1016/J.SURFCOAT.2017.11.036.

[72] S. Geng, Q. Zhao, Y. Li, J. Mu, G. Chen, F. Wang, S. Zhu, Sputtered MnCu metallic coating on ferritic stainless steel for solid oxide fuel cell interconnects application, Int. J. Hydrogen Energy. 42 (2017) 10298–10307. doi:10.1016/J.IJHYDENE.2017.01.178.

[73] M. Stanislowski, J. Froitzheim, L. Niewolak, W.J. Quadakkers, K. Hilpert, T. Markus, L. Singheiser, Reduction of chromium vaporization from SOFC interconnectors by highly effective coatings, J. Power Sources. 164 (2007) 578–589. doi:10.1016/J.JPOWSOUR.2006.08.013.

[74] R. Steinberger-Wilckens, L. Blum, H.P. Buchkremer, B. De Haart, J. Malzbender, M. Pap, Recent results in solid oxide fuel cell development at Forschungszentrum Juelich, in: ECS Trans., 2011: pp. 53–60. doi:10.1149/1.3569978.

[75] K. Huang, P.Y. Hou, J.B. Goodenough, Reduced area specific resistance for iron-based metallic interconnects by surface oxide coatings, Mater. Res. Bull. 36 (2001) 81–95. doi:10.1016/S0025-5408(01)00506-2.

[76] X. Chen, P.Y. Hou, C.P. Jacobson, S.J. Visco, L.C. De Jonghe, Protective coating on stainless steel interconnect for SOFCs: Oxidation kinetics and electrical properties, Solid State Ionics. 176 (2005) 425–433. doi:10.1016/j.ssi.2004.10.004.

[77] C. Collins, J. Lucas, T.L. Buchanan, M. Kopczyk, A. Kayani, P.E. Gannon, M.C. Deibert, R.J. Smith, D.-S. Choi, V.I. Gorokhovsky, Chromium volatility of coated and uncoated steel interconnects for SOFCs, Surf. Coatings Technol. 201 (2006) 4467–4470. doi:10.1016/J.SURFCOAT.2006.08.053.

[78] H. Kurokawa, C.P. Jacobson, L.C. DeJonghe, S.J. Visco, Chromium vaporization of bare and of coated iron–chromium alloys at 1073 K, Solid State Ionics. 178 (2007) 287–296. doi:10.1016/j.ssi.2006.12.010.

[79] W.N. Liu, X. Sun, E. Stephens, M.A. Khaleel, Life prediction of coated and uncoated metallic interconnect for solid oxide fuel cell applications, J. Power Sources. 189 (2009) 1044–1050. doi:10.1016/j.jpowsour.2008.12.143.

[80] M. Bianco, M. Linder, Y. Larring, F. Greco, J. Van herle, Lifetime Issues for Solid Oxide Fuel Cell Interconnects, in: Solid Oxide Fuel Cell Lifetime Reliab., Academic Press, 2017: pp. 121–144. doi:10.1016/B978-0-08-101102-7.00007-6.

[81] J.C.W. Mah, A. Muchtar, M.R. Somalu, M.J. Ghazali, Metallic interconnects for solid

oxide fuel cell: A review on protective coating and deposition techniques, Int. J. Hydrogen Energy. 42 (2017) 9219–9229. doi:10.1016/J.IJHYDENE.2016.03.195.

[82] S. Chevalier, G. Bonnet, G. Borchardt, J.C. Colson, J.P. Larpin, Mechanisms Involved by Reactive Elements upon High Temperature Chromia Scale Growth, Mater. Sci. Forum. 369–372 (2001) 327–336. doi:10.4028/www.scientific.net/MSF.369-372.327.

[83] P. Piccardo, P. Gannon, S. Chevalier, M. Viviani, A. Barbucci, G. Caboche, R. Amendola, S. Fontana, ASR evaluation of different kinds of coatings on a ferritic stainless steel as SOFC interconnects, Surf. Coatings Technol. 202 (2007) 1221–1225. doi:10.1016/J.SURFCOAT.2007.07.096.

[84] W. Qua, J. Lia, D.G. Iveyb, Sol–gel coatings to reduce oxide growth in interconnects used for solid oxide fuel cells, J. Power Sources. 138 (2004) 162–173. doi:10.1016/J.JPOWSOUR.2004.06.063.

[85] S. Fontana, R. Amendola, S. Chevalier, P. Piccardo, G. Caboche, M. Viviani, R. Molins, M. Sennour, Metallic interconnects for SOFC: Characterisation of corrosion resistance and conductivity evaluation at operating temperature of differently coated alloys, J. Power Sources. 171 (2007) 652–662. doi:10.1016/J.JPOWSOUR.2007.06.255.

[86] J.W. Fergus, Lanthanum chromite-based materials for solid oxide fuel cell interconnects, Solid State Ionics. 171 (2004) 1–15. doi:10.1016/j.ssi.2004.04.010.

[87] J.H. Zhu, Y. Zhang, A. Basu, Z.G. Lu, M. Paranthaman, D.F. Lee, E.A. Payzant, LaCrO3-based coatings on ferritic stainless steel for solid oxide fuel cell interconnect applications, Surf. Coatings Technol. 177–178 (2004) 65–72. doi:10.1016/J.SURFCOAT.2003.05.003.

[88] L. V Gambino, Evaluation of Solid Oxide Fuel Cell Interconnect Coatings: Mechanisms Behind Structure and Property Change During Reaction Layer Formation, University of Connecticut, 2015. doi:S0002-9440(10)60775-4 [pii]\r10.2353/ajpath.2009.080945.

[89] Y. Liu, D.Y. Chen, Protective coatings for Cr2O3-forming interconnects of solid oxide fuel cells, Int. J. Hydrogen Energy. 34 (2009) 9220–9226. doi:10.1016/j.ijhydene.2009.09.022.

[90] W. Qu, L. Jian, J.M. Hill, D.G. Ivey, Electrical and microstructural characterization of spinel phases as potential coatings for SOFC metallic interconnects, J. Power Sources. 153 (2006) 114–124. doi:10.1016/J.JPOWSOUR.2005.03.137.

[91] H. Zhang, J. Wu, X. Liu, A. Baker, Studies on elements diffusion of Mn/Co coated ferritic stainless steel for solid oxide fuel cell interconnects application, Int. J. Hydrogen Energy. 38 (2013) 5075–5083. doi:10.1016/J.IJHYDENE.2013.02.026.

[92] Y. Larring, T. Norby, Functional Layers Between Plansee Metallic Interconnect (Cr-5 wt% Fe-1 wt% Y 2 O 3) and Ceramic (La0. 85Sr0. 15) 0.91 MnO3 Cathode Materials for Solid Oxide, J. Electrochem. Soc. 147 (2000) 3251–3256. http://jes.ecsdl.org/content/147/9/3251.short.

[93] Z. Yang, G.G. Xia, X.H. Li, J.W. Stevenson, (Mn,Co)3O4 spinel coatings on ferritic stainless steels for SOFC interconnect applications, Int. J. Hydrogen Energy. 32 (2007) 3648–3654. doi:10.1016/j.ijhydene.2006.08.048.

[94] Spinel, Perovskite, and Rutile structures. https://chem.libretexts.org/Bookshelves/Inorganic_Chemistry/Book%3A_Introduction_to_Inorganic_Chemistry/08%3A_Ionic_and_Covalent_Solids__Structures/8.07%3A_Spinel%2C_Perovskite%2C_and_Rutile_Structures (accessed July 8, 2019).

[95] Z. Yang, G.-G. Xia, G.D. Maupin, J.W. Stevenson, Conductive protection layers on oxidation resistant alloys for SOFC interconnect applications, Surf. Coatings Technol. 201 (2006) 4476–4483. doi:10.1016/J.SURFCOAT.2006.08.082.

[96] A. Petric, H. Ling, Electrical Conductivity and Thermal Expansion of Spinels at Elevated Temperatures, J. Am. Ceram. Soc. 90 (2007) 1515–1520. doi:10.1111/j.1551-2916.2007.01522.x.

[97] Y. Xu, Z. Wen, S. Wang, T. Wen, Cu doped Mn-Co spinel protective coating on ferritic stainless steels for SOFC interconnect applications, Solid State Ionics. 192 (2011) 561–564. doi:10.1016/j.ssi.2010.05.052.

[98] R. Spotorno, P. Piccardo, F. Perrozzi, S. Valente, M. Viviani, A. Ansar, Microstructural and Electrical Characterization of Plasma Sprayed Cu-Mn Oxide Spinels as Coating on Metallic Interconnects for Stacking Solid Oxide Fuel Cells, Fuel Cells. 15 (2015) 728–734. doi:10.1002/fuce.201400189.

[99] W. Qu, L. Jian, J.M. Hill, D.G. Ivey, Electrical and microstructural characterization of spinel phases as potential coatings for SOFC metallic interconnects, J. Power Sources. 153 (2006) 114–124. doi:10.1016/j.jpowsour.2005.03.137.

[100] B. Talic, Metallic Interconnects for Solid Oxide Fuel Cells: High Temperature Corrosion and Protective Spinel Coatings, Norwegian University of Science and Technology, 2016. doi:10.1128/JVI.78.5.2187-2200.2004.

[101] B. Talic, P.V. Hendriksen, K. Wiik, H.L. Lein, Thermal expansion and electrical conductivity of Fe and Cu doped MnCo2O4 spinel, Solid State Ionics. 326 (2018) 90–99. doi:10.1016/J.SSI.2018.09.018.

[102] B. Talic, S. Molin, K. Wiik, P.V. Hendriksen, H.L. Lein, Comparison of iron and copper doped manganese cobalt spinel oxides as protective coatings for solid oxide fuel cell interconnects, J. Power Sources. 372 (2017) 145–156. doi:10.1016/J.JPOWSOUR.2017.10.060.

[103] T. Brylewski, A. Kruk, M. Bobruk, A. Adamczyk, J. Partyka, P. Rutkowski, Structure and electrical properties of Cu-doped Mn-Co-O spinel prepared via soft chemistry and its application in intermediate-temperature solid oxide fuel cell interconnects, J. Power Sources. 333 (2016) 145–155. doi:10.1016/J.JPOWSOUR.2016.09.136.

[104] A. Magrasó, H. Falk-Windisch, J. Froitzheim, J.-E. Svensson, R. Haugsrud, Reduced long term electrical resistance in Ce/Co-coated ferritic stainless steel for solid oxide fuel cell metallic interconnects, Int. J. Hydrogen Energy. 40 (2015) 8579–8585. doi:10.1016/J.IJHYDENE.2015.04.147.

[105] H.W. Nie, T.-L. Wen, H.Y. Tu, Protection coatings for planar solid oxide fuel cell interconnect prepared by plasma spraying, Mater. Res. Bull. 38 (2003) 1531–1536. doi:10.1016/S0025-5408(03)00166-1.

[106] D.P. Lim, D.S. Lim, J.S. Oh, I.W. Lyo, Influence of post-treatments on the contact resistance of plasma-sprayed La0.8Sr0.2MnO3 coating on SOFC metallic

interconnector, Surf. Coatings Technol. 200 (2005) 1248–1251. doi:10.1016/J.SURFCOAT.2005.08.131.

[107] J. Malzbender, P. Batfalsky, R. Vaßen, V. Shemet, F. Tietz, Component interactions after long-term operation of an SOFC stack with LSM cathode, J. Power Sources. 201 (2012) 196–203. doi:10.1016/j.jpowsour.2011.10.117.

[108] J. Puranen, M. Pihlatie, J. Lagerbom, G. Bolelli, J. Laakso, L. Hyvärinen, M. Kylmälahti, O. Himanen, J. Kiviaho, L. Lusvarghi, P. Vuoristo, Post-mortem evaluation of oxidized atmospheric plasma sprayed Mn–Co–Fe oxide spinel coatings on SOFC interconnectors, Int. J. Hydrogen Energy. 39 (2014) 17284–17294. doi:10.1016/j.ijhydene.2014.08.105.

[109] Y.-Z. Hu, S.-W. Yao, C.-X. Li, C.-J. Li, S.-L. Zhang, Influence of pre-reduction on microstructure homogeneity and electrical properties of APS Mn1.5Co1.5O4 coatings for SOFC interconnects, Int. J. Hydrogen Energy. 42 (2017) 27241–27253. doi:10.1016/J.IJHYDENE.2017.09.073.

[110] M.J. Garcia-Vargas, M. Zahid, F. Tietz, A. Aslanides, Use of SOFC metallic interconnect coated with spinel protective layers using the APS technology, in: ECS Trans., 2007: pp. 2399–2405. doi:10.1149/1.2729362.

[111] C. Ostwald, H.J. Grabke, Initial oxidation and chromium diffusion. I. Effects of surface working on 9-20% Cr steels, Corros. Sci. 46 (2004) 1113–1127. doi:10.1016/j.corsci.2003.09.004.

[112] L. Cooper, S. Benhaddad, A. Wood, D.G. Ivey, The effect of surface treatment on the oxidation of ferritic stainless steels used for solid oxide fuel cell interconnects, J. Power Sources. 184 (2008) 220–228. doi:10.1016/J.JPOWSOUR.2008.06.010.

[113] I. Belogolovsky, P.Y. Hou, C.P. Jacobson, S.J. Visco, Chromia scale adhesion on 430 stainless steel: Effect of different surface treatments, J. Power Sources. 182 (2008) 259–264. doi:10.1016/J.JPOWSOUR.2008.03.080.

[114] T. Bergamo, M. Technology, Effect of Nitridation on High Temperature Corrosion of Ferritic Stainless Steel, Chalmers University of Technology, 2013.

[115] H. Nii, A. Nishimoto, Surface modification of ferritic stainless steel by active screen plasma nitriding, J. Phys. Conf. Ser. 379 (2012). doi:10.1088/1742-6596/379/1/012052.

[116] Y. Cao, M. Norell, Role of nitrogen uptake during the oxidation of 304L and 904L austenitic stainless steels, Oxid. Met. 80 (2013) 479–491. doi:10.1007/s11085-013-9391-1.

[117] S. Leigh, M. Samandi, G.A. Collins, K.T. Short, P. Martin, L. Wielunski, The influence of ion energy on the nitriding behaviour of austenitic stainless steel, Surf. Coatings Technol. 85 (1996) 37–43. doi:10.1016/0257-8972(96)02876-9.

[118] A.M. Kliauga, M. Pohl, Effect of plasma nitriding on wear and pitting corrosion resistance of X2 CrNiMoN 22 5 3 duplex stainless steel, Surf. Coatings Technol. 98 (1998) 1205–1210. doi:10.1016/S0257-8972(97)00240-5.

[119] S.P. Hannula, P. Nenonen, J.P. Hirvonen, Surface structure and properties of ion-nitrided austenitic stainless steels, Thin Solid Films. 181 (1989) 343–350. doi:10.1016/0040-6090(89)90502-6.

[120] J.H. Sung, J.H. Kong, D.K. Yoo, H.Y. On, D.J. Lee, H.W. Lee, Phase changes of the AISI 430 ferritic stainless steels after high-temperature gas nitriding and tempering heat treatment, Mater. Sci. Eng. A. 489 (2008) 38–43. doi:10.1016/J.MSEA.2007.11.078.

[121] Lord Rayleigh, On the Instability of Jets, Writing. 1873 (1879).

[122] A. Soleimani-Gorgani, S. Thomas, A. Soleimani-Gorgani, Inkjet Printing, in: Print. Polym., Elsevier, 2016: pp. 231–246. doi:10.1016/B978-0-323-37468-2.00014-2.

[123] L. Lan, J. Zou, C. Jiang, B. Liu, L. Wang, J. Peng, Inkjet printing for electroluminescent devices: emissive materials, film formation, and display prototypes, Front. Optoelectron. 10 (2017) 329–352. doi:10.1007/s12200-017-0765-x.

[124] M.A. Sukeshini, R. Cummins, T.L. Reitz, R.M. Miller, Ink-jet printing: A versatile method for multilayer solid oxide fuel cells fabrication, J. Am. Ceram. Soc. 92 (2009) 2913–2919. doi:10.1111/j.1551-2916.2009.03349.x.

[125] J. Castrejon-Pita, W. Baxter, Future , Opportunities and Challenges of Inkjet Technologies, At. Sprays. (2013) 1–13. doi:10.1615/AtomizSpr.2013007653.

[126] E. Venezia, M. Viviani, S. Presto, V. Kumar, R.I. Tomov, Inkjet Printing Functionalization of SOFC LSCF Cathodes, Nanomaterials. 9 (2019) 654. doi:10.3390/nano9040654.

[127] B. Tawiah, E.K. Howard, B.K. Asinyo, The Chemistry of Inkjet Inks for Digital Textile Printing - Review, Int. J. Manag. Inf. Technol. Eng. 4 (2016) 61–78.

[128] A. Kosmala, R. Wright, Q. Zhang, P. Kirby, Synthesis of silver nano particles and fabrication of aqueous Ag inks for inkjet printing, Mater. Chem. Phys. 129 (2011) 1075–1080. doi:10.1016/j.matchemphys.2011.05.064.

[129] M. Romagnoli, M. Lassinantti Gualtieri, M. Cannio, F. Barbieri, R. Giovanardi, Preparation of an aqueous graphitic ink for thermal drop-on-demand inkjet printing, Mater. Chem. Phys. 182 (2016) 263–271. doi:10.1016/J.MATCHEMPHYS.2016.07.031.

[130] M. Özkan, K. Dimic-Misic, A. Karakoc, S.G. Hashmi, P. Lund, T. Maloney, J. Paltakari, Rheological characterization of liquid electrolytes for drop-on-demand inkjet printing, Org. Electron. 38 (2016) 307–315. doi:10.1016/J.ORGEL.2016.09.001.

[131] Z. Pan, Y. Wang, H. Huang, Z. Ling, Y. Dai, S. Ke, Recent development on preparation of ceramic inks in ink-jet printing, Ceram. Int. 41 (2015) 12515–12528. doi:10.1016/J.CERAMINT.2015.06.124.

[132] M. Mosiadz, R.I. Tomov, S.C. Hopkins, G. Martin, D. Hardeman, B. Holzapfel, B.A. Glowacki, Inkjet printing of Ce0.8Gd0.2O2 thin films on Ni-5%W flexible substrates, J. Sol-Gel Sci. Technol. 54 (2010) 154–164. doi:10.1007/s10971-010-2170-4.

[133] C. Wang, R.I. Tomov, R.V. Kumar, B.A. Glowacki, Inkjet printing of gadolinium-doped ceria electrolyte on NiO-YSZ substrates for solid oxide fuel cell applications, J. Mater. Sci. 46 (2011) 6889–6896. doi:10.1007/s10853-011-5653-y.

[134] S.H. Rahul, K. Balasubramanian, S. Venkatesh, Inkjet printing of yttria stabilized zirconia nano particles on metal substrates, Int. J. Precis. Eng. Manuf. 16 (2015) 2553–2561. doi:10.1007/s12541-015-0327-3.

[135] B. Derby, Inkjet Printing of Functional and Structural Materials: Fluid Property Requirements, Feature Stability, and Resolution, Annu. Rev. Mater. Res. 40 (2010) 395–414. doi:10.1146/annurev-matsci-070909-104502.

[136] J.E. Fromm, Numerical Calculation of the Fluid Dynamics of Drop-on-Demand Jets, IBM J. Res. Dev. 28 (1984) 322–333. doi:10.1147/rd.283.0322.

[137] B. Derby, Inkjet printing ceramics: From drops to solid, J. Eur. Ceram. Soc. 31 (2011) 2543–2550. doi:10.1016/j.jeurceramsoc.2011.01.016.

[138] B. Derby, N. Reis, Inkjet Printing of Highly Loaded Particulate Suspensions, MRS Bull. 28 (2003) 815–818. doi:10.1557/mrs2003.230.

[139] P.C. Duineveld, M.M. de Kok, M. Buechel, A. Sempel, K.A.H. Mutsaers, P. van de Weijer, I.G.J. Camps, T. van de Biggelaar, J.-E.J.M. Rubingh, E.I. Haskal, Ink-jet printing of polymer light-emitting devices, Org. Light. Mater. Devices V. 4464 (2003) 59. doi:10.1117/12.457460.

[140] R. Bhola, S. Chandra, Parameters controlling solidification of molten wax droplets falling on a solid surface, J. Mater. Sci. 4 (1999) 4883–4894.

[141] D. Young, A.M. Sukeshini, R. Cummins, H. Xiao, M. Rottmayer, T. Reitz, Ink-jet printing of electrolyte and anode functional layer for solid oxide fuel cells, J. Power Sources. 184 (2008) 191–196. doi:10.1016/J.JPOWSOUR.2008.06.018.

[142] G.D. Han, K.C. Neoh, K. Bae, H.J. Choi, S.W. Park, J.-W. Son, J.H. Shim, Fabrication of lanthanum strontium cobalt ferrite (LSCF) cathodes for high performance solid oxide fuel cells using a low price commercial inkjet printer, J. Power Sources. 306 (2016) 503–509. doi:10.1016/J.JPOWSOUR.2015.12.067.

[143] Z. Chen, J. Ouyang, W. Liang, Z. Yan, F. Stadler, C. Lao, Development and characterizations of novel aqueous-based LSCF suspensions for inkjet printing, Ceram. Int. 44 (2018) 13381–13388. doi:10.1016/J.CERAMINT.2018.04.174.

[144] R.I. Tomov, R. Duncan, M. Krauz, R. Vasant Kumar, B.A. Glowacki, Inkjet printing and inkjet infiltration of functional coatings for SOFCs fabrication, in: M. Filipowicz, M. Dudek, T. Olkuski, K. Styszko (Eds.), E3S Web Conf., 2016: p. 00098. doi:10.1051/e3sconf/20161000098.

[145] E. Özkol, J. Ebert, K. Uibel, A.M. Wätjen, R. Telle, Development of high solid content aqueous 3Y-TZP suspensions for direct inkjet printing using a thermal inkjet printer, J. Eur. Ceram. Soc. 29 (2009) 403–409. doi:10.1016/j.jeurceramsoc.2008.06.020.

[146] N. Yashiro, T. Usui, K. Kikuta, Application of a thin intermediate cathode layer prepared by inkjet printing for SOFCs, J. Eur. Ceram. Soc. 30 (2010) 2093–2098. doi:10.1016/J.JEURCERAMSOC.2010.04.012.

[147] N. Faino, W. Rosensteel, B. Gorman, N.P. Sullivan, Progress toward inkjet deposition of segmented-in-series solid-oxide fuel cell architectures, ECS Trans. 35 (2011) 593–600. doi:10.1149/1.3570037.

[148] R.I. Tomov, M. Krauz, A. Tluczek, R. Kluczowski, V. V. Krishnan, K. Balasubramanian, R. V. Kumar, B.A. Glowacki, Vacuum-sintered stainless steel porous supports for inkjet printing of functional SOFC coatings, Mater. Renew. Sustain. Energy. 4 (2015) 1–11. doi:10.1007/s40243-015-0056-7.

[149] C. Li, H. Chen, H. Shi, M.O. Tade, Z. Shao, Green fabrication of composite cathode with attractive performance for solid oxide fuel cells through facile inkjet printing, J. Power Sources. 273 (2015) 465–471. doi:10.1016/J.JPOWSOUR.2014.09.143.

[150] C.J. Dileep Kumar, Y. Liu, J. Ganley, W. Tilson, A. Dekich, J. Fergus, Transition Metal Doping of Manganese Cobalt Spinel Oxides for Coating SOFC Interconnects, Energy Technol. 2012 Carbon Dioxide Manag. Other Technol. 161 (2012) 305–311. doi:10.1002/9781118365038.ch37.

[151] Y. Liu, J.W. Fergus, K. Wang, C. Dela Cruz, Crystal Structure, Chemical Stabilities and Electrical Conductivity of Fe-Doped Manganese Cobalt Spinel Oxides for SOFC Interconnect Coatings, J. Electrochem. Soc. 160 (2013) F1316–F1321. doi:10.1149/2.114311jes.

[152] V. Miguel-Pérez, A. Martínez-Amesti, M.L. Nó, A. Larrañaga, M.I. Arriortua, The effect of doping (Mn,B)3O4 materials as protective layers in different metallic interconnects for Solid Oxide Fuel Cells, J. Power Sources. 243 (2013) 419–430. doi:10.1016/J.JPOWSOUR.2013.05.109.

[153] A. Masi, M. Bellusci, S.J. McPhail, F. Padella, P. Reale, J.E. Hong, R. Steinberger-Wilckens, M. Carlini, The effect of chemical composition on high temperature behaviour of Fe and Cu doped Mn-Co spinels, Ceram. Int. 43 (2017) 2829–2835. doi:10.1016/j.ceramint.2016.11.135.

[154] J.G. Grolig, P. Alnegren, J. Froitzheim, J.-E. Svensson, Copper Iron Conversion Coating for Solid Oxide Fuel Cell Interconnects, J. Power Sources. 297 (2015) 534–539. doi:10.1016/j.jpowsour.2015.06.139.

[155] Dispersing process. http://www.inkline.gr/inkjet/newtech/tech/dispersion/ (accessed December 10, 2017).

[156] Vanderbilt Minerals, DARVAN® C-N, (2006).

[157] T. Fengqiu, H. Xiaoxian, Z. Yufeng, G. Jingkun, Effect of dispersants on surface chemical properties of nano-zirconia suspensions, Ceram. Int. 26 (2000) 93–97. doi:10.1016/S0272-8842(99)00024-3.

[158] B.P. Singh, S. Bhattacharjee, L. Besra, D.K. Sengupta, Evaluation of dispersibility of aqueous alumina suspension in presence of Darvan C, 30 (2004) 939–946. doi:10.1016/j.ceramint.2003.11.007.

[159] B.P. Singh, S. Bhattacharjee, L. Besra, D.K. Sengupta, Electrokinetic and adsorption studies of alumina suspensions using Darvan C as dispersant, J. Colloid Interface Sci. 289 (2005) 592–596. doi:10.1016/J.JCIS.2005.03.096.

[160] G. Suárez, M.P. Albano, L.B. Garrido, E.F. Aglietti, Dispersion of concentrated aqueous yttria-stabilized zirconia with ammonium polyacrylate, Ceram. Int. 33 (2007) 925–929. doi:10.1016/J.CERAMINT.2006.02.003.

[161] B.P. Singh, S. Nayak, S. Samal, S. Bhattacharjee, L. Besra, The role of poly ( methacrylic acid ) conformation on dispersion behavior of nano TiO2 powder, Appl. Surf. Sci. 258 (2012) 3524–3531. doi:10.1016/j.apsusc.2011.11.107.

[162] A. Kristoffersson, E. Roncari, C. Galassi, Comparison of different binders for water-based tape casting of alumina, J. Eur. Ceram. Soc. 18 (1998) 2123–2131. doi:10.1016/S0955-2219(98)00165-4.

[163] J.M. LeBeau, Y. Boonyongmaneerat, Comparison study of aqueous binder systems for slurry-based processing, Mater. Sci. Eng. A. 458 (2007) 17–24. doi:10.1016/j.msea.2007.01.112.

[164] C.W. NIES, G.L. MESSING, Effect of Glass-Transition Temperature of Polyethylene Glycol-Plasticized Polyvinyl Alcohol on Granule Compaction, J. Am. Ceram. Soc. 67 (1984) 301–304. doi:10.1111/j.1151-2916.1984.tb18852.x.

[165] P.P. Nampi, S. Kume, Y. Hotta, K. Watari, M. Itoh, H. Toda, A. Matsutani, The effect of polyvinyl alcohol as a binder and stearic acid as an internal lubricant in the formation, and subsequent sintering of spray-dried alumina, Ceram. Int. 37 (2011) 3445–3450. doi:10.1016/J.CERAMINT.2011.05.149.

[166] R. Taktak, S. Baklouti, J. Bouaziz, Effect of binders on microstructural and mechanical properties of sintered alumina, Mater. Charact. 62 (2011) 912–916. doi:10.1016/J.MATCHAR.2011.06.011.

[167] D. Hotza, P. Greil, Review: aqueous tape casting of ceramic powders, Mater. Sci. Eng. A. 202 (1995) 206–217. doi:10.1016/0921-5093(95)09785-6.

[168] O. Introduction, M. Experimental, P. Sample, P. Results, D. Conclusions, A. Horiba, Determination of the Isoelectric Point Using Zeta Potential, (2011) 1–9.

[169] Malvern Instruments Ltd., Zeta potential: An Introduction in 30 minutes, 2011. https://www.malvernpanalytical.com/en/learn/knowledge-center/technical-notes/TN101104ZetaPotentialIntroduction (accessed July 12, 2019).

[170] Matc Applied Sciences, What is Zeta Potential? A brief description., (n.d.). http://www.matecappliedsciences.com/mas/applications/WhatIsZetaPotential/.

[171] Malvern Instruments Ltd., Getting Started - Manual Malvern Instruments, MAN 0101. (1997). http://www.malvern.com/Assets/Mastersizer-S-X-getting-started-manual-English-MAN0101-1-3.pdf.

[172] Z. Zhou, P.J. Scales, D. V Boger, Chemical and physical control of the rheology of concentrated metal oxide suspensions, Chem. Eng. Sci. 56 (2001) 2901–2920. doi:10.1016/S0009-2509(00)00473-5.

[173] CROW © 2015 polymerdatabase.com, Polymer Properties Database, (n.d.). https://polymerdatabase.com/polymer physics/Viscosity2.html (accessed September 10, 2018).

[174] B. Medina Rodriguez, Inkjet and screen printing for electronic applications, University of Barcelona, 2016. http://hdl.handle.net/2445/107156.

[175] S.D. Hoath, I.M. Hutchings, G.D. Martin, T.R. Tuladhar, M.R. Mackley, D. Vadillo, Links Between Ink Rheology, Drop-on-Demand Jet Formation, and Printability, J. Imaging Sci. Technol. 53 (2009) 041208. doi:10.2352/j.imagingsci.technol.2009.53.4.041208.

[176] D.C. Vadillo, T.R. Tuladhar, A.C. Mulji, M.R. Mackley, The rheological characterization of linear viscoelasticity for ink jet fluids using piezo axial vibrator and torsion resonator rheometers, J. Rheol. (N. Y. N. Y). 54 (2010) 781–795. doi:10.1122/1.3439696.

[177] D.C. Vadillo, S.D. Hoath, W. Hsiao, M.R. Mackley, The effect of inkjet ink

composition on rheology and jetting behavior, in: 27th Int . Conf . Digit. Print. Technol. , NIP27 , Minneap. , MN , USA , 2011 , 568-572 , ', 2011: pp. 568–572.

[178] S.D. Hoath, D.C. Vadillo, O.G. Harlen, C. McIlroy, N.F. Morrison, W.-K. Hsiao, T.R. Tuladhar, S. Jung, G.D. Martin, I.M. Hutchings, Inkjet printing of weakly elastic polymer solutions, J. Nonnewton. Fluid Mech. 205 (2014) 1–10. doi:10.1016/j.jnnfm.2014.01.002.

[179] H. Yoo, C. Kim, Generation of inkjet droplet of non-Newtonian fluid, Rheol. Acta. 52 (2013) 313–325. doi:10.1007/s00397-013-0688-4.

[180] Kruss-scientific, Wilhelmy plate method, (n.d.). https://www.kruss-scientific.com/services/education-theory/glossary/wilhelmy-plate-method/ (accessed March 10, 2019).

[181] Art Gatenby, Initiation to contact angle., CSC Sci. Blog. (n.d.). https://www.cscscientific.com/csc-scientific-blog/initiation-to-contact-angle (accessed March 11, 2019).

[182] J. Tallgren, M. Bianco, O. Himanen, O. Thomann, J. Kiviaho, J. van Herle, Evaluation of Protective Coatings for SOFC Interconnects, in: ECS Trans., 2015: pp. 1597–1608. doi:10.1149/06801.1597ecst.

[183] J. Tallgren, O. Himanen, M. Bianco, J. Mikkola, O. Thomann, M. Rautanen, J. Kiviaho, J. Van herle, Method to Measure Area Specific Resistance and Chromium Migration Simultaneously from Solid Oxide Fuel Cell Interconnect Materials, Fuel Cells. (2019) 570–577. doi:10.1002/fuce.201800169.

[184] C.A. Schneider, W.S. Rasband, K.W. Eliceiri, NIH Image to ImageJ: 25 years of image analysis, Nat. Methods. 9 (2012) 671–675. doi:10.1038/nmeth.2089.

[185] D. Sette, Functional printing : from the study of printed layers to the prototyping of flexible devices, Univerite De Grenoble, 2014.

[186] S. Kittaka, T. Morimoto, Isoelectric point of metal oxides and binary metal oxides having spinel structure, J. Colloid Interface Sci. 75 (1980) 398–403. doi:10.1016/0021-9797(80)90464-6.

[187] D. Houivet, E. Fallah, J. Haussonne, Dispersion and Grinding of Oxide Powders into an Aqueous Slurry, 28 (2002) 321–328.

[188] L. Jin, X. Mao, S. Wang, M. Dong, Optimization of the rheological properties of yttria suspensions, Ceram. Int. 35 (2009) 925–927. doi:10.1016/j.ceramint.2008.03.009.

[189] J.-H. Jean, H.-R. Wang, Dispersion of Aqueous Barium Titanate Suspensions with Ammonium Salt of Poly(methacrylic acid), J. Am. Ceram. Soc. 81 (2005) 1589–1599. doi:10.1111/j.1151-2916.1998.tb02521.x.

[190] J. Jean, H. Wang, Effects of Solids Loading , pH , and Polyelectrolyte Addition on the Stabilization of Concentrated Aqueous BaTiO 3 Suspensions, 80 (2000) 277–280.

[191] V.A. Hackley, Colloidal Processing of Silicon Nitride with Poly(acrylic acid): I, Adsorption and Electrostatic Interactions, J. Am. Ceram. Soc. 80 (2005) 2315–2325. doi:10.1111/j.1151-2916.1997.tb03122.x.

[192] M. Victoria, A. Umaran, R. Labandera, Aqueous Dispersion of Red Clay-based

Ceramic Powder with the Addition of Starch, 16 (2013) 375–384. doi:10.1590/S1516-14392013005000002.

[193] M. Singlard, A. Aimable, M. Lejeune, C. Dossou-yovo, M. Poncelet, R. Noguéra, C. Modes, Aqueous suspensions of glass silicate dielectric powders for ink-jet printing applications, Powder Technol. 266 (2014) 303–311. doi:10.1016/j.powtec.2014.06.044.

[194] B. Bitterlich, C. Lutz, A. Roosen, Rheological characterization of water-based slurries for the tape casting process, Ceram. Int. 28 (2002) 675–683. doi:10.1016/S0272-8842(02)00027-5.

[195] C. Miao, R. Shen, M. Wang, S.N. Shafrir, H. Yang, S.D. Jacobs, Rheology of aqueous magnetorheological fluid using dual oxide-coated carbonyl iron particles, J. Am. Ceram. Soc. 94 (2011) 2386–2392. doi:10.1111/j.1551-2916.2011.04423.x.

[196] M. Michálek, G. Blugan, T. Graule, J. Kuebler, Comparison of aqueous and non-aqueous tape casting of fully stabilized ZrO2suspensions, Powder Technol. 274 (2015) 276–283. doi:10.1016/j.powtec.2015.01.036.

[197] A. Karppinen, A.H. Vesterinen, T. Saarinen, P. Pietikäinen, J. Seppälä, Effect of cationic polymethacrylates on the rheology and flocculation of microfibrillated cellulose, Cellulose. 18 (2011) 1381–1390. doi:10.1007/s10570-011-9597-9.

[198] D. Gardini, M. Deluca, M. Nagliati, C. Galassi, Flow properties of PLZTN aqueous suspensions for tape casting, Ceram. Int. 36 (2010) 1687–1696. doi:10.1016/J.CERAMINT.2010.03.011.

[199] A.U. Khan, B.J. Briscoe, P.F. Luckham, Interaction of binders with dispersant stabilised alumina suspensions, Colloids Surfaces A Physicochem. Eng. Asp. 161 (2000) 243–257. doi:10.1016/S0927-7757(99)00374-X.

[200] J. A.Lewis, Colloidal processing of ceramics and composites, Jounal Am. Ceram. Scociety. 111 (2000) 246–253. doi:10.1179/1743676111Y.0000000075.

[201] W.D. Teng, M.J. Edirisinghe, J.R.G. Evans, Optimization of Dispersion and Viscosity of a Ceramic Jet Printing Ink, J. Am. Ceram. Soc. 80 (2005) 486–494. doi:10.1111/j.1151-2916.1997.tb02855.x.

[202] K. Woo, D. Jang, Y. Kim, J. Moon, Relationship between printability and rheological behavior of ink-jet conductive inks, Ceram. Int. 39 (2013) 7015–7021. doi:10.1016/j.ceramint.2013.02.039.

[203] D. Soltman, V. Subramanian, Inkjet-Printed Line Morphologies and Temperature Control of the Coffee Ring Effect, Langmuir. 24 (2008) 2224–2231. doi:10.1021/la7026847.

[204] R.D. Deegan, O. Bakajin, T.F. Dupont, G. Huber, S.R. Nagel, T.A. Witten, Capillary flow as the cause of ring stains from dried liquid drops, Nature. 389 (1997) 827–829. doi:10.1038/39827.

[205] D. Der Ingenieurwissenschaften, A. Soleimani-dorcheh, Oxidation-Nitridation of Chromium at High Temperatures and its Mitigation by Alloying, 2017.

[206] N.J. Magdefrau, L. Chen, E.Y. Sun, J. Yamanis, M. Aindow, Formation of spinel reaction layers in manganese cobaltite – coated Crofer22 APU for solid oxide fuel cell

interconnects, J. Power Sources. 227 (2013) 318–326. doi:10.1016/J.JPOWSOUR.2012.07.091.

[207] M. Bednarz, S. Molin, M. Bobruk, M. Stygar, E. Długoń, M. Sitarz, T. Brylewski, High-temperature oxidation of the Crofer 22 H ferritic steel with Mn1.45Co1.45Fe0.1O4 and Mn1.5Co1.5O4 spinel coatings under thermal cycling conditions and its properties, Mater. Chem. Phys. 225 (2019) 227–238. doi:10.1016/J.MATCHEMPHYS.2018.12.090.

[208] J. Niittynen, R. Abbel, M. Mäntysalo, J. Perelaer, U.S. Schubert, D. Lupo, Alternative sintering methods compared to conventional thermal sintering for inkjet printed silver nanoparticle ink, Thin Solid Films. 556 (2014) 452–459. doi:10.1016/J.TSF.2014.02.001.

[209] N. Grünwald, D. Sebold, Y.J. Sohn, N.H. Menzler, R. Vaßen, Self-healing atmospheric plasma sprayed Mn1.0Co1.9Fe0.1O4 protective interconnector coatings for solid oxide fuel cells, J. Power Sources. 363 (2017) 185–192. doi:10.1016/J.JPOWSOUR.2017.07.072.

[210] J. Yang, W. Huang, X. Wang, J. Li, D. Yan, J. Pu, B. Chi, J. Li, Study on component interface evolution of a solid oxide fuel cell stack after long term operation, J. Power Sources. 387 (2018) 57–63. doi:10.1016/J.JPOWSOUR.2018.03.040.

[211] N. Grünwald, Y.J. Sohn, X. Yin, N.H. Menzler, O. Guillon, R. Vaßen, Microstructure and phase evolution of atmospheric plasma sprayed Mn-Co-Fe oxide protection layers for solid oxide fuel cells, J. Eur. Ceram. Soc. 39 (2019) 449–460. doi:10.1016/J.JEURCERAMSOC.2018.08.027.

[212] C. Goebel, A.G. Fefekos, J.-E. Svensson, J. Froitzheim, Does the conductivity of interconnect coatings matter for solid oxide fuel cell applications?, J. Power Sources. 383 (2018) 110–114. doi:10.1016/J.JPOWSOUR.2018.02.060.

[213] E. Konysheva, H. Penkalla, E. Wessel, J. Mertens, U. Seeling, L. Singheiser, K. Hilpert, Chromium poisoning of perovskite cathodes by the ODS alloy Cr5Fe1 Y2 O3 and the high chromium ferritic steel Crofer22APU, J. Electrochem. Soc. 153 (2006) 2–10. doi:10.1149/1.2172563.

[214] L. V. Gambino, N.J. Magdefrau, M. Aindow, Microstructural effects of the reduction step in reactive consolidation of manganese cobaltite coatings on Crofer 22 APU, Mater. High Temp. 32 (2015) 142–147. doi:10.1179/0960340914Z.00000000090.

# Appendix I

**Python code used for the K-clustering in surface SEM images to estimate the pore volume of inkjet printed layers.**

```
import numpy as np
from scipy.cluster import vq
import matplotlib.pyplot as plt
img = plt.imread(file name')
z = img.reshape((-1,1))
z = z.astype(np.float32)
k = 4 # Number of clusters
center,dist = vq.kmeans(z,k)
code,distance = vq.vq(z,center)
res = center[code]
res2 = res.reshape((img.shape))
"""
res2_cpy = np.copy (res2)
res2_unique_vals = np.unique(res2_cpy)
for index, val in enumerate(res2_unique_vals):
   res2_cpy[res2_cpy == val] = np.abs((index-3))
plt.figure()
plt.imshow(res2_cpy, cmap=plt.get_cmap('gray'))
"""
plt.figure()
plt.imshow(res2, cmap=plt.get_cmap('gray'))
plt.figure()
plt.imshow(img, cmap=plt.get_cmap('gray'))
```

# Appendix II

Images of K-clustering performed on surface SEM images for the pore volume calculation:

**1.SEM images of as deposited coatings ( SEM micrographs shown in, Chapter 5, Fig. 5.2 (a-c)).**

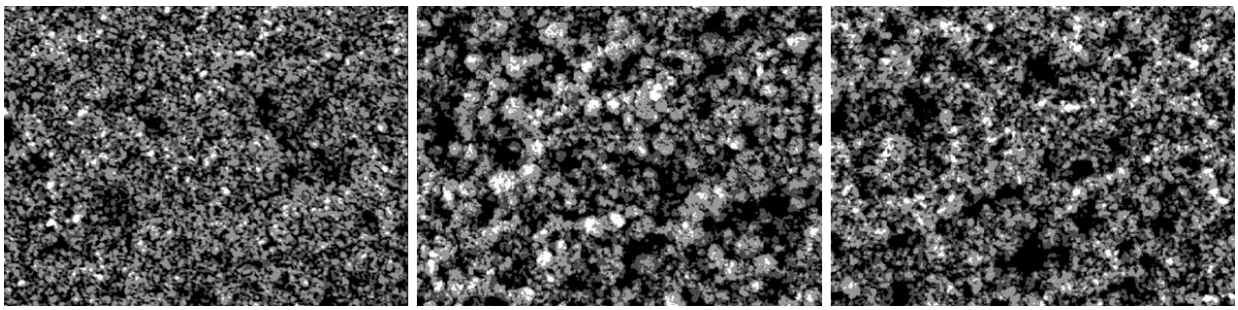

**2. SEM images after oxidation of Batch I samples ( SEM micrographs shown in, Chapter 5, Fig. 5.8)**

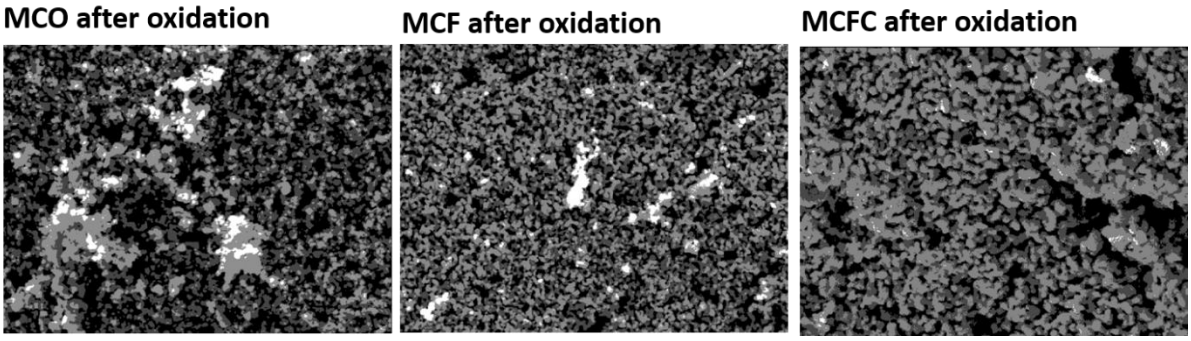


3. **SEM images of Batch II, as deposited coatings( SEM micrographs shown in, Chapter 5, Fig. 5.31 (a-b).**

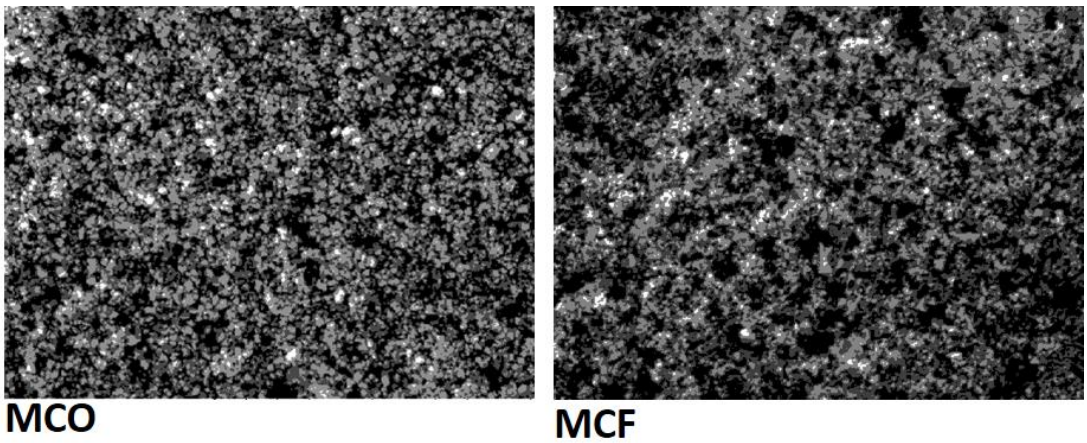

**4. SEM images after reactive sintering ,Batch II samples ( SEM micrographs shown in, Chapter 5, Fig. 5.31, (c) and (d)).**

MCO reactive sintered

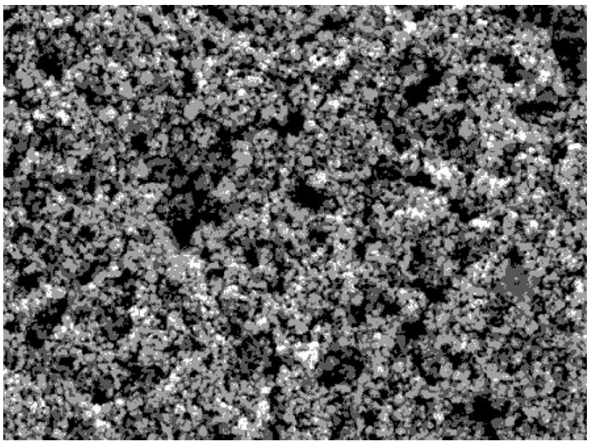

MCF reactive sintered

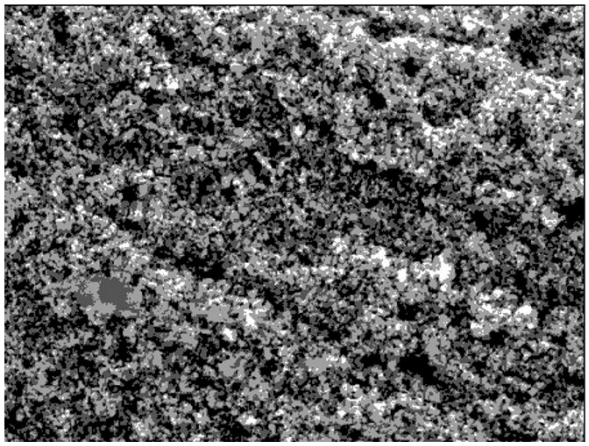

**5. SEM images after oxidation, K41 substrate, Batch II samples ( SEM micrographs shown in, Chapter 5, Fig. 5.34).**

MCO before oxidation

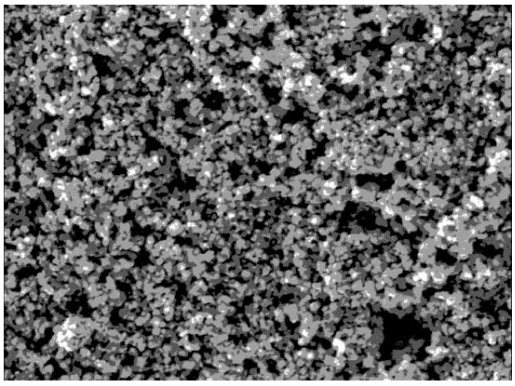

MCF before oxidation

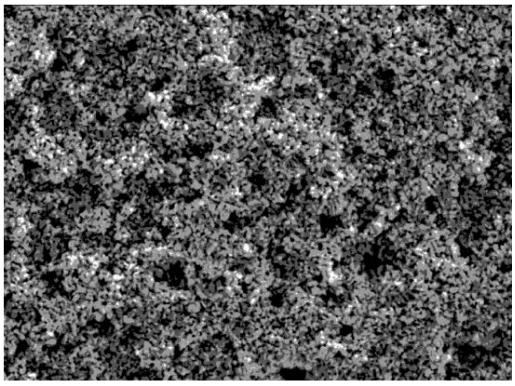

MCO after oxidation

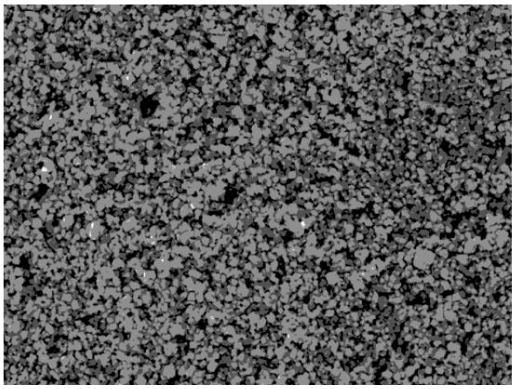

MCO after oxidation

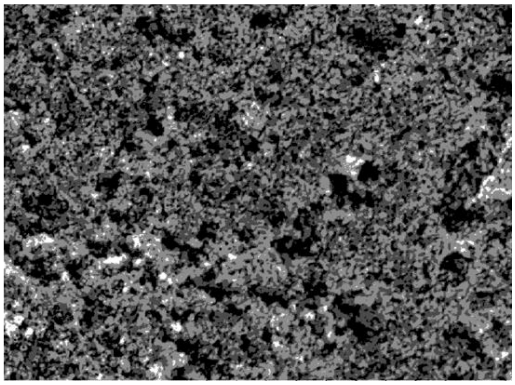

# Appendix III

**SEM micrographs of Batch II samples after 1000 hours of oxidation.**

Few micrographs from the samples are shown here.

MCO and MCF coating on K41

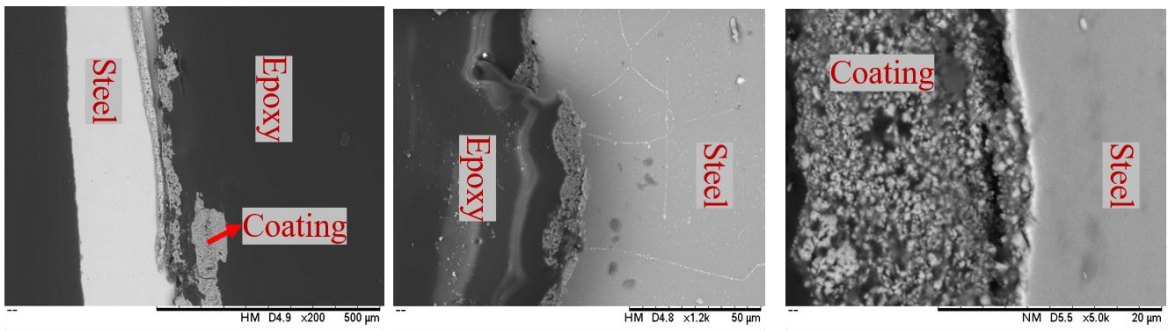


MCO and MCF coating on Crofer

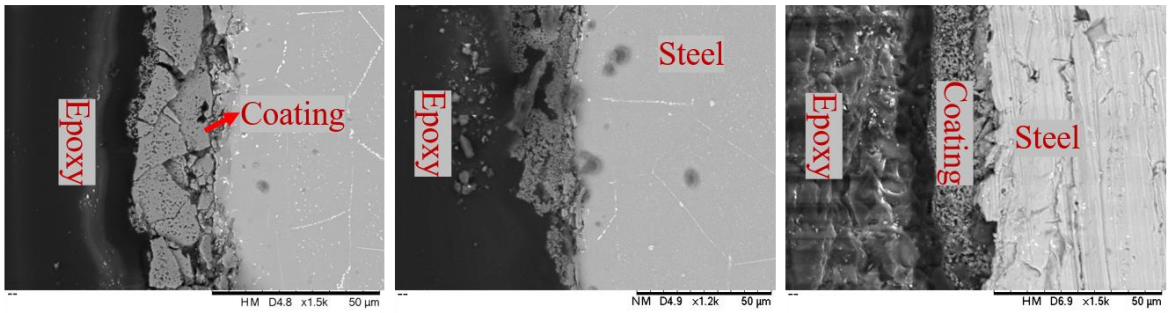

# Appendix IV

An attempt was made to adapt Epson 1400 desktop inkjet printer for printing the formulated spinel inkjet inks. The inkjet printer was modified as (shown in the image) based on the manual from Alienbunker DTG tutorial. The inkjet printer's print head was rested on a wooden block set-up equipped with a moving plate like a slider. The slider moves to and fro through the printhead and acts a sample carrier. The height of the slider can be adjusted thus allowing to place the sample over a hot substrate during the printing process.

Prior to test printing on the built model, spinel inkjet inks were filled in ink cartridges on dismantled printer. The formulated inks were able to print through in paper. However, after modification the ink cartridges did not function properly, displaying cartridge empty always, even when original epson inks were used. It was figured out that issue could be because of hardware issues and so the attempt was suspended. The tutorial for the printer set-up can be found at https://alienbunker.com/.

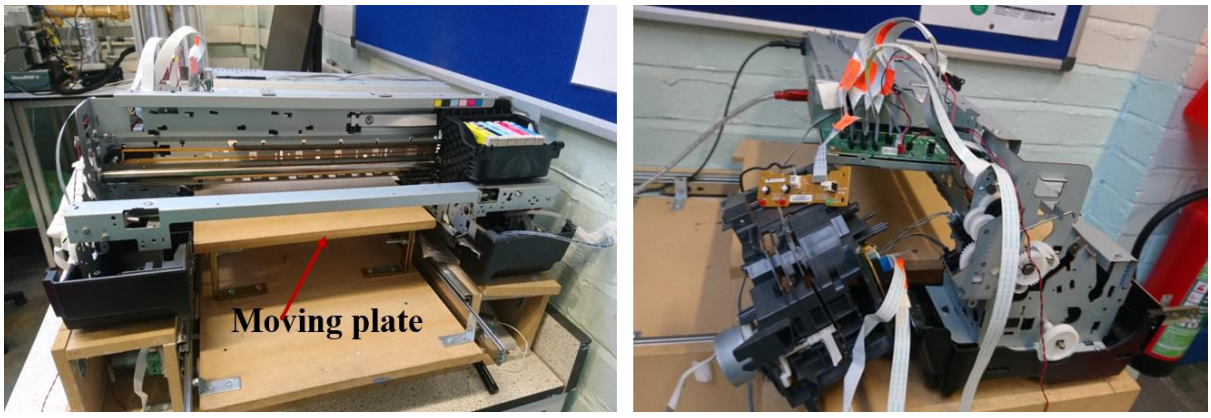


**Images of modified EPSON 1400 printer.**